Electrode Structuring by Ultrashort Laser Pulses

A new Tool for the Hydrogen Economy

Von der **NATURWISSENSCHAFTLICHEN FAKULTÄT** der
GOTTFRIED WILHELM LEIBNIZ UNIVERSITÄT HANNOVER

zur Erlangung des Grades

Doktor der Naturwissenschaften
(Dr. rer. nat.)

genehmigte Dissertation
von

Karsten Lange, M. Sc.

2019

Referent: Prof. Dr. Jürgen Caro
Korreferent: Prof. Dr. Uwe Schröder
Tag der Promotion: 29.03.2019

ABSTRACT

Our energy system and the energy market have changed radically with the use of energies from the renewable sources solar and wind due to their highly fluctuating power generation. The share of renewable energies in the energy mix can therefore only be further increased, if economically viable solutions for the storage of energy are considered. In the concept of the hydrogen economy, hydrogen will be used as the main energy carrier. The sustainable production of hydrogen achieved by the electrochemical splitting of water into hydrogen and oxygen and their later utilization in fuel cells include the exchange of electrons on an electrode. Due to the fast kinetics of the hydrogen related reactions, the catalysis of the electrochemical oxygen reactions become the actual bottleneck, namely the oxygen evolution reaction—OER (water electrolysis) and the oxygen reduction reaction—ORR (fuel cells). By enlarging the electrochemically usable electrode surface area, the efficiency of these reactions can be increased.

In the present thesis, ultrashort laser pulses (shorter than a few picoseconds) were used to generate various surface-rich structures on metal electrodes. For this purpose, the first systematic study of the surface area enlargement of platinum electrodes using the laser-induced surface structures LIPSS, CLP and black metal was examined.

Especially, the black metal surface structure exhibited an exceptionally high surface area increase of 1500 times compared to a polished platinum surface. Subsequently, the black metal surface structure was transferred to less expensive electrode materials, especially to nickel. In order to prevent oxidation of the material during the process and therefore to ensure good electrical conductivity of the electrode, the laser structuring was carried out in argon atmosphere. During the investigations, a new highly porous surface structure was discovered and it was called laser-induced nano-foam (LINF). Therefore, a nickel electrode was scanned with a laser beam in a line pattern. Thus, the surface of the LINF nickel electrodes was increased by a factor of 1600. The surface area of the LINF electrodes is adjustable by variation of the distance between the lines. In addition, this thesis shows how ultrashort laser pulses can be used to activate or deactivate certain areas of an electrode surface for gas evolving reactions, e. g. OER. The analysis of the irradiated surfaces with X-ray photoelectron spectroscopy (XPS) showed that the laser treatment produces defect sites close to the surface. The defects promote the formation of catalytically active phases such as the OER-active β-NiOOH phase, which increases wettability and thus facilitates the removal of gas bubbles from the laser-structured electrodes.

Keywords: femtosecond laser structuring, surface structures, surface area enlargement, black metals, oxygen evolution reaction, oxygen reduction reaction

KURZZUSAMMENFASSUNG

Unser Energiesystem und der Energiemarkt haben sich mit dem Einsatz von erneuerbaren Energien wie Sonne und Wind aufgrund ihrer stark schwankenden Stromerzeugung grundlegend verändert. Der Anteil der erneuerbaren Energien am Energiemix kann nur dann weiter erhöht werden, wenn wirtschaftlich sinnvolle Lösungen zur Speicherung von Energie in Betracht gezogen werden. Im Konzept der Wasserstoffwirtschaft wird Wasserstoff als Hauptenergieträger eingesetzt. Die nachhaltige Erzeugung von Wasserstoff durch die elektrochemische Spaltung von Wasser in Wasserstoff und Sauerstoff und die spätere Nutzung in Brennstoffzellen beinhalten den Übergang von Elektronen aus einer bzw. in eine Elektrode. Aufgrund der schnellen Kinetik der wasserstoffbezogenen Reaktionen besteht der eigentliche Engpass in der Katalyse der elektrochemischen Sauerstoffreaktionen, nämlich der Sauerstoffentwicklungsreaktion - OER (Wasserelektrolyse) und der Sauerstoffreduktions-reaktion - ORR (Brennstoffzellen). Durch eine Vergrößerung der elektrochemisch verwendbaren Elektrodenoberfläche kann die Effizienz dieser Reaktionen gesteigert werden.

In der vorliegenden Arbeit wurden ultrakurze Laserpulse (kürzer als einige Pikosekunden) verwendet, um verschiedene oberflächenreiche Strukturen auf Metallelektroden zu erzeugen. Hierfür wurde die erste systematische Studie über die Vergrößerung der Oberfläche von Platinelektroden mittels laserinduzierter Strukturen LIPSS, CLPs und „black metal“ durchgeführt. Besonders die Oberflächenstruktur „black metal“ zeigte eine hervorragende Oberflächenzunahme um den Faktor 1500 im Vergleich zu einer polierten Platinoberfläche. Anschließend wurde die „black metal“ Struktur auf kostengünstigere Elektrodenmaterialien, insbesondere auf Nickel, übertragen. Um eine gute elektrische Leitfähigkeit der Elektrode zu gewährleisten, wurde der Laser-strukturierungsprozess in Argon-Atmosphäre durchgeführt, dies verhinderte die Oxidation des Materials während der Strukturierung. Im Rahmen der Untersuchungen wurde eine neue hochporöse Oberflächenstruktur entdeckt und laserinduzierter Nanoschaum (LINF) genannt. Hierfür wurde eine Nickelelektrode mit dem Laserstrahl in einem Linienmuster bearbeitet. So konnte die Oberfläche der Nickelelektrode durch LINF um den Faktor 1600 vergrößert werden. Die Oberflächenvergrößerung der LINF-Elektroden ist durch Variation des Abstands zwischen den Linien einstellbar. Darüber hinaus wird in dieser Arbeit beschrieben, wie durch Bestrahlung mit ultrakurzen Laserpulsen bestimmte Bereiche auf einer Elektrodenoberfläche für Gasentwicklungsreaktionen, z. B. OER, entweder aktiviert oder deaktiviert werden können. Die Analyse der bestrahlten Oberflächen mit Röntgenphoto-elektronenspektroskopie (XPS) ergab, dass die Laserbehandlung oberflächennahe Defektstellen erzeugt. Die Defekte begünstigen die Bildung katalytisch aktiver Phasen wie der OER-aktiven β-NiOOH Phase, was die Benetzbarkeit erhöht und somit die Entfernung von Gasblasen von den laserstrukturierten Elektroden erleichtert.

Stichworte: Laserstrukturierung, Oberflächenstrukturen, Oberflächenvergrößerung, „Schwarze Metalle“, Sauerstoffentwicklungsreaktion, Sauerstoffreduktionsreaktion

ACKNOWLEDGMENT

At this point, I would like to thank all those who accompanied me in the context of this work.

First of all, I would like to thank Prof. Dr. Jürgen Caro for the opportunity, the freedom and the confidence he provided to me to work on this exciting topic. Further, I enjoyed the support and encouragement of Prof. Dr. Uwe Schröder and the whole ELEKTROBAK project group.

I thank LPKF LASER & ELECTRONICS AG for the laser structuring of numerous samples and especially Dr. Malte Schulz-Ruhtenberg for the many hours in the lab working with me and for his constructive comments regarding the papers. I would like to offer my special thanks to the FRAUNHOFER ILT for the opportunity to work at an ultrashort pulse laser system and particularly Dr. Christian Hördemann for the valuable contribution to the discovery of the laser-induced nano-foam structure. Further thanks go to Jürgen Koch of the LASER ZENTRUM HANNOVER E.V., for the preparation of the spiky electrodes and the help with the associated paper. I would like to extend my thanks to Dr. Gerhard Lilienkamp and Wanja Dziony of the TU CLAUSTHAL for the XPS measurements and interpretation of the associated results.

My greatest appreciations to Mario Wolf and Felix Rieck genannt Best for the excellent work during their master's theses. Moreover, I would like to thank the whole work group for the friendly atmosphere.

Special thanks to Wilfried Becker, Peter Mühr and Markus Köhler for the manufacturing of several reactors and sample holders. From them, I learned a lot about mechanical material processing. In addition, I would like to thank Jan Kuckuck for the preparation of the electronics used in this work. Furthermore, I would like to thank Prof. Dr. Armin Feldhoff and Frank Steinbach for preparing and analyzing TEM samples and cross-section SEM samples, as well as for the general support concerning these techniques.

My deepest appreciation goes to my father Bernd Lange who accompanied my work with his professional and personal advice. Furthermore, a big thanks goes to my sister Katja Lange, who has made a tremendous contribution to the quality of this work and all of the papers discussed here with her outstanding English skills. In addition, I would like to thank my parents, who have enabled my studies through their personal and financial support.

Finally, I would like to express my heartfelt thanks to my wife Maria Lange for her unconditional support and motherly care for our son Henry.

LIST OF ABBREVIATIONS

AEM	anion exchange membrane
AWE	alkaline water electrolyzer
CAES	compressed air energy storage
CCPP	combined-cycle power plant
CLPs	cone-like protrusions
CNG	compressed natural gas
CV	cyclic voltammetry
CVD	chemical vapor deposition
DHTD	dynamic hydrogen template deposition
EDXS	energy dispersive X-ray spectroscopy
EEX	european energy exchange
GDL	gas diffusion layer
HER	hydrogen evolution reaction
HOR	hydrogen oxidation reaction
LINF	laser-induced nano-foam
LIPSS	laser-induced periodic surface structures
LNG	liquefied natural gas
LOHC	liquid organic hydrogen carrier
LSV	linear sweep voltammetry
MEA	membrane electrode assembly
MOF	metal–organic framework
NSTF	nanostructured thin films
OER	oxygen evolution reaction
ORR	oxygen reduction reaction
P2G	power-to-gas
pCLPs	porous cone-like protrusions
PEM	proton exchange membrane
RHE	reverse hydrogen electrode
SEM	scanning electron microscopy
SHE	standard hydrogen electrode
UPD	underpotential deposition
vs	versus
XPS	X-ray photoelectron spectroscopy
XRD	X-ray diffraction
XRM	X-ray microscopy

TABLE OF CONTENTS

1 Introduction

In recent decades, increasing demands of energy and heightened awareness of negative environmental impact have accelerated the transition from fossil fuels to green alternative “renewable” energies (such as solar, wind, and tidal energy). [1] This will fundamentally change the energy system and the energy market, because the renewable energies are substantially different from the traditional energy sources: their electricity production depends on weather conditions. This makes the associated electricity production discontinuous due to daily, seasonal and regional factors. The share of renewable energies in the energy mix can therefore only be increased, if renewable energies become manageable. [2] This requires ways to store energy on a large scale over a longer period of time. Therefore, it is essential to develop innovative reliable energy conversion and storage technologies.

With the term of the "Energiewende", Germany characterized its claim to an international pioneering role in energy supply. Until today, the share of renewable energies in the energy mix has been pushed to more than 30 %, as a result of targeted promotion. [3] This share is to increase up to 50 % until 2030 according to the Federal Government of Germany. [3] While wind and solar energy can already be predicted quite reliably, the challenge of integrating the highly fluctuating energies into the grid still remains. The result is reflected in the spot price behavior of electric energy that is traded at the European Energy Exchange (EEX). The typical structure of the daily price curve shifts: peak prices are no longer reached at noon, but rather when solar and wind are underrepresented in the electricity mix. [4] Since September 2008, the occurrence of negative prices is accepted, see **Figure 1**. [5] The lack of storage capacity has an absurd consequence: when supply exceeds demand, it is possible to make profit with the consumption of electricity.

The state-of-the-art technology for large scale energy storage in the long-term are pumped-storage power plants, where water is pumped in an upper reservoir in times of low electricity prices. Unfortunately, the missing geological requirements of the landscape in many countries, strictly limits the application of this technology. Hence, chemical energy storage systems are the only technically and economically feasible option to store renewable energy in large quantities in the long-term. Hydrogen plays a key role here, as the most promising energy carrier and storage medium. Hydrogen gas can be produced by water electrolysis using excess energy and can be consumed

on-site, stored, or injected into the natural gas grid. This process is also known as power-to-gas (P2G). [6] In the ambitious concept of the hydrogen economy, hydrogen will eventually replace the classical fossil energy carrier's coal, crude oil and natural gas as well as nuclear energy. As hydrogen can be generated from water with the help of electricity, therefore the hydrogen economy will bring economic independence for countries with low fossil deposits. For example, Japan wants to develop a hydrogen-based energy system as the first country on the planet. To underpin this transition, Japan intends to run the Olympic Games 2020 on a completely hydrogen-based energy infrastructure. [7]

Even though hydrogen is considered one of the most promising technologies in the large-scale integration of renewable energies, only a small share of the currently produced hydrogen is generated by water electrolysis and is further utilized in the energy sector. In this framework, electrochemistry plays an essential role as it allows transformations between electrical and chemical energy, thereby enabling the storage of energy in the form of chemical bonds. [2]

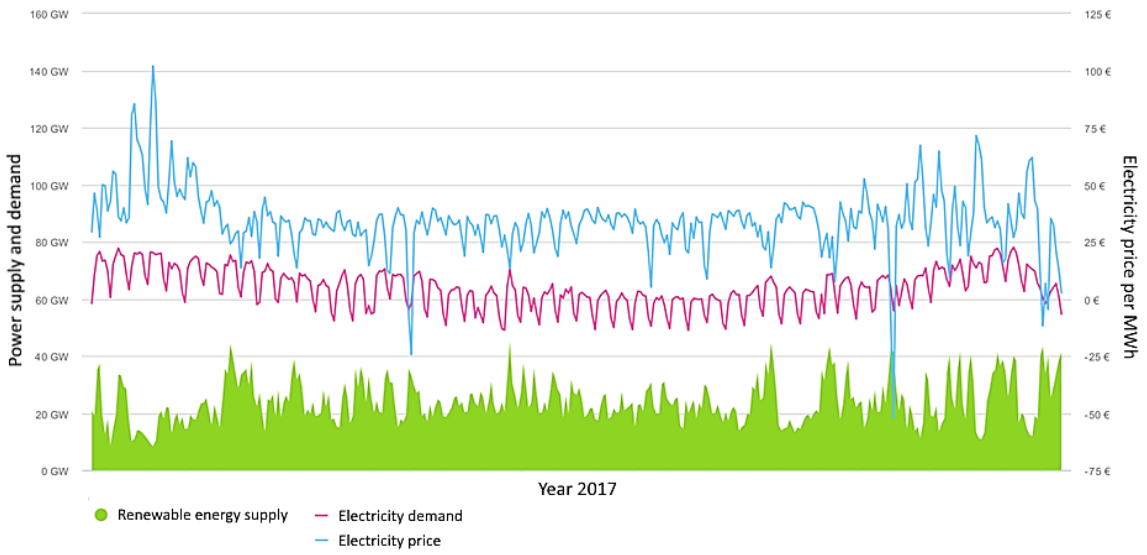

Figure 1: Germany's electric power demand and the supply by renewable energies as well as the resulting electricity price of 2017. During the year, three times electricity was traded for more than 24 hours at negative prices. Reproduced from [8].

1.1 Motivation

For a successful transformation towards a hydrogen economy, researchers and engineers must overcome several challenges to make production, storage and utilization of hydrogen more efficient and therefore hydrogen as an energy carrier competitive to fossil fuels. [9] The sustainable production of hydrogen achieved by the electrochemical splitting of water into hydrogen and oxygen through electricity and the later utilization in fuel cells includes electrochemical reactions. Such surface related processes are based on the exchange of electrons on an electrode. Because the kinetics of hydrogen related reactions are very fast, the actual bottleneck leading to a sustainable efficient hydrogen economy is the development of electrodes for the catalysis of the electrochemical oxygen reactions, namely the oxygen evolution reaction—OER (water electrolysis) and the oxygen reduction reaction—ORR (fuel cells). [2] To improve the efficiency of those reactions, research explores three different approaches:

- find suitable catalytic material; to reduce the activation energy of the electrochemical reaction (potential/voltage),
- provide large accessible surface area; to increase the yield, and
- ensure that the electrode and catalytic active phase have good electrical conductivity.

In recent years, theoretical tools and computational studies have led to significant progress in the atomic-level understanding of the OER and ORR. In parallel, several experimental studies have explored new catalytic materials with advanced activities. [9] Unfortunately, the catalytic materials actually used in both technologies (water electrolysis and fuel cells) so far are more than 20 years old. The focus of many researchers in the field is to synthesize sophisticated electrocatalysts with ultrahigh OER/ORR activities - at least in lab-scale. Most of those electrocatalysts are nano-scaled materials with different shapes and compositions. However, the majority are too difficult and, therefore, too expensive to synthesize in larger scales. Another problem is the durability of those materials. For industrial use in water electrolysis they should last at least 10 years without significant performance loss [10] and for application in fuel cell powered cars at least 250,000 km mileage with stable performance is required. [11]

Alternatively, an obvious but non-trivial approach to increase efficiency is the enlargement of the electrode's surface area. [12] In this respect, the electrocatalytic activity of electrode materials is predominantly connected to the increase of reaction

site density at the electrode-electrolyte interface. [13] For industrial electrodes, three basic concepts are approved:

- mechanical treatment, such as grit blasting,
- coating, such as thermospraying, physical vapor deposition (PVD), chemical vapor deposition (CVD) or roll-to-roll techniques (coating with porous carbon inks), and
- leaching out one compound to obtain microporous surfaces.

Mechanical treatments are in most cases the cheapest option to increase the surface area of electrodes, especially if they are made of metal. However, the surface area enlargement compared to other techniques is relatively low. In addition, material is removed by the mechanical treatment, which limits the application of these techniques to inexpensive electrode materials.

Usually, in industrial electrode processing the desired solid material is coated on top of a highly conductive substrate (typically metal). With thermal spraying, the most common coating technique in the electrode industry, a large variety of materials can be applied including metals, alloys, ceramics, plastics and glass. In general, the coating materials are supplied as powders or wires that are heated to a molten state and accelerated towards the substrates in the form of micro-sized particles. The resulting coatings are made by the accumulation of numerous sprayed particles. An interesting alternative method to obtain three-dimensional porous metal electrodes in large-scale areas was published by Marozzi et al., they realized the electrochemical deposition of metal ions with a simultaneous evolution of H_2 bubbles. The bubbles act as dynamic template for the deposition process (so called dynamic hydrogen template deposition). [14]

In some cases, it is advisable to leach out a component from the previously produced coating to further increase the surface area. The most prominent example is RANEY Ni, where a porous surface structure is obtained by a controlled leaching process of specific phases, e.g. $NiAl_3$ and Ni_2Al_3. [15] Accordingly, this electrode benefits from a tremendously increased accessible surface area and therefore RANEY Ni is the industrial standard catalytic material for alkali water electrolysis cathodes (hydrogen related reactions).

However, large-scale manufacturing of high-performance electrocatalysts remained very difficult. Maintaining a stable adhesion of the catalysts on the conducting substrates to ensure stable performance of the electrode is still a great challenge. Coated electrodes suffer from instability and peeling-off effects, severely limiting their long-term activities. [16] Especially the modification of electrodes with

nanoscale electrocatalysts requires additional binders and additives to assist the adhesion on the substrate. [17]

In this work, an alternative strategy for manufacturing of hierarchical nano- and micro-structured electrodes by laser radiation is pursued. The use of ultrashort laser pulses, shorter than a few picoseconds, allows completely new machining processes that were inconceivable so far with conventional tools. In the medical field, they open up completely new therapeutic options, for example through highly precise and low-damage incisions in the eye. When extremely short laser pulses act on a material, it results in non-linear interaction processes, which practically lead to material removal without heat, which is also referred to as ablation. In addition, this single-step technology enables a contactless machining of almost all materials in almost any shape. The laser beam can be focused to micrometer areas, but, via laser beam scanning large surface areas in the square meter range are also processible. [18] As a result, this high-precision processing leads to more efficient production in various fields, such as solar cell, LED and computer chip manufacturing.

For a long time, ultrashort pulse lasers were only used for researching purpose. In recent years, the development of high-performance ultrashort pulse lasers has achieved substantial progress with medium laser powers of 100 W to 1000 W, which now enables large-scale industrial applications. Besides their conventional applications as a precise tool for drilling and cutting, ultrashort pulse lasers are ideal for the production of micro- and nanostructured surface structures. These laser-induced structures make it possible to provide material surfaces with new properties, for example wettability, adhesive properties or catalytic activity.

1.2 Objectives of the Thesis

Laser-induced surface structures are known for more than 20 years. In the literature a large variety of surface structures namely LIPSS, CLPs, black metals and subtypes are well described and characterized in terms of their optical and mechanical behavior as well as their wettability. On the other hand, a systematic description of their chemical and electrochemical properties is still missing.

The present work will showcase the tremendous potential of laser-induced surface structures for electrochemical applications. For this purpose, fundamental chemical and electrochemical characterization of laser-induced surface structures on well-known electrode materials is carried out. Furthermore, in this thesis the first systematic quantification of the surface area enlargement of already described laser-induced surface structures will be given. Therefore, a representative structure of each type of laser-induced surface structures (LIPSS, CLPs and black metal) is generated on platinum electrodes by variation of the laser parameters (power, scan speed and line distance) and subsequently analyzed by electrochemical methods (cyclic voltammetry and linear sweep voltammetry) in order to determine the surface area and the electrocatalytic activity towards ORR.

The electrocatalytic activity of an electrode material is predominantly connected with the accessible surface area of the electrode. Therefore, the laser structuring process will be optimized in order to develop new highly porous surface structures on catalytic active electrode materials.

The high heating and cooling rates within the laser structuring process may cause a wide range of structural defects in the resulting surface structures, which should positively influence the catalytic behavior. Hence, electrochemical and material analytics such as XRD and XPS will be performed on different kinds of laser-induced surface structures to investigate the structural changes induced by ultrashort laser pulses and their effect on the catalytic activity of the OER and ORR.

Lastly, the localized tuning of the catalytic activity by irradiating only a region on an electrode with ultrashort laser pulses will be addressed.

2 Hydrogen Economy

Hydrogen is an important raw material for the chemical industry, and it may play a central role in the future energy industry. A total of about 19 billion Nm^3 * [19] of hydrogen are generated in Germany and about 600 billion Nm^3 worldwide each year. [20] About half of hydrogen produced in Germany is produced from natural gas, the other half is a by-product of refineries, where it is widely used for hydrogenation. A small proportion (about 2 %) is obtained as a by-product in the chlor-alkali electrolysis. [19] Around 40 % of current demand could be met by using the hydrogen that is produced as a by-product in the industry. 95 % of produced hydrogen is for in-house consumption, only 5 % is sold on the market. [21] The main part of the worldwide produced hydrogen is used for ammonia production. Most of the rest is utilized in the petroleum industry. Only 1 % of hydrogen is related to the food industry (fat hardening), the semi-conductor industry (as carrier gas for silicon deposition and crystal growing), the glass industry (to create a reductive atmosphere over the tin bath in the glass production process) and the metallurgical industry (for instance for direct reduction of iron ore). [22]

In view of the shortage of fossil energy resources, the energy industry is facing a radical change. Amongst the "green" energy technologies, hydrogen will play a leading role as the secondary energy carrier, if a low-cost and climate-neutral hydrogen production from renewable energy sources like wind or solar power can be achieved. In general, primary energy sources as wind and solar must be transformed in energy conversion processes to more suitable forms of energy, so called secondary energy, to make use of it as electrical energy or in the form of synthetic fuels such as hydrogen. Hydrogen is considered as "the ultimate clean energy carrier" because it has the highest mass energy density (33.3 kWh kg^{-1}) [23] of all chemical energy carriers and water is the only by-product of its use. The main benefits of hydrogen as energy storage medium are the full scalability, the ability of long-term/seasonal storage of different renewable energies and the possibility to use it (optionally) as fuel for transportation. [21] To advance the utilization of this green energy carrier, a hydrogen energy cycle of the four stages: **production**, **transportation**, **storage** and **utilization** must be established, see **Figure 2**. In the following, each stage will be

* Nm^3: Standard cubic metre (Normkubikmeter) is the volume of a gas at standard conditions, p = 1.01325 bar, humidity = 0 % and T = 273.15 K.

discussed. Thereby, this thesis is focusing on the production and utilization of hydrogen and in particular on the electrode design.

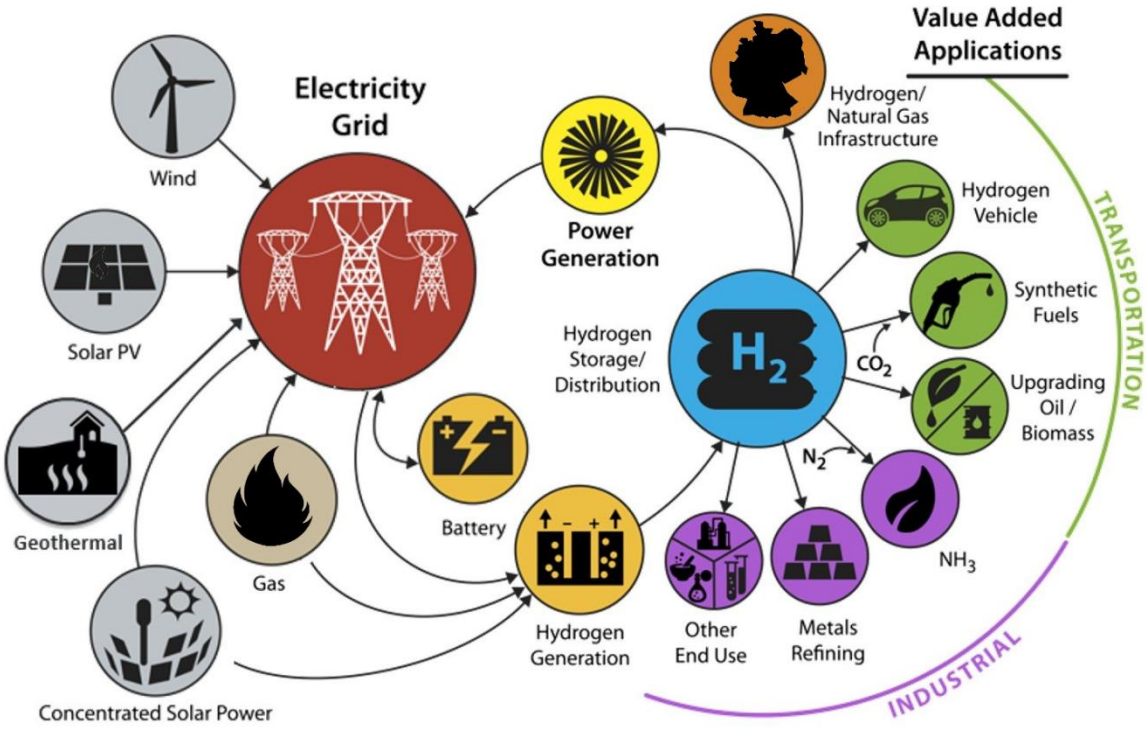

Figure 2: Basic scheme of the hydrogen economy. Different renewable energies produce electricity. The excess electricity is used for hydrogen production via water electrolysis. The hydrogen is either used directly by the industry or as a fuel for fuel cells vehicles. Excess hydrogen is stored or injected in the natural gas grid. In times of low solar and wind power, the stored hydrogen will be burned in gas power plants together with natural gas or electrochemical converted to water in stationary fuel cells. Reproduced form [24].

2.1 Hydrogen Production

Hydrogen production has to satisfy three major requirements in the future:

- It has to follow sustainable pathways,
- use abundant and renewable feedstocks, and
- the produced hydrogen is required to be of high purity, as impurities are harmful for most applications, such as fuel cells.

2.1.1 Fossil-based Hydrogen Production

These days, about 95 % of the industrially used hydrogen is produced by **steam reforming of natural gas** (1). According to the principle of LE CHATELIER this

endothermic process must be carried out at a high temperature, a high steam to methane ratio, and a low pressure to achieve maximum conversion.

$$CH_4 + H_2O \rightleftharpoons 3\,H_2 + CO \quad (1)$$

Subsequently, the carbon monoxide can be utilized to produce additional hydrogen by the **water-gas shift reaction** (2).

$$CO + H_2O \rightleftharpoons H_2 + CO_2 \quad (2)$$

Large-scale plants producing hydrogen from fossil fuels reach a daily capacity of more than 4 million Nm^3 per day. [19] As mentioned before, the main part is used in the HABER-BOSCH process to produce ammonia. For hydrogen production, industrial steam reforming is currently unrivalled in terms of costs and production capacity. However, this hydrogen is still contaminated with CO impurities. The utilization of this hydrogen as a fuel to run fuel cells requires expensive post purification with either membranes [25,26] or by pressure swing adsorption. [27] As a result, the hydrogen is purified to a quality of 99.999 % and delivered to customers as pure hydrogen, mostly compressed to 200 bar. More about hydrogen storage and transportation is given in chapter 2.2.

The second largest hydrogen production process is the technically advanced **partial oxidation process** (3), where heavy hydrocarbons, e.g. heavy fuel oil or residual oils from petroleum processing, react with oxygen in an exothermic reaction. The process is also referred to as gasification because it converts liquid hydrocarbons to gaseous products, essentially H_2 and CO with only small amounts CO_2 and CH_4 when high-purity oxygen is used. [28] Subsequently, the CO reacts, within a water-gas shift reaction, to additional hydrogen. In contrast to the steam reforming process, which is rather limiting with respect to acceptable feedstock properties, for the partial oxidation process, it is only necessary that the viscosity of the feedstock be low to atomize effectively. Thus, nearly any fluid hydrocarbon can serve as a suitable feedstock. [28]

$$C_nH_m + n/2\ O_2 \rightleftharpoons n\,CO + m/2\ H_2 \quad (3)$$

Among the industrially established production processes of hydrogen, the Kvaerner process represents an interesting alternative. Since 1980, the KVAERNER ENGINEERING S.A. from Norway developed a so-called plasma arc process, which separates hydrocarbons between 1200 °C and 2000 °C in carbon black and hydrogen. Only the hydrocarbon (in most cases natural gas), cooling water and electricity are necessary to run this process, which itself does not cause any significant emissions. A

wide range of carbon blacks can be produced by varying the process parameters, such as the gas flow rate, the temperature and the location of gas injection points in the plasma. [29] A pilot plant, which has been operating since April 1992, produces 48000 Nm^3 of hydrogen per day. Considering all potentially exploitable products, such as carbon black, hydrogen and the hot steam from the cooling process, the system works with almost 100 % efficiency. [29] As an alternative to electrical energy as the heat source, solar energy can be used within the solar methane cracking process. Quality and structure of produced carbon have a major impact on the economy of this process. Temperatures above 1816 °C are necessary to produce high quality carbon, which leads to problems regarding material properties and process efficiency. [30] Achievable market price for carbon black is a major factor for the resulting hydrogen costs.

2.1.2 Hydrogen as a By-product in the Chemical Industry

In the petrochemical industry large quantities of hydrogen are produced as by-products. In most cases, this hydrogen is thermally utilized. By far the largest amount of by-product hydrogen is originating from the steam cracking, where long-chain hydrocarbons (naphtha) break down into short-chain hydrocarbons in the presence of water vapor. The main products are hydrogen, methane, ethene and propene. Furthermore, substantial quantities of hydrogen are produced in the large-scale production of acetylene by means of high-temperature pyrolysis of light or medium petroleum fractions or natural gas at 2000 °C. Additionally, some hydrogen is generated via the direct conversion of methane and ammonia to hydrogen cyanide in the DEGUSSA process. Most of the hydrogen coming from petrochemical processes is contaminated by carbon monoxide and therefore not suitable for fuel cell applications.

Alternatively, large quantities of pure hydrogen are produced by chlor-alkali electrolysis, which is the largest electrolytic process producing hydrogen, so far. Thereby, aqueous sodium chloride is electrolyzed to convert chloride ions to chlorine on the anode. At the same time, sodium hydroxide solution and hydrogen are formed on the cathode. The worldwide chlorine production capacity accounts to 80 million tons per year (Germany 4 million tons per year) [31] with a mean energy demand of 3000 kWh per ton of Cl_2 [32]. Thus makes chlorine production one of the most energy intensive industrial processes in the world, with a worldwide energy demand of around 240 TWh per year. It is obvious, that a significant reduction of the energy demand in the chlor-alkali industry is highly desirable. In contrast to water

electrolysis, however, the past forty years have seen a revolution in chlor-alkali technology with the development of both membranes and electrode catalysts specifically for the membrane cell technology. The modern membrane cells use corrosion-resistant anodes made of titanium mixed with ruthenium oxide and steel net cathodes. But the economics of the chlor-alkali industry depend on the sale of chlorine and sodium hydroxide; expansion of hydrogen production on the scale being discussed would produce a vast excess of unsaleable chlorine. However, much can be learned from experience in the chlor-alkali industry, where commercial cathode coatings operate at low overpotential with lifetimes of several years. [33]

2.1.3 Sustainable Hydrogen Production

In order to achieve a hydrogen society in the future, hydrogen production systems need to be able to meet the large demand of hydrogen usage. The most commonly used sustainable method uses fluctuating solar and wind energy to generate hydrogen via electrochemical water splitting. In general, all primary energies - solar radiation, wind energy, water power, tidal energy, and geothermal heat - can be harnessed in the form of electricity and can therefore be converted into hydrogen. Renewable energy is becoming more affordable these days and accordingly the production costs of hydrogen decrease as well. Even though many studies expect water electrolysis to become economically viable in the long run, conventional fossil-based hydrogen production is still hard to underprice. [34]

Alternatively, water can also be photocatalytically split in hydrogen and oxygen. However, this technology is still in the lab-phase of research and might be a suitable supporting option in the future. [35,36] There still remains one question: why should we install photocatalytic water splitting modules instead of well-developed high performance photovoltaic solar panels? There is only one answer that is sufficient satisfiying, the efficiency of photocatalytic water splitting must be higher than the photovoltaic power production and electrochemical water splitting combined. Today, photocatalytic water splitting modules produce hydrogen under natural sun with 0.4 % efficiency. [37]

Another approach to generate hydrogen from solar radiation is to use concentrated solar radiation as the main source for high temperature water decomposition. A solar thermal plant consists of a central receiver system comprised of a circular heliostat field focusing direct solar radiation on a receiving reactor, which is mounted on a tower. On the inside of the reactor, the thermal decomposition of water is performed

on a ceramic support coated with metal oxide, which acts as active redox reagent. In the first step, the activated redox material (reduced metal oxide) is oxidized by the water at 800 °C and pure hydrogen is released. The fully oxidized reagent is regenerated during the second step by increasing temperature to about 1200 °C in an oxygen-lean atmosphere. The release of absorbed oxygen is induced by using nitrogen as flushing gas. The process is expected to achieve an efficiency of more than 70 % related to the solar heat input. [21]

2.1.3.1 Electrochemical Water Splitting

In general, the water splitting reaction can be represented as follows, with molecular hydrogen and oxygen generated at the cathode and anode, respectively.

$$2\,H_2O \xrightarrow{>1.23\ V} 2\,H_2 + O_2 \tag{4}$$

In order to generate hydrogen and oxygen at a specific rate, a voltage at least equal to the standard potential E^0 = 1.23 V must be supplied to the system. The supplied operational voltage E_{op} depends on the kinetics of the water splitting reactions as well as on the design of the electrolyzer and follows [38]:

$$E_{op} = E^0 + \eta_C + \eta_A + \eta_\Omega + \eta_{\text{mass}} + \eta_{\text{bubble}} \tag{5}$$

where η_C and η_A are the overpotentials† required to overcome the kinetic barriers for the hydrogen evolution reaction (HER) at the cathode and the oxygen evolution reaction (OER) at the anode, respectively. η_Ω is the additional overpotential required to compensate for resistance losses within the electrolyzer unit. Mass transport (η_{mass}) of ions to the electrodes via diffusion requires an additional voltage as well as the formation of gas bubbles (η_{bubble}) on the surface of the electrodes. The efficiency of the electrolyzer unit is therefore reflected in the degree to which E_{op} deviates from E^0. In reality, the kinetic limitations are significant, accounting for up to 85 % of the total efficiency losses [39], see **Figure 3**. In alkaline solution, the OER and HER can be described by the following two electrochemical reactions: [38]

$$\text{HER} \quad 4\,H_2O + 4\,e^- \rightarrow 2\,H_2 + 4\,OH^- \qquad (E^0 = 0.0\ V) \tag{6}$$

$$\text{OER} \quad 4\,OH^- \rightarrow O_2 + 2\,H_2O + 4\,e^- \qquad (E^0 = 1.23\ V) \tag{7}$$

† Overpotential η is the potential that needs to be additionally supplied to the system to start the desired reaction. $E_{op} = E^0 + \eta$

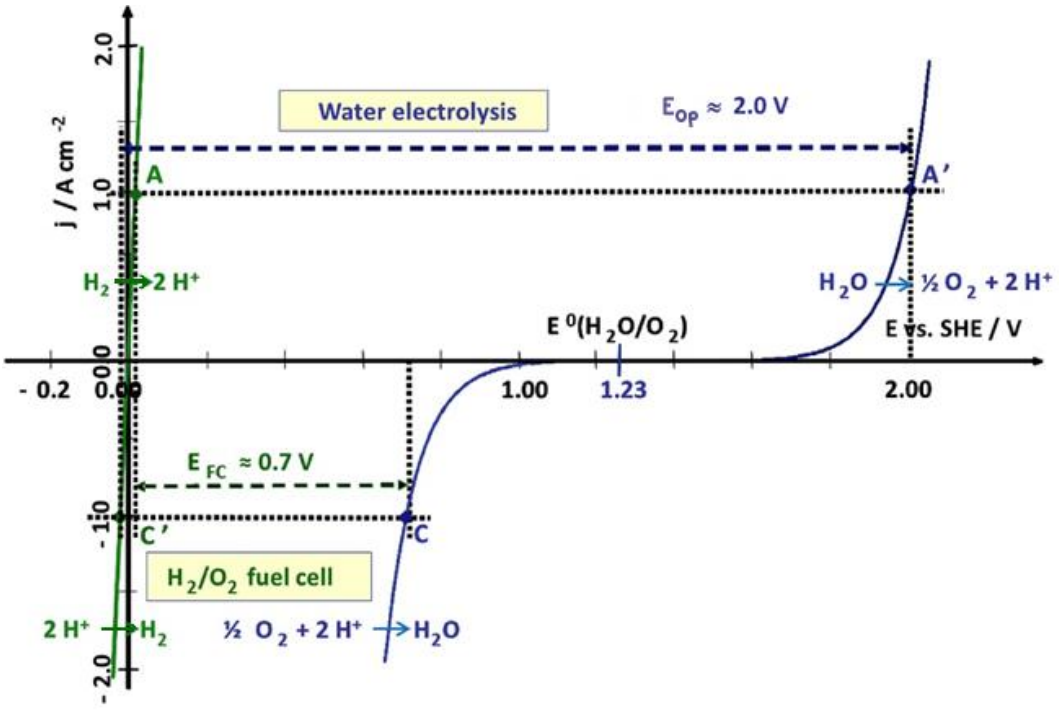

Figure 3: Green: The polarization curves of the hydrogen evolution reaction (HER) and the hydrogen oxidation reaction (HOR) with rather small overpotentials. Blue: the polarization curves of the oxygen reduction reaction (ORR) and the oxygen evolution reaction (OER), both exhibit high overpotentials. Water electrolysis and fuel cell operation voltages E_{op} and E_{FC} showcase the efficiency issue of the hydrogen economy well, which is largely due to the slow kinetics of the oxygen reactions. Reproduced from [40].

Hydrogen Evolution Reaction

The hydrogen evolution reaction (HER) involves reduction of protons with electrons on an electrode surface, generally resulting in a high coverage of adsorbed hydrogen, some of this hydrogen reacts to produce gaseous H_2. It is widely accepted that the HER in alkaline solutions proceeds via three steps, where S represents a surface active site [41]:

Water dissociation: $S + H_2O + e^- \rightleftharpoons S\cdots H_{ad} + OH^-$ (VOLMER) (8)

hydrogen emission: $2\,S\cdots H_{ad} \rightleftharpoons 2\,S + H_2$ (TAFEL) or (9)

$S\cdots H_{ad} + H_2O + e^- \rightleftharpoons S + OH^- + H_2$ (HEYROVSKY) (10)

In a simple thermodynamic analysis, entropy change for the VOLMER reaction is negative, since the H adsorption orders the system, while HEYROVSKY and TAFEL reactions have positive entropy changes due to the desorption of one and two adsorbed H, respectively, to release H_2(g). There are several results reported for HER kinetics on nickel in alkaline solutions indicating that the VOLMER reaction with the transference of one electron is the rate-determining step. [42,43] Subsequently, the TAFEL - and the HEYROVSKY reaction proceed in parallel. In fact, the rates of HER are

so fast that close to the standard potential E^0 the true reaction kinetic is very difficult to measure experimentally. But, due to the high population of participating molecules in alkaline solution hydrogen evolution is not limited by diffusion either. Hence, close to the standard potential HER is one of the least inhibited electrochemical reactions known. The H-adsorption/desorption mechanism requires hydrogen binds well, but not too strongly, to the reaction site S. The exchange currents as a function of the S-H bond strengths describe a "volcano curve", whose maximum is at a bonding energy of 240 kJ mol^{-1}, close to that of Pt-H. [10] Numerous publications [44–47] are available on the characteristics of the HER on platinum catalysts, as it is the most active electrode material. But due to the high price of Pt, steel and nickel usually have been the cathode materials of choice. [34] To optimize the hydrogen bond strength, the combination of nickel and Molybdenum provides the highest catalytic activity with respect to HER. Thus, Mo doped RANEY Ni is utilized for industrial HER electrodes. [48]

Oxygen Evolution Reaction

At first, the HER seems to be the more important reaction because it determines the amount of hydrogen produced. However, the oxygen evolution reaction (OER) kinetics are more sluggish than the HER kinetics and as a consequence, the performance of water electrolysis depends strongly on the OER. The OER occurs at high overpotentials on oxidized metal surfaces and follows a complex multistep mechanism via four electrons and four OH^- transfer steps in alkaline media. In alkaline solutions, all of the proposed reaction mechanisms have the initial adsorption of the hydroxide ions on the catalytically active site as a common step, followed by different highly energetic reaction steps. [9] One of the earliest OER mechanisms in alkaline media has been proposed by YEAGER [49] in 1974 with a reported reaction order of 1, where S represents a surface active site:

$$S + OH^- \rightleftharpoons S - OH + e^- \quad (11)$$

$$S - OH \rightleftharpoons S^+ - OH + e^- \quad (12)$$

$$2\,S^+ - OH + 2\,OH^- \rightleftharpoons O_2 + 2\,S + 2\,H_2O \quad (13)$$

A different mechanism was proposed by BOCKRIS in 1984 [50]:

$$S + OH^- \rightleftharpoons S - OH + e^- \quad (14)$$

$$S - OH + OH^- \rightleftharpoons S\cdots H_2O_2 + e^- \quad (15)$$

$$S\cdots H_2O_2 + OH^- \rightleftharpoons S\cdots HO_2{}^- + H_2O \quad (16)$$

$$S\cdots H_2O_2 + S\cdots HO_2{}^- \rightleftharpoons O_2 + H_2O + OH^- + 2\,S \quad (17)$$

Due to the high overpotential required for the OER, the potential for the anodic oxygen evolution is larger than 1.23 V vs RHE, independent of the used electrocatalyst. This has two consequences: (i) all metal surfaces in an aqueous electrolyte are in fact covered by an oxide layer [9] (ii) at the more positive potential, the driving force for corrosion is higher. Corrosion of both the electrocatalyst and the catalyst support are major concerns for water electrolysis cell technology. [33] RuO_2 and IrO_2, alone or in combination, are often considered the reference OER catalysts, but neither is "ideal"; thermodynamic calculations indicate that RuO_2 binds oxygen a little too weakly, while IrO_2 binds oxygen a little too strongly. [51] RuO_2 and IrO_2 are generally the electrocatalysts of choice in acid solutions but there are doubts concerning their stability in alkaline media as they suffer slow dissolution in alkaline solution. [33] Layered NiFe oxides/hydroxides have been demonstrated as the most active non-noble catalysts in alkaline electrolyte. [1] But, the performance of the catalyst further depends not only on the catalyst material, the support material, the pretreatment, and the resulting microstructure and morphology of the catalyst should be taken into account as well.

Water Electrolyzer

Electrolyzers are a mature technology and able to produce large quantities of hydrogen. Many commercial systems are available; most of them still use separators and catalysts developed centuries ago. The first commercial system was installed by NEL HYDROGEN, formerly NORSK HYDRO from Norway in 1927 to produce pure hydrogen via electrolysis for the HABER-BOSCH ammonia fertilizer process. [34] The crucial factor in hydrogen production technologies is the system efficiency, which is the ratio between the theoretical energy demand to produce 1 Nm^3 of H_2 at 1.23 V (3.0 kWh) and the energy required by the real overall system. [10]

An electrolyzer can be built using either a unipolar or bipolar configuration. When built with a unipolar layout, all positive electrodes, and all negative electrodes respectively, are coupled in parallel. The electrodes are all submerged in one electrolyte bath. The total voltage is the same as that applied to the single cell. This configuration is simple to build, but it does bring rather large ohmic losses.

The bipolar configuration, however, usually uses a zero-gap configuration and each electrode except the end plates is used as both anode and cathode, respectively. The electrodes are coupled in series in that case and the overall voltage is the sum of the voltages of the individual cells. Therefore, this type of electrolyzer is operated at

high voltages and low current densities. This is undesirable as the current density determines the rate of hydrogen production and therefore bipolar modules are usually connected in parallel to increase the current density. Bipolar electrolysis systems show lower ohmic losses than unipolar systems, yet leakage is a more severe issue, resulting in a more complex design, see **Figure 4**. The bipolar layout is also commonly used for PEM fuel cells, see chapter 2.3.2.1.

The electrolyte is one of the most common properties chosen to categorize the electrolyzer unit. It can be distinguished by its pH value (alkaline and acid) or state (liquid electrolyte, polymer electrolyte, or solid oxide electrolyte). Polymer electrolyte membranes used to be based on acidic polymers, but with the rise of anion exchange membranes (AEMs) in past years, membranes are no longer solely proton exchange membranes (PEMs). In the following, the "conventional" alkaline water electrolyzer, the oldest and most common system, as well as the modern PEM - and AEM electrolyzer systems will be showcased.

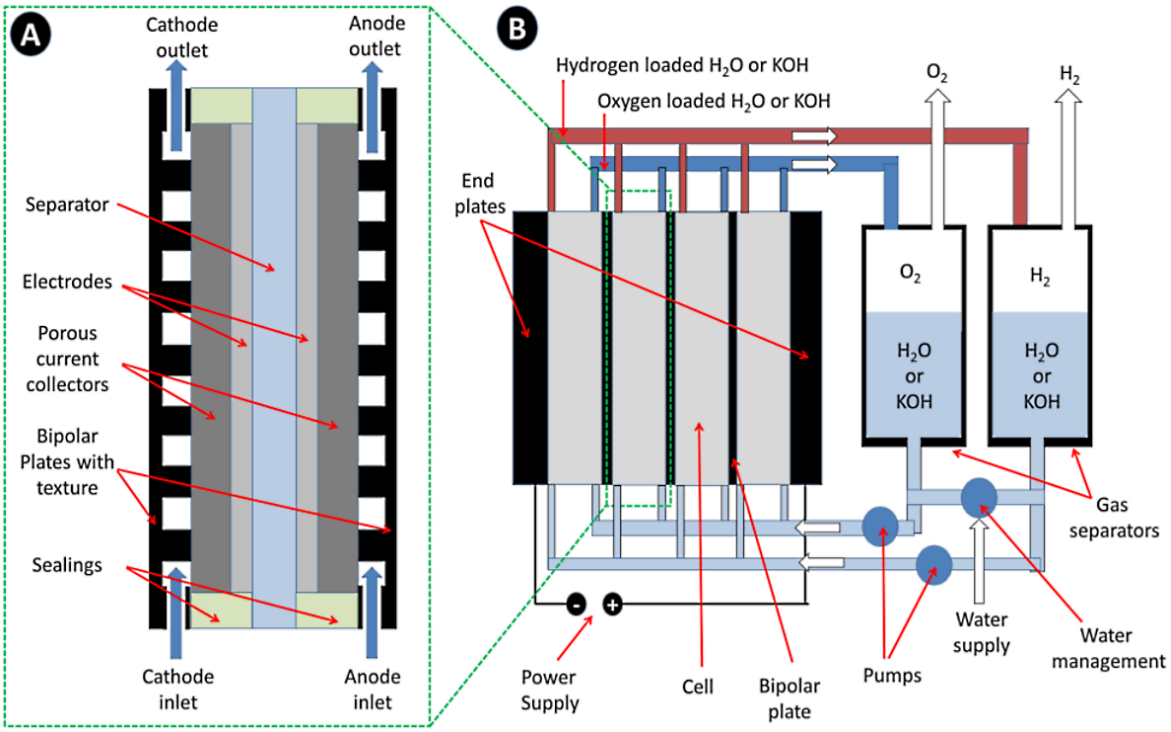

Figure 4: Schematic illustrations of a water electrolysis cell with zero-gap configuration (A) and of a bipolar water electrolyzer (B). Reproduced from [52].

The Alkaline Water Electrolyzer

The alkaline water electrolyzer (AWE) is typically built in a unipolar layout with a cell potential near 2 V at current densities up to 300 mA cm^{-2}. Such systems reach efficiencies near 60 % and demonstrate lifetimes in excess of 10 years and in some cases more than 20 years. [10] AWE is one of the most common technologies to produce hydrogen on a large scale from renewable energy.[53] One major advantage of the alkaline conditions is the viable use of non-precious metals typically nickel foams or stainless steel, which lowers the capital costs of the system significantly. [33]

Polymer Electrolyte Membrane Water Electrolyzer

Polymer electrolyte membrane based electrolysis systems are classified into proton exchange membrane (PEM) and anion exchange membrane (AEM) water electrolyzers depending on the type of ions passed through the polymer membrane. PEM water electrolyzers have been reported to show higher hydrogen production energy efficiency than AEM electrolyzers, owing to the high conductivity of the employed electrolyte membrane and faster proton transport compared to hydroxide ions. [34]

Proton Exchange Membrane Water Electrolyzer

In comparison with the alkaline variant, a proton exchange membrane (PEM) electrolyzer is an advanced, reverse PEM fuel cell. On this account, a PEM electrolyzer consists mainly of a catalyst-coated membrane sandwiched by two electrodes. At the anode side, water (pH 7) is circulated through a flow field to the membrane electrode assembly (MEA), where it electrochemically reacts and is split into oxygen and protons. Within the MEA, a gas diffusion layer (GDL) is located between the catalyst layer and current-collecting bipolar plates. The purpose of the GDL is to transport electrons, heat, reactants and products to as well as from the catalyst layer with minimum voltage, current, thermal, interfacial, and fluidic losses. Carbon-based materials (carbon paper or carbon cloth), typically used in PEM fuel cells, are undesirable for PEM electrolyzers due to the high potential of the anode electrode. The corrosion and consumption of the carbon will degrade the GDL and result in poor interfacial contacts, which will degrade performance and efficiency of the PEM electrolyzer. [54] The generated protons are then transported through the proton conductive membrane, react with electrons from an electrical force, and form hydrogen gas at the cathode, which exits through the flow channel. Meanwhile, the oxygen is transported along with the water out of the anode. In contrast to the

alkaline water electrolyzer, the cathodic half-cell is not necessarily filled with water. If it is filled with electrolyte, a two-way application as PEM electrolyzer and as PEM fuel cell is possible, which is interesting in regards to fluctuating energy demand. This sophisticated concept provides the generation of hydrogen and oxygen during charge (or the storage of energy) and the recombination back to water during discharge (or the release of stored energy) in a single cell. [33]

The main advantages of PEM electrolyzers are fast kinetics of the cathodic hydrogen evolution reaction and high-voltage efficiencies at high current densities. Furthermore, they can produce pure hydrogen at relatively high pressures demonstrated with over 150 bar, offering the possibilities of storing hydrogen directly without or only with small further mechanical compression. [55] However, under typical operation conditions of a PEM electrolyzer, several disadvantages like more stringent requirements on feed water and components, including expensive electrocatalyst materials (IrO_2 and Pt) and costly polymer membranes, are associated with PEM electrolyzers. [39]

The ability of the PEM electrolyzer to operate, not only under highly dynamic conditions but also in part-load and overload conditions, is one of the reasons for the recently renewed interest in this technology. The electrical demand is relatively stable and predictable, however when coupling these to energy sources such as wind and solar, the demand of the grid rarely matches the generation of the renewable energy.

Water electrolysis by PEM technology has offered up to now only theoretical advantages over traditional large-scale alkaline water electrolysis, such as higher energy efficiency (about 70 % [40]), better adaptability to power fluctuations, higher specific production rates and more compact designs. With the recent launch of a MW-scaled unit, it has moved into the field of large-scale hydrogen production as a realistic alternative. For example, AIR LIQUIDE has recently installed a 1.2 MW PEM electrolyzer in Denmark to use surplus electricity of a wind park to produce hydrogen. [56] In addition, SHELL together with ITM POWER plan to install the world's largest PEM electrolyzer with 10 MW of power in Cologne Wesseling. With this, SHELL will provide hydrogen for mobility purposes. [57] Furthermore, SIEMENS offers with their new PEM electrolyzer series SILYZER 300 a system in the power range of double-digits MW. [58]

Anion Exchange Membrane Water Electrolyzer

A very promising method to improve the performance of the alkaline water electrolyzer is the implementation of an anion exchange membrane (AEM) and a zero-gap configuration, respectively. [34] In such systems the electrodes are contacting the two membrane surfaces, to minimize the voltage drop (iR-drop) between the electrodes, [33] resulting in significantly lower energy consumption. AEM water electrolyzers hold many advantages in comparison to PEM electrolyzer systems. As cheaper, non-noble metals are stable in alkaline media, the relatively low cost of the electrode materials is one of the main advantages of alkaline systems over PEM electrolyzers. Therefore, the majority of published literature on alkaline electrolysis describes electrodes based on low cost materials such as nickel for both anode and cathode. [43,59–61]

The possibilities for low cost, energy efficiency water electrolyzers are excellent. The general target to be reached is a cell voltage lower than 2 V at current densities greater than 1 A cm^{-2} for cells operating below 373 K. [33] At the present stage:

- Stable hydrogen evolution catalysts, offering low overpotential, are available.
- Stable oxygen evolution catalysts have also been developed but the overpotentials are much higher than what would be desirable. In view of the very extensive research already focused on this problem, no major reduction in overpotential seems likely. Water electrolysis technology probably has to live with this inefficiency. [33]

The potential for improvement lays in the development of:

- Large-scale electrode design to increase accessible electrocatalytic surface area and to facilitate the bubble detachment from the electrode's surface.
- The next major improvement is likely to arise from hydroxide conducting membranes. By improving the conductivity of the membrane, resistance losses can be reduced, thereby the efficiency of the system increased.

The Gas Bubble Issue

The physics of gas evolution proceed through three phases: nucleation, growth and detachment. Bubbles start nucleating at the electrode surface from solution once the solution becomes highly supersaturated with produced gas. Subsequently, bubbles grow or coalescence with others, and finally detach from the electrode. [62] During the electrolysis, gas bubbles rise from the electrodes and thus increase the electrical resistance of the electrolyte. [48] Due to faster reaction kinetics, the effect of bubble

formation on the electrode surface is especially severe on electrodes with a high catalytic activity. At the position where the gas bubbles arise at the electrode, the electrode surface is blocked and the electron transfer between electrode and electrolyte is hindered, which increase the internal resistance of the electrode. With further gas evolution, the bubbles will grow and move along the electrode surface to coalesce with other bubbles. Especially at high current densities, bubble coalescence can be problematic, since a gas film can block the contact area between electrolyte and electrode completely. [63] Bubble overpotential can be even higher than the OER's activation overpotential. Consequently, resistance means power loss and heating, resulting in a major efficiency loss. Hence, to decrease the overpotential of the OER, the detachment of the formed bubbles has to be facilitated. [34] Several methods have been tested to reduce the negative effects of gas bubbles in electrochemical processes.

Application of centrifugal fields [64] , super gravity fields [65], magnetic fields [66], and ultrasound [67] result in a more complex system setup, yet do not improve the efficiency significantly and for this reason they have little technological implication. [48]. Instead, a larger surface roughness improves the catalyst activity and increases the hydrophilicity, benefiting the bubble detachment. Therefore, catalysts with hierarchical morphologies are favorable for the water electrolysis cell. [34]

2.2 Hydrogen Storage and Transportation

Renewable energy is understood to be the key source of a future sustainable energy system. The fundamental problem of the most renewable energy sources is their intermittent character. Namely countries with a large share of wind and solar energy producers have already experienced energy over-production on very windy or sunny days while facing significant energy shortages during high demand periods with unfavorable weather or seasonal conditions. There are two solutions to this circumstance:

First, these countries run their large technical installations (power plants, chemical plants, plants for the production of consumer products, etc.) in an intermittent way, giving up the benefits of continuously operated facilities as described above. Today, Germany uses a double structure strategy, where basically coal power plants compensate the fluctuating wind and solar power.

Or second, storage technologies are developed and installed, which are able to compensate over- and underproductions of energy through wind and solar, but also on longer time scales (e.g. to compensate seasonal differences). [5] The state-of-the-art technology to store energy long-term and in large scale is by pumped-storage power plants, where water is pumped in an upper reservoir in times of high wind and solar power share. Thus, the potential energy stored can then be used, for example, at night or during a doldrums. In this case, the water flows into the lower reservoir, thereby driving a turbine, which thus generates electrical energy (electricity) via a generator. Pumped-storage power plants are able to store energy in the GWh-scale with 70 % to 80 % overall efficiency. [68] Although these losses are still significant, there is no other large scale and inexpensive method of storing energy with similar or even lower losses. Nevertheless, some other electricity storage technologies are deployed, including compressed air energy storage (CAES), battery energy storage systems, power-to-gas (P2G) and flywheels. [69]

Suppose Germany wanted to achieve a wind-solar market share of 50 %. A pumped-storage volume of 2.1 TWh must be installed to not waste the overshooting power spikes of the wind and solar installations. [70] In contrast, Germany's current pumped-storage volume is 0.038 TWh. The European ESTORAGE project has estimated that this volume can be extended to 0.045 TWh. [71] In other words, to realize an efficient implementation of 50 % wind and solar energy in Germany's energy mix, the storage volume has to be 46 times larger than the maximum pumped-storage volume possible. Consequently, alternative storage technologies have to be considered.

Like electricity, hydrogen is a secondary energy source. By contrast, it is a general principle that electricity must be used immediately upon being generated. However, the main benefits of hydrogen as energy storage medium are full scalability, ability of long-term storage of different renewable energies and the possibility to use it optionally as fuel for transportation. The fact, that hydrogen is a very light gas makes its storage and transportation a real challenge. However, while gravimetric energy density of hydrogen is excellent (33.3 kWh kg^{-1}), the volumetric energy density of even liquefied hydrogen (2.4 kWh L^{-1}) is critical. [72] The energy density of gasoline is about three times higher. Therefore, the aim of hydrogen storage technologies is to reduce the volume that hydrogen naturally occupies in its thermodynamically stable state under ambient conditions, where 1 kg of H_2 occupies 11 m^3.

The conventional hydrogen storage technologies are compressed hydrogen and liquid storage as well as cryogenically compressed hydrogen as a hybrid technology. More advanced hydrogen storage approaches can be categorized into physically bound

hydrogen, where the hydrogen gas is physisorbed to high surface area substrate and chemically bound hydrogen, where hydrogen has formed a chemical compound with the substrate. [73]

With the storage of hydrogen some safety issues need to be considered. Constant exposure to hydrogen causes embrittlement in many materials, which can lead to leakage in both metal and non-metallic components. If a hydrogen leak develops, then hydrogen disperses out rapidly. Due to the low density and high diffusivity, hydrogen dilutes in air considerably faster than gasoline. In ambient air, hydrogen is flammable in 4 – 75 % concentrations (which is much broader than gasoline range, 1 - 7.6 %) and is explosive in 15 - 59 % concentration range. Therefore, due to the significantly narrower explosion limit – when ignited early, hydrogen burns off before explosion limits are reached. Hence, the autoignition temperature is relatively high (560 °C [74] - 585°C [75]). This makes it difficult to ignite a hydrogen-air mixture on the basis of heat alone without some additional ignition source.

2.2.1 Compressed and Liquefied Hydrogen

Although hydrogen is extremely bulky, making transport in its gaseous state quite difficult. Therefore, hydrogen is kept under pressure to increase the density. At ambient conditions the energy density of hydrogen is only 0.003 kWh L^{-1}. By compressing hydrogen to 700 bar the energy density rises to 1.3 kWh L^{-1}. [72] If the hydrogen is to be stored as a liquid at -254 °C the energy density further increases to 2.4 kWh L^{-1}. [72] Alternatively, the energy density can be extended up to 3 kWh L^{-1} by cooling compressed hydrogen down to -240 °C, which is termed as cryogenic compressed hydrogen. **Figure 5** gives storage density of hydrogen under certain pressures and temperature conditions.

The relevant large volumes for hydrogen storage can only be provided by suitable underground geological formations. [76] Hydrogen storage in underground structures is not a new concept. Natural gas, for example, has been stored in depleted oil wells since the early 1900s. There are two main types of underground facility applicable to hydrogen storage. These are the use of pore storage (generally in naturally formed structures such as depleted oil and gas fields as well as water aquifers) and man-made structures such as salt mines and salt caverns. [77]

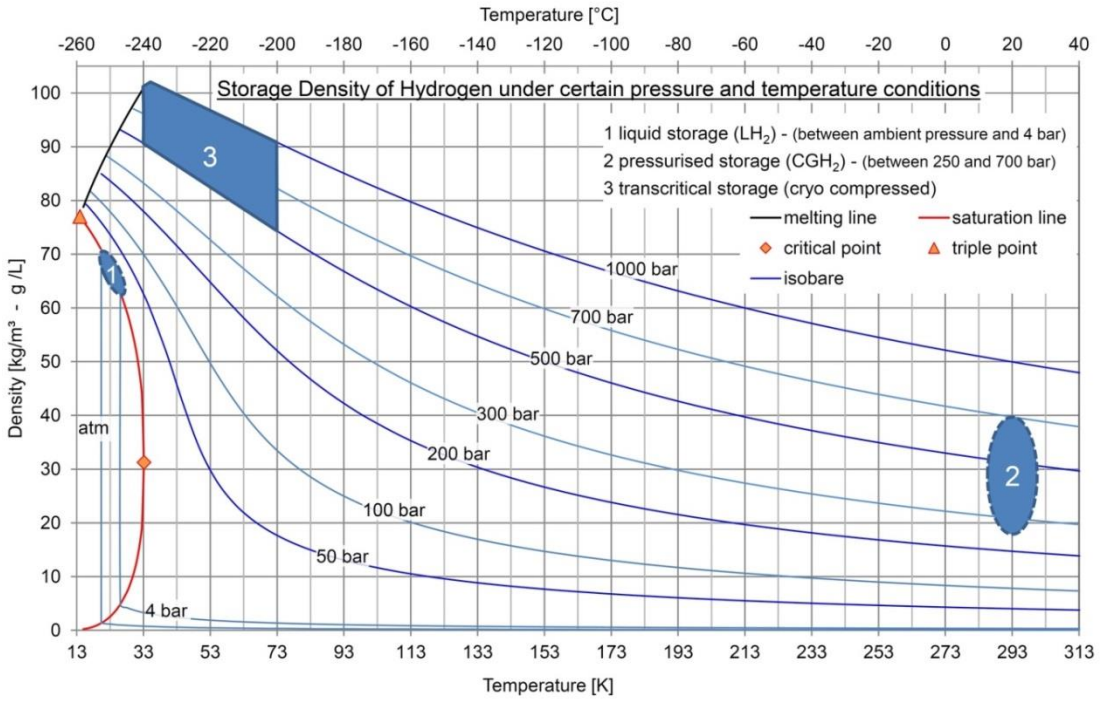

Figure 5: Storage density of hydrogen under technical relevant pressure and temperature conditions. Note, the energy density of compressed hydrogen (700 bar) at room temperature equals 1.3 kWh L^{-1}. Reproduced from [78].

Cavern storage uses cavities in underground salt mines, which are created by a sol process. There are two large underground hydrogen storage facilities in the world. One in Teesside (UK) with three 150,000 m^3 caverns at a constant pressure of 45 bar, which enables an energy storage capability of 24.4 GWh. Another one in Chevron (Texas-USA) with 580,000 m^3 of storage volume at a variable pressure of 70-135 bar, which corresponds to a maximum energy storage capacity of 83.3 GWh. [76] The pressure and therefore the storage capability of underground storage facilities is limited by the strength characteristics of the containing rock or salt formations. To increase the efficiency of hydrogen storage in large caverns, the hydrogen should ideally also be produced nearby. Therefore, this storage technology is rather restricted to location with appropriate geological formations and with high wind and solar power shares.

In addition to storing hydrogen in underground storage facilities, it is also possible to feed hydrogen into the existing natural gas grid and thus use the storage capacities of the grid. At present the DEUTSCHER VEREIN DES GAS- UND WASSERFACHES investigates a possible injection of hydrogen from renewable sources into natural gas networks. However in Germany, the admixture is limited to 5 vol-% hydrogen at each point of the network according to the DVGW Arbeitsblatt G 262 and therefore also at the entry point. The German gas network has a total length of 511,000 km and an

energy storage capacity of 217 TWh in form of natural gas. [79] If the German gas network holds 5 vol-% hydrogen form renewable sources, an energy storage capacity of 3 TWh could be realized. This corresponds to 1.8 TWh of electrical energy, if the methane/hydrogen mixture is used as a fuel in gas turbine power plants.

Natural gas is thus the suitable fossil "transition energy source" for a transformation of the energy system towards renewable energies and hydrogen as the main source of energy. This applies in particular to the infrastructure problem, which is often the limiting factor for the introduction of new energy sources. [19] A lot can be learned and substituted form natural gas storage and distribution technology. There are two main transportation concepts of natural gas called CNG (compressed natural gas) and LNG (liquefied natural gas). The LNG's transport economy is around 2,500 km, for shorter distances the transportation by natural gas pipeline as CNG is more economical. The transport and storage of natural gas by LNG-tankers is particularly important for countries in the Far East, such as Japan, because of the long transport routes.

Currently, compressed and liquid hydrogen storage technologies are most mature. A significant drawback is the large amount of energy input necessary for cooling and compressing, in particular for long-term storage, which is approximately 40 – 50 % of the hydrogen's lower heating value. [80] Thus, some more contemporary hydrogen storage technologies are under research.

2.2.2 Advanced Hydrogen Storage Technologies

2.2.2.1 Physisorbed Hydrogen

To reduce the mechanical requirements of pressurized vessels highly porous materials have been investigated for their ability to physically adsorb molecular hydrogen. The storage of hydrogen can rely on physisorption because the adsorbed gas can be released reversibly. Physisorption is based on resonant fluctuations in charge distributions, which are called VAN DER WAALS interactions. There are different mechanisms of adsorption depending on the geometry of the adsorbent and the temperature of adsorption. On an exposed surface and in pores larger than 50 nm multilayer adsorption occurs. The interaction force received by the first layer molecules is, in most cases, higher than the force received by the subsequent layers. In pores narrower than 50 nm capillary condensation could happen. [81] It can be concluded that the amount of adsorbed hydrogen is proportional to the specific surface

area and the pore size of the storage material (absorbent). Materials with a large specific surface area like activated or nanostructured carbon and carbon nanotubes (CNTs) are possible substrates for physisorption. The main difference between CNTs and high surface area graphite is the very narrow cavity inside the tube. [82] Back in 1997 Dillon et al. reported a hydrogen storage amount of 4.2 mass-% at ambient temperature under 100 bar pressure for single wall carbon nanotubes and triggered a worldwide research hype on CNTs. [83] They claim, hydrogen would condensate in the tube's cavities. However, later on this result was rebutted. According to the phase diagram of hydrogen, condensation at ambient temperature is absolutely impossible. [84] Under comparable conditions SONY could only realize a hydrogen amount of 0.3 mass-%.

As an alternative to microporous carbon materials metal–organic frameworks (MOFs) came up in the discussion as hydrogen storage materials in the early 2000s. MOFs are crystalline solids that are assembled through the connection of metal ions or clusters through molecular linkers. [80] One major benefit of the molecular linkers is the extension of the length between the metal centers, which defines the size of the inner pores. Thus, MOFs can provide very large surface areas of up to 6000 $m^2\ g^{-1}$ or more and are therefore ideal candidates for hydrogen storage. [85] In the last two decades, a considerable number of different MOF materials were investigated due to their hydrogen storage capability. There is still substantial scatter in the reports on hydrogen storage of different MOF materials, which is partly due to the different conditions under which the storage properties have been evaluated. [86] As a result, hydrogen storage capacities from 0.2 to 3.8 mass-% can be found in the literature. [80,85,87,88]

2.2.2.2 Metal Hydrides

The metal hydrides as storage mediums are based on the reversible chemical reaction of certain metals or metal alloys with hydrogen. The adsorption/desorption kinetics are very fast in most hydrides thus allowing fast hydrogen storage and release. [89] Unfortunately, nearly all metal hydrides exhibit rather low mass absorption capacities (except magnesium hydrides). Therefore, the amount of hydrogen in classical metal hydrides is limited to roughly 2 mass-%, due to the fact that most metal hydrides are intermetallic transition metal compounds with an associated high atomic weight. [86] Typically, the hydrogen stored as metal hydride is released through a chemical reaction with water (hydrolysis) or through a thermal

decomposition. This results in some disadvantages. In the case of hydrolysis, the regeneration of storage material is still an issue and needs thermal or chemical post-treatment of the storage material, which makes it not suitable for large storage applications. Alternatively, a thermal management system is required, because the absorption of hydrogen is an exothermic reaction while desorption of hydrogen is endothermic.

Nevertheless, these metal hydrides are still implemented in fuel cell systems with solid state hydrogen storage in niche applications. For example a Fe/Ti/Mn/Zr alloy distributed under the name HYDRALLOY C by the ADVANCED METALLURGICAL GROUP (AMG) is used in the German Type 212 submarine class that runs on a PEM fuel cell. [90] Another promising approach comes from the FRAUNHOFER IFAM. They have invented a so called POWERPASTE on MgH_2 base. This highly viscose liquid releases hydrogen by contact with water. It has a hydrogen capacity of more than 10 mass-%, which is 1.6 kWh kg^{-1} and 1.9 kWh L^{-1} and therefore more than compressed hydrogen. Due to the possibility to pump the paste into tanks and to store it lossless, even over longer periods of time, this technique enables seasonal hydrogen storage.

2.2.2.3 Liquid Organic Hydrogen Carrier

Liquid organic hydrogen carrier (LOHC) systems typically comprise a pair of organic molecules, a hydrogen-lean and a hydrogen-rich compound. During the hydrogen storage process, the hydrogen-lean LOHC compound is transformed into the hydrogen-rich compound by a catalytic hydrogenation reaction; most frequently Ru/Al_2O_3 is used as catalytic material. [72] The hydrogen uptake in the hydrogenation reaction requires elevated pressures of about 30 to 50 bar. The dehydrogenation on the other hand can be operated at ambient pressure, but necessitates high temperatures of up to 300 °C. [91] However, during storage time, hydrogen can be stored at room temperature and under high storage densities using conventional tank technology. In this way, LOHCs enable a decoupling of energy generation and energy usage in terms of both space and time. [5]

This is one of the most important advantages compared to most other hydrogen storage technologies. In contrast to conventionally compressed or liquid hydrogen, the organic compounds used have little risk potential. They are almost non-toxic, only slightly flammable and non-explosive. Coupled with electrolysis and fuel cells, LOHC technology will potentially become one of the energy storage technologies of the future. Since 2016, the HYDROGENIOUS TECHNOLOGIES GMBH runs a commercial

LOHC plant for storage of hydrogen in dibenzyltoluene. Dibenzyltoluene is a commercially available thermofluid. The wide liquid range between -39 °C (melting point) and 390 °C (boiling point) as well as the high hydrogen storage density of 6.2 mass-%, corresponding to an energy content of 2.05 kWh kg^{-1}, make dibenzyltoluene a promising LOHC candidate. Hence, 1 m^3 of hydrogenated dibenzyltoluene stores 57 kg hydrogen (624 Nm^3 or 1.9 MWh).

2.3 Utilization of Hydrogen as Energy Carrier

The key for a widespread application of hydrogen is to not only use it in the transportation sector but also in stationary power production. There are basically two technological ways to reconvert hydrogen to electricity and heat. One is the combustion of hydrogen within gas power plants or to reach even higher efficiencies in combined cycle power plants. However, the controlled combustion of pure hydrogen is rather challenging particularly in large scale power plants. Thus, the natural gas as the standard fuel in such power plants will be enriched with hydrogen. Second is the reconversion of pure hydrogen to electricity by electrochemical fuel cells. Fuel cells have higher efficiencies and through the direct utilization of pure hydrogen they produce only water as exhaustion gas.

This chapter opens with a short overview about the current hydrogen combustion technologies. A brief discussion of the challenges that need to be overcome for a successful implementation in the hydrogen economy follows. The second part of the chapter introduces the proton exchange membrane fuel cell (PEM fuel cell) and the solid-oxide fuel cell (SOFC) as the most promising solutions to utilize pure hydrogen in mobile and stationary power generation. Special focus is placed on the proton exchange membrane fuel cell. The state-of-the-art technology is put in context by combining it which forward-looking examples of their successful application. Subsequently, the current bottlenecks of the PEM fuel cell technology will be highlighted. The chapter consequently closes with a critical discussion of currently used catalysts and strategies to improve PEM fuel cells.

2.3.1 Combustion of Hydrogen

All current heat engines (flame burners for heating systems, turbines, as well as gasoline combustion engines) can also be operated with hydrogen or hydrogen-rich gas mixtures with certain adjustments. [19] Like all other heat engines the efficiency of a hydrogen-fueled heat engine is limited by the second law of thermodynamics and is known as CARNOT'S rule. The CARNOT'S rule describes the highest, theoretically possible, efficiency in converting thermal energy into mechanical or electrical energy. Therefore, the efficiency of a heat engine depends simply on the temperature difference between the hot and cold reservoirs.

$$\eta_{\text{Carnot}} = 1 - \frac{T_{\text{cold}}}{T_{\text{hot}}}$$

In modern steam power plants temperature difference of 400 °C to 600°C are realized, which equals to a CARNOT efficiency of 50 – 65 %, depending on the cooling concept. Under operating conditions average efficiencies are 35 % for coal, 45 % for natural gas and 38 % for oil-fired power generation. [92]

For the conversion of hydrogen into electrical energy, a combined-cycle power plant (CCPP) is the first choice, see **Figure 6**. [93] A CCPP uses both a gas and a steam turbine together to produce more electricity from the same amount of fuel than a traditional gas or steam power plant. The gas turbine compresses air and combusts it with fuel (usually natural gas or pure methane) at very high temperature (about 1350 °C). [94] The hot air-fuel mixture moves through the gas turbine blades and rotates the turbine. The fast spinning turbine drives a generator that converts a portion of the mechanical energy into electricity. Furthermore, the gas turbine serves as a heat source for a downstream waste heat boiler, which in turn acts as a steam generator for a steam turbine. About 2/3 of the electric power is provided by the gas turbine and about 1/3 by the steam turbine. The combination of both turbine types results in excellent power plant efficiencies. The world record holder in efficiency is the CCPP Nishi-Nagoya Thermal Power Station No. 7-1 located in Japan. The three installed gas turbines from GENERAL ELECTRIC together with the steam turbine and generator technology from the TOSHIBA ENERGY SYSTEMS & SOLUTIONS CORPORATION provide an efficiency of 63.08 %. [95]

CCPPs can be built relatively quickly and inexpensively. Thus, the investment costs and the construction time amount to only about half of a coal-fired power plant of the same power. Due to short start times and the possibility of rapid load changes,

CCPPs can be used very flexibly in power plant management. Therefore, they are the ideal match for fluctuating wind and solar power.

In principle, the natural gas used to fuel current gas turbines can be substituted by hydrogen or hydrogen/natural gas mixtures. [96] The addition of hydrogen to the fuel of the gas turbine has a positive effect on the efficiency and performance of the CCPP. [93] The efficiency gain is due to the higher water content in the combustion gas by increasing the hydrogen content in the fuel gas. Thus, the specific heat capacity increases in the combustion gas and by that a 3 % greater enthalpy difference can be degraded. Thereby, the overall efficiency of a CCPP fueled with hydrogen-rich natural gas will improve by 1 %. [93] However, the use of hydrogen as a fuel in gas turbine technology brings with it some technical challenges. Hydrogen burns with a flame velocity about 7 times faster than that of natural gas and also at a higher combustion temperature. For this reason, technically, burners that use hydrogen-rich natural gas mixtures or even pure hydrogen need to overcome a range of problems such as fuel nozzle burnout, unstable combustion, and increasing NO_x emission. In practice, this means that water must be injected to the gas mixture to re-

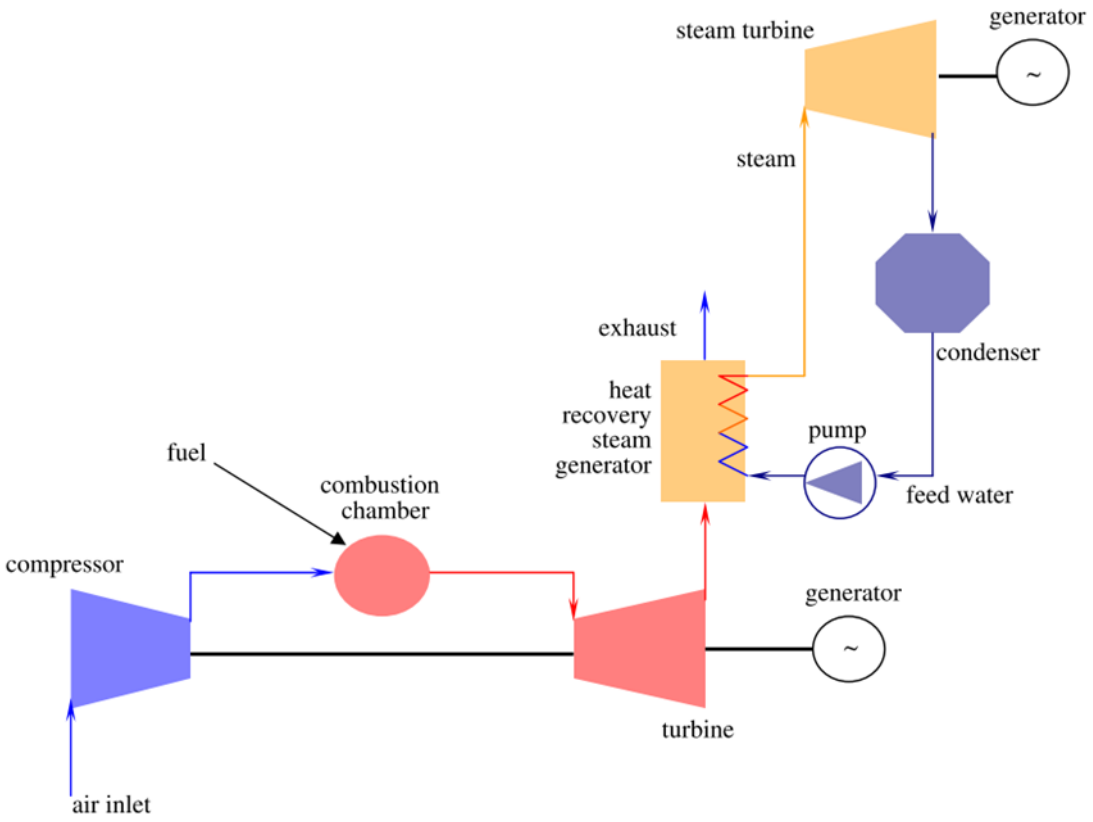

Figure 6: Schematic construction of a combined-cycle power plant (CCPP), where natural gas and compressed air fuels a one or more gas turbines. The exhaust heat from the open gas turbine circuit is recovered in a heat recovery steam generator. In the following, the generated steam is used by a steam turbine generator to produce additional electricity. Reproduced from [97].

duce the combustion temperature, which goes hand in hand with efficiency losses. Furthermore, new high temperature materials or coatings are required in order to develop a combustor that can cope with the characteristics of hydrogen combustion. [98] The formation of the NO_x emissions can be suppressed by enhancing the mixing process of the reactants. By premixing the hydrogen fuel with air, significant NO_x reduction can be achieved, but due to the high reactivity of hydrogen/air mixtures, the potential risk of flash back needs to be considered.

Alternatively, a new fuel injection system developed at the AACHEN UNIVERSITY OF APPLIED SCIENCES together with the KAWASAKI Company will enable pure hydrogen usage in gas turbines without water injection. [99] The principle is to subdivide the fuel and eject it from tiny nozzles, so that a cross-flow mixing of air and fuel is obtained. This leads to a fast and intense mixing, which takes place simultaneously to the combustion process. As a result, a micro flame develops at the burner segment edge downstream of the injector nozzle. [100]

In the mobility sector, the hydrogen combustion engine was discussed as a transition technology from the gasoline combustion engine to the hydrogen fuel cell. Between 2005 and 2007 BMW tested this concept in a luxury car named HYDROGEN 7. [101] Typically, hydrogen engines are designed to use about twice as much air as theoretically required for complete combustion to reduce the formation of NO_x. [102] Unfortunately, this also reduces the power output of the hydrogen engine to half of a similarly sized gasoline engine. To overcome this drawback BMW has engineered a 12-cylinder hydrogen combustion engine. Obviously, to implement hydrogen in the mobility sector the concept cannot come along with the double-up of the engine size.

2.3.2 Electrochemical Conversion of Hydrogen to Electric Power

In traditional combustion technologies, the chemical energy of the fuel is converted into mechanical energy and subsequently, if desired, into electrical energy. In contrast, in a fuel cell the fuel (hydrogen, methane or methanol) is converted directly into electricity by undergoing an electrochemical reaction. Fuel cells have the potential to replace the internal combustion engine in vehicles and to provide power in stationary applications, because they achieve excellent energy conversion efficiencies of about 80 %. [6] This is up to three times more than in state-of-the-art combustion engines, because their efficiency is not restricted to the CARNOT limit. [103] Furthermore, fuel cells do not burn the fuel to supply electric power, making the process quiet and pollution-free. A fuel cell system can be a truly zero-emission source

of electricity by using hydrogen, produced from renewable sources, as fuel. There are different types of fuel cells; however, they are all made up of three adjacent segments: the anode, the electrolyte layer, and the cathode.

This work will focus on the proton exchange membrane fuel cell (PEM fuel cell), because it is the ideal technology for the use of hydrogen as fuel in the mobility sector. Additionally, the solid-oxide fuel cells (SOFC) will be briefly discussed, since they become attractive for stationary power generation for backup and remote systems as well as for exposed locations like islands.

2.3.2.1 Proton Exchange Membrane Fuel Cells for Mobile Power Generation

The high efficiency (theoretically 83 %) and the compact design coupled with relatively low operation temperatures (80 °C) make PEM fuel cells particularly interesting for transportation applications. [104] In general, a PEM fuel cell is manufactured as a stack of identical repeating unit cells comprising a membrane electrode assembly (MEA), in which hydrogen gas (H_2) is oxidized to protons on the anode (hydrogen oxidation reaction, HOR). The generated protons pass through the solid polymer electrolyte membrane, while the electrons are forced through a circuit, generating an electric current and excess heat. On the MEA cathode, the protons and electrons re-combine with oxygen gas (O_2) to water (oxygen reduction reaction, ORR).

$$\text{HOR} \quad 2\,H_2 \rightarrow 4\,H^+ + 4\,e^- \qquad (E^0 = 0.0\ \text{V}) \tag{18}$$

$$\text{ORR} \quad O_2 + 4\,H^+ + 4\,e^- \rightarrow 2\,H_2O \qquad (E^0 = 1.23\ \text{V}) \tag{19}$$

Porous gas diffusion layers transport H_2, air and product water between the catalyst surface and the bi-polar plates while electrically conduct them both. Most MEA catalysts used today are based on platinum nanoparticles dispersed onto larger high-surface-area carbon black supports (Pt/C) to increase the Pt surface-to-volume ratio and thus the electrochemical reaction rate. [105] One of the most significant advantages of Pt/C is the widespread availability and low cost of the carbon black in various forms. [106] To protect the Pt catalyst from impurities (catalyst poisons), mainly CO that causes deactivation, only pure hydrogen can be utilized in a PEM fuel cell.

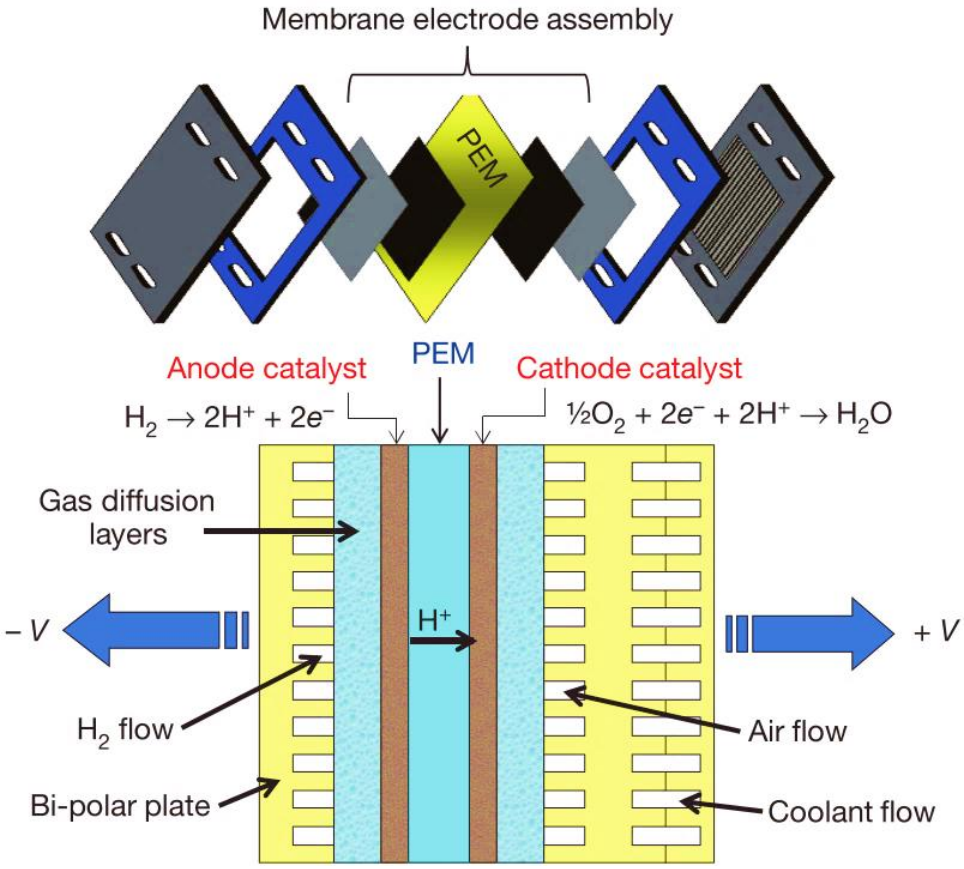

Figure 7: Scheme of a PEM fuel cell. Reproduced from [106].

Hydrogen Oxidation Reaction

Hydrogen evolution reaction (HER) as the counterpart of the hydrogen oxidation reaction (HOR) was already discussed in Chapter 2.1.3.1. Like the HER, the HOR is one of the simplest reactions in electrocatalysis due to the simplicity of reactants. In fact, the fast reaction kinetic of the HER is comparable to the HOR. The HOR involves the oxidation of hydrogen on an electrode surface, generally resulting in a high coverage of adsorbed hydrogen. It is generally accepted that the HOR proceeds via three steps, where S represents a surface active site [107]:

$$2\,S + H_2 \rightleftharpoons 2\,S\cdots H_{ad} \qquad \text{(TAFEL) or} \qquad (20)$$

$$2\,S + H_2 \rightleftharpoons 2\,S\cdots H_{ad} + e^- + H^+ \qquad \text{(HEYROVSKY)} \qquad (21)$$

$$S\cdots H_{ad} \rightleftharpoons S + e^- + H^+ \qquad \text{(VOLMER)} \qquad (22)$$

The H-adsorption/desorption mechanism requires that hydrogen binds well, but not too strongly, to the reaction site S. The bond strength of Pt-H is almost ideal for the HOR. Thus, the reaction kinetic and therefore the exchange-current density for hydrogen oxidation at platinum surfaces is six orders of magnitude higher than that for the oxygen reduction. In the case of hydrogen fuel cells, it is generally considered

that the overpotential of the HOR is negligible compared to that of the ORR. [108] However, the adsorption of impurities that significantly reduces the availability of active metal sites can reduce the long-term activity of the platinum catalyst. Significant catalytic performance losses can arise when either CO-contaminated hydrogen feeds, or other oxidizable fuels that produce CO, are used in the anode feed streams. [39]

Oxygen Reduction Reaction

The oxygen reduction reaction (ORR) is a multi-electron reaction that includes a number of elementary steps involving different reaction intermediates. [106] Of various reaction schemes proposed for ORR, a modified WROBLOWA et al. [105] scheme appears reasonable to describe the complicated reaction pathway by which O_2 is reduced at metal surfaces:

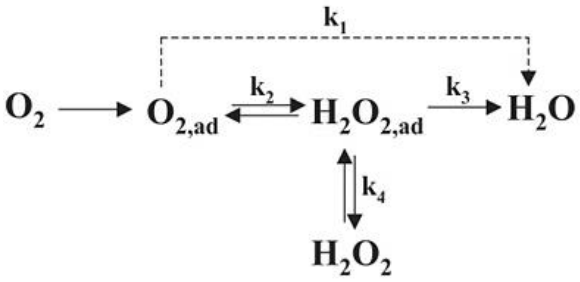

Based on this reaction scheme, O_2 can be electrochemically reduced either directly to water with the rate constant k_1 without intermediate formation of $H_2O_{2,ad}$ (so-called "direct $4e^-$ reduction"). The adsorbed peroxide can be electrochemically reduced to water with the rate constant k_3 ("series $4e^-$ reduction") or desorbed into the bulk of the solution (k_4). [109] The detailed mechanisms of the ORR are complicated and depend primarily on the surface properties of the electrode. For the direct $4e^-$ reduction, there are two possible mechanisms (the dissociative and the associative mechanism). Thus, ORR proceeds through a dissociation mechanism, where the O-O bond of oxygen breaks directly upon adsorbing at one or two catalytic active metal sites S and the formed O_{ad} is reduced successively to OH_{ad} and further to H_2O_{ad}. [2]

$$2\,S + O_2 \rightleftharpoons 2\,S - O \tag{23}$$

$$2\,S - O + 2\,e^- + 2\,H^+ \rightleftharpoons 2\,S - OH \tag{24}$$

$$2\,S - OH + 2\,e^- + 2\,H^+ \rightleftharpoons 2\,S + 2\,H_2O \tag{25}$$

Alternatively, ORR can also proceed according to the following associative mechanism. [110]

$$S + O_2 \rightleftharpoons S \cdots O_2 \quad (26)$$

$$S \cdots O_2 + e^- + H^+ \rightleftharpoons S - OOH \quad (27)$$

$$S - OOH + e^- + H^+ \rightleftharpoons S - O + H_2O \quad (28)$$

$$S - O + e^- + H^+ \rightleftharpoons S - OH \quad (29)$$

$$S - OH + e^- + H^+ \rightleftharpoons S + H_2O \quad (30)$$

The association mechanism for the ORR involves the formation of OOH_{ad}, which breaks into O_{ad} and OH_{ad}. Unfortunately, the OOH_{ad} species can also lead to just a $2e^-$ reduction, which will form $H_2O_{2,ad}$ with the rate constant k_2. In fuel cell operations, a direct $4e^-$ reduction is highly preferred in order to get high efficiency as well as suppress catalyst and support degradation through H_2O_2.

Out of all metals, platinum shows the greatest catalytic activity for the ORR. Nevertheless, the ORR at platinum surfaces is six orders of magnitude slower than the anode HOR and thus limits performance, so almost all research and development focuses on improving the cathode catalysts and electrodes. [106] Currently, almost half of the produced platinum, the majority of palladium and 80 % of rhodium are used for the production of auto catalytic converters for exhaust gas purification. [111] A typical light vehicle catalytic converter contains around 3 to 5 grams Pt and for heavy-duty trucks up to 15 grams Pt. [112] Diesel cars with EURO 6 emission standards need around 10 grams of Pt and other catalytic active metals to fulfill the emission requirements. [112] Thus, to reduce air pollution the combustion engine technology will need higher Pt contents to improve the catalytic exhaustion treatment.

In contrast, fuel cell development exhibits the reverse trend. In the early days of the development of fuel cells, around 28 mg of platinum was required per cm^2 of electrode surface area for each electrode (anode and cathode). Much progress has been made in reducing the Pt loading in H_2/air-fed PEM fuel cells. Today's platinum content has been reduced to below 0.2 mg cm^{-2} electrode surface area. [108] As a result, for a modern 100 kW PEM fuel cells around 20 grams of Pt are required.

PEM Fuel Cell Applications

The wide-spread implementation of PEM fuel cells in the transportation sector suffers from a lack of re-fueling stations and of high vehicle prices. Nowadays, the versatile benefits of fuel cells are often best realized in niche applications. But in the following, trendsetting examples are given, where fuel cell technology showcases their great potential for the widespread use towards a hydrogen economy. One of the first PEM fuel cell, developed by GENERAL ELECTRIC, was installed in the GEMINI V spacecraft

back in 1965. This fuel cell was used as the main electric power source, and furthermore the water produced by the fuel cells was used as drinking water by the astronauts. [113]

More recently PEM fuel cell technology has been receiving more attention as a possible alternative to the internal combustion engine. All major car manufacturers have demonstrated prototype fuel cell vehicles and announced plans for commercialization. The main obstacles for fuel cell commercialization in automobiles are the cost of fuel cells and the cost and availability of hydrogen. [104] In contrast to an internal combustion engine, where the maximum efficiency is achieved at or near its maximum power, a fuel cell has its maximum efficiency at partial load. Therefore, most fuel cell powered vehicles are supported by a small to medium sized battery. Thus, the fuel cell only provide the base load, but the peak power for acceleration of the vehicle is provided by the battery or similar peaking devices (such as ultracapacitors). Furthermore, a battery allows recapturing the braking energy known as recuperation, resulting in a more efficient driving system. The disadvantages of having a battery onboard are the extra cost, weight and volume of the battery system.

Buses for city and regional transport are considered to be the most likely types of vehicles for an early market introduction of fuel cell technology. Buses require more torque than power, because they frequently accelerate in a typical driving cycle and drive at relatively low speed. Hence, electric engines powered by fuel cell/battery hybrid system can perfectly meet these requirements. Buses operate in urban areas where pollution is already a problem. Moreover, buses are almost always operated in a fleet, and refueled in a central facility. This makes refueling with hydrogen much easier. In addition, storing larger quantities of hydrogen on board (typically above 20 kg) is less of a problem, thus fuel cell buses typically store hydrogen on the roof. [104] Consequently, they require no infrastructure along route lines and can therefore operate like conventional diesel buses, which can facilitate there implementation. Over the past 10 years, 84 fuel cell buses have been put into service in 17 cities in eight European countries; they have proven their flexibility and safety in operation, and they are ready to be rolled out on a larger scale. [114] In addition, fuel cell buses are showing improved fuel economy over diesel buses. But, at this point in development, capital costs for fuel cell buses are still much higher than those of conventional diesel technology. As a result, fuel cell buses are viable options to meet emission reduction goals in cities. The costs of fuel cell buses are expected to drop significantly and become increasingly competitive with diesel technology.

To implement fuel cell cars in the passenger car market is a much greater challenge. Prominent arguments pro fuel cell passenger cars are high range and short re-fueling time in comparison to battery electric vehicles. Moreover, with the increasing number of battery electric vehicles in urban regions the electrical charging infrastructure and the electric power supply will be a technological challenge. In the near future, battery-electric vehicles will be a cheaper vehicle option than fuel cell electric vehicles for the majority of the passenger cars. But fuel cell vehicles will offer notable cost advantages within larger vehicle size classes and for long driving distances. According to MORRISON et al. there will be a competitive market space for both fuel cell vehicles and battery electric vehicles in the future to meet different needs of the car owners. [115] TOYOTA and HYUNDAI have started the mass production of fuel cell cars with the MIRAI and the iX 35 FUEL CELL in 2014. HONDA has followed suit with the CLARITY FUEL CELL. Today's most advanced fuel cell vehicle is the HYUNDAI NEXO with a real driving range of over 550 km and a hydrogen consumption of 0.95 kg per 100 km (WLTP). In 2018, TOYOTA has unveiled a heavy-duty fuel cell truck prototype called CLASS 8, which is powered by two fuel cell stacks from the MIRAI. [116]

Hydrogen-powered rails became a reality in 2016 when ALSTOM presented the CORADIA ILINT, a fuel cell-powered train. [117] As an alternative to diesel trains, the fuel cell train is to be used in rural areas, where no overhead cables are installed. The train is powered by a 200 kW PEM fuel cell supported by a high power Lithium-ion battery, reaching almost 150 km h^{-1}, traveling up to 1000 km per tank of hydrogen, and accommodating 300 passengers. The German railway operators ELBE-WESER-VERKEHRSBETRIEBE and RHEIN-MAIN-VERKEHRSVERBUND have ordered 14 and 26 of these fuel cell trains, respectively. [118,119]

For the naval forces, the properties of a fuel cell system like silent and low-temperature propulsion provide some benefits as well. [120] In 2004, the HOWALDTSWERKE-DEUTSCHE WERFT KIEL successfully showcased the first non-nuclear air-independent submarine with the U 212 A. The 306 kW PEM fuel cell is fueled with oxygen from pressure tanks and hydrogen from metal hydride storage tanks to allow complete electrical operation of the submarine. [121] Another maritime fuel cell pioneer is the ENERGY OBSERVER, a 30.5 m long self-sufficient ship that circumnavigates the world testing new energy solutions in a marine environment. This vessel is only powered by renewable energy and hydrogen, the latter is produced on board via electrolysis using ocean water and is utilized in a 22 kW PEM fuel cell. [122]

Strategies to improve PEM Fuel Cells

The two major challenges for PEM fuel cell technology are cost and durability. An argument often used to reduce costs is the scaling effect of mass production. However, this only affects the costs for the production and for the individual components. The major contributor to the cost is still the platinum electrocatalyst of the cathode (ORR).

As a result, platinum is used in form of nanoparticles with 3 – 5 nm in diameter. Following down this path, the actually catalytic active surface atoms could be maximized. Nevertheless, even in such small particles the majority of Pt atoms do not contribute as catalytic sizes. Therefore, decreasing the Pt-loading of the cathode electrodes is mainly pursued along two strategies: (i) optimization of electrode structures so that the effect of reducing the cathode Pt-loading (number of nanoparticles) is limited purely to kinetical voltage losses, even at high current densities, and (ii) implementation of more active Pt-alloy catalysts with reported mass activity gains. [123]

Setting aside practical issues such as manufacturing and materials costs, the fundamental technical problem of PEM fuel cells is the slow reaction rate of the oxygen reduction reaction, which leads to low levels of current and power. [108] Therefore, the polarization curve is most suited to describe the fuel cell's performance. [104] In theory, a fuel cell should supply a voltage of 1.23 V. When current is drawn from a fuel cell, the voltage decreases as a result of three primary sources of voltage losses [108]:

- **Activation losses**: These represent the slowness of the reactions taking place on the surface of the electrodes. A proportion of the voltage generated is lost in driving the chemical reaction that transfers the electrons to or from the electrode.
- **Ohmic losses**: This voltage loss is the straightforward resistance to the flow of electrons through the material of the electrodes and the various interconnections, as well as the resistance to the flow of ions through the electrolyte. The voltage drop is linearly proportional to the current density.
- **Mass-transport losses**: These losses arise from the change in concentration of the reactants at the surface of the electrodes as the fuel is consumed. Especially at high current densities, it is difficult to get enough oxygen (air) to the catalyst. [106]

As shown in **Figure 3**, the main cause of voltage losses is the sluggish kinetic of the ORR. The five main ways of dealing with the slow reaction rates are to:

- raise the temperature,
- increase reactant concentration,
- increase the pressure,
- use more active catalysts, and
- increase the electrode surface area.

Whereas the first four options can be applied to almost any chemical reaction, the electrode area has a special significance for electrochemical cells. [108] Today's PEM fuel cells operate at 80 °C, at this temperature a balance between performance and degradation of currently used membrane and electrode materials is achieved. High temperature PEM fuel cells (> 100 °C) have distinct advantages in order to increase the mass transport and the inherent rates of the electrochemical reactions. [124] Unfortunately, the electrocatalysts and the polymer membrane experience significantly higher structural and chemical degradation at elevated temperatures. Therefore, to boost the performance of PEM fuel cells an increase of the operation temperature is a good option, but the performance gain is associated with a shorter lifetime of the cell. Alternatively, the power output often improves with increased pressure due to the increasing reactant concentration at the electrodes. However, the compression of air requires energy and therefore the total system efficiency is reduced. That's the reason why research has been focused on the development of more active catalysts (improved kinetics) and more efficient utilization of platinum by enlarging the catalytic active surface area.

For the characterization and evaluation of a materials electrochemical surface area (available surface area for the electrode reaction), approved electrochemical methods, like cyclic voltammetry (CV) and linear sweep voltammetry (LSV) are used. For a closer look into these methods see **Box 1**.

Box 1: Voltammetry

Voltammetry comprises a group of electroanalytical methods in which the current at an electrode is measured as a function of the applied potential to the electrode. As the applied potential becomes more negative, the electrode becomes more strongly reducing. In return, as the potential becomes more positive, the electrode becomes more strongly oxidizing. Therefore, redox reactions occurring on the electrode can be controlled by adjusting the potential. Most commonly, a three-electrode setup consisting of working electrode, counter electrode and reference electrode is used with a liquid electrolyte. The potential is controlled and measured by means of a potentiostat, so that no current is drawn from the reference electrode. If the potential of the working electrode is swept linear at a specific sweep rate (in mV s-1) the resulting current vs time curve is termed linear sweep voltammogram (LSV). The measured current is always a combination of the capacitive and the faradaic current. Only the latter is proportional to the concentration of the redox active species. Usually the potential sweep is reversed at a specific switching potential. If the reaction of interest is reversible, then the reverse sweep will show this as a current flowing in the opposite direction. Since the sweep rate is constant, one can easily convert time to potential, hence the plot of current versus applied potential is known as a cyclic voltammogram (CV), see **Figure 8**.

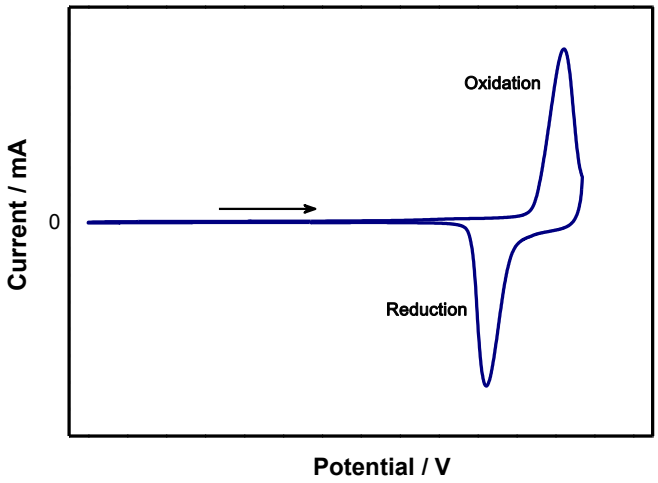

Figure 8: Schematic cyclic voltammogram.

Clearly, the rate at which either electrode reaction proceeds will be proportional to the area of the respective electrode. The performance of electrocatalysts is usually evaluated by using the total electrode activity (current density expressed in mA $cm^{-2}_{geometric}$). In the case of platinum, the mass activity (current density expressed in mA mg^{-2}_{Pt}) is even more important, thus they provide the efficiency platinum is utilized. The ORR take place at a multi-phase boundary and therefore the cell

performance highly depends on the distribution of the catalyst and its interaction with the electrode. [108]

On this account, most electrocatalytic electrodes are highly porous to provide a large surface area for the actual catalytically active nanoparticles. Currently in fuel cell technology, carbon black as supporting material has been widely accepted. Alternatively, nanostructuring of bulk electrodes is a simple and effective strategy to enlarge the electrochemical surface area, which results in a higher number of exposed electrocatalytically active sites per unit geometric area. [110] The electrochemical double layer capacitance has turned out to be a proper parameter to determine the electrochemical surface area of structured bulk electrodes, refer **Box 2**.

Boosting Kinetics by Alloying Platinum with Transition Metals

In the oxygen reduction reaction (ORR), the surface of the platinum catalyst tends to be shielded by a hydroxyl-layer. As a result, the active sites on the platinum surface are reduced in number, and the efficiency of the catalyst is limited. To improve the activity of Pt for the ORR the binding strength between platinum atoms and oxygen species should be lowered. [125] The strength of the chemical bond between oxygen atoms and atoms on the metal surface is dependent on the crystal planes and edges exposed. [108] Furthermore, the oxygen–metal bond strength can also be influenced

Box 2: Double layer capacitance

When a metallic electrode is brought in contact with a liquid ionic conductor (electrolyte), an electrochemical double layer among the two phases appears. Typically, two charged layers are present at the phase boundary, which carry opposite signs as in each capacitor. Therefore, the electrochemical double layer is to be understood as a plate capacitor of molecular dimensions, in which the metal electrode and adsorbed ions represent the plates of the capacitor. Thereby, the distance between the layers is to be understood as the radius of the hydrated ions.

With electrochemical methods, such as cyclic voltammetry, the double layer charge and discharge determines the capacitance of the electrochemical double layer, which is proportional with the surface area of the electrode. If double layer charging is the only process taking place in a given potential region, the only current measured will be the double layer charging current i_{dl}. Thus, i_{dl} is a function of the potential sweep rate the double layer capacitance C_{dl} can be determined according to:

$$i_{dl} = C_{dl} \frac{\delta E}{\delta t}$$

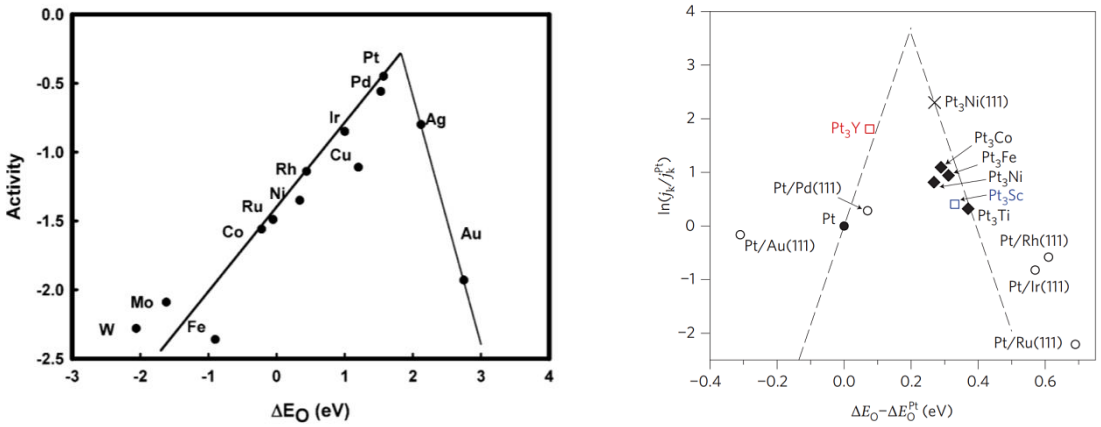

Figure 9: Volcano plots of pure metals (left) and of Pt-based transition metal alloys (right) as a function of the oxygen binding energy. Reproduced from [126,127].

by alloying platinum with certain 3d-transition metals, see **Figure 9**. [110] The transition metals like Ni, Co or Fe induce:

- heterometallic bonding interactions, termed the "ligand effect", between the active platinum atoms on the surface and the alloying metal atoms in the second or third layer, which result in a modification of the electronic structure, thereby changing the surface chemical properties (reduced adsorption energy for oxygen) [128], and
- a "strain effect", which originates from the shorter interatomic distance between the platinum atoms. [2] The smaller Pt–Pt bond distance leads to an enhanced dissociative adsorption of oxygen. [123]

Over the last few years, extensive efforts have been directed towards the preparation of bimetallic nanostructured electrocatalysts with an enhanced activity for the ORR. [129–132] Thus, nanoparticles based on a stoichiometry of Pt_3M (M: Cu, Co and Ni) are generally more active than pure platinum particles. [2]

A further development of this strategy has been reported as the selective electrochemical dissolution (dealloying) of the non-noble metal. [133] Hereby, the non-noble metals like Ni and Co serve as "sacrificial" elements in Pt-Ni and Pt-Co nanoparticles, because they are oxidized at much lower potentials than Pt. [105] As a result, Pt-skeleton nanoparticles (see **Figure 10**) or particles that consist of a Pt-enriched shell are realized. [132] A remarkably high activity for the ORR was observed on such particles. [134] However, for large-scale industrial synthesis the electrochemical dealloying approach is not very practical.

Finally, the world record for ORR specific activity was measured on bulk crystals of $Pt_3Ni\{111\}$. The $Pt_3Ni\{111\}$ surface is 10-fold more active for the ORR than the

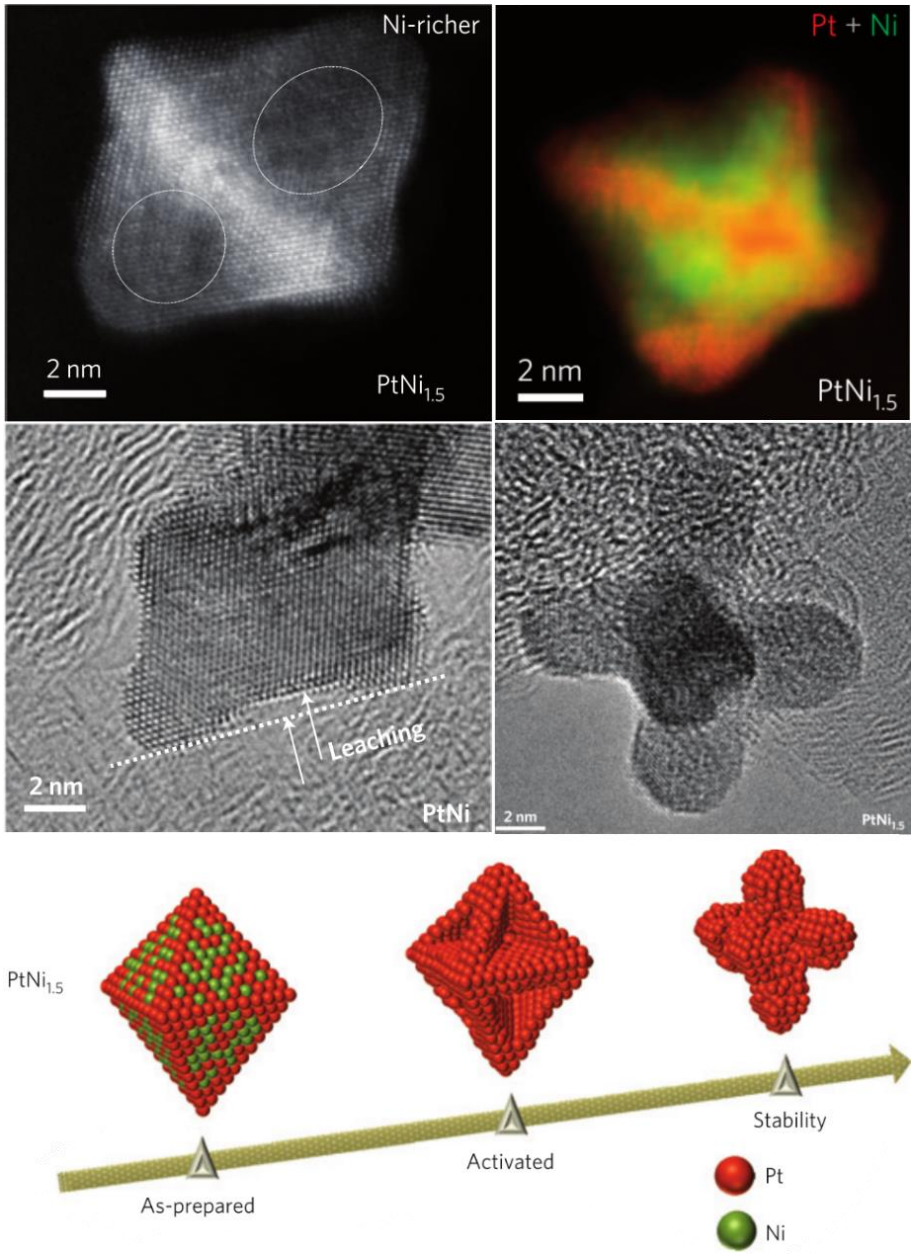

Figure 10: HRTEM image of a $PtNi_{1.5}$ octahedral nanoparticle shows that selective leaching in the facets of the Ni rich $PtNi_{1.5}$ results in the formation of an orthogonal skeleton structure. Reproduced from [130].

corresponding pure Pt(111) surface and 90-fold more active than the current state-of-the-art Pt/C catalysts. [135] So far, several catalyst systems have shown ORR kinetics adequate for automotive applications, including the commercially available heat-treated PtCo/C. As recent progress with "designer" catalyst particles suggests, they will reach their maximum kinetic performance over the next few years something close to the specific activity of $Pt_3Ni\{111\}$. [106]

But impressive kinetic activity will not automatically make a catalyst system attractive for large-scale automotive fuel cell production. As DEBE stated: "it has been 25 years since the first PtCo/C catalyst was investigated, but it is still not generally

accepted for use in current fuel-cell vehicles; it may take even longer to implement any of the newer catalyst approaches into realistic electrodes." [106]

Today, it simply is no longer sensible that the majority of researchers in the field are concentrating on synthesis of sophisticated electrocatalysts with ultrahigh ORR activities at least in lab-scale. Especially since the activity improvements are in the range of some tens of millivolts. At practical current densities of 0.1 to 2.5 A cm^{-2}, improvements in cell resistance can have a much larger impact on the actual cell voltage than improvements in reaction kinetics. [106] Instead, the focus should lay on robust electrocatalytic systems that can be manufactured at high volumes with the requisite quality, throughput and yields, at the required low Pt loadings. [123]

Nanostructured Thin Films

Nanostructured thin films (NSTF) are a novel extended surface electrode structure with significant advantages in specific activity, durability, and cost due to the combination of surface area enlargement and Pt-alloying. [136] The NSTF technology is to date the only practical example of an extended surface area catalyst shown to effectively address several of the performance, cost and durability barriers faced by cathode and anode catalysts for fuel cell vehicles. [137] In general, NSTF consists of two compounds: (i) the nanostructured substrate, which provides as much surface area as possible and at the same time facilitates mass transport within the electrode, and (ii) a ultra-thin layer of catalytic active material. One major advantage of such polycrystalline thin film catalysts is the fact, that their specific activity for oxygen reduction is 5 to 10 times higher than for 2 - 3 nm diameter particles. The NSTF developed by the 3M Company (see **Figure 11**) is different from Pt/C or PtM blacks to the effect, that the catalyst support is a pure, organic molecular solid in the form of a crystalline whisker. The chemical compound is a perylene based heterocyclic organic solid used commercially in high volumes as a pigment. [137] The single crystalline nature of the whiskers assures highly reproducible and uniform surface properties for subsequent coating with catalysts. The crystallinity of the whisker can also influence the nucleation, growth and thin film morphology of an over-coated material such as a PtNi catalyst applied by the preferred methods of physical vapor deposition. [137] Even though Pt/C exhibits almost an order of magnitude higher surface area per gram Pt than the NSTF catalysts, the specific activity enhancement of the PtNi alloy NSTF catalysts is substantial, so that they actually have a higher mass activity than the carbon supported Pt nanoparticles.

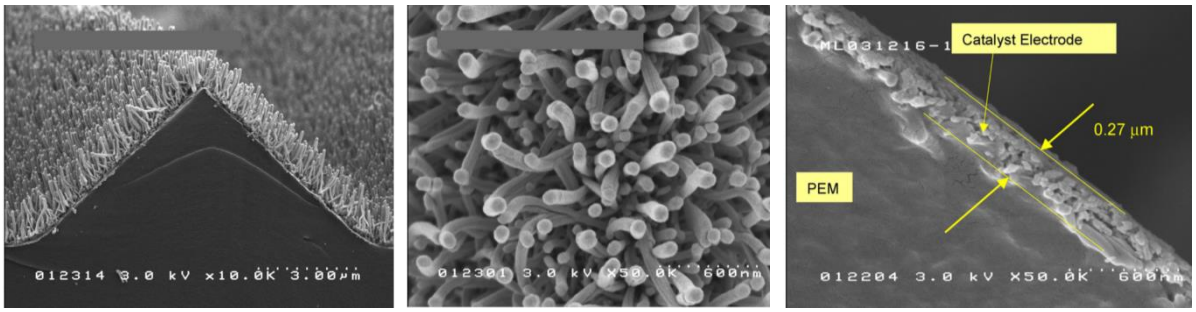

Figure 11: The catalyst coated whiskers end-up partially embedded in the PEM surface into which they were transferred by heat and pressure during the lamination step. This means a very short proton pathway from the catalyst surface to the membrane ionomer. Reproduced from [137,138].

Furthermore, the geometry of the NSTF catalyst makes it less susceptible to agglomeration and dissolution, whereby the durability could be improved in contrast to conventional nanoparticle catalysts.

Catalyst Degradation and Platinum Exposition

Considering that the prospect of further significant enhancement in the ORR activity is probably limited, the long-term performance of fuel cells has become the most important challenge that currently needs to be addressed. To compete with conventional internal combustion engines, a fuel cell should maintain at least 90 % of its performance after 5000 h of operation (equivalent to 250,000 km), including thousands of start-up and shut-down events. [2] Within the lifetime of a fuel cell, the electrodes, especially the carbon black support and the dispersed platinum nanoparticles, are exposed to electrochemical stress, which lead to degradation of the catalyst. In particular on high demanding conditions like cold start or power peaks the catalyst suffers. This results in a power output loss of the fuel cell, which will be caused mainly by five degradation phenomena's:

- **Platinum dissolution**: Smaller particles are more vulnerable for dissolution due to their higher surface energy.
- **Ostwald ripening**: The dissolved platinum from smaller particles accumulates on larger particles in consequence of surface energy reduction.
- **Agglomeration**: Particle cluster together, which leads to a decrease of the platinum/electrolyte surface area.
- **Particle detachment**: The detachment of platinum particles from the support result in a complete platinum loss. Platinum will be exposed to the environment and therefore it is not recyclable anymore.
- **Corrosion of the carbon support**: At the cathode the carbon support tends to oxidize due to high oxygen concentration and high positive potentials. The

oxidation of carbon to CO_2 is thermodynamically possible above +0.207 V vs RHE, but it is kinetically limited below +1.2 V vs RHE. [139] Carbon corrosion can accelerate secondary degradation such as agglomeration and particle detachment.

Through the degradation the Pt catalyst exhibits loss of active surface area. In contrast to catalytic converters in combustion engines cars, the degradation in fuel cells does not lead to a massive weight loss of the catalyst, as it is discharged from the system with the hot exhaust gases. [112] As a result, the recycling rates of Pt, Pd and Rh in conventional catalytic converters are in the range of 50 to 60 %. [112] However, fuel cells also expel small portion of platinum (typical under 5 mass-%) in the environment. Promising degradation resistance was observed at the former mentioned NSTF structure by using ultrathin layers of catalyst instant of nanoparticles.

2.3.2.2 Solid-Oxide Fuel Cells for Stationary Power Generation

The solid oxide fuel cell (SOFC) belongs to the high temperature fuel cells, with operating temperatures of 600–1000 °C. [108] In contrast to low temperature fuel cells such as PEM fuel cells, a solid ceramic inorganic oxide, generally ytteria-stabilised zirconia (YSZ), is used as the electrolyte. On the electrolyte gas-permeable electrical conductors are attached as the cathode and the anode. At the cathode, oxygen is reduced to oxygen ions, which pass through the solid electrolyte to the anode, where they react with the fuel, generally hydrogen and carbon monoxide, producing water and CO_2 as well as electricity and heat. [140] In general, as the main fuel, methane is inserted into the cell stack, together with water vapor methane reacts to hydrogen and carbon monoxide inside the cell stack due to the internal reforming reaction that is a characteristics of SOFC. Alternatively, in contrast to today's gas turbines, SOFC can be fueled with pure hydrogen. Another advantage over gas turbine power plants, which convert chemical energy into heat, mechanical power and then into electricity, is the direct electricity generation in a SOFC. Thus, their efficiency is not limited by the CARNOT efficiency. Moreover, SOFCs are excellent candidates for stationary power generation (hundreds of MW) [103], where the hot reaction products are usually used in a subsequent cycle such as a gas turbine, steam turbine, or combined cycle to produce additional electricity and increase the system efficiency to levels as high as 80 %, which is significantly higher than any conventional electricity generation. [140]

Nevertheless, there are a few systems commercially available yet. For stationary power supply of single-family homes, for instance, SOLIDPOWER commercially distribute the BLUEGEN combined power house with 1.5 kW electric power (60 % efficiency) and 0.54 kW thermal power supply. [141] Furthermore, ELCOGEN OY offers a 3 kW all-electric power solution. [142] For large-scale implementation of SOFCs MITSUBISHI HITACHI POWER SYSTEMS showcased with their SOFC-MGT hybrid system a 1000 kW combined cycle electric power plant, where in the first stage fuel gas is inserted into a SOFC to generate electricity and subsequently the hot exhaust gases are inserted into the micro gas turbine to generate additional power with an overall efficiency of 65 %. [143]

SOFCs are still actively developed for clean and efficient electric power generation. The main focus of research lies on the oxygen-conducting electrolyte and on the oxygen reduction on the cathode. The electrolyte must be highly conductive for oxygen ion and at the same time electrical isolating at high temperatures. In order to reduce the transport resistance of the oxygen ions the membrane should be as thin as possible. Today's YSZ membranes have a thickness of some hundreds of micrometer. On top of the YSZ membrane some tens of micrometers thick cathodic and anodic layers are coated. The cathode in state-of-the-art SOFCs is typically a porous gas permeable layer of $La_{1-x}Sr_xMnO_3$ that facilitates the critical oxygen reduction reaction. [144] The anode is instead made of Ni/YSZ to facilitate the conversion of methane to H_2 and CO. [126] As already reported for SOFC cathodes, electrode microstructure is highly required to get efficient oxygen diffusion and a simultaneous water exhaust. [145] Consequently, the electrode active surface area is limited to the interface area, where electrolyte and cathode are in close contact.

2.3.2.3 The Microbial Fuel Cell

As a hybrid of PEM technology and stationary power supply the microbial fuel cell (MFC) will be briefly introduced in the following paragraph. The MFC is a bio-electrochemical system that produces electricity by using bacteria for microbial-catalyzed anodic oxidation processes. In contrast to the common PEM fuel cell, where hydrogen is anodically oxidized to protons, in a MFC microorganisms, like the *Geobacter sulfurreducens,* on the anode oxidize organic substances such as acetate, lactate or glucose to H^+, CO_2 and electrons. [146] The maintained protons will be transferred through a proton exchange membrane (PEM) to the cathode, whereas the electrons pass an external circuit. At the cathode, oxygen is reduced analogously to

the hydrogen-powered PEM fuel cell and water is formed with the protons from the anodic half-reaction. Unfortunately, ORR active catalysts such as platinum are still required for the cathodic reaction in a MFC. On the upside, the slow reaction kinetics of the microorganisms at the anodic site enables the application of less active but more affordable non-noble metal-based ORR catalysts like cobalt tetramethoxyphenyl-porphyrin (CoTMPP). [147]

The greatest potential of MFCs lays in the use of wastewater as fuel, which allows combining wastewater treatment and energy recovery. [148] In Germany, for example, 5000 million m^3 of wastewater require 3 TWh of electrical energy for wastewater treatment every year. [149,150] On the other hand, 10.5 TWh of primary energy is contained in Germany's wastewater of one year. [151] Due to the direct energetic utilization of wastewater ingredients by electrochemically active bacteria, the wastewater treatment is to be transformed from an energy-consuming to an energy-producing process. The low coulombic efficiencies and low power outputs of MFCs are major limitations and, however, still do not allow economical large-scale implementation. [104] One key factor for commercial success of this technology will be lowering the cost of electrodes and associated materials to enable recovery of capital costs within only a few years. [152]

2.4 Summary

With the progressing expansion of renewable energies, energy storing and releasing technologies become mandatory as a consequence of their fluctuating power supply behavior. Storage of renewable energy in chemical bonds, in particular hydrogen, is attractive due to the high energy density, the elemental abundance, the long-term storability and the ability to transfer renewable electricity into other energy sectors. Usage of hydrogen as the main energy carrier also allows bridging the electricity and the gas grid as well as diffusing renewable energy to the heat and transport sector, and the chemical industry.

In the so-called hydrogen economy, excess electric power will be used to generate hydrogen via water electrolysis. The scalability of water electrolysis, as well as its ability to easily operate in an on-demand mode makes this technology ideal to couple with renewable, time-varying energy sources. [153] Normally, "conventional" alkaline water electrolyzers are coupled with wind and solar power. The more efficient proton exchange membrane (PEM) electrolyzer technology requires the use of expensive noble catalysts such as iridium, ruthenium and platinum in order to facilitate the catalysis of the oxygen evolution reaction (OER) and the hydrogen evolution reaction (HER) in corrosive acid electrolytes at high positive potentials. By contrast, performing polymer membrane-based water electrolysis under alkaline conditions allows the use of non-noble metals such as nickel and stainless steel as electrode materials and simultaneously profits from the lower electrolyte and cell resistances. This approach harbors a great advantage of AEM electrolyzers over PEM electrolyzers and can significantly reduce the associated costs. It is clear that there remains significant room for improvement in the performance of AEM in order to achieve operational current densities comparable with PEM electrolyzers. [154] However, regardless of the route taken, the viability of these systems as sustainable hydrogen production technologies is, in the end, dependent on the electrochemistry of oxygen. The generation of molecular oxygen at the anode is the most energy-intensive step in the overall water splitting process. [38] In order to improve the overall performance of the oxygen evolution reaction (OER), this work focuses on electrode structuring to increase accessible electrocatalytic surface area and to facilitate the bubble detachment from the electrode's surface.

The electrochemically produced hydrogen can be used directly as a fuel in the transportation sector or can be stored in underground formations for later usage. The fact that hydrogen is a very light gas makes its storage and transportation a real

challenge. However, while gravimetric energy density of hydrogen is excellent (33.3 kWh kg^{-1}), the volumetric energy density of even liquefied hydrogen (2.4 kWh L^{-1}) is critical. [72] Therefore, the aim of hydrogen storage technologies is thus to reduce the volume that hydrogen naturally occupies. The relevant large volumes for hydrogen storage can only be provided by suitable underground geological formations. [76] The pressure and therefore the storage capability of those underground storage facilities are limited by the strength characteristics of the contained rock or salt formations. In addition, it is also possible to feed hydrogen into the existing natural gas grid and thus use the storage capacities of the natural gas grid. However, in Germany, the admixture is limited to 5 vol-% hydrogen at each point of the network. But with a total energy storage capacity of 217 TWh [79] the German gas network can store 3 TWh of hydrogen. However, hydrogen as an energy source will always be less efficient and more expensive than the direct usage of the electricity from renewable energy sources. Consequently, it will only be used to compensate the gap between power demand and supply. Nevertheless, hydrogen storage is regarded as the most cost-efficient solution, which enables the storage of large quantities of electrical energy at 100 GWh energy storage capacity for inter-seasonal energy storage.

There are basically two technological ways to reconvert hydrogen to electricity and heat. One is the combustion of hydrogen within gas power plants or to reach even higher efficiencies in combined cycle power plants, which is the most feasible technology for hydrogen-based stationary power supply so far. However, the controlled combustion of pure hydrogen is rather challenging in particular in large scale power plants. Thus, the natural gas as the standard fuel in such power plants will be enriched with hydrogen. The second is the reconversion of pure hydrogen to electricity by electrochemical fuel cells. Fuel cells have higher efficiencies and through the direct utilization of pure hydrogen they produce only water as exhaustion gas. Especially in the transport sector, PEM fuel cell technology is of particular interest due to its high efficiency (theoretically 83 %) and compact design at relatively low operation temperatures (80 °C). [104] Most catalysts used today in PEM fuel cells are based on platinum nanoparticles dispersed onto larger high-surface-area carbon black supports (Pt/C) to increase the Pt surface-to-volume ratio and thus the electrochemical reaction rate, especially of the oxygen reduction reaction (ORR). [105] To protect the Pt catalyst from impurities (catalyst poisons), mainly CO that causes deactivation, only pure hydrogen can be utilized in a PEM fuel cell.

Electrochemistry will play a vital role in creating sustainable energy solutions in the future, particularly for the conversion and storage of electrical into chemical energy in water electrolysis cells, and the reverse conversion and utilization of the stored energy in fuel cells. [2] The large-scale operation of these technologies is currently limited by the serious challenges in the design of efficient, endurable and affordable electrodes for the OER and ORR. The three main deficiencies are related to:

- the activity of the electrodes, since both oxygen reactions exhibit significant overpotential even with noble metal catalysts, thereby resulting in higher energy consumption for water electrolysis and in lower energy recovery for the recombination of H_2 and O_2 in fuel cells;
- the stability of the electrodes, as the OER and ORR catalysts are exposed to harsh conditions that are obstructive for long-term performance of the device; and
- the abundance of the materials used, because the most active catalysts for the OER and the ORR are based on noble metals such as platinum and iridium that are rare and pricy.

Although specifically designed materials like bimetallic nanostructured electrocatalysts in form of particle or thin films already satisfy some of these requirements – at least in lab-scale, under real conditions in large-scale devices, this is still a huge challenge. The scalability of any new catalyst approach needs to be considered seriously. For many of the new catalyst approaches such as Pt-skeleton nanoparticles prepared by electrochemical leaching, it is unclear how their generation process could be scalable by keeping the quality consistent.

In general, electrocatalytic activity of the electrode material can be enhanced (overpotential decreased) by increasing the electrochemical surface area. Therefore, in the present work, ultrashort pulse laser structuring was utilized to modify metal electrode with laser-induced micro- and nanostructures in order to dramatically increase the accessible surface area of well-known electrode materials such as nickel and platinum.

3 Ultrashort Pulse Laser Structuring

Laser structuring is an emerging technology for generating surface functionalities on basis of optical, mechanical, or chemical properties. Lasers provide the ability to accurately deliver large amounts of energy into confined regions of a material in order to achieve a desired response. For opaque materials, this energy is absorbed near the surface and causing material ablation without altering the bulk. [155]

Laser ablation is usually discussed in the context of pulsed lasers. The onset of ablation occurs above a threshold fluence, which will depend on the absorption mechanism, particular material properties, microstructure, morphology, the presence of defects, and on laser parameters such as wavelength and pulse duration. Typical threshold fluences for metals are between 1 and 10 J cm^{-2}. With multiple pulses in the same region, the ablation thresholds may decrease due to accumulation of defects. [155] During material ablation with pulsed laser radiation different beam-matter interaction mechanisms become dominant. For short laser pulses in the micro- and nanosecond range, the ablation process is dominated by heat conduction, melting, evaporation and plasma formation. [156] In this case, the pulse duration is long enough that the absorption of laser radiation and ablation of a target material occur at the same time. Thereby, a thermal wave propagates into the target and creates a relatively large amount of molten material. The molten material is pushed out by the recoil pressure produced by the vaporization process. [157]

Shortening of the pulse duration to a time scale shorter than a couple of picoseconds (ps) fundamentally changes the interaction physics of the laser radiation with the solid, which results in rapid and precise energy deposition into the materials. [158] During ultrashort pulsed laser irradiation, the laser energy is absorbed by free electrons, which occurs within hundreds of femtosecond by the absorption of photons. [159] At this stage, the electronic system is rapidly heated up to temperatures in the order of tens of thousands of Kelvin (10^9 K s^{-1} or more) [160] while the lattice remains largely undisturbed (cold). This phenomenon is described by means of the **two temperature model**. Efficient energy transfer from the electrons to the lattice occurs by electron-lattice scattering after the end of the laser pulse. The thermalization between free electrons and the lattice typically occurs on the time scale of 1–100 ps depending on the electron–phonon coupling strength of the material. [159] Via ablation extreme pressures, densities and temperatures build up and accelerate the

ionized material to enormous velocities. [156] Therefore, ultrashort pulse laser ablation is a machining technique with a marginal heat-affected zone. Usually, melting can be neglected, even in high thermal conductivity materials such as metals [159], because most of the heat is led away by convection with the hot ablated particles. [161] The resulting features can be broadly categorized into laser-inscribed and laser-induced structures. Laser-inscribed structures consist of machined features such as grooves and holes, with dimensions equal to or greater than the effective laser beam diameter. On the other hand, laser-induced surface structures that are formed under laser irradiation have feature sizes smaller than the effective beam diameter. [162]

The first application of ultrashort pulse lasers in mass production processes was drilling inkjet nozzles with specific shapes by picosecond laser ablation. [163] Due to the precise material ablation, ultrashort pulse lasers are further utilized in the fabrication of medical coronary stents. [159] Currently, they are also used for scribing and patterning thin-film photovoltaic solar cells based on copper indium gallium selenide (CIGS) or cadmium telluride (CdTe). [164]

In contrast to the classical machined features, laser-induced surface texturing is a process that allows the change of surface properties without changing the chemical composition of the material. Properly designed surface structures on the micro- or nanoscale can have very beneficial effects on friction and wear. [18] Thus, ultrashort pulse laser structuring is a promising approach for enhancing the tribological performance of mechanical components. Some concepts were already transferred to the automotive industry, for example the process of “laser-honing”, where laser structuring for reducing friction and wear is applied in the range of the upper piston reversal point of cylinders in combustion engines. [165] This additional manufacturing step is supposed to result in reduced oil and fuel consumption, less exhaust gas emissions, and an increased lifetime of the engine. [18]

The development of laser structuring has been stimulated by recent advances in the development of high performance pump diodes, enabled the use of new laser media, especially ytterbium-doped fibers and crystals. The development of high-performance ultrashort pulse lasers has achieved medium laser powers of 100 to 1000 W in recent years, which makes large-scale industrial applications possible. Now, high power ultrashort pulse lasers allow 3D micro-structuring of large-scale metal surfaces for embossing and printing applications due to the shorter processing times. [166] The FRAUNHOFER Cluster of Excellence ADVANCED PHOTON SOURCES is

currently developing new ultrashort pulse laser systems, which should surpass all previous ones by an order of magnitude in the average laser power. [167]

3.1 Laser-induced Surface Structures

3.1.1 Laser-induced Periodic Surface Structures

The laser-induced periodic surface structures (LIPSS), often referred to as surface ripples, discovered by BIRNBAUM in 1965 [168], are the most researched surface structure caused by laser irradiation. They are formed by irradiating materials with linearly polarized nanosecond or longer laser pulses with a fluence near the ablation threshold. [169] The formation of these LIPSS on metals is often explained by the interference of the incident laser light with the excited surface plasmon polaritons that results in spatial periodic energy distribution on the surface. [170] Consequently, the ripples are generally oriented perpendicular to the incident polarization. Therefore, the spacing is in the order of the wavelength or greater, see **Figure 12** and **Figure 13**. Various mechanisms, including the self-organization of surface instability, second-harmonic generation, refractive index change, nano-plasma formation and the excitation of surface plasmon polaritons, have been proposed for the formation of LIPSS; however, no consensus has been reached until now. [159]

Several application fields have been exploited taking advantage of the surface micro- and nanostructuring influencing the optical, mechanical and chemical properties of metals and other materials. [171] The most obvious application of LIPSS arises from the fact that their periods lie in the same range as the wavelength of visible optical radiation. [169] Hence, they efficiently act as diffraction gratings for dye-free structural coloration of metals and semiconductors. [170,172] Furthermore, LIPSS can be used in applications where the redistribution of light is intended, e.g. in thin-film solar cells. [173] LIPSS can have a positive effect on mechanical properties such as friction to reduce wear and fuel consumption in combustion engines. LIPSS modified surface reduces the friction by a factor of two compared to a polished surface. [174]

There are only a few studies addressing the chemical and electrochemical properties of LIPSS so far. In 2014, NEALE et al. have established that the formation of LIPSS on nickel electrodes yields 2.5 times more surface area in alkaline solution. [175] They described a possible application of LIPSS in the field of Ni-H battery

electrodes, where larger surface area per electrode results in higher charge storage capacity at a stable battery size.

Nevertheless, the transfer of a successfully established laser structuring method for generating LIPSS from one material to another remains difficult. The main reason are different material specific electron-phonon coupling strengths, which describe the capability to transfer energy from the hot electron system to the cold lattice. In practice, therefore, the parameter set of the laser structuring process must be determined empirically for each material.

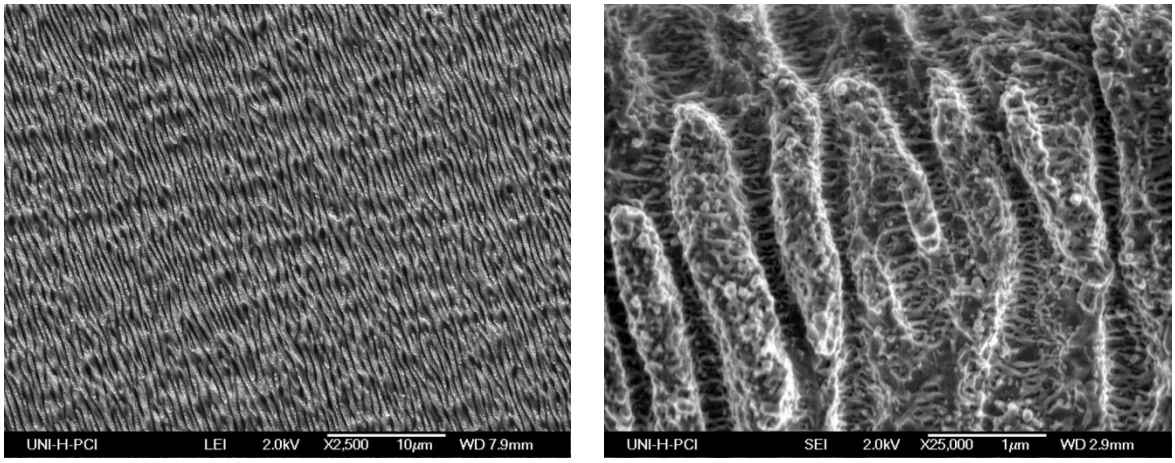

Figure 12: LIPSS produced on a polished nickel plate with a Yb:YAG (λ = 1030 nm) one picosecond laser system.

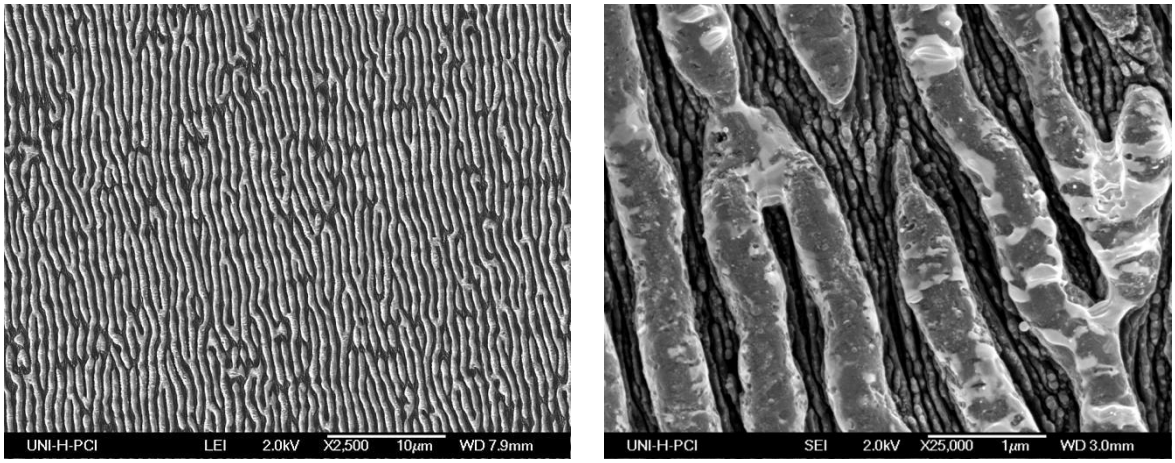

Figure 13: Platinum LIPSS produced on a glassy carbon substrate with a Yb:YAG (λ = 1030 nm) one picosecond laser system. Therefore, 1 µm platinum was sputtered on the glassy carbon substrate and laser structured afterwards.

3.1.2 Cone-like Protrusions

Another promising structure type formed by ultrashort pulse laser irradiation is based on regular arrays of conical microstructures often called cone-like protrusions (CLPs) or spikes, see **Figure 14** and **Figure 15**. The physical mechanisms attributed

to the formation of these 3D-surface structures are highly dependent on the properties of the substrate material as well as on the specific illumination conditions including the laser fluence, repetition rate, number of pulses incident on the sample as well as the angle of incidence, and the atmospheric conditions during processing. [176] In general, the formation of CLPs can be categorized in three steps. [176] Firstly, the introduction of nano- and microdefects in the surface that ultimately leads to the creation of precursor sites that affect the distribution of laser energy from subsequent laser pulses on the sample. Secondly, the growth of the precursor sites and the associated formation of larger self-organized features. And lastly, the evolution of the self-organized conical structures upon continued illumination. Thereby, the laser fluence and material properties like surface roughness, electro-phonon coupling strength and chemical composition have a significant impact on both the development of the precursor sites as well as on the growth mechanism. As a result, the laser fluence significantly affects the morphology of the CLPs. [170]

The surface modification with CLPs leads to topography-based functionalization of a large variety of materials. This offers the possibility to introduce localized surface properties like enhanced wettability or water repelling behavior known as “Lotus effect” by laser irradiation. [177] Several efforts were undertaken to control and guide cellular behavior by introduction of CLPs in order to generate an “intelligent” biomaterial. [178–180] This would have a great impact in the field of medical implants, where the controlled interaction of proteins and cells with the implant surface plays an important role. [181]

In 2017, RAUSCHER et al. showcased for the first time the great potential of CLPs-modified nickel electrodes for water electrolysis application (hydrogen evolution reaction). [182] The CLP electrodes exhibited an increase in surface area of 73 times compared to a smooth nickel plate. In addition, the same group recently demonstrated that ultrashort pulse laser structuring in combination with thin layer catalyst deposition can dramatically boost the performance of cathodes for the hydrogen evolution reaction due to the enormous increase in specific surface area in combination with superhydrophilic properties leading to a rapid gas bubble detachment. [183]

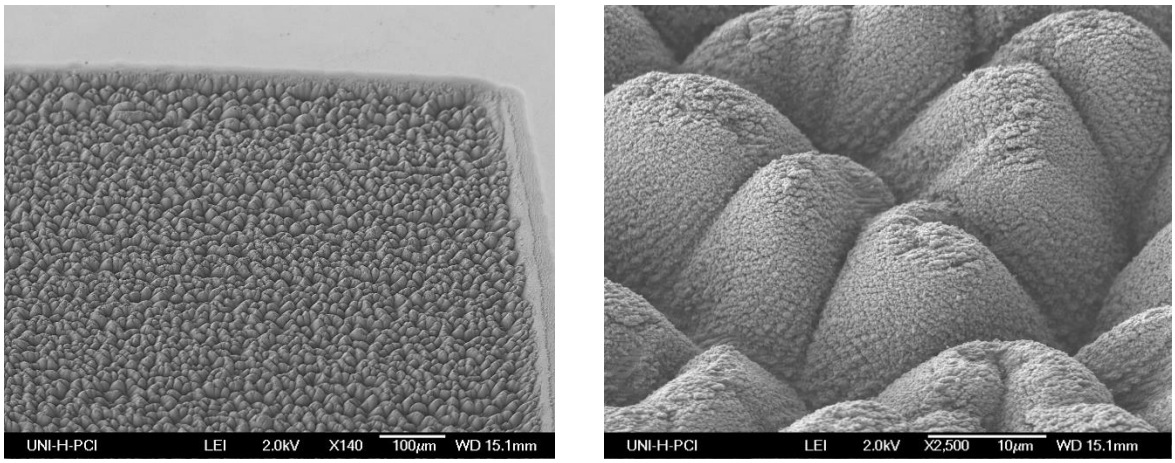

Figure 14: CLPs produced on a polished Cobalt plate with a Yb:YAG (λ = 1030 nm) one picosecond laser system.

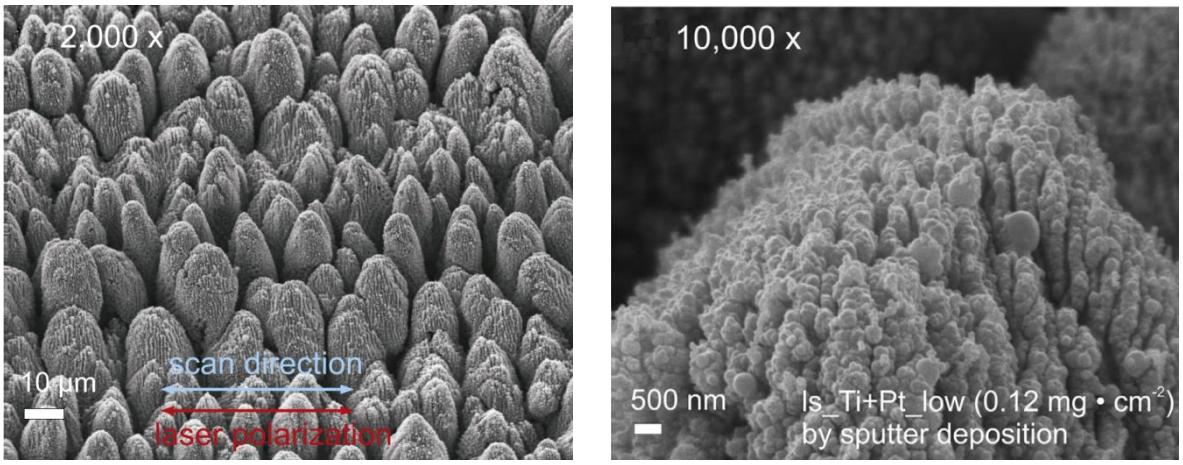

Figure 15: CLPs produced on a Titanium foil with a Ti:Sapphire (λ = 800 nm) 60 femtosecond laser system (left) and the same structure coated with 0.12 mg cm^{-2} platinum catalyst via sputter deposition (right). Reproduced from [183].

3.1.3 Black Metals

A decade ago, VOROBYEV et al. demonstrated a femtosecond laser blackening technique that made reflective metals highly absorptive, creating the so-called "black metals." [184] In essence, this metal blackening technique applies intense femtosecond laser pulses on a metal surface and creates a variety of unique surface structures at nano- and micro-scales dramatically enhancing light coupling into the metal. These structures allow the transformation of highly reflective metals into totally absorptive surfaces in a broad wavelength range from 250 nm to 2500 nm. [185] The "pitch black" effect results from the aggregates of coalesced nanoparticles, which cause a broadening of the plasmon resonances into a band of frequencies. In contrast to isolated metal nanoparticles, at which surface-plasmon resonances occur at sharp individual frequencies. [170]

Surprisingly, there is no chemical or electrochemical study of black metals produced by ultrashort pulse laser structuring in the literature, yet. OU et al. used a nanosecond laser system to fabricate hierarchical nano- and microstructures on large 10 x 10 cm^2 nickel electrodes for water electrolysis application. [16]

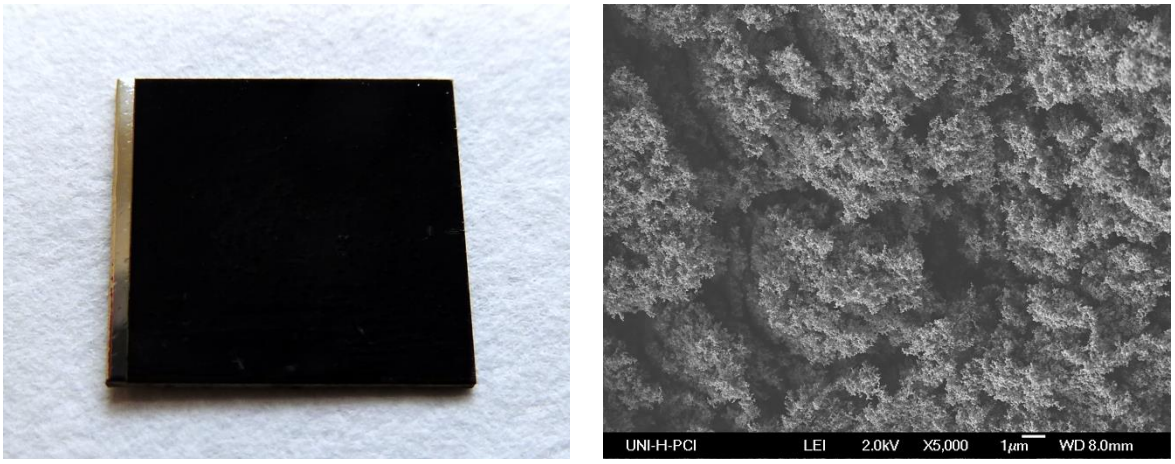

Figure 16: Black platinum produced on a polished platinum plate with a Yb:YAG (λ = 1030 nm) one picosecond laser system.

4 Published Results

In **Chapter 4.1 Platinum Electrodes for Oxygen Reduction Catalysis designed by Ultrashort Pulse Laser Structuring**, the first systematic quantification of the surface area enlargement of the three main types of laser-induced surface structures is given. In cooperation with the LPKF LASER & ELECTRONICS AG a representative structure of each structure type (LIPSS, CLPs and black metals) was generated on platinum electrodes in air by varying the laser parameters average power, scan speed and line distance. In the related paper, the structure type of the black metals (in this case black platinum) is referred to as porous cone-like protrusions (pCLPs). The structured Pt electrodes were subsequently analyzed by cyclic voltammetry to determine the possible suitability of laser-induced surface structures as a strategy to increase the performance of electrochemical electrodes. The surface area enlargement was stated as the multiple of a smooth plane Pt reference sample the so-called roughness factor.

The investigation of the electrochemical surface area revealed roughness factors of 1.75, 7.4 and 1527 for the LIPSS, CLPs and black platinum, respectively. The result of our LIPSS concur with former investigated LIPSS on nickel that showed a roughness factor of 2.5. [175] Moreover, the CLPs possessed a considerable surface area enlargement, but may as well have other advantages as we will explore in chapter 4.3. By far the largest increase in electrochemical surface area was achieved with the black platinum structure. The reason behind was discovered by SEM analysis. Through the tightly hatched scan pattern with only 1 µm line distance a considerable amount of ablated material was ejected out of the Pt electrode and subsequently redeposited to form a filigree network comprising of nanoparticles with diameters of 10 nm to 90 nm. To study the aging behavior of this nanoparticle network, we electrochemically stressed the electrode by 1000 CV cycles. Consequently, a moderate aggregation of the nanoparticles was observed in the SEM, which slightly reduces the electrochemical surface area. After the aging process, the crystallinity of the black platinum remained the same. In addition, XRD examinations did not show any preferential direction of crystallinity for any of the investigated laser-induced surface structures.

In conclusion, laser-induced surface structures, especially the black metal structure type, exhibit major surface area enlargement and good electrochemical stability, which makes this structure type ideal for electrode modification.

Thus, further development of high surface area structures on the basis of the black metal structure type was pursued. The laser structuring process was optimized in order to develop new highly porous surface structures on a more practical and more affordable electrode material. Nickel was chosen as one of the most common electrode materials due to its beneficial catalytic properties especially for HER and OER and its good stability in alkaline solutions.

One challenge we had to overcome was the fact that structuring non-noble materials with high spot energy densities (pulse overlap of more than 99 %) in air results in oxide formation and therefore in a substantial reduction of the structure's electrical conductivity. To prevent oxidation the laser structuring needs to be performed under inert gas atmosphere. Therefore, a gas-tight reactor chamber with an inert gas inlet and a port for suction was constructed. Furthermore, a femtosecond infrared laser beam was coupled into the chamber through a glass window with more than 90 % infrared transparency.

In productive cooperation with the LPKF LASER & ELECTRONICS AG and the FRAUNHOFER INSTITUTE OF LASER TECHNOLOGY (ILT) a new structure type generated by ultrashort pulsed laser radiation was discovered – the laser-induced nano-foam short LINF. In **Chapter 4.2 Porous Nickel Nano-Foam by Femtosecond Laser Structuring for Supercapacitors Application,** the enlargement of the surface area through LINF modification of Ni electrodes is presented. 1 cm^2 arrays of LINFs on Ni were created with the objective to generate preferably a highly accessible surface area for electrochemical charge storage. The capability of Ni/NiO surfaces to store electrical charges by the fast reversible redox reaction of $Ni(OH)_2$ to NiOOH in alkaline solution, makes high surface area nickel electrodes attractive for supercapacitor applications.

In the literature there are only a few studies about porous surface structures generated by laser radiation. [186,187] None of them have determined the surface area enlargement or the real surface area of the produced structures. To the best of our knowledge, we demonstrate for the first time the use of femtosecond laser pulses to fabricate metallic porous surface structures that form on top of the original surface. The laser structuring conducted in this work leads to the development of a foam-like structure that emerges up to 100 µm on top of the surface of the Ni substrate. Contrary to other laser structuring processes based on ablation, our method uses

electrode material most efficiently by re-depositioning the ablated particles to form the porous network.

For this purpose, a femtosecond laser beam was scanned across a nickel electrode in a line pattern. At the start of the structuring process, the laser beam is shaping a kerf in the material. The more lines are scanned by the laser beam, the wider and deeper the kerf becomes. Consequently, projection effects of the incident laser beam occur on the steep walls of the kerf, which results in the preferred ablation of material from the bottom of the kerf. After each scan, the ejected particles with diameters from 15 nm to 200 nm redeposit on the electrode's surface and form a filigree network. The network becomes even more filigree with decreasing the distance of the scanned lines from 5 µm to 1 µm.

In conclusion, there are two substructures, one below and one on top of the original surface, which together form the LINF structure. The substructure below the original surface is made of porous bars with a thickness that is equal to the line distance of the scanned line pattern. In contrast, the substructure on top of the original surface is made of redeposited particles aggregated in a porous network. After the structuring, the Ni LINF electrodes were stored in air to induce the formation of a thin NiO passivation layer.

The surface area of the LINF electrodes was estimated by measuring the double layer capacitance, which is proportional to the real surface area. Hence, the surface area enlargement can be expressed by the ratio of the double layer capacitances of a structured electrode and a plane surface of the same material. The accessible surface area and therefore the charge storage capacity can be tuned by the distance of the scanned lines. Thus, the 5 µm LINF electrode exhibited a surface area enlargement by a factor of 730, whereas the 1 µm LINF electrode exhibited an excellent enlargement factor of 1600.

The total charge-discharge behaviors of the LINF electrodes were further examined by galvanostatic charge-discharge measurements. The total charge storage capacity increases with decreasing line distance analogous to the double layer capacitance. In particular, the 1 µm Ni LINF electrode showed an excellent capacity of up to 2 C cm^{-2} by virtue of the filigree laser-induced 3D structure.

In the previously discussed publications, we were focusing on the enlargement of the electrode's surface area to increase the number of surface sites for catalysis or charge storage purposes. In the case of gas-evolving reactions, such as OER and HER, an increase of the surface area through the modification of the electrode with porous

structures will not automatically increase the electrode's performance. The gas formed inside the porous structure can block the pores and therefore parts of the active surface area. When part of the surface area is deactivated by gas bubbles, the remaining uncovered surface has to produce a higher current density to make up for the loss of active area, which drives the overpotential up. Furthermore, gas bubble growth inside of pores can lead to high mechanical stress due to increasing capillary pressure, which results in the mechanical degradation of the porous structures. [188]

On this account, in cooperation with the LASER ZENTRUM HANNOVER E.V., electrode modification on the base of micro-sized spikes (CLPs) is proposed in **Chapter 4.3 Spiky Nickel Electrodes for Electrochemical Oxygen Evolution Catalysis created by Femtosecond Laser Structuring**. Through the modification of nickel electrodes with CLPs a considerable enlargement of the electrode's surface area is coupled with enhanced gas bubble detachment by improving the wettability of alkaline water splitting anodes (OER). A superhydrophilic electrode surface attracted the electrolyte more than the bubbles and decreased the bubble-electrode surface attraction, accordingly bubbles detached easier.

Cyclic voltammetry analysis was performed to determine the double layer capacitance and subsequently calculate the roughness factor (surface area enlargement) of the structured electrodes. The resulting data revealed a significant increase of up to 87 times in surface area for the CLP-modified Ni electrodes. Examination of the CLP electrodes with scanning electron microscopy (SEM) and X-ray microscopy (in cooperation with the INSTITUT FÜR WERKSTOFFKUNDE of the LEIBNIZ UNIVERSITÄT HANNOVER) revealed two reasons for the surface area enlargement. Firstly, the surface area enlargement is caused by the formation of the micrometer-sized spikes and secondly by a significant amount of a re-deposited nano-sized ablation product, which covers the spike structure. Our results are in good agreement with published data. [182] Moreover, through cyclic voltammetric cycling (activation process) we discovered the preferred electrochemical oxidization of β-$Ni(OH)_2$ to β-NiOOH on the CLP electrodes. The letter exhibit excellent catalytic OER activity and therefore, the structured electrodes demonstrated OER overpotentials of 0.20 V to 0.23 V at a current density of 10 mA cm^{-2}. The electrochemical stability and durability of the CLP-modified electrodes were tested under demanding conditions at 100 mA cm^{-2} for 48 hours. As a result, the electrodes exhibited only a slight increase of the OER overpotential during the test period, indicating excellent electrochemical stability at high current densities.

To give an explanation for the emergence of the large amount of highly active β-NiOOH sites, the CLP-modified electrodes were investigated in cooperation with the INSTITUTE OF ENERGY RESEARCH AND PHYSICAL TECHNOLOGIES of the TU CLAUSTHAL with X-ray photoelectron spectroscopy (XPS). Based on the XPS data, the emergence of β-NiOOH sites could be attributed to the formation of defect sites at the surface of the laser-structured electrodes. Due to the high cooling rates within the ultrashort pulse laser structuring, the nano-sized decoration on the spikes showed a wide range of structural defects such as a higher emergence of steps, cavities, low-coordination sites, and compositional imperfections. These structural defects favor the formation of the highly active β-NiOOH species on the CLP electrodes.

In addition, the formation of $Ni(OH)_2$ and NiOOH positively influence the wettability of the structured electrodes. However, fresh laser-structured CLP electrodes revealed high contact angles of up to 101°, which is in good agreement with the literature. [189] Only after the electrochemical activation process, the wettability clearly improves. The electrodes become superhydrophilic due to the preferred formation of $Ni(OH)_2$ and NiOOH at defect sites.

In conclusion, an ultrashort pulsed laser was used to generate Ni/NiO spiky microstructures (CLPs) on bulk Ni electrodes with the objective to reduce the overpotential of the oxygen evolution reaction (OER). The electrode modification with CLPs has several positive effects. Firstly, an enlargement of the surface area by over 80 times due to the unique topography of the micro-sized spikes covered with nanoparticular decorations. Secondly, the increased formation of defect sites at the CLP electrodes by virtue of the high cooling rates that occur in the laser structuring process. These structural defects favor the formation of the OER-active β-NiOOH. Thirdly, the formation of NiOOH and its precursor stage $Ni(OH)_2$ enhance the wettability of the laser-structured electrodes, which facilitates the detachment of gas bubbles. Lastly, the CLPs modifications demonstrate good long-term stability especially at high current densities, where heavy gas evolution occurs.

Finally, in **Chapter 4.4 Laser directed dynamic Hydrogen Template Deposition of porous Pt@Ag Networks** the possibility to locally tune the catalytic activity of an electrode by ultrashort pulse laser treatment is presented. The dynamic hydrogen template deposition (DHTD) technique is a promising deposition method for producing porous gradient metal networks (e.g. Ag) on electrodes by electrochemical reduction of an ion precursor while hydrogen is generated at the surface of the

electrode. The ascending hydrogen gas bubbles act as a soft-template for the deposited metal.

We used the DHTD technique to generate gradient porous Ag networks on Ni electrodes and subsequently functionalized the Ag networks with Pt via galvanic replacement reaction. Furthermore, we demonstrated the concept to direct the DHTD of the porous Ag network by previously laser structuring the Ni electrode. Our approach was to reduce the overpotential of the hydrogen evolution reaction by sputtering a 10 nm thin platinum film on top of a nickel electrode. Subsequently, a hexagonal structure was engraved in the electrode by an ultrashort pulse laser beam. During the laser structuring Pt was ablated and the treated Ni electrode was locally oxidized. By virtue of the localized NiO formation, the hydrogen evolution and electrical conductivity were suppressed in the laser irradiated areas. Therefore, the Ag deposition occured mainly in the unstructured regions. Thus, the engraved structure created suitable diffusion paths and enhanced near-electrode mass transport.

In general, the double layer capacitance and therefore the electrochemical surface area of the porous Ag nickel electrodes can be increased by laser engravement, although non-conducting NiO formed. The increase in double layer capacitance by roughly a factor of two can be associated with the porous Ag walls, which were formed alongside the hexagonal structure. In addition, we discovered by SEM and TEM imaging that the laser-engraved structure facilitates the galvanic replacement of the Ag network by Pt. SEM cross-section image and elemental mapping of Pt@Ag network on non-structured electrode showed Pt only on top of the Ag network. In contrast, the laser-engraved electrode demonstrated several Pt sites inside the Ag network. This observation is most probably due to diffusion-induced inhibition of the galvanic replacement inside the porous Ag network. After the consumption of the infiltrated Pt precursor by the galvanic replacement reaction, further Pt precursor is supplied by diffusion and deposits mainly on top of the Ag network. The engraved hexagonal structure creates suitable diffusion paths and therefore enhances the supply of the Pt-precursor inside the Ag network. As a result, 25 % more Pt sites were electrochemically accessible.

4.1 Platinum Electrodes for Oxygen Reduction Catalysis designed by Ultrashort Pulse Laser Structuring

Karsten Lange*, Malte Schulz-Ruhtenberg, and Jürgen Caro,

ChemElectroChem, 2017, 4, 570–576.

DOI: 10.1002/celc.201600630

ChemPubSoc Europe

DOI: 10.1002/celc.201600630

CHEMELECTROCHEM Articles

Platinum Electrodes for Oxygen Reduction Catalysis Designed by Ultrashort Pulse Laser Structuring

Karsten Lange,*[a] Malte Schulz-Ruhtenberg,[b] and Jürgen Caro[a]

Compact platinum plates have been micro- and nanostructured by using a one-step process with ultrashort laser pulses. Depending on the parameters of the laser treatment (power, line distance, and scan speed), distinct surface structures can be produced by different spot energy densities. The platinum plates structured this way were tested for their electrochemical activity in the oxygen reduction reaction in aqueous $HClO_4$ by using cyclic voltammetry and rotating disk electrode approaches. The laser-induced surface structuring yields a substantial enhancement in the electrochemical activity of platinum surfaces. The observed rise of the electrochemical activity by a factor of 1500 is attributed to the considerable increase of the surface area.

1. Introduction

The oxygen reduction reaction is one of the most extensively studied topics in the fields of electrochemistry and catalysis owing to its importance for electrochemical energy conversion and storage devices.[1] In the past decades plenty of platinum-based heterogeneous electrocatalyst approaches have been explored.[2–5] It has been definitively proven that micro and nano structuring of plain platinum surfaces increases the electrochemically active surface area.[6–8]

In this paper a direct surface structuring approach was used to generate micro- and nano-sized surface topographies solely achieved by an ultrashort pulse laser beam incident directly on the surface of the bulk Pt metal without re-deposition of ejected particles onto specially prepared substrates. Laser treatment provides a unique method to modify materials by focusing a tremendous amount of energy onto a certain surface area of a material in a highly controlled manner. Essentially, two processes lead to the increase of the surface area: i) through ablation, the surface roughness of a plain metal plate increases, and ii) the precipitated metal nano droplets form a porous coating. The energy of a laser pulse is first absorbed by electrons in the irradiated volume and then transferred to the bulk of the material and its lattice through heat conduction processes due to electron-phonon coupling.[9] This energy transfer from electrons to lattice phonons takes several picoseconds.[10] Ultrashort laser pulses with pulse durations of less than 10 picoseconds can rapidly heat the electron system to temperatures in the order of tens of thousands of Kelvin (10^9 K s^{-1} or more),[11] while the lattice remains at room temperature during the first picosecond or picoseconds.[12] Thus, with properly selected pulse duration, electron-phonon coupling takes place only after the laser pulse. The heated region then acts as the source of a thermal wave which propagates to the bulk of the material. If the cooling rate exceeds the crystallization rate, amorphous structures can be produced due to a fast quenching of the precipitated metal dust and/or a molten and later solidified metal film on a bulk metal because of the high thermal conductivity of the metal.[13,14] To create tailor-made surfaces with improved catalytic activity, the number of overlapping laser pulses irradiating the Pt plate was varied from 81 to 27000 at different laser energy densities in the range of 0.15 J cm^{-2} to 0.47 J cm^{-2} per pulse. The generation of different surface structures appears to be the result of the interference between the incident laser beam and a surface wave (polariton), randomly scattered on the surface asperities.[15]

Laser-induced periodic surface structures (LIPSS) on solid surfaces can be understood as a universal phenomenon, which have been observed on all kinds of materials, such as metals, semiconductors and dielectrics[16–19] and occurs at a broad range of wavelengths.[20] LIPSS are usually termed nanoscale "ripples" and consist of wavy surfaces with a periodicity and an amplitude equal to or smaller than the wavelength of the laser beam.[21] They are oriented perpendicular to the polarization of the incident light.[22] It has already been established that the formation of LIPSS yields a considerable enhancement in the electrochemical activity of nickel surfaces in aqueous KOH.[23] By increasing the spot energy density E_s to 1628 J cm^{-2} (see the Experimental Section for further details), another type of self-organized surface structures, the so called cone-like protrusions (CLPs) decorated with micro-ripples and nanoparticles, can be generated.[24–27] The topology of CLPs can be customized to a certain extent by the laser parameters. At very high spot energy density (in the range of 7000 J cm^{-2}) metals, e.g. platinum are transformed into a mixture of liquid droplets and vapor, which expand at high velocity.[28] However, the ablated material cools down quickly and leads to the formation of porous micro- and nanostructures on the surface.[29] While the re-deposition of the ablated particles further dictates the morphology of the

[a] K. Lange, Prof. J. Caro
Institute of Physical Chemistry and Electrochemistry
Leibniz University Hannover
Callinstr. 3 A, 30167 Hannover (Germany)
E-mail: karsten.lange@pci.uni-hannover.de
juergen.caro@pci.uni-hannover.de
[b] Dr. M. Schulz-Ruhtenberg
LPKF Laser & Electronics AG
Osteriede 7, 30827 Garbsen (Germany)

ChemPubSoc Europe

CHEMELECTROCHEM Articles

irradiated surface.[25] These porous cone-like protrusions (pCLPs) exhibit deep, irregular vertical grooves between the porous nanoparticle networks. In the particular case of platinum, this surface structure is known as black platinum[30] by virtue of their high optical absorption.

In this paper we investigated, for the first time, the catalytic properties of different laser-induced surface structures using platinum plates as electrode material. The following techniques were employed to characterize the electrochemical performance and topology of the structured Pt electrodes. Firstly, powder X-ray diffraction (XRD) was applied to detect changes in the crystal structure created by laser structuring. Secondly, scanning electron microscopy (SEM) images were obtained to characterize the surface topology. Thirdly, cyclic voltammetry (CV) curves were measured to determine the electrochemical roughness factor (ϕ) and the catalytic stability in N_2 saturated 0.1 M $HClO_4$. Finally, linear sweep voltammetry curves were obtained using a rotating disk electrode (RDE) to receive half wave potential and the number of transferred electrons.

2. Results and Discussion

Figure 1 shows schematically the structuring process of the Pt electrodes. In the first step, the Pt plates were polished with diamond polishing suspension and cleaned with isopropyl alcohol as well as ultrapure water. In a second step, the cleaned plain Pt plates were irradiated with 1 ps laser pulses (λ = 1.030 µm) of different energy density to produce low, medium and high spot energy density samples. The focused laser beam, with a diameter (d) of 45 µm, was scanned across the material surface in a meander pattern. The laser parameters, specifically the mean laser power (P), line distance (r) and scan speed of the laser (v) were varied (see the experimental section for further details). Table 1 gives an overview of the used laser parameters and arithmetic mean surface roughness (R_a) of the samples.

We performed a detailed SEM study of the surface topography. The topographical and structural characterization of the laser structured Pt plates is pictured in Figure 2. In particular, the evolution of LIPSS with a solidified melt nanostructure produced on the Pt plates by irradiation with a spot energy density of 38 J cm^{-2} is depicted in Figure 2a–b. As expected, the LIPSS shows a groove periodicity of 0.78 µm, which is slightly less than the wavelength of the laser radiation (λ = 1.030 µm), with an orthogonal direction to the polarization.[22] Figure 2c–d show hierarchical surface structures consisting of micro patches, which are decorated with LIPSS generated by a spot energy density of 1628 J cm^{-2}. These LIPSS are deeper and slightly broader (0.91 µm) than those in Figure 2a–b. Similar structures were created on titanium by Oliveira et al.[31] Furthermore, the molten Pt surface film solidifies by quick quenching to nano-sized particle agglomerates. According to Zheng et al.,[32] a decreasing scanning speed leads to an increase in nano-sized particles on the surface, which is consistent with our results. With an increase in the spot energy density to 7121 J cm^{-2}, the Pt surface exhibits a wave-like superstructure with a wave front distance of approximately 20 µm. This superstructure exhibits a rich variety of subsurface structures, such as nano- and microporous protrusions along with microscale aggregates formed by agglomerated nanoparticles (see Figure 2e–f).

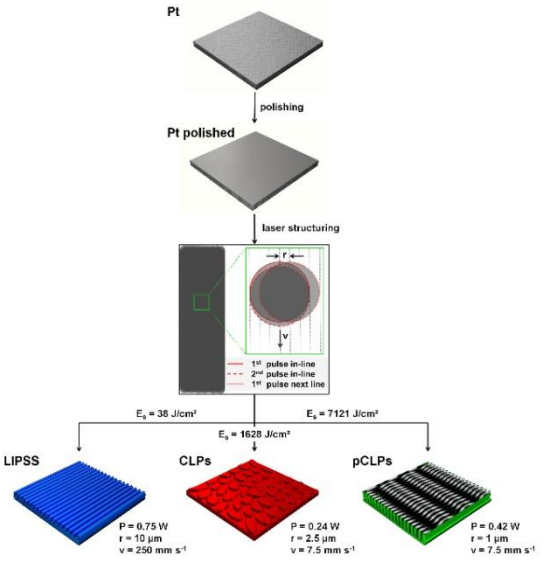

Figure 1. Preparation of the laser structured Pt electrodes with schematic illustrations of the LIPSS, CLPs, pCLPs, and the corresponding spot energy densities E_s.

Table 1. Summary of laser treatment parameters, spot energy density E_s and arithmetic mean surface roughness R_a of the laser structured Pt plates as determined by confocal laser microscopy.

Sample name	Structure type	Laser parameters	E_s [J cm^{-2}]	R_a [µm]
Blank	polished	–	–	0.02
LIPSS	laser-induced periodic surface structures	P = 0.75 W r = 10 µm v = 250 mm s^{-1}	38	0.21
CLPs	cone-like protrusions	P = 0.24 W r = 2.5 µm v = 7.5 mm s^{-1}	1628	0.79
pCLPs	porous cone-like protrusions	P = 0.42 W r = 1 µm v = 7.5 mm s^{-1}	7121	2.49

The analysis of the XRD data of the differently treated platinum samples under study (Figure 3) indicates that the surface of the Blank, LIPSS and CLPs samples consists of polycrystalline platinum with a random orientation of the crystallites. This experimental finding is not surprising since the solid bulk Pt phase will not exert any epitaxial influence on the crystal orientation of the solidified Pt melt. However, for the sample pCLPs, only very weak XRD signals of crystalline Pt could be detected. We ascribe this experimental finding to a less crystalline, more glassy state of the platinum near to the surface. Due to the high energy density of 7121 J cm^{-2}, Pt evaporates and the condensed droplets are quickly quenched

ChemPubSoc Europe

CHEMELECTROCHEM Articles

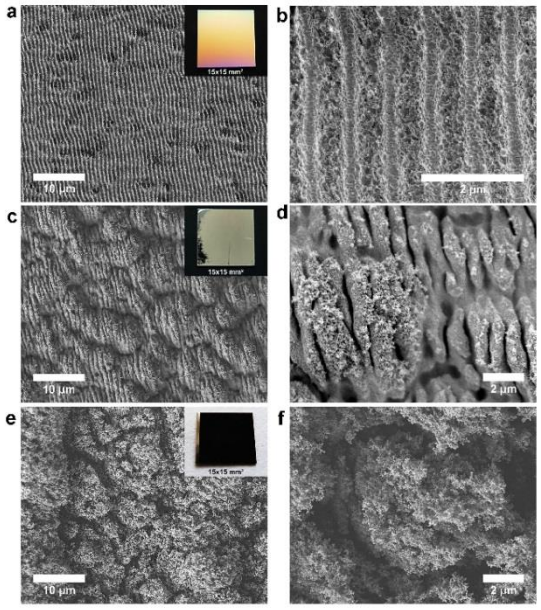

Figure 2. SEM images of laser-induced periodic surface structures as LIPSS (**a**, **b**), cone-like protrusions as CLPs (**c**, **d**) and porous cone-like protrusions as pCLPs (**e**, **f**) at different magnifications. Inset: Photographs of the Pt electrodes after laser treatment. The corresponding XRD patterns are shown in Figure 3.

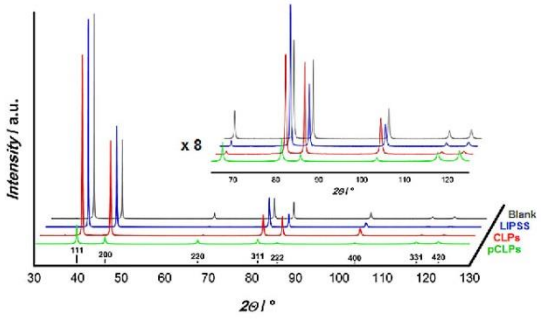

Figure 3. XRD patterns of laser structured Pt electrodes with an enlargement of the region $65° < 2\Theta < 125°$. Theoretical reflex position of face-centered cubic Pt is shown with corresponding Miller indices. The corresponding SEM images are displayed in Figure 2.

without crystallization. This observation is in complete agreement with a similar result of Hirayama et al.[14]. As we discuss later in this paper, this amorphous pCLPs layer re-crystallizes at 500 °C into a polycrystalline Pt coating.

For the electrode, the most useful quantity is the dimensionless roughness factor ϕ.[33] It is calculated as a ratio of the charge densities associated with the oxidation of hydrogen of structured Pt electrodes and the generally accepted charge density of 0.21 mC cm^{-2} for plain Pt.[34] The CV curves in Figure 4, show properly defined hydrogen adsorption/desorption peaks in typical potential region of −0.25 V to +0.1 V, which enable the calculation of the transferred charges for hydrogen adsorption/desorption.[35] The formation/reduction of Pt oxide and Pt hydroxide existed at the potential range of +0.4 V to +1.0 V.[36,37] Especially the CLPs (Figure 4c) and pCLPs (Figure 7d) structures indicate a well-defined Pt hydroxide signal at 0.65 V ($Pt + 2\ H_2O \rightarrow Pt(OH)_2 + 2\ H^+ + 2\ e^-$) and a Pt oxide signal at 0.8 V ($Pt(OH)_2 \rightarrow Pt(O)_2 + 2\ H^+ + 2\ e^-$).[38,39] The difference in the current densities is attributable to the varying surface area of the structures.[40–42]

For the aging test, 1000 CV cycles were run repeatedly and the ϕ of the Pt plates was calculated subsequently. Figure 4 shows the corresponding CV curves (black), whereas Figure 5a illustrates the initial ϕ and the ϕ after the aging process. We observed only a slight decrease of the ϕ after the aging treatment for all samples. CLPs and pCLPs exhibit a slight and comparable aging behavior. However, after annealing of the pCLPs sample at 500 °C, a dramatic reduction of the ϕ can be stated. The detailed consideration of the aging process performed for pCLPs is outlined later in this paper.

Figure 5b depicts the oxygen reduction reaction (ORR) polarization curves for polished and structured Pt electrodes obtained at room temperature in O_2-saturated 0.1 M $HClO_4$ with a RDE at 1600 rpm. LIPSS and CLPs exhibit slightly negative potential shifts of −10 mV respectively −20 mV in comparison to polished Pt. The half-wave potential $E_{1/2}$ for the pCLPs demonstrates an obvious positive shift of +140 mV relative to the polished Pt (blank), indicating a higher catalytic activity caused by a preferred O_2 adsorption and dissociation, which are two important steps of the ORR.

To get the number of transferred electrons, LSV curves using RDE were measured for the laser-structured Pt plates. The RDE rotation speed was increased from 400 to 3100 rpm. The correlations between $-J^{-1}$ and $\omega^{-1/2}$ are displayed as insets in Figure 6. The results indicate that oxygen reduction to water takes place. For the pCLPs electrode, the four-electron ORR pathway for producing H_2O is undercut by a little peroxide intermediate formation. It turns out that the complete oxygen reduction to water happened near half-wave potential. In the range of lower potentials the peroxide formation is competing. However, the topology of the Pt electrodes may have an influence on the flow properties of the RDE. Table 2 summerizes the results of the electrochemical characterization.

From comparing the SEM image of the freshly as-prepared pCLPs (Figure 7a) and the sample after 1000 CV aging cycles (Figure 7b) one can state that a topology change took place,

Table 2. The half-wave potentials ($E_{1/2}$), the roughness factor (ϕ) and the number of transferred electrons (n) of the polished and structured Pt electrodes

Sample	$E_{1/2}$ [V]	ϕ [$cm^2_{Pt}\,cm^{-2}$]	n[a]
Blank	0.43	1.0	3.3
LIPSS	0.42	1.75	3.9
CLPs	0.41	7.4	3.6
pCLPs	0.57	1527	3.8

[a] number of transferred electrons near ORR half-wave potential

ChemPubSoc Europe
CHEMELECTROCHEM Articles

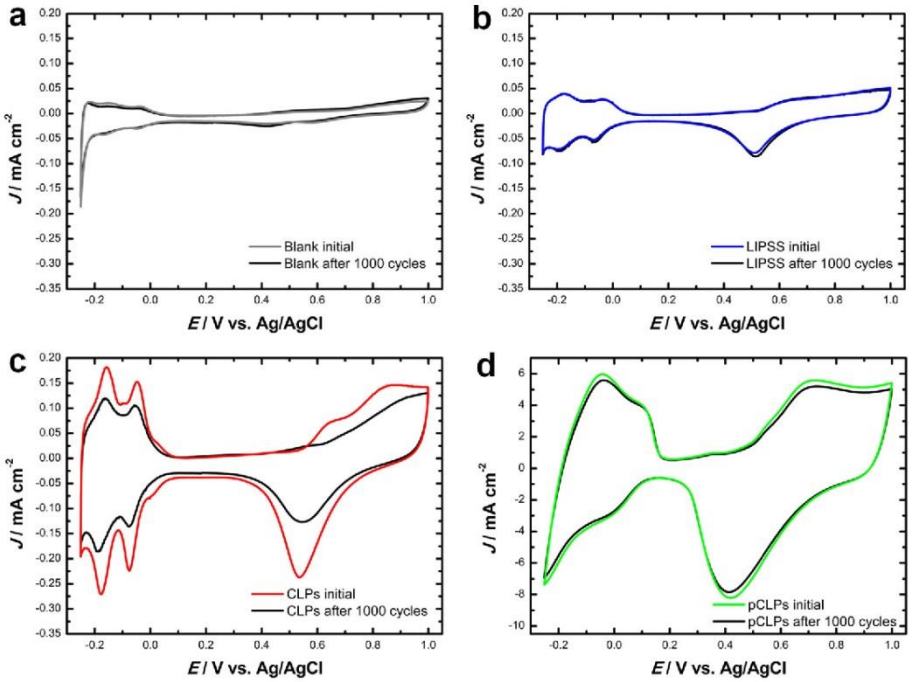

Figure 4. Cyclic voltammograms of **a** Blank, **b** LIPSS, **c** CLPs and **d** porous CLPs measured directly after structuring (initial) and after 1000 CV aging cycles in N_2-saturated 0.1 M $HClO_4$ solution at room temperature with a sweep rate of 20 mV s^{-1} for Blank, LIPSS, CLPs and 5 mV s^{-1} for pCLPs.

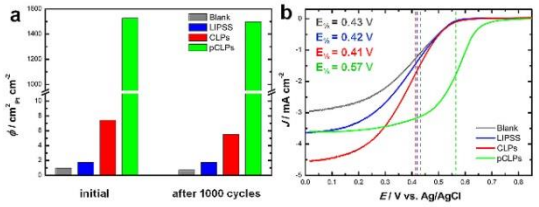

Figure 5. a Roughness factor (ϕ) of the structured Pt plates after laser treatment (initial) and after 1000 CV aging cycles. **b** Oxygen reduction reaction (ORR) polarization curves using polished and structured Pt plates as RDE. Measurements were performed at 1600 rpm in O_2-saturated 0.1 M $HClO_4$ at room temperature. Potential was measured vs. Ag/AgCl (3 M KCl) and sweep rates were 5 mV s^{-1} for Blank, LIPSS, CLPs and 0.5 mV s^{-1} for pCLPs. Half-wave potentials $E_{1/2}$ are shown as dashed lines for comparison.

but the mean particle size remained almost constant. From SEM, the mean particle size of the as-prepared pCLP sample was about 37 nm and 27 nm after the aging process. Accordingly, the mean Pt particle size calculated by Rietveld analysis responds to 29 nm for the as-prepared pCLPs and 27 nm after the aging process (see Figure 8b). Correspondingly, the cyclic voltammograms are almost unchanged (Figure 7d). Only a marginal loss of catalytic active surface area caused by the electro chemical sintering process can be observed.

However, after heat treatment at 500 °C, spontaneous crystallization takes place (see Figure 8a) and grain coarsening is observed (Figure 7c). The aggregated Pt nanoparticles of formerly 27 nm form polycrystalline Pt clusters of several micrometers. Mass transport most probably takes place via surface diffusion and grain boundary transport. Due to this reduced surface area, the cyclic voltammogram (Figure 7d) shows a considerable drop of the current density (*J*).

3. Conclusions

Different parameters for picosecond laser structuring of platinum have been identified, and their effect on the electrochemical properties has been discussed in this paper. Finally, we have shown an easy way to generate micro- and nano-sized surface topographies via a direct ultrashort pulse laser structuring approach. The laser treatment provides the opportunity to modify material surfaces, enlarge the amount of accessible active sites for catalysis by 1500 times in comparison to a polished surface. Because of the rapid quenching process, it is not possible to build up large surface area modification with defined crystal structures. Aging experiments have shown an electrochemical sinter process within the laser-induced structures, which reduce the catalytic activity slightly. XRD studies exhibited no change of the crystalline properties of Pt by the electrochemical sintering. Platinum was chosen only as a case study, by virtue of its well-known electrochemical properties. In principle, all metal surfaces can be modified by ultrashort pulse laser structuring. Therefore, a large number of applications in the fields of producing H_2 and O_2 from electrocatalytic splitting

ChemPubSoc Europe
CHEMELECTROCHEM Articles

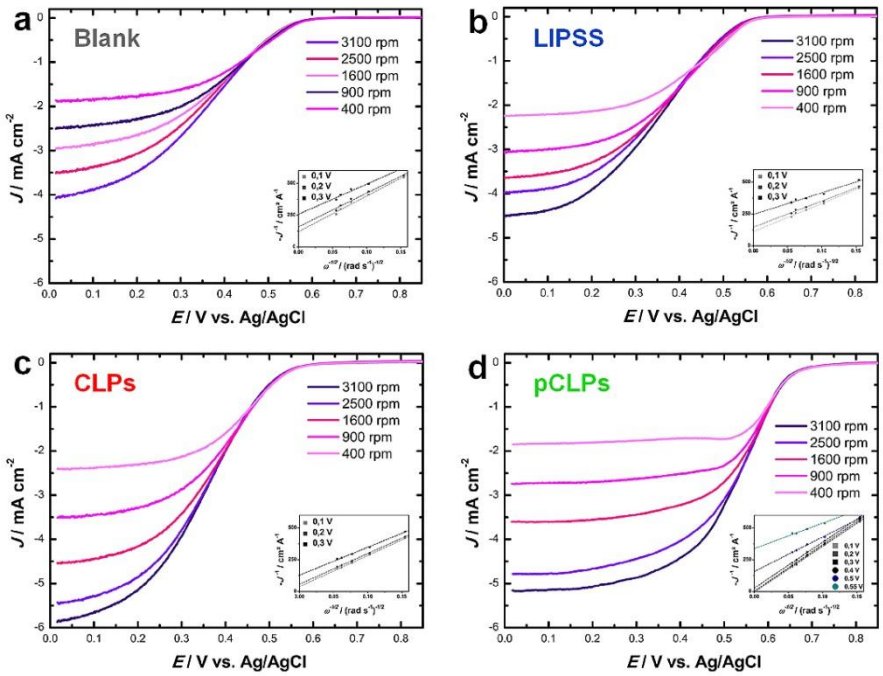

Figure 6. Linear sweep voltammetry (LSV) curves for the using polished and laser structured Pt plates as the RDE for various rotation rates. **a** Blank **b** LIPSS **c** CLPs and **d** pCLPs. Measurements were performed in O_2-saturated 0.1 M $HClO_4$ at room temperature. The Potential was measured vs. Ag/AgCl (3 M KCl) and sweep rates were 5 mVs^{-1} for **a**, **b**, **c** and 0.5 mVs^{-1} for **d**. Inserts: the corresponding Koutecký–Levich plots at different potentials.

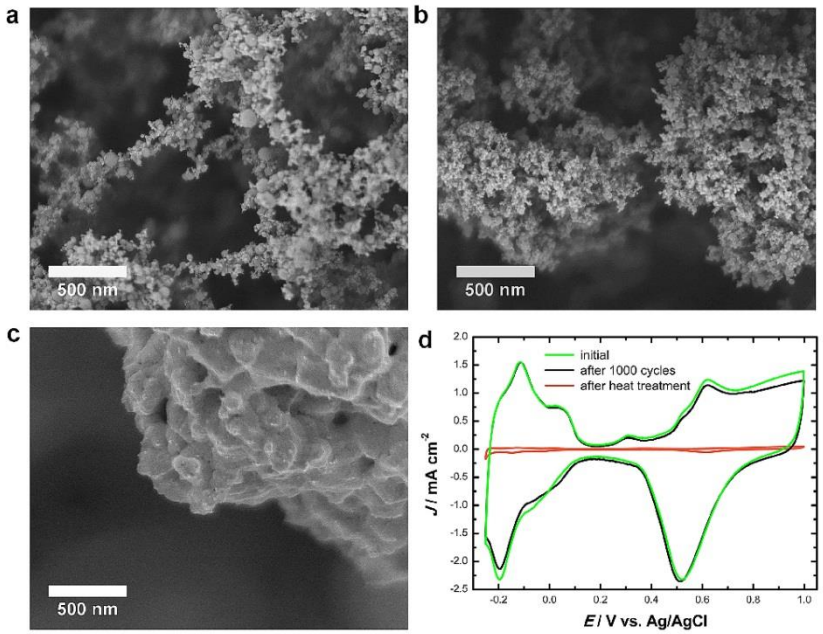

Figure 7. SEM images of Pt surface with pCLPs structure. **a** shows the as-prepared surface after the laser-treatment, **b** after 1000 CV aging cycles and **c** after the heat treatment at 500 °C for 3 h. **d** corresponding cyclic voltammograms of pCLPs measured after structuring (initial), after 1000 CV aging cycles and after heat treatment of 500 °C for 3 h. Measurements were performed in N_2-saturated 0.1 M $HClO_4$ solution at room temperature with a sweep rate of 1 mVs^{-1}. The XRD patterns of the samples are given in Figure 8.

ChemPubSoc Europe

CHEMELECTROCHEM Articles

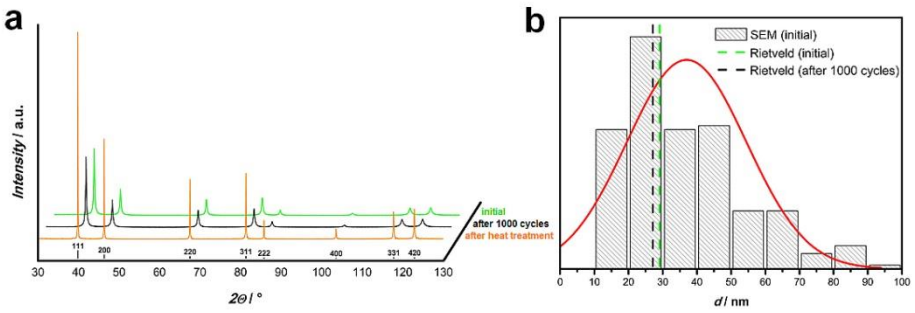

Figure 8. a XRD patterns of pCLPs initially as-prepared, after 1000 CV aging cycles and after heat treatment at 500 °C for 3 h. Theoretical reflex position of face-centered cubic Pt is shown with corresponding Miller indices. The SEM images of the samples are given in Figure 7. **b** Particle size distribution of pCLPs as-prepared (initial) determined by SEM image (Figure 7 a) and mean particle size calculated by Rietveld analysis for pCLPs initial (dashed green, right) and after 1000 CV aging cycles (dashed black, left).

of water by the hydrogen evolution reaction (HER) and oxygen evolution reaction (OER) are possible. Furthermore, certain applications in heterogeneous catalysis in general are conceivable.

Experimental Section

Laser Structuring

Before the laser treatment, the platinum plates (Goodfellow) are mechanically polished with 15 µm, 6 µm, 3 µm, 1 µm and 0.25 µm diamond polishing suspensions (Buehler) and further cleaned with isopropyl alcohol and ultra-pure water ($\rho = 18.2$ MΩ cm). The laser structuring was done with a AMPHOS 10 system (Yb:YAG, $\lambda =$ 1.030 µm) that generates linear polarized laser radiation with 1 ps pulses at a repetition rate of $f = 100$ kHz with a spot diameter of $d = 45$ µm in air. There are two changeable parameters to generate the desired textures, the average power of the laser beam P measured by a power meter and the spatial overlap of the laser pulses. The spatial overlap can be distinguished in an in-line overlap of consecutive laser pulses (ratio of spot diameter and product of the scanning speed of the laser v and the repetition rate f) and a between-line overlap (ratio of spot diameter and line distance r between the lines).

$$\text{overall overlap} = \frac{d}{v \times f} + \frac{d}{r}$$

Spot energy density E_s appears from the product of energy density per pulse E_p and the overall overlap. E_p is calculated with the spot area A.

$$E_p = \frac{P}{f \times A}$$

Physical Characterization

After the laser treatment, the morphology of the surface structural modifications are studied using a field-emission scanning electron microscope (FESEM, JEOL JSM-6700F operating at 2 kV and 10 µA), which was equipped with an energy-dispersive X-ray spectrometer (EDXS). The crystallinities, of the samples were determined by powder XRD measurements were performed on a Bruker D8 Advance diffractometer operating at 40 kV and 40 mA with Cu-K_α-radiation (wavelengths $\lambda = 0.154$ nm). The data were collected in locked couple mode in the range of 7.5°–140° with step-width of 0.01° and an interval time of 0.3 s. The arithmetic mean surface roughness R_a was determined with a 3D laser scanning confocal microscope (Keyence VK–X200) from an area of 80×80 µm² at 150-times of magnification. R_a is defined as the average of the absolute height (y_n) of every plotted data point (N).

$$R_a = \frac{1}{N}\sum_{n=1}^{N}|y_n|$$

Electrochemical Characterization

A three-electrode configuration was used with graphite rod as counter electrode and an Ag/AgCl (3 M KCl) reference electrode. All potentials were referred to Ag/AgCl (3 M KCl). As working electrode a self-designed rotating disk electrode tip with changeable electrode plate was used. The roughness factor ϕ were calculated by measuring the charge (Q_H) associated with the oxidation of hydrogen ($Pt{-}H_{ads} \rightarrow Pt + H^+ + e^-$) between −0.25 V and 0.1 V after double-layer correction and assuming that $q_{ref} = 0.21$ mC cm^{-2}, corresponding to a surface density of 1.31×10^{15} Pt atoms per cm², which is generally accepted for polycrystalline Pt electrodes. The ϕ of the Pt was calculated based on the following relationship:

$$\phi = \frac{Q_H}{q_{ref} \times A_{geo}}$$

where A_{geo} is the geometric surface area of the electrode (cm²), and q_{ref} is the charge required for the adsorption of a hydrogen monolayer on a Pt surface (0.21 mC cm^{-2}).[43] The number of transferred electrons n was calculated with Koutecký–Levich (K–L) equation

$$\frac{1}{J} = \frac{1}{J_L} + \frac{1}{J_K} = \frac{1}{0.62nFC_O(D_O)^{2/3}\nu^{-1/6}\omega^{1/2}} + \frac{1}{nFkC_O}$$

where J_L is the diffusion-limiting current density, J_K is the kinetic-limiting current density, F is the Faraday's constant (96485 C mol^{-1}), ω is the angular velocity in unit of rad s^{-1}, n is the number of transferred electrons, C_O and D_O are the bulk concentration and diffusion coefficient of O_2 in the electrolyte (1.26×10^{-6} mol cm^{-3} and 1.93×10^{-5} cm² s^{-1} for 0.1 M $HClO_4$),[44] ν is the kinematic

ChemPubSoc Europe

CHEMELECTROCHEM Articles

viscosity of the electrolyte (1.009×10^{-2} $cm^2 s^{-1}$ for 0.1 M $HClO_4$),[45] and *k* is the electron-transfer rate constant. n and k can be obtained from the slope and intercept of K–L equation, respectively.

Conflict of Interest

The authors declare no conflict of interest.

Acknowledgements

This work was done within the framework of the ElektroBak graduate program organized by Uwe Schröder (TU Braunschweig). Furthermore, we thank LPKF AG for the laser structuring, the technical expertise, and general support. We are grateful to the German Federal Ministry of Education and Research for supporting part of this work within the project "LAMINA".

Keywords: oxygen reduction reaction · platinum electrode · ultrashort pulse laser structuring · black platinum · laser-induced periodic surface structures

[1] X. Ge, A. Sumboja, D. Wuu, T. An, B. Li, F. W. T. Goh, T. S. A. Hor, Y. Zong, Z. Liu, *ACS Catal.* **2015**, *5*, 4643–4667.
[2] M. K. Debe, A. K. Schmoeckel, G. D. Vernstrom, R. Atanasoski, *J. Power Sources* **2006**, *161*, 1002–1011.
[3] V. R. Stamenkovic, B. Fowler, B. S. Mun, G. Wang, P. N. Ross, C. A. Lucas, N. M. Markovic, *Science* **2007**, *315*, 493–497.
[4] C. Wang, H. Daimon, T. Onodera, T. Koda, S. Sun, *Angew. Chemie – Int. Ed.* **2008**, *47*, 3588–3591.
[5] M. K. Debe, *Nature* **2012**, *486*, 43–51.
[6] J. M. Elliott, G. S. Attard, P. N. Bartlett, N. R. B. Coleman, D. A. S. Merckel, J. R. Owen, *Chem. Mater.* **1999**, *11*, 3602–3609.
[7] G. S. Attard, P. N. Bartlett, N. R. B. Coleman, J. M. Elliott, J. R. Owen, J. H. Wang, *Science* **1997**, *278*, 838–840.
[8] D. V. Pugh, A. Dursun, S. G. Corcoran, *J. Mater. Res.* **2003**, *18*, 216–221.
[9] I. N. Zavestrovskaya, *Quantum Electron.* **2010**, 942–954.
[10] Kurt W. Kolasinski, *Surface Science: Foundations of Catalysis and Nanoscience*, Wiley & Sons, **2012**.
[11] I. N. Zavestovskaya, A. P. Kanavin, N. A. Men'kova, *J. Opt. Technol.* **2008**, *75*, 353–358.
[12] I. N. Zavestovskaya, *Fundamentals of Laser-Assisted Micro- and Nanotechnologies*, Springer AG, **2014**.
[13] P. Mazzoldi, G. Della Mea, G. Battaglin, *Phys. Rev. Lett.* **1980**, *44*, 88–91.
[14] Y. Hirayama, M. Obara, *Appl. Surf. Sci.* **2002**, *197–198*, 741–745.
[15] Z. Guosheng, P. M. Fauchet, A. E. Siegman, *Phys. Rev. B* **1982**, *26*, 5366–5381.
[16] P. Simon, J. Ihlemann, *Appl. Surf. Sci.* **1997**, *109/110*, 25–29.
[17] S. K. Das, K. Dasari, A. Rosenfeld, *Nanotechnology* **2010**, *21*, 1–8.
[18] S. Watanabe, Y. Yoshida, S. Kayashima, S. Yatsu, M. Kawai, T. Kato, *J. Appl. Phys.* **2010**, *108*.
[19] J. F. Young, J. S. Preston, H. M. Van Driel, J. E. Sipe, *Phys. Rev. B* **1983**, *27*, 1155–1172.
[20] H. M. van Driel, J. E. Sipe, J. F. Young, *Phys. Rev. Lett.* **1982**, *49*, 1955–1959.
[21] R. Jagdheesh, B. Pathiraj, E. Karatay, A. J. Huis, *Langmuir* **2011**, *27*, 8464–8469.
[22] A. Y. Vorobyev, V. S. Makin, C. Guo, *J. Appl. Phys.* **2007**, *101*.
[23] A. R. Neale, Y. Jin, J. Ouyang, S. Hughes, D. Hesp, V. Dhanak, G. Dearden, S. Edwardson, L. J. Hardwick, *J. Power Sources* **2014**, *271*, 42–47.
[24] M. Tsukamoto, T. Kayahara, H. Nakano, M. Hashida, M. Katto, M. Fujita, M. Tanaka, N. Abe, *J. Phys. Conf. Ser.* **2007**, *59*, 666–669.
[25] K. M. T. Ahmmed, C. Grambow, A.-M. Kietzig, *Micromachines* **2014**, *5*, 1219–1253.
[26] S. Bruening, G. Hennig, S. Eifel, A. Gillner, D. Graphics, *Phys. Procedia* **2011**, *12*, 105–115.
[27] B. K. Nayak, M. C. Gupta, *Opt. Lasers Eng.* **2010**, *48*, 940–949.
[28] C. Wu, L. V Zhigilei, *Appl. Phys. A* **2014**, *114*, 11–32.
[29] A. Y. Vorobyev, C. Guo, *Phys. Rev. B* **2005**, *72*.
[30] A. Y. Vorobyev, C. Guo, *J. Appl. Phys.* **2008**, *104*.
[31] V. Oliveira, S. Ausset, R. Vilar, *Appl. Surf. Sci.* **2009**, *255*, 7556–7560.
[32] Y. Zheng, J. Prall, H. J. Seifert, W. Pfleging, *IEEE* **2015**, 329–333.
[33] A. M. Feltham, M. Spiro, *Chem. Rev.* **1970**, *71*, 177–193.
[34] P. Horsman, B. E. Conway, E. Yeager, S. Sarangapani, Eds., *Comprehensive Treatise of Electrochemistry Electrodics: Experimental Techniques*, Plenum Press, **1984**.
[35] V. R. Stamenkovic, B. S. Mun, M. Arenz, K. J. J. Mayrhofer, C. a Lucas, G. F. Wang, P. N. Ross, N. M. Markovic, *Nat. Mater.* **2007**, *6*, 241–247.
[36] K. Hyun, J. H. Lee, C. W. Yoon, Y. Kwon, *Int. J. Electrochem. Sci.* **2013**, *8*, 11752–11767.
[37] G. Jerkiewicz, G. Tremiliosi-Filho, B. E. Conway, *J. Electronanal. Chem.* **1992**, *334*, 359–370.
[38] J. S. Mayell, S. H. Langer, *J. Electrochem. Soc.* **1964**, *111*, 438–446.
[39] B. E. Conway, H. Angerstein-Kozlowska, W. B. A. Sharp, E. E. Criddle, *Anal. Chem.* **1973**, *45*, 1331–1336.
[40] S. Park, J. Y. Song, J. Han, H. Boo, D. T. Chung, *Electrochim. Acta* **2010**, *55*, 2029–2035.
[41] J. Huang, *Elect* **2008**, *20*, 2229–2234.
[42] J. Snyder, T. Fujita, M. W. Chen, J. Erlebacher, *Nat. Mater.* **2010**, *9*, 904–907.
[43] H. A. Gasteiger, S. S. Kocha, B. Sompalli, F. T. Wagner, *Appl. Catal. B Environ.* **2005**, *56*, 9–35.
[44] X. Feng, *Nanocarbons for Advanced Energy Conversion*, Wiley-VCH, **2015**.
[45] D. R. Lide, *Handbook of Chemistry and Physics*, CRC Press, **2004**.

Manuscript received: October 13, 2016
Accepted Article published: December 19, 2016
Final Article published: February 2, 2017

4.2 Porous Nickel Nano-Foam by Femtosecond Laser Structuring for Supercapacitors Application

Karsten Lange*, Christian Hördemann, Malte Schulz-Ruhtenberg, and Jürgen Caro

ChemElectroChem, 2018, 5, 3688–3694.

DOI: 10.1002/celc.201801152

ChemPubSoc Europe

DOI: 10.1002/celc.201801152

CHEMELECTROCHEM Articles

Porous Nickel Nano-Foam by Femtosecond Laser Structuring for Supercapacitor Application

Karsten Lange,*[a] Christian Hördemann,[b] Malte Schulz-Ruhtenberg,[c] and Jürgen Caro[a]

A focused femtosecond laser beam was scanned across a nickel electrode in a line pattern with different line distances to generate a large electrochemical surface area for charge storage. During the laser structuring process, small metal particles were generated and sintered to a porous foam-like structure, the so-called laser-induced nano-foam (LINF), which strongly adheres to the substrate surface. The structuring was carried out in argon atmosphere, in order to prevent oxidation of the LINF structure during the structuring process. The topography of the LINF was investigated by scanning electron microscopy and laser scanning microscopy. The electrochemical surface area of the electrodes was determined by cyclic voltammetry based on the charging of the double-layer. The total capacity of the nickel LINF electrodes was measured by galvanostatic charge-discharge to test their capability for supercapacitor applications. The surface area enlargement and therefore the total capacity increases with decreasing line distance. The LINF structure provides a surface area enlargement up to a factor of 1600 and a total capacity up to 2 C cm^{-2}.

1. Introduction

Electrochemical supercapacitors are unique electrochemical devices with high power density, high charge–discharge cycle life and high energy efficiency.[1] They are easily categorized by their energy storage mechanism into double-layer capacitors and redox supercapacitors.[2] Double-layer capacitance arises from the separation of charge at the interface between a solid electrode and an electrolyte, whereas pseudocapacitance arises from fast, reversible faradaic reactions occurring at or near a solid electrode surface over an appropriate potential range.[3] The double-layer capacitance of a solid/electrolyte interface is typically in the range of 10 to 40 μF cm^{-2}.[4] To make use of the electrical double-layer capacitance as a mechanism of energy storage, materials with a high specific surface area are required.[5] Note that the electrochemical pseudocapacitance is 10 to 100 times higher compared to the double-layer capacitance.[6] Therefore, the noble metal oxides, such as the amorphous phases of ruthenium oxide[7] and iridium oxide,[8] have been demonstrated as promising electroactive materials for supercapacitors. Due to high prices of these materials, their use is restricted. Transition metal oxides such as nickel oxide,[4,5] cobalt oxide[9,10] and manganese oxide[3,11] have been proven as inexpensive alternative electroactive materials for supercapacitors, because of their favorable pseudocapacitive properties and good stability in alkaline solution. In the past, a lot of effort has been made to synthesize these oxides in multiple shapes for instants as nanoparticles, nanowires, nanorods, nanotubes and nanosheets, by a wide selection of preparation techniques, such as hydrothermal, solvothermal, chemical precipitation, chemical bath deposition, sol-gel, electrodeposition and microwave assisted methods.[12–14] Furthermore, various template-based (hard-template and soft-template) and surfactant-based approaches were coupled with the aforementioned fabrication techniques to obtain porous oxide nanostructures.[15]

However, these techniques may involve a thermal impact, an aggressive environment; a multi-step treatment or require complicated machinery. In contrast, direct femtosecond laser surface structuring does not involve usage of foreign agents and offers great processing flexibility: it is computer controlled, and allows the fabrication of precise, well-defined patterns.[16] Femtosecond laser surface structuring is emerging as a powerful and flexible tool for the fabrication of functionalized multiscale surfaces.[17] Tailored surface properties are obtained by the generation of self-organized micro- and nano-scale features for all kinds of materials, such as metals,[18] semiconductors,[19–21] dielectrics,[22] polymers[23,24] and glass.[25] A large variety of femtosecond laser-induced surface micro/nanostructures have been reported. In the past, most of the studies using ultrashort laser pulses for surface texturing have focused on so-called pillars,[26] cones[27,28] or spikes.[29] In general, these are tightly-packed stochastically arranged structures with an aspect ratio of 2:1 or higher.[30] Tailored surfaces imitating naturally occurring structures exhibit properties like enhanced wettability (super hydrophilic),[31] water repelling/self-cleaning (super hydrophobic),[32–34] surface-coloring[35,36] and optical absorption[37] can be created. There are only a few studies about the catalytic properties of such laser-structured surfaces.[38–40]

[a] K. Lange, Prof. J. Caro
Institute of Physical Chemistry and Electrochemistry
Leibniz University Hannover
Callinstr. 3 A, D-30167 Hannover, Germany
E-mail: karsten.lange@pci.uni-hannover.de
[b] Dr. C. Hördemann
Fraunhofer Institute for Laser Technology
Steinbachstr. 15, D-52074 Aachen, Germany
[c] Dr. M. Schulz-Ruhtenberg
LPKF Laser & Electronics AG
Osteriede 7, D-30827 Garbsen, Germany

Supporting information for this article is available on the WWW under https://doi.org/10.1002/celc.201801152

ChemPubSoc Europe
CHEMELECTROCHEM Articles

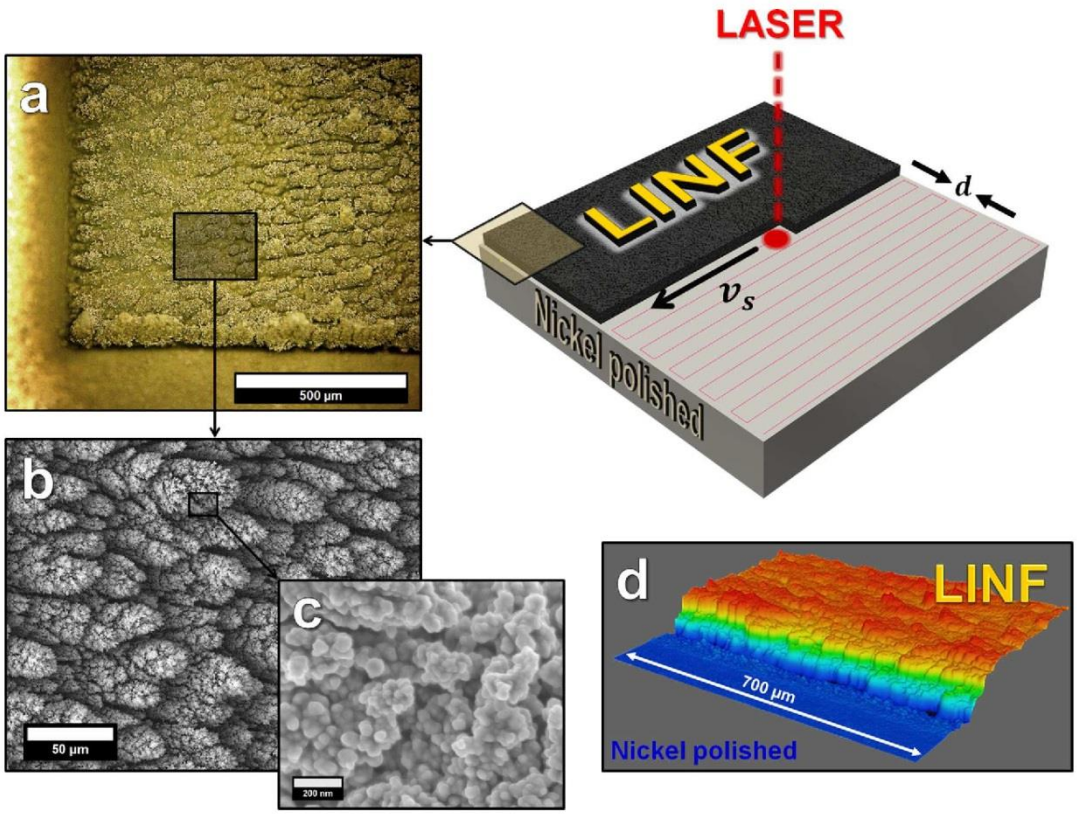

Figure 1. Schematic illustration of the laser structuring process, which results in the laser-induced nano-foam (LINF) structure. The focused laser beam was scanned across the Ni surface in a line pattern with different line distances d and a scanning speed v_s of 80 mm s^{-1}. Optical microscope (a), scanning electron microscope (b and c) and laser scanning microscope (d) images of a Ni LINF prepared with a line distance $d = 5$ µm.

In this paper, femtosecond laser surface structuring was utilized to enlarge the accessible surface area of Ni electrodes for energy storage applications. To the best of our knowledge, we demonstrate for the first time the use of femtosecond laser pulses to fabricate metallic porous surface structures that form on top of the original surface. We created 1 cm^2 arrays of laser-induced nano-foam (LINF) on Ni with the objective to generate preferably a highly accessible surface area for electrochemical charge storage. Furthermore, we were able to adjust the capacity of the electrode by modifying only one laser parameter. The formation of self-organized micro cones that form on top of the original surface was first reported on silicon,[20] nickel [30] and stainless steel.[41]

The morphology of the LINF was investigated by scanning electron microscopy (SEM) and laser scanning microscopy (LSM). The electrochemical surface area of the electrode was determined by cyclic voltammetry based on the charging of the double-layer. The total capacity of our Ni LINF electrodes was determined by the galvanostatic charge–discharge method. Furthermore, a formation process based on preferential ablation first described by Zuhlke et al.[30,41] is demonstrated.

2. Results and Discussion

The laser structuring conducted in this work leads to the development of a foam-like structure that emerges up to 100 µm on top of the surface of the Ni substrate, see Figure 1. Similar formation of microstructures with enhanced surface area has been previously reported by Zuhlke et al.[30,41] and Li et al.[42] In the aforementioned works, the generation of these structures is divided into different phases and includes the formation of nano ripples or so called LIPSS (laser-induced periodic surface structures) as well as precursor-areas for a following change in topography, where the laser intensity is unevenly distributed on the sides of cones and valleys. Through this irregular ablation as well as the re-deposition of ablation products, structures growing randomly on top of the surface by repetitive irradiation of the substrate. In contrast to the described studies, where multiple irradiations of the same area were made, in this paper, the bare Ni surface was irradiated only once, but with high spatial pulse overlap.

SEM analysis was conducted in order to evaluate the structuring process and, more interestingly, to describe the surface structure, see Figure 2 and 3.

ChemPubSoc Europe
CHEMELECTROCHEM Articles

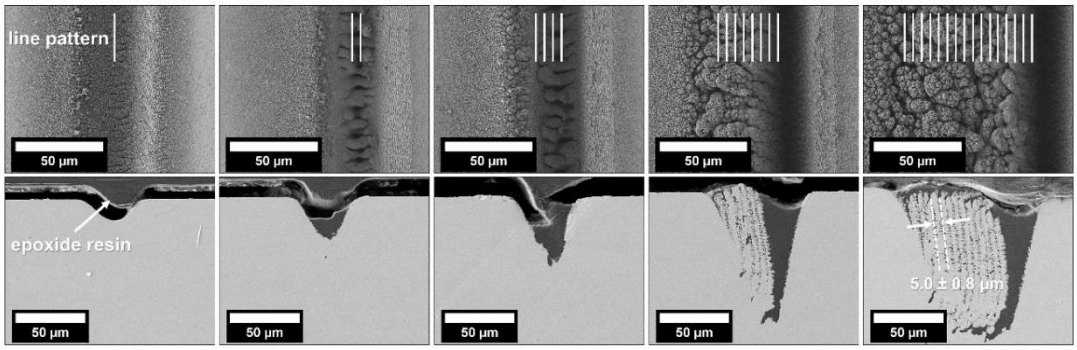

Figure 2. Top view and cross-section SEM images of the LINF formation process. Scanned line patterns with a line distance of 5 µm are given true to scale. From left to right the number of scanned lines increases. Within the cross-section sample preparation epoxy resin was utilized to protect the structure.

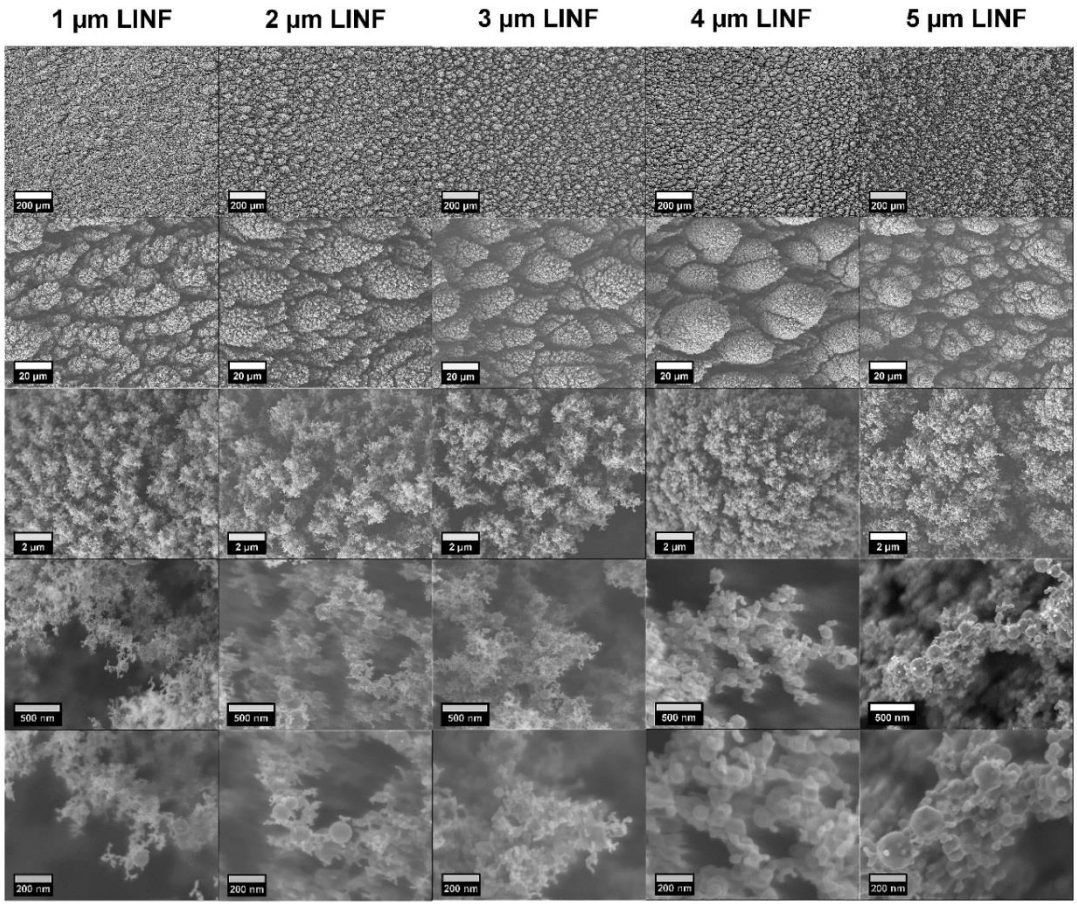

Figure 3. Top view SEM images of 1 µm–5 µm LINF electrodes taken under 100 x, 1000 x, 10,000 x, 50,000 x and 100,000 x magnification.

In Figure 2, the formation of the structures is shown in SEM top view and cross-sectional view. The porous structure that forms on top of the surface could not be conserved during the cross-section sample preparation. The left image in the figure shows the ablation kerf and the formation of small ripples in the center of the ablated kerf after one scanned line. The further to the right, the more lines are placed next to each other, resulting in a buildup of a porous structure. After each

ChemPubSoc Europe

CHEMELECTROCHEM Articles

scan, some ablated material gets ejected from the bottom of the kerf and redeposits on the sample surface. Projection effects of the incident laser radiation occur on the steep groove walls that form when ablating a line in the Ni substrate. Therefore, from a peak intensity, that can only be achieved if the irradiated surface is perpendicular to the laser beam. The effective intensity decreases with increasing projection angle, as the projection forms a much higher surface area that is irradiated. Consequently, the intensity drops below the ablation threshold, which leads only to heating of the irradiated area. Here, the residual heat at the surface of the workpiece and the redeposited particles can form a new porous surface structure by a sintering process. This process is repeated more often by reducing the line distances of the scanned line pattern from 5 μm to 1 μm.

The SEM images of the micro- and the nanostructure of all LINF electrodes are given in Figure 3. At microscopic scale, randomly located dendritic cones cover the surface of all electrodes. The cones are tilted so that the tips of the cones are pointing to the next line that will be scanned. At nanoscopic scale, the cones become porous. They consist of particles with diameters from 15 nm to 200 nm, which are sintered together and form a filigree network. The network becomes more and more filigree with decreasing line distance. In conclusion, there are two substructures, one below and one on top of the original surface, which together form the LINF structure. The substructure below the original surface is made of porous bars with a thickness that is equal to the line distance of the scanned line pattern. In contrast, the substructure on top of the original surface is made of redeposited particles aggregated in porous cones.

The structuring was performed in argon atmosphere in order to prevent oxidation of the LINF structure during the structuring process. After the structuring, the Ni LINF electrodes were stored in air to induce the formation of a thin NiO passivation layer. Without the argon atmosphere the whole Ni LINF structure would instantly become electrically isolating and therefore would no longer be suitable for electrochemical applications.

X-ray diffraction (XRD) was conducted to study the crystallinity of the LINF electrodes (see supplementary information). The in air stored LINF electrodes show only the elemental nickel phase in the XRD patterns. After the electrochemical treatment no additional crystalline phase could be found. Since XRD has an information depth of several micrometers,[43] XRD measurements contain mostly information about the bulk material. However, EDX analysis of the LINF electrodes exhibited a weak O K_α signal, indicating a thin NiO passivation layer (supplementary information).

The LINF structure exhibits excellent stability in aqueous solution and furthermore does not collapse after drying. We carried out cyclic voltammetry (CV) analysis to visualize the two charge storage systems Ni surfaces offer. Figure 4a depicts an exemplary CV of the 1 μm Ni LINF electrode, which can be technically separated into two potential regions, the double-layer capacitance region, from −0.8 V to 0.1 V vs Ag/AgCl, and the pseudocapacitance region from, 0.1 V to 0.5 V vs Ag/AgCl. The CV potential range represents the stable potential range of the aqueous electrolyte. At higher potentials oxygen evolution reaction and at lower potentials, hydrogen evolution reaction would take place, which is unwanted in charge storage devices, due to pressure issues and the surface blocking behavior of gas bubbles. The CV clearly confirms that the redox transition of interfacial oxy-nickel species between Ni(II)$(OH)_2$ and Ni(III)OOH exhibit high electrochemical reversibility. As mentioned in the introduction the electrochemical pseudocapacitance is typically 10 to 100 times higher as the double-layer capacitance.[6] Thus, the main charge storage at a Ni/NiO surface is realized by this reversible faradaic reaction. As highlighted later on, the surface morphology of an electrode highly influences the occurrence of such redox active sites. Therefore, it is difficult to use the number of transferred charges, which is accessible through integration, to quantify the surface area enlargement of structured, coarse electrodes. A more accurate way to estimate the surface area of an electrode is to determine the double-layer capacitance, which is proportional to the real surface area. The surface area enlargement can be expressed by the roughness factor, which is the ratio of the double-layer capacitances of the structured electrode and a plane surface of the same material. The double-layer capacitance of a plane Ni/NiO surface is very well established.[44] Figure 4b shows the double-layer capacitance for all five LINF electrodes with respect to the line distance that was used within the laser structuring process. Please mind, the goal of our laser structuring approach was to generate preferably high electrochemical surface area. Figure 4c shows the roughness factor based on the previously determined double-layer capacitance over the line distance. For the 5 μm Ni LINF a surface area enlargement by a factor of about 730 was achieved. Note that the real surface area can differ from the electrochemically active surface area, if a part of the area is physically blocked by adherent gas bubbles or non-conductive materials such as contaminations or thick insulating oxide layers. As the line distance is reduced down to 1 μm, the surface area increases up to a roughness factor of about 1600, which is the best performing sample in this study. With increasing number of lines scanned, more ablated material gets ejected and forms a more and more filigree porous structure. But it has to be noted that the formation of the LINF structures and therefore their excellent electrochemical properties were only realized in a narrow parameter window. The total charge-discharge behaviors of the LINF electrodes were further examined by galvanostatic charge-discharge measurements in a potential window of −0.8 V to 0.45 V vs. Ag/AgCl. Figure 4d displays the discharge behavior of all five electrode types for one exemplary cycle out of a hundred. All electrodes show almost constant pseudocapacitance over the full operating voltage range, which reinforces the former mentioned CV results. This battery-like discharge behavior provides quasi-constant voltage during discharge.

Figure 4e–f depict the LINF total capacities and their retention with the number of charge-discharge cycles. In general, the total capacity increases with decreasing line distance from 5 μm LINF to 1 μm LINF, analogous to the double-layer capacitance of these electrodes. The highlighted

ChemPubSoc Europe
CHEMELECTROCHEM Articles

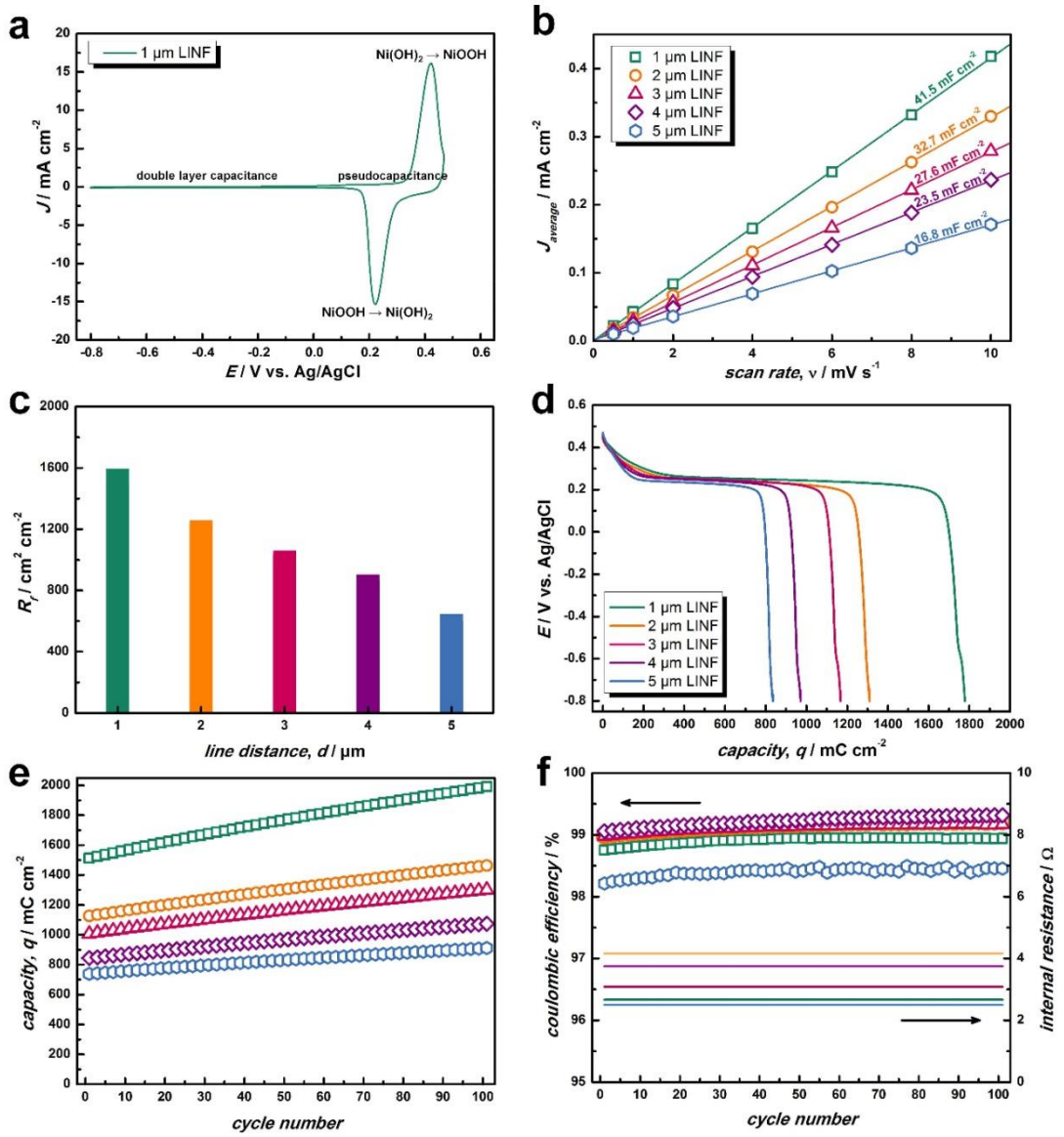

Figure 4. Exemplary cyclic voltammogram (CV) of a 1 µm Ni LINF electrode recorded with a scan rate of $\nu = 1$ mV s^{-1} (a). All electrochemical measurements were performed in 1 M KOH solution at room temperature. The average of the absolute current densities versus the scan speed ν (b). The slope of the resulting linear fit curves implies the double-layer capacitances C_{dl} of all LINF electrodes. The corresponding CV cascades were carried out at non-faradaic regions in a potential window of $\Delta E = 0.1$ V around the open circuit potential, see supporting information. Roughness factor R_f against line distance d of the laser scan pattern (c). Galvano static discharge curves with discharge current density of 12 mA cm^{-2} (d). The development of the LINF electrodes total capacity q, coulombic efficiency and their internal resistance with the number of charge-discharge cycles (e and f). The charge-discharge current density was set to 12 mA cm^{-2}.

bars in Figure 2 within the LINF structure become narrower and their distance decreases with decreasing line distance from 5 µm to 1 µm. As a result, more bars are formed and consequently more Ni is ablated, adding to the build-up of the nano-foam and contributing to the surface area enlargement of the LINF structure. Additionally, the total capacity increases with the number of charge-discharge cycles but the coulombic efficiency remains close to 100%. By cycling over the redox couple $Ni(OH)_2$/NiOOH (0.1 V to 0.5 V vs Ag/AgCl) during galvanostatic charge-discharge measurements, the thickness of the inner NiO and outer $Ni(OH)_2$ layer increases.[45] Due to this swelling behavior while cycling, the surface area grows

ChemPubSoc Europe

CHEMELECTROCHEM Articles

increasing the capacity of the electrodes. According to Medway et al., the thickening of the compact inner NiO layer leads to a self-limiting oxide growth, which results in a capacity limit as well.[46] The minimal potential drop observed in the initial discharge cycle (Figure 4d) indicates an internal resistance of the LINF electrodes in the range of 2–4 Ω. The internal resistances of all LINF electrodes are stable while charge-discharge cycling, see Figure 4f.

3. Conclusions

For the first time, a femtosecond laser structuring approach is used to produce a porous foam-like Ni/NiO structure, the so-called laser-induced nano-foam (LINF) that emerges up to 100 μm on top of the surface. Contrary to other laser structuring processes based on ablation, our method uses electrode material most efficiently by re-depositioning the ablated particles. We propose a formation mechanism based on the preferred ablation of material from the bottom of the kerfs driven by projection effects of the incident laser radiation and the re-deposition of the ejected nanoparticles followed by a sintering process. The resulting Ni LINF electrodes were evaluated with regard to their charge storage properties for possible supercapacitor applications. The electrochemical surface area was enlarged by a factor of 1600 with a line distance of 1 μm, which was the best performing sample in this study. The capability for supercapacitor applications was tested by galvanostatic charge-discharge measurements, where all LINF electrodes provide quasi-constant voltage during discharge. This indicates excellent pseudocapacitive behavior. The total capacity increases with decreasing line distance, due to the surface area enlargement. In particular, the 1 μm Ni LINF electrode exhibited excellent capacity of up to 2 $C\,cm^{-2}$ (5.56 $Ah\,m^{-2}$) by virtue of this filigree laser-induced 3D structure. We concede that the processing rate of 21 $min\,cm^{-2}$ (1 μm LINF) achieved by using 10 W of average laser power is less practical for industrial application. However, for structures that are regular and repetitive, which is the case in the LINF formation process since the surface is scanned within a line pattern, beam splitting enables process parallelization.[47] The use of high power femtosecond laser systems, e.g. an industrial 1 kW laser,[48] could allow a 100-fold decrease in processing time, which equals a processing rate of 12.6 $sec\,cm^{-2}$.

Ultimately, we showcased that our laser-based surface modification improves the electrochemical properties of the electrode material making them suitable for energy-related devices such as supercapacitors, batteries and fuel cells.

Experimental Section

Laser Structuring

Before the laser treatment, the Ni plates 10×10×1 mm^3 (Alfa Aesar) were mechanically polished on a Phoenix 4000 with 15 μm, 6 μm, 3 μm, 1 μm and 0.25 μm polycrystalline diamond polishing suspensions (Buehler) and further cleaned with isopropyl alcohol and ultra-pure water (ρ = 18.2 MΩ cm).

The laser structuring was carried out with a Lightconversion Pharos system (Yb:KGW, λ = 1028 nm) to generate linearly polarized laser radiation with 200 fs pulse length. A reaction chamber was designed, so that a laser surface texturing could be performed in an argon atmosphere under a normal beam incidence. The focused laser beam with a focus diameter d_f of 60 μm was scanned across the Ni surface along parallel lines with line spacing between 1 μm and 5 μm. The beam was moved using a galvanometer scanner and the scanning speed v_s was set to a value of 80 $mm\,s^{-1}$. The repetition rate f_{Rep} of the laser source equaled 400 kHz. Therefore, within a scanned line, a spatial pulse overlap of 99.67 % was achieved. The spatial pulse overlap P_O was calculated according to Equation (1):

$$P_O = 1 - \frac{P_D}{d_f} \quad (1)$$

where P_D is the pulse distance, which was calculated by Equation (2):

$$P_D = \frac{v_s}{f_{Rep}} \quad (2)$$

A positive value of P_O indicates that within a scanned line, the surface is consecutively irradiated by more than one laser pulse. For a value of $P_O = 0$, the pulse-to-pulse distance equals the spot diameter and therefore each surface area would be irradiated by a single pulse. After the laser structuring process all samples were stored in air. Thus, a thin NiO passivation layer has formed.

Physical and Electrochemical Characterization

The morphology of the laser-induced nano-foam was studied with a field-emission scanning electron microscope (SEM, Jeol JSM-6700F operating at 2 kV and 10 μA). The SEM was coupled with an energy-dispersive X-ray (EDX) detector. The height profile images were shot with a 3D laser scanning confocal microscope (Keyence VK–X200). The X-ray diffraction (XRD) patterns were acquired on a Bruker D8 Advance diffractometer operating at 40 kV and 40 mA with Cu-K_α-radiation (λ = 0.154 nm).

The electrochemical characterization was realized using a Bio-Logic Science Instruments VMP3 potentiostat, where a three-electrode configuration with a graphite rod as counter electrode and an Ag/AgCl (3 M KCl) reference electrode was used. All potentials refer to this reference electrode. A self-designed electrode tip was utilized as the working electrode. All measurements were conducted in 1 M KOH. The double-layer capacitances of the porous LINF electrodes were determined by cyclic voltammetry (CV) in a potential window of 0.1 V (from −0.2 V to −0.1 V vs. Ag/AgCl) in the non-faradaic region where the electrode is ideally polarized and, therefore, the net current reflects only the double-layer charging. The CVs were carried out with different scan rates from 0.5 to 10 $mV\,s^{-1}$. The double-layer charging current density j_{dl} [Eq. (3)] is equal to:

$$j_{dl} = v \cdot C_{dl} \quad (3)$$

where v is the scan rate and C_{dl} is the electrochemical double-layer capacitance. Therefore, electrochemical double-layer capacitance can be extracted by plotting the double-layer charging current density (j_{dl}) as a function of the scan rate v.[49]

ChemPubSoc Europe

CHEMELECTROCHEM Articles

The roughness factor R_f [Eq. (4)] describes the increase of double-layer capacitance C_{dl} relative to a smooth polycrystalline metal surface $C_{theo} = 26\ \mu F\ cm^{-2}$.

$$R_f = \frac{C_{dl}}{C_{theo}} \tag{4}$$

The galvanostatic charge-discharge (CD) measurements were performed at a current density of 12 $mA\,cm^{-2}$ in a potential window of 0.45 V to −0.8 V vs. Ag/AgCl. The charge and discharge curves (I vs t) were integrated to obtain the capacity q_{charge} stored at the electrode and the capacity $q_{discharge}$ released by the electrode. The coulombic efficiency [Eq. (5)] was defined as their ratio.

$$coulombic\ efficiency = \frac{q_{discharge}}{q_{charge}} \cdot 100 \tag{5}$$

Acknowledgements

This work was done within the framework of the NTH Research Group ElektroBak organized by Uwe Schröder (TU Braunschweig) and financed by the German state of Lower Saxony. We thank the Fraunhofer ILT and the LPKF AG for the laser structuring, the technical expertise and the general support.

Conflict of Interest

The authors declare no conflict of interest.

Keywords: laser structuring · materials science · nickel foam · nickel oxide electrode · ultracapacitor

[1] B. E. Conway, Electrochemical Supercapacitors: Scientific Fundamentals and Technological Applications, Kluwer Academic/Plenum Publishers, New York, **1999**.
[2] S. G. Kandalkar, J. L. Gunjakar, C. D. Lokhande, *Appl. Surf. Sci.* **2008**, *254*, 5540–5544.
[3] S.-C. Pang, M. A. Anderson, T. W. Chapman, *Jounal Electrochem. Soc.* **2000**, *147*, 444–450.
[4] V. Srinivasan, J. W. Weidner, *J. Electrochem. Soc.* **1997**, *144*, L210.
[5] K.-C. Liu, M. A. Anderson, *J. Electrochem. Soc.* **1996**, *143*, 124–130.
[6] B. E. Conway, *J. Electrochem. Soc.* **1991**, *138*, 1539–1548.
[7] V. Birss, R. Myers, B. E. Conway, *J. Electrochem. Soc.* **1984**, *131*, 1502–1510.
[8] B. E. Conway, J. Mozota, *Electrochim. Acta* **1983**, *28*, 9–16.
[9] J. Xu, L. Gao, J. Cao, W. Wang, Z. Chen, *Electrochim. Acta* **2010**, *56*, 732–736.
[10] R. B. Rakhi, W. Chen, D. Cha, H. N. Alshareef, *Nano Lett.* **2012**, *12*, 2559–2567.
[11] R. Jiang, T. Huang, J. Liu, J. Zhuang, A. Yu, *Electrochim. Acta* **2009**, *54*, 3047–3052.
[12] M. Sk, C. Y. Yue, K. Ghosh, R. K. Jena, *J. Power Sources* **2016**, *308*, 121–140.
[13] X. Xia, Y. Zhang, D. Chao, C. Guan, Y. Zhang, L. Li, *Nanoscale* **2014**, *6*, 5008–5048.
[14] X. Guo, G. Zhang, Q. Li, H. Xue, H. Pang, *Energy Storage Mater.* **2018**, *15*, 171–201.
[15] X.-Y. Liu, K.-X. Wang, J.-S. Chen, *Energy Storage Mater.* **2016**, *3*, 1–17.
[16] K. Kurselis, R. Kiyan, B. N. Chichkov, *Appl. Surf. Sci.* **2012**, *258*, 8845–8852.
[17] C. A. Zuhlke, T. P. Anderson, D. R. Alexander, *Appl. Phys. Lett.* **2013**, *103*, 121603–1-121603–5.
[18] A. Y. Vorobyev, C. Guo, *Appl. Surf. Sci.* **2007**, *253*, 7272–7280.
[19] S. K. Das, K. Dasari, A. Rosenfeld, R. Grunwald, *Nanotechnology* **2010**, *21*, 155302.
[20] J. Bonse, S. Baudach, J. Krüger, W. Kautek, M. Lenzner, *Appl. Phys. A* **2002**, *74*, 19–25.
[21] M. Barberoglou, V. Zorba, E. Stratakis, E. Spanakis, P. Tzanetakis, *Appl. Surf. Sci.* **2009**, *255*, 5425–5429.
[22] J. Reif, F. Costache, M. Henyk, S. V. Pandelov, *Appl. Surf. Sci.* **2002**, *197–198*, 891–895.
[23] E. Rebollar, P. Susana, J. J. Hern, I. Martín-fabiani, D. R. Rueda, T. A. Ezquerra, M. Castillejo, *Langmuir* **2011**, *27*, 5596–5606.
[24] E. Rebollar, J. R. V. de Aldana, I. Martín-Fabiani, M. Hernández, D. R. Rueda, T. A. Ezquerra, C. Domingo, P. Moreno, M. Castillejo, *Phys. Chem. Chem. Phys.* **2013**, *15*, 11287–11298.
[25] S. Gräf, C. Kunz, F. A. Müller, *Materials* **2017**, *10*, 1–12.
[26] K. M. Tanvir Ahmmed, C. Grambow, A. M. Kietzig, *Micromachines* **2014**, *5*, 1219–1253.
[27] T. Y. Hwang, C. Guo, *J. Appl. Phys.* **2012**, *111*, 83518.
[28] M. Tsukamoto, T. Kayahara, H. Nakano, M. Hashida, M. Katto, M. Fujita, M. Tanaka, N. Abe, *J. Phys. Conf. Ser.* **2007**, *59*, 666–669.
[29] D. Kam, J. Kim, L. Song, J. Mazumder, *J. Micromech. Microeng.* **2015**, *25*, 45007.
[30] C. A. Zuhlke, T. P. Anderson, D. R. Alexander, *Opt. Express* **2013**, *21*, 8460–8473.
[31] A. Y. Vorobyev, C. Guo, *J. Nano Res.* **2011**, *14*, 57–67.
[32] G. Li, J. Li, C. Zhang, Y. Hu, X. Li, J. Chu, W. Huang, D. Wu, *ACS Appl. Mater. Interfaces* **2015**, *7*, 383–390.
[33] S. Moradi, S. Kamal, P. E. Hatzikiriakos, S. G. Hatzikiriakos, *Nanotechnology* **2013**, *24*, 1–12.
[34] A. Y. Vorobyev, C. Guo, *J. Appl. Phys.* **2015**, *117*, 33103.
[35] A. Y. Vorobyev, C. Guo, *Appl. Phys. Lett.* **2008**, *92*, 41914.
[36] B. Dusser, Z. Sagan, H. Soder, N. Faure, J. P. Colombier, M. Jourlin, E. Audouard, *Opt. Express* **2010**, *18*, 2913–2924.
[37] B. K. Nayak, V. V Iyengar, M. C. Gupta, *Prog. Photovoltaics* **2011**, *19*, 631–639.
[38] A. R. Neale, Y. Jin, J. Ouyang, S. Hughes, D. Hesp, V. Dhanak, G. Dearden, S. Edwardson, L. J. Hardwick, *J. Power Sources* **2014**, *271*, 42–47.
[39] T. Rauscher, C. Immanuel, A. Gabler, T. Gimpel, M. Köhring, B. Kieback, W. Schade, L. Röntzsch, *Electrochim. Acta* **2017**, *247*, 1130–1139.
[40] K. Lange, M. Schulz-Ruhtenberg, J. Caro, *ChemElectroChem* **2017**, *4*, 570–576.
[41] C. A. Zuhlke, T. P. Anderson, D. R. Alexander, *Proc. SPIE* **2014**, *8968*, DOI 10.1117/12.2040348.
[42] Y. Li, Z. Cui, W. Wang, C. Lin, H. Tsai, *Appl. Surf. Sci.* **2015**, *324*, 775–783.
[43] M. Grasserbauer, *Mikrochim. Acta* **1983**, *3*, 415–448.
[44] H. Bode, K. Dehmelt, J. Witte, *Electrochim. Acta* **1966**, *11*, 1079–1089.
[45] B. E. Conway, M. A. Sattar, *J. Electroanal. Chem. Interfacial Electrochem.* **1968**, *19*, 351–364.
[46] S. L. Medway, C. A. Lucas, *J. Electroanal. Chem.* **2006**, *587*, 172–181.
[47] A. Gillner, M. Jüngst, P. Gretzki, in *Adv. Solid State Lasers Conf.* **2015**, pp. 3–6.
[48] C. Freitag, M. Wiedenmann, J. Negel, A. Loescher, V. Onuseit, R. Weber, M. A. Ahmed, T. Graf, *Appl. Phys. A* **2015**, *119*, 1237–1243.
[49] M. Shalom, D. Ressnig, X. Yang, G. Clavel, T. P. Fellinger, M. Antonietti, *J. Mater. Chem. A* **2015**, *3*, 8171–8177.

Manuscript received: August 20, 2018
Version of record online: October 15, 2018

Supporting Information

Porous Nickel Nano-Foam by Femtosecond Laser Structuring for Supercapacitor Application

Karsten Lange,* Christian Hördemann, Malte Schulz-Ruhtenberg, and Jürgen Caro

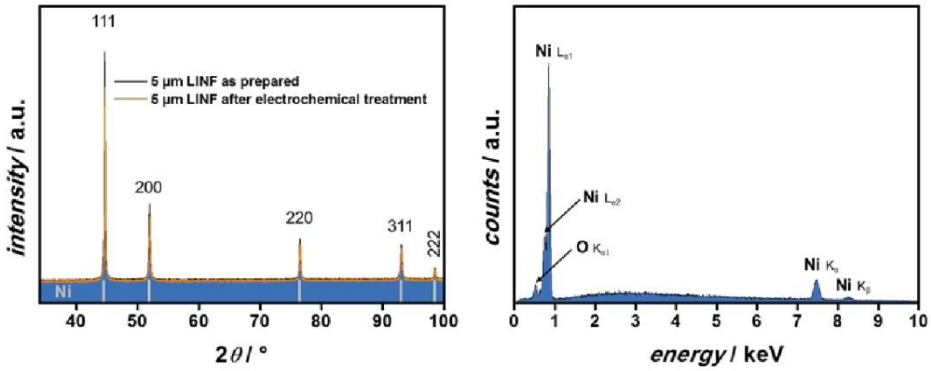

Figure 1. Left: X-ray diffraction pattern of a 5 µm LINF electrode as prepared and after the electrochemical treatment of the region 30° < 2θ < 100°. Theoretical reflex position of Ni is shown with corresponding Miller indices. Right: Energy-dispersive X-ray spectrum of a 5 µm LINF electrode.

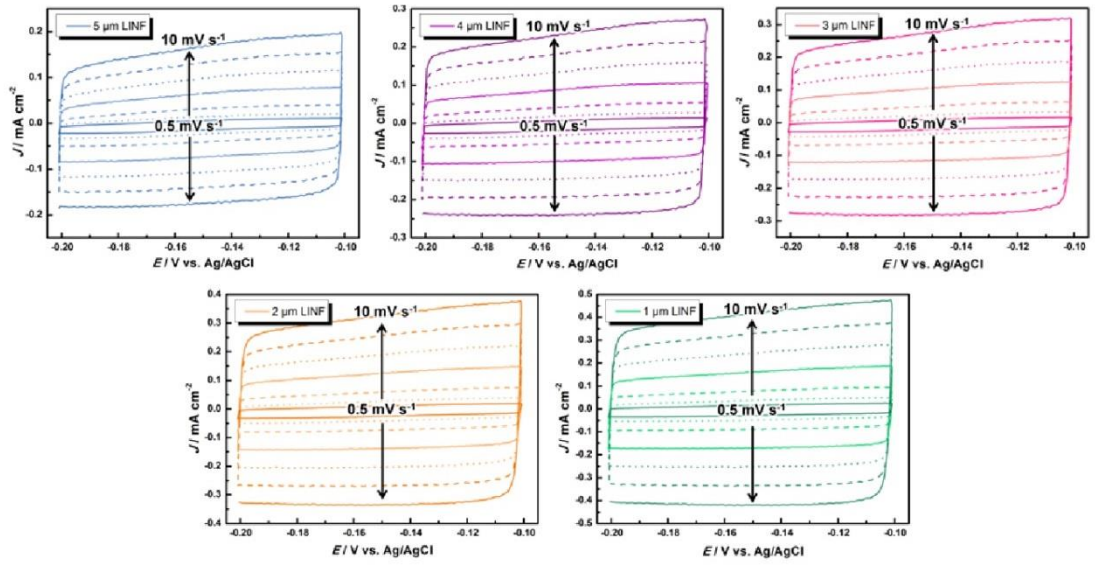

Figure 2. Cyclic voltammogram cascades for 5 µm to 1 µm LINF electrodes, measured with scan speeds between 0.5 mV s^{-1} and 10 mV s^{-1}.

4.3 Spiky Nickel Electrodes for Electrochemical Oxygen Evolution Catalysis created by Femtosecond Laser Structuring

Felix Rieck genannt Best, Jürgen Koch, Gerhard Lilienkamp, Franz Körkemeyer, Hans Jürgen Maier, Jürgen Caro, and **Karsten Lange***,

International Journal of Electrochemistry, 2018, vol. 2018, Article ID 9875438, 12 pages.

DOI: 10.1155/2018/9875438

Hindawi
International Journal of Electrochemistry
Volume 2018, Article ID 9875438, 12 pages
https://doi.org/10.1155/2018/9875438

Research Article

Spiky Nickel Electrodes for Electrochemical Oxygen Evolution Catalysis by Femtosecond Laser Structuring

Felix Rieck genannt Best,[1] Jürgen Koch,[2] Gerhard Lilienkamp,[3] Franz Körkemeyer,[4] Hans Jürgen Maier,[4] Jürgen Caro,[1] and Karsten Lange[1]

[1]*Institute of Physical Chemistry and Electrochemistry, Leibniz Universität Hannover, Callinstr. 3A, 30167 Hannover, Germany*
[2]*Laser Zentrum Hannover e.V., Hollerithallee 8, 30419 Hannover, Germany*
[3]*Institute of Energy Research and Physical Technologies, TU Clausthal, Leibnizstr. 4, 38678 Clausthal-Zellerfeld, Germany*
[4]*Institut für Werkstoffkunde (Material Science), Leibniz Universität Hannover, An der Universität 2, 30823 Garbsen, Germany*

Correspondence should be addressed to Karsten Lange; karsten.lange@pci.uni-hannover.de

Received 17 August 2018; Accepted 22 October 2018; Published 19 November 2018

Guest Editor: Jinmei Liu

Micro- and nanostructured Ni/NiO surfaces were generated by femtosecond laser structuring for oxygen evolution reaction in alkaline water electrolysis cells. For two different angles between the laser beam and the nickel surface, two different types of laser-structured electrodes were prepared, characterized, and compared with a plane tempered nickel electrode. Their electrochemical activities for the oxygen evolution reaction were tested by using cyclic and linear sweep voltammetry. The chemical surface composition was investigated by X-ray photoelectron spectroscopy. Laser structuring increased the overall electrochemical performance by more than one order of magnitude. The overpotential of the laser-structured electrodes for the oxygen evolution reaction was decreased by more than 100 mV due to high defect densities of the structures created by the laser ablation process.

1. Introduction

Water electrolysis provides a simple and clean method to produce hydrogen using renewable energies, while both water and the energy source (wind and solar energy) are practically infinite. In alkaline water electrolysis, two important reactions take place: the hydrogen evolution reaction (HER) at the cathode and simultaneously the oxygen evolution reaction (OER) at the anode. Platinum shows the best catalytic activity for the HER [1, 2]. Due to its high price, platinum is in most cases replaced in industrial alkaline water electrolysis cells by cathodes made of stainless steel or high-area nickel on steel [3]. However, the efficiency of the water electrolysis cell is limited by the sluggish anodic kinetics of the OER compared to the HER [4, 5]. IrO_2 and RuO_2 are considered to be state-of-the-art electrode material for the OER, as they show the lowest overpotentials [6, 7]. Consequently, the high cost and the lack of long-term stability in alkaline water electrolysis conditions prevent an industrial application and lead to the search for different cost-efficient and highly active catalysts for the OER [8]. First-row transition metal oxides, like nickel [9], cobalt [10], iron [11], and manganese [12] oxides and mixed oxides in the spinel [13] and perovskite [14] structure seem to fit the demands for OER anode active materials.

The overall efficiency of a water electrolysis cell is determined by the combined resistances of all components and chemical processes. In addition to the electrode materials and the resulting overpotential, mass transport problems always occur during reactions in aqueous solution [15]. Apart from mass transfer, temperature distribution, bubble size, and bubble detachment affect the potential and current density distribution in a gas evolution cell [16, 17]. Thus, the bubble attachment will affect the efficiency adversely by blocking the catalytic active sites of the electrode [18]. Calculations show that the energy loss caused by bubbles is the major contributor to the total energy loss of a gas evolution cell [16]. Forced electrolyte convection, supergravity [19], and ultrasonication [20] are ways to address the problem of bubble attachment, although the electrolyte management cost would increase

and additional energy consumption would arise. Therefore, researchers are focusing on electrode design to facilitate gas bubble detachment from the electrode [21–23]. A superhydrophilic electrode surface would attract the electrolyte more than the bubbles and decrease the bubble-electrode surface attraction, accordingly smaller bubbles would detach easier on their own [24, 25]. Another approach to reduce the forces, that hold the bubble at the surface, is to minimize the bubble-electrode contact area. There are several studies, which utilize the nanostructuring of gas evolution electrodes to create "superaerophobic" surfaces [17, 26–28]. However, creating electrodes with nanowire surfaces is difficult to implement in an industrial-scale fabrication process for gas evolution electrodes.

Modern femtosecond lasers represent a new powerful tool for customized electrode structuring. Specifically, the generation of ordered nano- and microstructures on bulk substrates is an upscalable process for large-area applications, thanks to recently available high power femtosecond lasers [30, 31]. Via the high variety of process parameters, the surface morphology can be customized. One type of laser-induced self-organized surface structures is the micrometer-sized cone-like protrusions (CLPs, also often called spike structures), which are superimposed by nanostructures [32–37].

CLPs are stochastically ordered structures oriented antiparallel to the direction of the incident laser beam. Their heights, flank angles, and average distances can be controlled by choosing process parameters such as laser fluence, laser wavelength, and environmental conditions. Furthermore, they are influenced by material properties. CLPs can be processed on many metals [38–40] and semiconductors [41, 42]. Suitable lasers are pulsed lasers with nanosecond (ns) down to femtosecond (fs) pulse duration. In general, shorter pulse durations prevent melting and lead to higher surface area [43, 44]. The process of CLP formation is not yet fully understood. The formation of CLPs is done with a laser focus diameter of around 10 μm or bigger and a relatively high laser fluence of usually a few 10 J cm^{-2}. Since the CLPs are directed antiparallel to the incident laser beam, tilting the workpiece surface leads to CLPs with the same tilting angle [45, 46] but requires higher laser pulse energy.

The main objective of the present study was to enlarge the surface area and simultaneously activate the Ni electrode for high current density OER application via our femtosecond laser structuring approach. Blank Ni plates were used as substrate material, which were polished and afterwards structured by femtosecond laser pulses under irradiation angles of 0° or 45° to create two different types of Ni CLPs electrodes. The topography of the sample surfaces was studied with the help of scanning electron microscopy and X-ray microscopy. In addition, the chemical compositions of the surfaces were investigated by X-ray photoelectron spectroscopy. The electrodes were placed vertically in a reactor cell and were characterized by cyclic and linear sweep voltammetry to determine the accessible surface area and the activity for the OER with realistic gas bubble behavior.

2. Experimental Section

2.1. Electrode Preparation. First the Ni plates (Alfa Aesar) with a size of 10 mm × 10 mm were polished with a Phoenix 4000 polishing machine using 15 μm, 6 μm, 3 μm, and 1 μm diamond suspensions (Buehler) and cleaned with acetone and ultra-pure water. Afterwards the plates were either tempered or laser structured. The reference sample had been tempered at 650°C in air for 1 h with a heating rate of 5°C min^{-1}. The irradiation angle of the laser was set to 0° or 45°, to create two different types of CLP structures.

The laser structuring was performed with a femtosecond laser system (Femtopower Compact Pro, Femtolasers Produktions GmbH) with a fundamental wavelength of 800 nm, a sub-30 fs pulse duration, and a pulse repetition rate of 1 kHz. The laser pulses were focused using an achromatic lens with 200 mm focal distance resulting in a focus with Gaussian intensity distribution and a $1/e^2$ diameter of 34 μm. The compressor of the laser system was adjusted for shortest pulse duration in the focus. The linear polarization was constantly rotated at 800 rpm using a motorized rotation mount with a half wave plate placed in the beam path in front of the focusing optics. A XYZ-positioning system (Physik Instrumente) controlled by laser machining software and synchronized with laser switching was used for sample movement and focus positioning. The focus position was set onto the sample surface. In case of the 45° incident laser beam, the sample was placed on a 45° holder mounted to the XY-stage with the Z-stage keeping the focus constantly on the sample surface. It was possible to almost completely prevent accumulation of ablation particles on the sample surface by a combination of a compressed air cross jet, particle fume extraction, and by choosing process parameters optimized for particle generation with high kinetic energy. Processing was done in the form of hatch patterns consisting of parallel lines with constant line-to-line distance. Processing directions were alternated from line to line. After the completion of every hatch pattern the orientation was rotated by 90° before the next hatch pattern was scanned. This process was repeated eight times. Different processing parameters were tested for achieving dense and uniformly distributed CLP topographies. Table 1 lists the processing parameters for the Ni CLPs 0° and the Ni CLPs 45° sample.

2.2. Physical Characterization. The topography of the laser-structured surfaces was studied by scanning electron microscopy (SEM) on a JEOL JSM-6700F operating at 2 kV and 10 μA. The SEM was coupled with an energy-dispersive X-ray (EDX) detector. X-ray diffraction (XRD) patterns were acquired on a Bruker D8 Advance diffractometer operating at 40 kV and 40 mA with Cu-K_α-radiation (λ = 0.154 nm). The X-ray photoelectron spectroscopy (XPS) was performed with nonmonochromatized Al-K_α-radiation. A hemispherical analyzer (Omnicron GmbH) with 20 eV pass energy and an acquisition time of 10 s per energy step of 100 meV was used. The X-ray microscopy (XRM) was performed using a Zeiss Xradia Versa 520. The X-rays were generated by a Nordson DAGE NT100 transmissive source with a tungsten target

Table 1: Processing parameters for the laser-structured samples Ni CLPs 0° and Ni CLPs 45°.

Sample name	Laser pulse energy	Laser peak fluence	Sample movement velocity	Hatch line-to-line distance	Hatch repetitions
Ni CLPs 0°	175 μJ	38.5 J cm^{-2}	v_x, v_y = 6 mm s^{-1}	d_x,d_y = 6 μm	8
Ni CLPs 45°	400 μJ	62.3 J cm^{-2} (on the tilted surface)	v_x = 6 mm s^{-1} v_y = v_z = 3 mm s^{-1}	d_x, d_y, d_z = 6 μm	8

at 140 kV acceleration voltage, 72 μA current, and filtered using a proprietary filter. The distance from the source to the rotating sample axis was set to 9 mm and from rotating sample axis to the detector 20 mm, respectively, resulting in a geometric magnification of 3.2x. A scintillator and 20x optical objective was used to further magnify the image onto a 1024 pixel x 1024 pixel CCD detector, resulting in a voxel size of 425 nm. The estimated reconstructed spatial resolution was 900 nm. 2001 projections with 45 s exposure were taken while the sample was rotated through 360°, resulting in a total scan time of 27 h. Scout-and-Scan Control System Reconstructor software was used to generate the reconstruction. The visualization of the data was done using Dragonfly Pro 3.0 from Object Research Systems. Otsu's thresholding algorithm was used to split the absorption dataset into nickel and epoxy resin-filled cavities. The contact angle measurements were performed on a Krüss Mobile Surface Analyzer with a 1 μL deionized water droplet.

2.3. Electrochemical Characterization. The electrochemical measurements were performed with a Bio-Logic Science Instruments VMP3 potentiostat. A three-electrode-setup with a steel mesh as the counter electrode and an Ag/AgCl (3 M KCl, E = 0.21 V) reference electrode was used, while the Ni plates served as the working electrodes. The working electrodes were placed vertically in the cell. 25 wt.-% KOH (Sigma Aldrich) served as the electrolyte. The cyclic voltammograms (CV) of the laser-structured and tempered Ni plates were recorded between E = -0.50 V and E = 0.52 V versus Ag/AgCl with a scan speed of ν = 20 mV s^{-1}. After the initial recording the linear sweep voltammograms (LSV) were termed "*as prepared*" and after 300 further CV cycles with a scan speed of ν = 10 mV s^{-1}, termed as "*activated*". The long-term stability test was carried out with chronopotentiometry at J = 100 mA cm^{-2} for 48 h. The data were not iR corrected. The OER overpotential was calculated on the basis of (1), with E^0 = 1.229 V. The potential conversion from the recorded $E_{Ag/AgCl}$ to E_{RHE} is given by (2).

$$\eta_{OER} = E_{RHE} - E^0 \quad (1)$$

$$E_{RHE} = E_{Ag/AgCl} + 0.21\,\text{V} + 0.059 \cdot pH \quad (2)$$

The double layer capacitance (C_{dl}) was determined from a CV cascade in a potential window of ΔE = 0.1 V at the open circuit potential (OCP) using the following equation:

$$C_{dl} = \frac{\Delta J}{2\nu} \quad (3)$$

where ΔJ describes the sum of the absolute anodic and cathodic current densities and ν the scan speed. In order to gain further information about the enlargement of the surface area, the roughness factor R_f was determined. For the latter, the double layer capacitance of a structured sample ($C_{dl,structured}$) was divided by the double layer capacitance of the plane reference sample ($C_{dl,plane}$), normalized to 1 cm^2:

$$R_f = \frac{C_{dl,structured}}{C_{dl,plane}} \quad (4)$$

3. Results and Discussion

The laser-structured Ni plates show high periodicity and excellent uniform topography across the whole 1 cm^2 area due to the overlap of parallel laser scans and the repetitive structuring process; see Figure 1. Comparisons between the laser-structured Ni CLPs 0° and Ni CLPs 45° show that the spike's orientation is almost identical to the laser irradiation angle, as the spikes form with an angle of 45° on the Ni plate at a laser irradiation angle of 45°. These observations correspond with previous studies on laser-structured surfaces [38, 45]. The mean distance between the spikes at Ni CLPs 0° is around 15 μm, while the average spike spacing at Ni CLPs 45° is a few micrometers larger. Moreover, the spikes are decorated with redeposited nanosized ablation product. In addition, the hierarchical surface structures exhibit laser-induced ripples. The ripples are not uniformly oriented since the polarization vector of the laser beam was constantly rotated during the processing.

X-ray diffraction (XRD) was carried out to study the crystallinity of the laser-structured and tempered plates (see supplementary information (Available here)). The only phase found in the XRD patterns of the laser-structured plates was elemental nickel. As expected, the pattern of tempered Ni depicted only small signals of a nickel oxide species, which can be assigned to a thin NiO layer. However, EDX analysis of the laser-structured plates exhibited an O K_α signal, indicating the presence of nickel oxide (supplementary information). Since XRD has an information depth of several micrometers [47], XRD measurements contain mostly information about the bulk material. Ni passivates at room temperature in three steps, where the first step is the chemisorption of oxygen at the Ni surface. In a second step, NiO nucleation and lateral growth lead to coalescence and the formation of ≈2 atomic layers of NiO. Over time, NiO growth up to 4 atomic layers [48]. The NiO passivation layer protects the Ni not well enough under high potential applications like OER, and thus, it is necessary to use thicker NiO layers. The

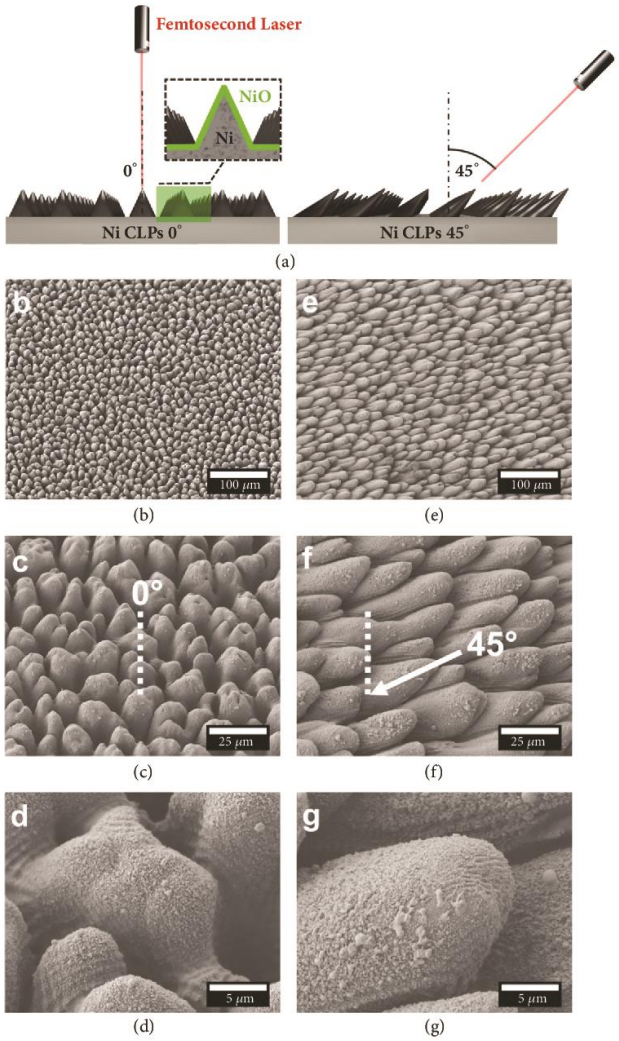

FIGURE 1: (**a**) Schematic illustrations of the preparation process of the laser-structured Ni electrodes in air. The direction of the formed spikes depends on the incident angle of the laser beam; simultaneously oxidation of the Ni surface occurs. (**b**-**g**) SEM images of laser-structured Ni electrodes at different magnifications. The irradiation angle of the laser during the structuring was set to 0° (**b-d**) and 45° (**e-g**). The SEM images were taken at a sample tilt angle of 25°.

present laser-structured Ni electrodes exhibit thicker oxide layer of 4 to 7 nm (see supplementary information). Usually, the drawback of metal oxide electrocatalysts is their poor electrical conductivity [49].

To determine the surface composition of the *as prepared* tempered and laser-structured Ni electrodes, X-ray photoelectron spectroscopy (XPS) measurements were carried out. In general, the oxidation state of nickel at the surface can be derived from the binding energies and their chemical shifts in the XPS [29]. Besides the laser-structured sample tempered Ni and NiO powder (Alfa Aesar, >99%) was used as reference samples. Figures 2(a) and 2(b) compare the normalized Ni $2p_{3/2}$ spectra as well as the O 1s spectra of the NiO powder, the tempered Ni electrode, and the laser-structured Ni CLPs 0° electrode.

The Ni $2p_{3/2}$ photoelectron transitions of the three samples (around 854 eV) show multiplet splitting and shake-up satellites (at 860 eV), which is typical for nickel oxide species and corresponds well with published data [50, 51]. Unfortunately, the complex main line splitting and the satellite structures at higher binding energies make nickel related XPS challenging to interpret. Similar to the procedure to

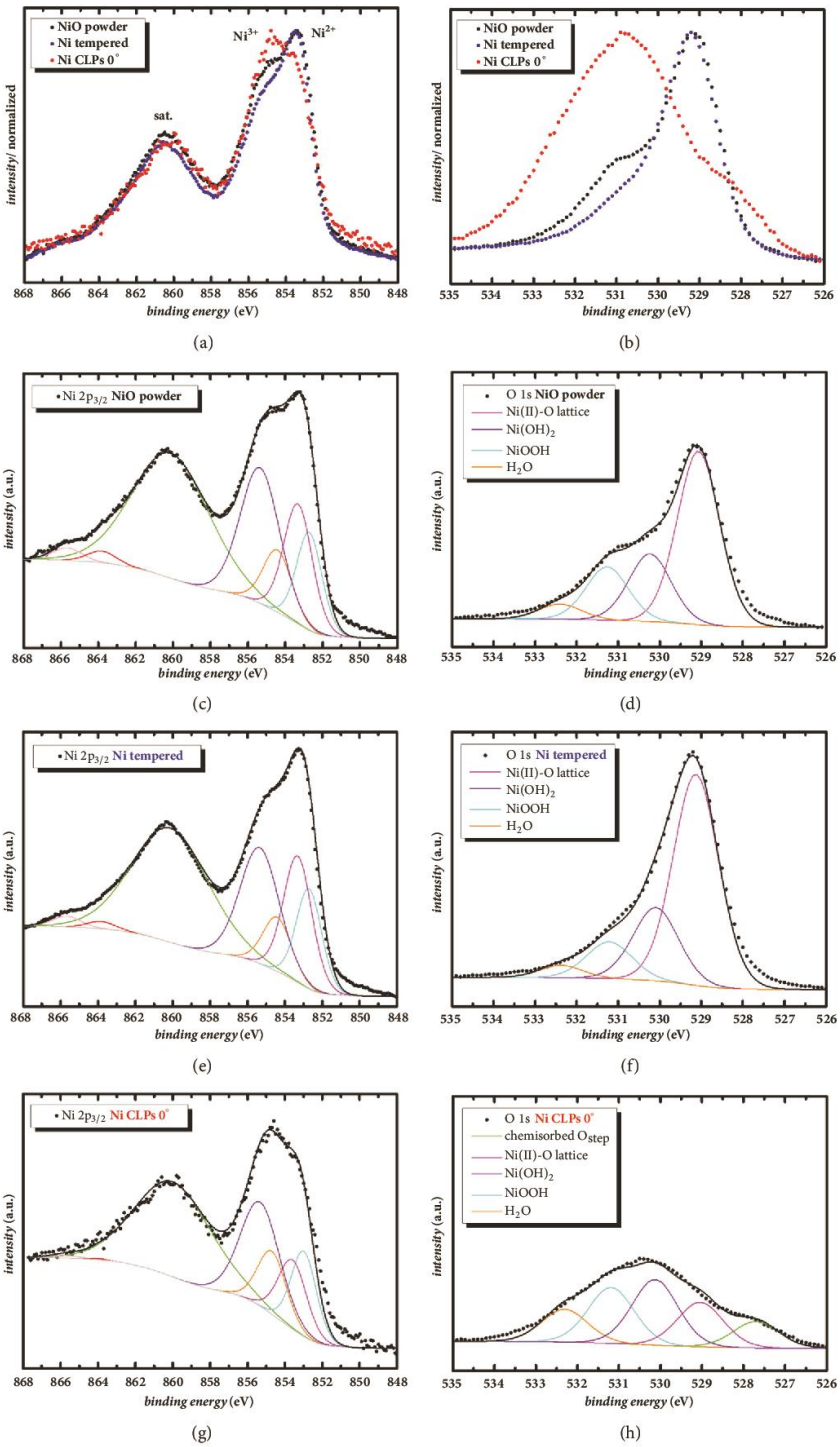

FIGURE 2: Normalized Ni $2p_{3/2}$ X-ray photoelectron spectrum (**a**) and the corresponding O 1s spectrum (**b**) of NiO powder used as reference sample and the tempered as well as laser-structured Ni electrodes. Fitted X-ray photoelectron spectra of NiO powder (**c-d**), Ni tempered (**e-f**), and Ni CLPs 0° (**g-h**). Data were fitted according to Grosvenor et al. [29].

Grosvenor et al. [29] and Biesinger et al. [52] we decomposed the Ni $2p_{3/2}$ and the O 1s signal. After subtraction of a Shirley-type background, four components to fit the Ni $2p_{3/2}$ spectra were used analog to the Ni^{3+} multiplet envelope in Grosvenor et al. [29] (Figures 2(c), 2(e), and 2(g)). The energetic positions of our fit components have been kept constant to allow a better comparison between our three samples. This causes slight deviations between spectra and fit, but do not affect the qualitative comparison. The Ni $2p_{3/2}$ spectrum of the tempered Ni electrode is almost identical to the NiO powder spectrum. As Payne et al. [53] have shown, pure NiO contributes to binding energies between 853 eV and 854 eV. Hence, the main signal at 853.3 eV was attributed to the Ni^{2+} compound in the NiO lattice. The NiO powder spectrum shows a stronger shoulder at higher binding energies as compared to the tempered Ni electrode (see the fit component at 854.4 eV), which is essentially related to the $Ni(OH)_2$ component. $Ni(OH)_2$ forms at the surface of the NiO powder due to exposure to atmosphere. In contrast, the main signal in the spectrum of the laser-structured Ni CLPs 0° electrode is found at 854.9 eV. The ratio of the areas of the four fit components correspond very well with the ratios of the Ni^{3+} multiplet peaks in Grosvernors [29] work. Accordingly, $Ni(OH)_2$ and NiOOH probably became the dominant surface components. As the spectra of both are practically equal, they are difficult to distinguish [54, 55]. Furthermore, the Ni^{3+} compound in NiOOH is chemically identical to NiO lattice defects [55]. Thus, Ni^{3+} related compounds are often interpreted as defects [56] and a clear allocation cannot be made.

The O 1s spectra of the reference NiO powder, of the tempered Ni electrode, and of the Ni CLPs 0° electrode were deconvoluted using four components for the powder as well as for the tempered sample, and five for the Ni CLPs, respectively. The full width at half maximum is kept equal for all the samples and all the components. The allocation to the particular O compound is in agreement with Ratcliff et al. [57]. The surface of the tempered Ni electrode primarily consists of NiO, which confirms the finding from the Ni $2p_{3/2}$ spectrum. The shoulder of the peak was allocated to a hydroxide signal, indicating the presence of $Ni(OH)_2$ and minor contributions of NiOOH as well as adsorbed water. In contrast to the tempered Ni electrode, the Ni CLPs 0° electrode shows dominant signals of $Ni(OH)_2$ and NiOOH species in the O 1s spectrum. Subsequently, the high intensities of the hydroxide species indicate that the transformation of NiO to $Ni(OH)_2$ or NiOOH is favored for the laser-structured surfaces. Again, the XPS signal of NiOOH species can also be interpreted as oxygen defects in the lattice [56]. The fifth component in the O 1s spectrum of the Ni CLPs 0° electrode has unusual low binding energies of about 527.7 eV. Bukhtiyarov et al. [58, 59] described this oxygen species as chemisorbed oxygen at atomic steps (O_{step}). Finally, the X-ray photoelectron spectroscopy (XPS) results in Figures 2(a)–2(h) show a significant difference in the surface composition between the tempered Ni electrode and the laser-structured Ni CLPs 0° electrode. The dominant high-binding-energy components in the Ni $2p_{3/2}$ and the O 1s spectra indicate a higher concentration of $Ni(OH)_2$ and NiOOH at the surface of the laser-structured Ni CLPs 0° electrode. During the laser structuring, the nickel is rapidly heated and thereby transformed into a mixture of liquid droplets and vapor [60]. Due to the fast quenching of the precipitated metal droplets, the solidified metal nanoparticles may show low-coordination sites at steps, cavities or compositional imperfections, which can act as catalytically active sites [61]. Still, the nickel oxide spectra pose a number of obstacles like complex multiplet splitting, satellite appearance and plasmon loss structures, which makes it difficult to assess the nature of the oxidized nickel species in detail [52]. Quantification of mixed nickel chemical states is even more challenging due to the different sample surface morphologies. Hereafter will be discussed how the defect containing structures, created during the laser structuring process, will affect the electrochemical OER behavior.

The laser-structured and the tempered Ni electrodes were evaluated in alkaline electrocatalytic water splitting as the oxygen evolution anode. Figure 3(a) depicts the cyclic voltammograms (CV) recorded between E = -0.50 V and E = 0.52 V versus Ag/AgCl reference electrode. Since there are no electrochemical processes and a non-faradaic current occurs in the potential range of -0.5 V to 0.1 V versus Ag/AgCl, the open circuit potential, which is located in this potential range, is suitable for determining the double layer capacitance [62]. Therefore, CV cascades at varying scan speeds were carried out around the open circuit potential; see supplementary information. The double layer capacitance was calculated by plotting the sum of the absolute anodic and cathodic current densities against the double scan speed. From (1), the double layer capacitance C_{dl} was determined, which was used to calculate the roughness factor R_f according to (2). The resulting data reveal a significant increase of the surface area by a factor of 49 (C_{dl} = 0.97 mF cm^{-2}) for Ni CLPs 0° and 87 for Ni CLPs 45° (C_{dl} = 1.74 mF cm^{-2}), respectively (see Figure 3(b)). Firstly, the surface area enlargement is caused by the formation of micrometer-sized spikes and secondly by a significant amount of a redeposited nanosized ablation product, which covers the spike structure. The present results for Ni CLPs 0° are in good agreement with published data on CLP structures [63, 64].

In order to understand why the surface area of Ni CLPs 45° is roughly two times larger in comparison to Ni CLPs 0°, X-ray microscopy (XRM) analysis was performed on the Ni CLPs 45° sample; see Figures 4(a)–4(c). The non-invasive XRM allows recording high quality 3D images with submicrometer resolution based on material density. In the SEM images shown above (Figure 1), it can be clearly seen that the flanks of the tilted spikes (Ni CLPs 45°) are larger than the flanks of the Ni CLPs 0° spikes. However, with SEM the backside of the tilted spikes cannot be studied. Thus, it is non-trivial to assess the contribution of the backsides of the tilted spikes to the double layer capacitance. As highlighted in Figure 4(c), however, there are deep cavities between the tilted spikes, which allow the electrolyte to reach the backside of the tilted spikes. Thus, the backsides of the tilted spikes seem to contribute significantly to the double layer

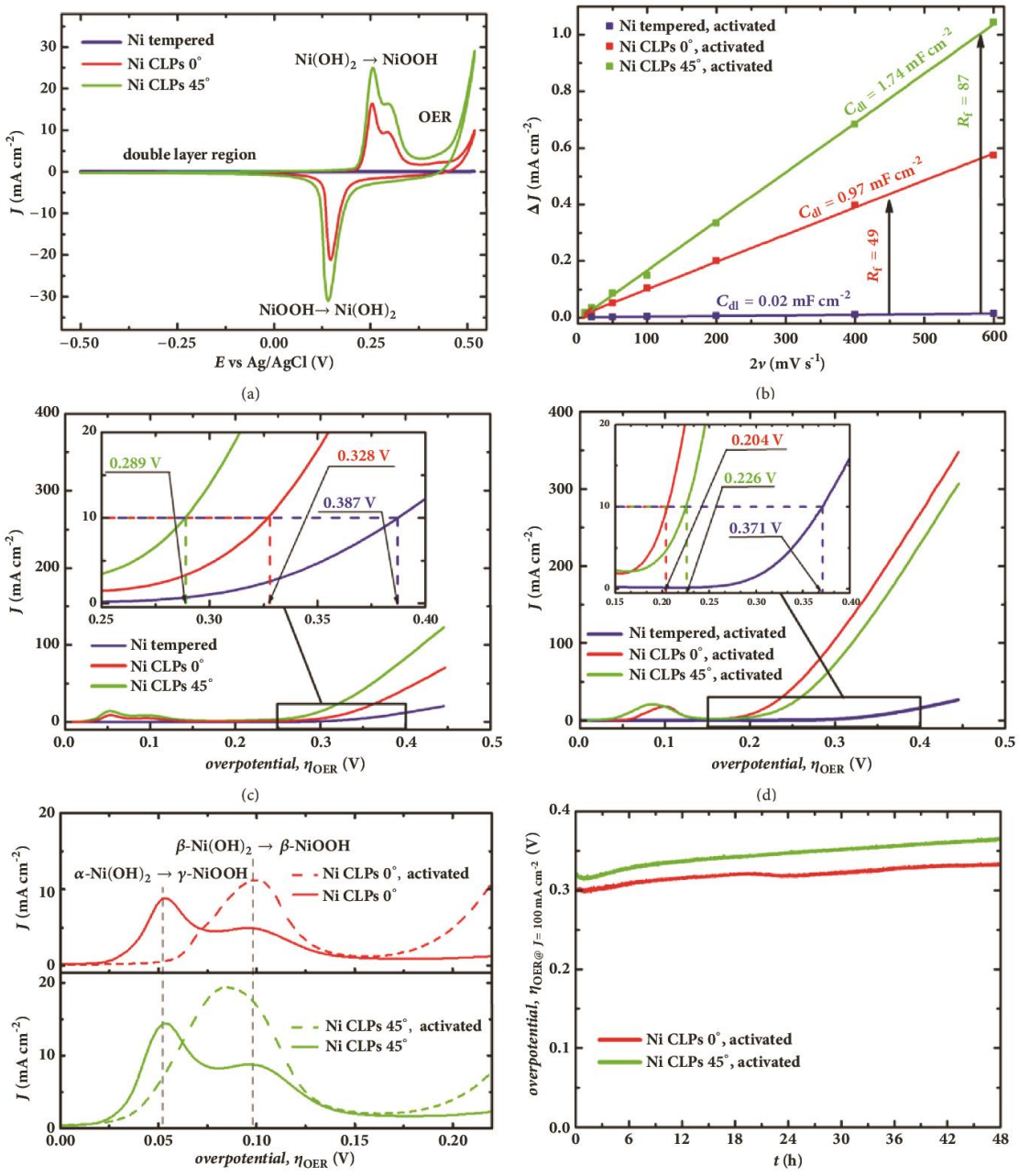

FIGURE 3: Cyclic voltammograms (CV) of *as prepared* laser-structured and tempered Ni plates (**a**) with a scan speed of $\nu = 20$ mV s^{-1}. All electrochemical measurements were performed in 25 wt.-% KOH solution at room temperature. The sum of the absolute anodic and cathodic current densities versus the scan speed ν (**b**). The slope of the resulting fit curves corresponds to the double layer capacitances of tempered and laser-structured Ni electrodes. The corresponding CV cascades can be found in the supplementary information. CVs were carried out at nonfaradaic regions in a potential window of $\Delta E = 0.1$ V around the open circuit potential. Linear sweep voltammograms *as prepared* (**c**) and *activated* (**d**) recorded with a scan speed of $\nu = 10$ mV s^{-1}. Inset: magnifications of the area at $J = 10$ mA cm^{-2} with markings highlighting the corresponding overpotentials at $J = 10$ mA cm^{-2}. Magnified linear sweep voltammograms in the potential region of the $Ni(OH)_2$ to NiOOH oxidation (**e**). Chronopotentiometric curves for long-term stability of the water electrolysis electrodes at a current density of $J = 100$ mA cm^{-2} (**f**).

Table 2: Overview of key indications: double layer capacitance C_{dl} and the corresponding roughness factor R_f as well as the oxygen evolution overpotential η_{OER} @ 10 mA cm^{-2} of the tempered Ni electrode and the laser-structured samples Ni CLPs 0° and Ni CLPs 45° *as prepared* and *activated*.

Sample name	C_{dl}	R_f	η_{OER}@ 10 mA cm^{-2} *as prepared*	η_{OER}@ 10 mA cm^{-2} *activated*
Ni tempered	0.02 mF cm^{-2}	1	0.387 V	0.371 V
Ni CLPs 0°	0.97 mF cm^{-2}	49	0.328 V	0.204 V
Ni CLPs 45°	1.74 mF cm^{-2}	87	0.289 V	0.226 V

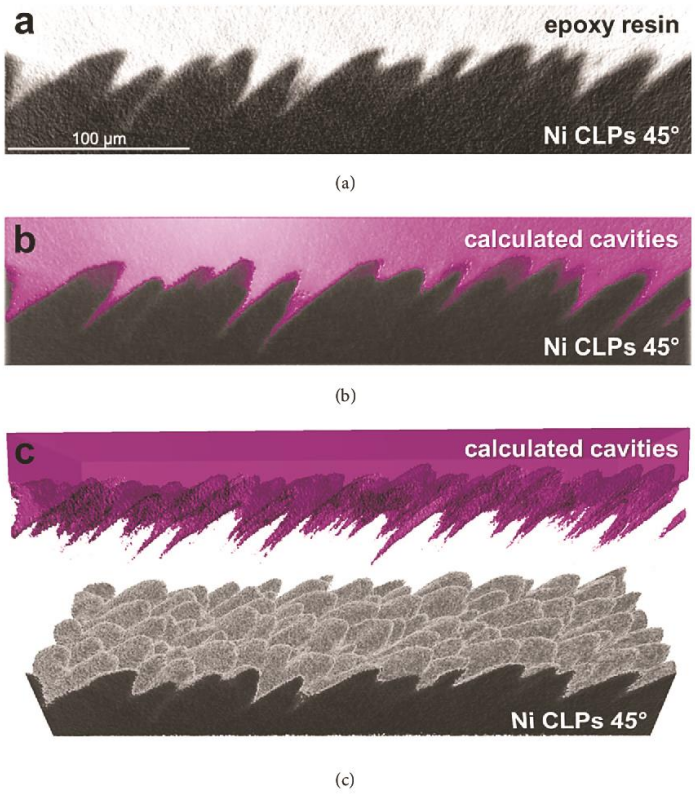

Figure 4: X-ray microscopy (XRM) data showing (**a**) absorption-contrast image of Ni CLPs 45° and representative density information. Reconstruction of the cavities within the Ni CLPs 45° structure based on absorption contrast of infiltrated epoxy resin in 2D (**b**) and 3D visualization (**c**).

capacitance and provide more surface area than in the case of the Ni CLPs 0° spikes.

According to Lyons et al. [14], the redox couple between E = 0.10 V and E = 0.40 V versus Ag/AgCl in Figure 3(a) corresponds to the oxidation of $Ni(OH)_2$ into NiOOH, which is a highly active intermediate within the OER [65]. This kind of layer-structure oxide usually exhibits good electric conductivity and has been used in alkaline batteries since the 1970s [49]. LSV of the *as prepared* electrodes were conducted to investigate their electrocatalytic behavior as OER anodes; see Figure 3(c). At the NiO alkaline electrolyte interface α-$Ni(OH)_2$ (3 $Ni(OH)_2$• 2 H_2O) is instantaneously formed [66]. α-$Ni(OH)_2$ is the hydrated species of β-$Ni(OH)_2$ and can be electrochemically oxidized to γ-NiOOH. In alkaline media α-$Ni(OH)_2$ is slowly transformed irreversibly into β-$Ni(OH)_2$ via an aging process [9]. Through electrochemical oxidization, β-$Ni(OH)_2$ is converted into β-NiOOH, which is commonly called "the right type of oxide" due to its excellent catalytic OER activity [14]. In the LSV, the conversion of β-$Ni(OH)_2$ to β-NiOOH appears shifted approximately 40 mV towards higher potentials in comparison with the conversion of α-$Ni(OH)_2$ to γ-NiOOH [66]. In the present activation process, α-$Ni(OH)_2$ is transformed into β-$Ni(OH)_2$ and therefore directs the oxidation to the preferred highly active β-NiOOH species. The corresponding LSV curves are shown in Figure 3(d). Furthermore, Table 2 compares the

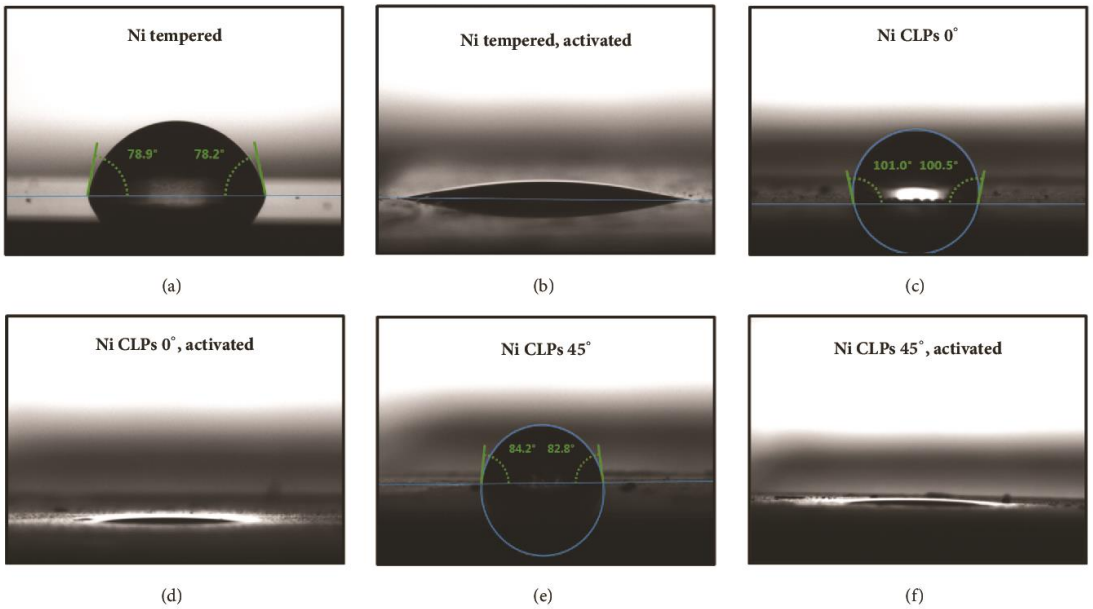

FIGURE 5: Contact angle measurements of the tempered Ni plate as prepared (a) and activated (b), Ni CLPs 0° as prepared (c) and activated (d), and Ni CLPs 45° as prepared (e) and activated (f). The measurements were carried out with a deionized water droplet (V = 1 μL). The activated electrodes show superhydrophilic behavior; therefore determination of the contact angle was not possible.

overpotentials at a current density of 10 mA cm^{-2} of the *as prepared* and *activated* electrodes. The *as prepared* laser-structured electrodes exhibit a noticeable improvement compared to the tempered one, where the *as prepared* Ni CLPs 45° (0.289 V) is slightly more active than the *as prepared* Ni CLPs 0° (0.328 V). Surprisingly, after the activation process the *activated* Ni CLPs 0° has the lowest overpotential (0.204 V) of all three samples. The Ni CLPs 0° electrode undergoes a complete conversion of α-Ni(OH)$_2$ to β-Ni(OH)$_2$ via the activation process and therefore a total transformation to the active β-NiOOH could be observed. In contrast, the Ni CLPs 45° electrode shows incomplete conversion of α-Ni(OH)$_2$ to β-Ni(OH)$_2$; see Figure 3(e).

Additionally, the maximum current density of Ni CLPs 0° is 10% higher than Ni CLPs 45°. In contrast, the expected performance of the Ni CLPs 45° electrode based on the roughness factor was significantly higher compared to the Ni CLPs 0° electrode. Especially at high current densities heavy gas evolution occurs and consequently bubble detachment becomes crucial.

To improve the bubble detachment during a gas evolution reaction, the electrode surface should be enhanced with respect to their wettability, resulting in decreased bubble-electrode attraction. Thus, the electrolyte can replace the bubbles on the electrocatalytic sites more easily. The *as prepared* tempered Ni plate as well as the laser-structured Ni CLPs 0° plate and Ni CLPs 45° plate revealed high contact angles of approximately 78°, 101° and 83°. As expected, the activation process clearly improves the wettability due to the formation of Ni(OH)$_2$ and NiOOH. Superhydrophilicity was observed on all types of electrodes; see Figure 5. That is probably the reason why our structured Ni CLPs electrodes outperform differently laser-structured electrodes studied by Ou et al. [67] in terms of their overall OER performance.

Nevertheless, the direct investigation of gas evolution on electrode surfaces remains challenging especially for coarse, not plane, electrodes like our spike structures. Zeradjanin et al. [68] was able to prove the existence of a link between surface morphology and the overall catalytic performance. Thus, the microstructure of the electrode surface has to be considered for the improvement of the efficiency of gas evolution electrodes. Hence, the electrochemical results indicate that the vertical Ni CLPs 0° electrode support more rapid gas bubble detachment compared to the Ni CLPs 45° electrode. But it has to be mentioned that we were not able to determine the actual gas bubble detachment frequencies of the laser-structured samples.

Electrochemical stability and durability tests (Figure 3(f)) were carried out under demanding conditions at 100 mA cm^{-2} for 48 h to assess the suitability as a long-term working OER electrode. Chronopotentiometry is found to be an appropriate and fast method to evaluate the electrochemical stability of such electrodes [69]. In the process, both types of laser-structured Ni electrodes exhibited only a slight increase of the overpotential during the test period, indicating excellent electrochemical stability

at high current densities. Thus, there is a stable adhesion of the catalytic active nanodecorations on the conducting CLP structures, which enable long-term process stability for OER applications. Furthermore, all electrodes show a similar Tafel slope of approximately 60 mV dec^{-1}, indicating that a chemical step is rate-determining for all different electrode types [11, 70, 71]. The corresponding Tafel plots can be found in the supplementary information. However, many different electrochemical processes may influence the slope of gas evolution electrodes especially at high current densities like mass transfer problems (varying depletion zone) [72]: bubble adhesion, coalescence, and detachment causing limiting current behavior [73].

4. Conclusion

A femtosecond laser was used as a novel tool for the generation of ordered nano- and microstructures on bulk Ni substrates. Two types of Ni/NiO spiky microstructures were created through variation of the incident angle of the laser beam and tested as electrodes for electrochemical water splitting. Currently, the oxygen evolution reaction (OER) is a key limiting factor for water splitting. Both investigated laser-structured Ni electrodes exhibited an increase in OER performance by more than one order of magnitude compared to a plane tempered Ni reference sample. Furthermore, the OER overpotential was decreased by over 100 mV compared to the reference sample. Based on X-ray photoemission spectroscopy data, this could be attributed to the formation of catalytic active defect sites at the surface of the laser-structured electrodes. Due to the high cooling rates within the laser structuring process, the nanosized decoration on the spikes shows a higher emergence of steps, cavities, low-coordination sites, and compositional imperfections, that all can act as catalytic active sites. This favors the formation of highly active NiOOH species on the laser-structured electrodes. In addition, femtosecond laser structuring combines excellent versatility and compatibility and is easy to adapt to other metal or semiconductor materials.

Data Availability

The XRD data used to support the findings of this study are included within the supplementary information file(s). The EDXS data used to support the findings of this study are included within the supplementary information file(s). The XRD and EDXS raw data used to support the findings of this study are available from the corresponding author upon request. The contact angle data used to support the findings of this study are included within the supplementary information file(s). The CV and LSV data used to support the findings of this study are available from the corresponding author upon request.

Conflicts of Interest

The authors declare that they have no conflicts of interest.

Acknowledgments

This study was conducted within the framework of the ElektroBak graduate program organized by Uwe Schröder (TU Braunschweig). Furthermore, the authors thank the Laser Zentrum Hannover e.V. for the laser structuring, the technical expertise, and general support, as well as Wanja Dziony (TU Clausthal) for the XPS measurements. The X-ray microscope used has been funded by the German Research Foundation under Contract MA 1175/67-1 as part of its major instrumentation initiative. In addition, they thank Frank Steinbach for the preparation of the X-ray microscopy sample.

Supplementary Materials

Supplementary material contains X-ray diffraction patterns of the laser-structured Ni electrodes and the tempered comparative sample as well as an energy-dispersive X-ray spectrum and an elementary depth profile of a laser-structured Ni electrode. Furthermore, cyclic voltammogram cascades of all samples carried out around the open circuit potential are given. Finally, Tafel plots of the laser-structured Ni electrodes and the tempered comparative sample are included. *(Supplementary Materials)*

References

[1] W. C. Sheng, H. A. Gasteiger, and Y. J. Shao-Horn, "Hydrogen oxidation and evolution reaction kinetics on platinum: acid vs alkaline electrolytes," *Journal of The Electrochemical Society*, vol. 157, no. 11, pp. B1529–B1536, 2010.

[2] I. E. L. Stephens and I. Chorkendorff, "Minimizing the use of platinum in hydrogen-evolving electrodes," *Angewandte Chemie International Edition*, vol. 50, no. 7, pp. 1476-1477, 2011.

[3] D. M. Santos, C. A. Sequeira, and J. L. Figueiredo, "Hydrogen production by alkaline water electrolysis," *Química Nova*, vol. 36, no. 8, pp. 1176–1193, 2013.

[4] M. T. M. Koper, "Thermodynamic theory of multi-electron transfer reactions: Implications for electrocatalysis," *Journal of Electroanalytical Chemistry*, vol. 660, no. 2, pp. 254–260, 2011.

[5] J. Rossmeisl, A. Logadottir, and J. K. Nørskov, "Electrolysis of water on (oxidized) metal surfaces," *Chemical Physics*, vol. 319, no. 1-3, pp. 178–184, 2005.

[6] A. Michas, F. Andolfatto, M. Lyons, and R. Durand, "Gas Evolution Reactions at Conductive Metallic Oxide Electrodes for Solid Polymer Electrolyte Water Electrolysis," *Key Engineering Materials*, vol. 72-74, pp. 535–550, 1992.

[7] E. Rasten, G. Hagen, and R. Tunold, "Electrocatalysis in water electrolysis with solid polymer electrolyte," *Electrochimica Acta*, vol. 48, no. 25-26, pp. 3945–3952, 2003.

[8] M. E. G. Lyons and S. Floquet, "Mechanism of oxygen reactions at porous oxide electrodes. Part 2—Oxygen evolution at RuO_2, IrO_2 and $Ir_xRu_{1-x}O_2$ electrodes in aqueous acid and alkaline solution," *Physical Chemistry Chemical Physics*, vol. 13, no. 12, pp. 5314–5335, 2011.

[9] I. J. Godwin and M. E. G. Lyons, "Enhanced oxygen evolution at hydrous nickel oxide electrodes via electrochemical ageing in alkaline solution," *Electrochemistry Communications*, vol. 32, pp. 39–42, 2013.

[10] J. Wang, W. Cui, Q. Liu, Z. Xing, A. M. Asiri, and X. Sun, "Recent Progress in Cobalt-Based Heterogeneous Catalysts for Electrochemical Water Splitting," *Advanced Materials*, vol. 28, no. 2, pp. 215–230, 2016.

[11] M. E. G. Lyons and M. P. Brandon, "A comparative study of the oxygen evolution reaction on oxidised nickel, cobalt and iron electrodes in base," *Journal of Electroanalytical Chemistry*, vol. 641, no. 1-2, pp. 119–130, 2010.

[12] F. Jiao and H. Frei, "Nanostructured cobalt oxide clusters in mesoporous silica as efficient oxygen-evolving catalysts," *Angewandte Chemie International Edition*, vol. 48, no. 10, pp. 1841–1844, 2009.

[13] I. Nikolov, R. Darkaoui, E. Zhecheva, R. Stoyanova, N. Dimitrov, and T. Vitanov, "Electrocatalytic activity of spinel related cobalties $M_xCo_{3-x}O_4$ (M = Li, Ni, Cu) in the oxygen evolution reaction," *Journal of Electroanalytical Chemistry*, vol. 429, no. 1-2, pp. 157–168, 1997.

[14] M. E. G. Lyons and M. P. Brandon, "The oxygen evolution reaction on passive oxide covered transition metal electrodes in aqueous alkaline solution. Part 1-Nickel," *International Journal of Electrochemical Science*, vol. 3, no. 12, pp. 1386–1424, 2008.

[15] L. Sigrist, O. Dossenbach, and N. Ibl, "Mass transport in electrolytic cells with gas sparging," *International Journal of Heat and Mass Transfer*, vol. 22, no. 10, pp. 1393–1399, 1979.

[16] K. Zeng and D. Zhang, "Recent progress in alkaline water electrolysis for hydrogen production and applications," *Progress in Energy and Combustion Science*, vol. 36, no. 3, pp. 307–326, 2010.

[17] T. Burdyny, P. J. Graham, Y. Pang et al., "Nanomorphology-Enhanced Gas-Evolution Intensifies CO_2 Reduction Electrochemistry," *ACS Sustainable Chemistry & Engineering*, vol. 5, no. 5, pp. 4031–4040, 2017.

[18] K. Wang, P. Pei, Z. Ma et al., "Growth of oxygen bubbles during recharge process in zinc-air battery," *Journal of Power Sources*, vol. 296, pp. 40–45, 2015.

[19] M. Wang, Z. Wang, and Z. Guo, "Water electrolysis enhanced by super gravity field for hydrogen production," *International Journal of Hydrogen Energy*, vol. 35, no. 8, pp. 3198–3205, 2010.

[20] W. Kim, K. Park, J. Oh, J. Choi, and H.-Y. Kim, "Visualization and minimization of disruptive bubble behavior in ultrasonic field," *Ultrasonics*, vol. 50, no. 8, pp. 798–802, 2010.

[21] S.-D. Li, C.-C. Wang, and C.-Y. Chen, "Water electrolysis in the presence of an ultrasonic field," *Electrochimica Acta*, vol. 54, no. 15, pp. 3877–3883, 2009.

[22] S. Marini, P. Salvi, P. Nelli et al., "Advanced alkaline water electrolysis," *Electrochimica Acta*, vol. 82, pp. 384–391, 2012.

[23] A. R. Zeradjanin, A. A. Topalov, Q. Van Overmeere et al., "Rational design of the electrode morphology for oxygen evolution-enhancing the performance for catalytic water oxidation," *RSC Advances*, vol. 4, no. 19, pp. 9579–9587, 2014.

[24] D. Kiuchi, H. Matsushima, Y. Fukunaka, and K. Kuribayashi, "Ohmic resistance measurement of bubble froth layer in water electrolysis under microgravity," *Journal of The Electrochemical Society*, vol. 153, no. 8, pp. E138–E143, 2006.

[25] H. Matsushima, Y. Fukunaka, and K. Kuribayashi, "Water electrolysis under microgravity. Part II. Description of gas bubble evolution phenomena," *Electrochimica Acta*, vol. 51, no. 20, pp. 4190–4198, 2006.

[26] C. Tang, N. Cheng, Z. Pu, W. Xing, and X. Sun, "NiSe Nanowire Film Supported on Nickel Foam: An Efficient and Stable 3D Bifunctional Electrode for Full Water Splitting," *Angewandte Chemie International Edition*, vol. 54, no. 32, pp. 9351–9355, 2015.

[27] T. Y. Ma, S. Dai, M. Jaroniec, and S. Z. Qiao, "Metal-organic framework derived hybrid Co_3O_4-carbon porous nanowire arrays as reversible oxygen evolution electrodes," *Journal of the American Chemical Society*, vol. 136, no. 39, pp. 13925–13931, 2014.

[28] Y. Fukunaka, M. Motoyama, Y. Konishi, and R. Ishii, "Producing shape-controlled metal nanowires and nanotubes by an electrochemical method," *Electrochemical and Solid-State Letters*, vol. 9, no. 3, pp. C62–C64, 2006.

[29] A. P. Grosvenor, M. C. Biesinger, R. S. C. Smart, and N. S. McIntyre, "New interpretations of XPS spectra of nickel metal and oxides," *Surface Science*, vol. 600, no. 9, pp. 1771–1779, 2006.

[30] P. Russbueldt, T. Mans, J. Weitenberg, H. D. Hoffmann, and R. Poprawe, "Compact diode-pumped 1.1 kW Yb:YAG Innoslab femtosecond amplifier," *Optics Expresss*, vol. 35, no. 24, pp. 4169–4171, 2010.

[31] T. Mans, J. Dolkemeyer, and C. Schnitzler, "High Power Femtosecond Lasers," *Laser Technik Journal*, vol. 11, no. 3, pp. 40–43, 2014.

[32] B. K. Nayak and M. C. Gupta, "Self-organized micro/nano structures in metal surfaces by ultrafast laser irradiation," *Optics and Lasers in Engineering*, vol. 48, no. 10, pp. 940–949, 2010.

[33] S. Bruening, G. Hennig, S. Eifel, and A. Gillner, "Ultrafast Scan Techniques for 3D-μm Structuring of Metal Surfaces with high repetitive ps-laser pulses," *Physics Procedia*, vol. 12, pp. 105–115, 2011.

[34] M. Tsukamoto, T. Kayahara, H. Nakano et al., "Microstructures formation on titanium plate by femtosecond laser ablation," *Journal of Physics: Conference Series*, vol. 59, pp. 666–669, 2007.

[35] K. M. Tanvir Ahmmed, C. Grambow, and A.-M. Kietzig, "Fabrication of micro/nano structures on metals by femtosecond laser micromachining," *Micromachines*, vol. 5, no. 4, pp. 1219–1253, 2014.

[36] E. Fadeeva, S. Schlie, J. Koch, B. N. Chichkov, A. Y. Yorobyev, and C. Guo, "Femtosecond Laser-Induced Surface Structures on Platinum and Their Effects on Surface Wettability and Fibroblast Cell Proliferation," in *Contact Angle, Wettability and Adhesion*, K. L. Mittal, Ed., vol. 6, pp. 163–171, CRC Press, Leiden, Netherlands, 2009.

[37] A. Gabler, C. I. Müller, T. Rauscher et al., "Ultrashort-pulse laser structured titanium surfaces with sputter-coated platinum catalyst as hydrogen evolution electrodes for alkaline water electrolysis," *International Journal of Hydrogen Energy*, vol. 43, no. 15, pp. 7216–7226, 2018.

[38] T. Yong Hwang and C. Guo, "Polarization and angular effects of femtosecond laser-induced conical microstructures on Ni," *Journal of Applied Physics*, vol. 111, no. 8, p. 083518, 2012.

[39] T. Jiang, J. Koch, C. Unger et al., "Ultrashort picosecond laser processing of micro-molds for fabricating plastic parts with superhydrophobic surfaces," *Applied Physics A: Materials Science & Processing*, vol. 108, no. 4, pp. 863–869, 2012.

[40] D. Kam, J. Kim, L. Song, and J. Mazumder, "Formation mechanism of micro-spikes on AISI 4340 steel with femtosecond laser pulses at near-threshold fluence," *Journal of Micromechanics and Microengineering*, vol. 25, no. 4, p. 045007, 2015.

[41] B. K. Nayak, V. V. Iyengar, and M. C. Gupta, "Efficient light trapping in silicon solar cells by ultrafast-laser-induced self-assembled micro/nano structures," *Progress in Photovoltaics*, vol. 19, no. 6, pp. 631–639, 2011.

[42] J. Bonse, S. Baudach, J. Krüger, W. Kautek, and M. Lenzner, "Femtosecond laser ablation of silicon-modification thresholds and morphology," *Applied Physics A: Materials Science & Processing*, vol. 74, no. 1, pp. 19–25, 2002.

[43] B. N. Chichkov, C. Momma, S. Nolte, F. Alvensleben, and A. Tünnermann, "Femtosecond, picosecond and nanosecond laser ablation of solids," *Applied Physics A Materials Science & Processing*, vol. 63, no. 2, pp. 109–115, 1996.

[44] A. Semerok, B. Sallé, J.-F. Wagner, and G. Petite, "Femtosecond, picosecond, and nanosecond laser microablation: Laser plasma and crater investigation," *Laser and Particle Beams*, vol. 20, no. 1, pp. 67–72, 2002.

[45] T. Y. Hwang and C. Guo, "Angular effects of nanostructure-covered femtosecond laser induced periodic surface structures on metals," *Journal of Applied Physics*, vol. 108, no. 7, p. 073523, 2010.

[46] C. Kruse, I. Somanas, T. Anderson et al., "Self-propelled droplets on heated surfaces with angled self-assembled micro/nanostructures," *Microfluidics and Nanofluidics*, vol. 18, no. 5-6, pp. 1417–1424, 2015.

[47] M. Grasserbauer, "Micro and surface analysis for environmental studies," *Microchimica Acta*, vol. 81, no. 5-6, pp. 415–448, 1983.

[48] S. L. Medway, C. A. Lucas, A. Kowal, R. J. Nichols, and D. Johnson, "In situ studies of the oxidation of nickel electrodes in alkaline solution," *Journal of Electroanalytical Chemistry*, vol. 587, no. 1, pp. 172–181, 2006.

[49] N.-T. Suen, S.-F. Hung, Q. Quan, N. Zhang, Y.-J. Xu, and H. M. Chen, "Electrocatalysis for the oxygen evolution reaction: Recent development and future perspectives," *Chemical Society Reviews*, vol. 46, no. 2, pp. 337–365, 2017.

[50] K. S. Kim, "X-ray and UV photoemission studies of valence electronic structure of NiO," *Chemical Physics Letters*, vol. 26, no. 2, pp. 234–239, 1974.

[51] A. M. Venezia, R. Bertoncello, and G. Deganello, "X-ray photoelectron spectroscopy investigation of pumice-supported nickel catalysts," *Surface and Interface Analysis*, vol. 23, no. 4, pp. 239–247, 1995.

[52] M. C. Biesinger, B. P. Payne, A. P. Grosvenor, L. W. M. Lau, A. R. Gerson, and R. S. C. Smart, "Resolving surface chemical states in XPS analysis of first row transition metals, oxides and hydroxides: Cr, Mn, Fe, Co and Ni," *Applied Surface Science*, vol. 257, no. 7, pp. 2717–2730, 2011.

[53] B. P. Payne, P. G. Keech, and N. S. McIntyre, "X-ray photoelectron study of oxides formed on Ni metal and Ni-Cr alloy surfaces under electrochemical control at 25 ∘C and 150 ∘C," *Surface and Interface Analysis*, vol. 49, no. 13, pp. 1316–1324, 2017.

[54] K. K. Lian, "Investigation of a "Two-State" Tafel Phenomenon for the Oxygen Evolution Reaction on an Amorphous Ni-Co Alloy," *Journal of The Electrochemical Society*, vol. 142, no. 11, p. 3704, 1995.

[55] M. C. Biesinger, B. P. Payne, L. W. M. Lau, A. Gerson, and R. S. C. Smart, "X-ray photoelectron spectroscopic chemical state quantification of mixed nickel metal, oxide and hydroxide systems," *Surface and Interface Analysis*, vol. 41, no. 4, pp. 324–332, 2009.

[56] M. W. Roberts and R. S. C. Smart, "The defect structure of nickel oxide surfaces as revealed by photoelectron spectroscopy," *Journal of the Chemical Society, Faraday Transactions 1: Physical Chemistry in Condensed Phases*, vol. 80, no. 11, pp. 2957–2968, 1984.

[57] E. L. Ratcliff, J. Meyer, K. X. Steirer et al., "Evidence for near-surface NiOOH species in solution-processed NiO_x selective interlayer materials: Impact on energetics and the performance of polymer bulk heterojunction photovoltaics," *Chemistry of Materials*, vol. 23, no. 22, pp. 4988–5000, 2011.

[58] V. Bukhtiyarov, A. Boronin, and V. Savchenko, "Two oxygen states and the role of carbon in partial oxidation of ethylene over silver," *Surface Science*, vol. 232, no. 1-2, pp. L205–L209, 1990.

[59] V. I. Bukhtiyarov, M. Hävecker, V. V. Kaichev, A. Knop-Gericke, R. W. Mayer, and R. Schlögl, "Atomic oxygen species on silver: Photoelectron spectroscopy and x-ray absorption studies," *Physical Review B: Condensed Matter and Materials Physics*, vol. 67, no. 23, 2003.

[60] C. Wu and L. V. Zhigilei, "Microscopic Mechanisms of Laser Spallation and Ablation of Metal Targets from Large-Scale Molecular Dynamics Simulations," *Applied Physics A: Materials Science and Processing*, vol. 114, pp. 11–32, 2014.

[61] K. Lange, M. Schulz-Ruhtenberg, and J. Caro, "Platinum Electrodes for Oxygen Reduction Catalysis Designed by Ultrashort Pulse Laser Structuring," *ChemElectroChem*, vol. 4, no. 3, pp. 570–576, 2017.

[62] R. K. Shervedani and A. R. Madram, "Kinetics of hydrogen evolution reaction on nanocrystalline electrodeposited Ni62Fe35C3 cathode in alkaline solution by electrochemical impedance spectroscopy," *Electrochimica Acta*, vol. 53, no. 2, pp. 426–433, 2007.

[63] A. Gabler, C. I. Müller, T. Rauscher et al., "Ultrashort pulse laser-structured nickel surfaces as hydrogen evolution electrodes for alkaline water electrolysis," *International Journal of Hydrogen Energy*, vol. 42, no. 16, pp. 10826–10833, 2017.

[64] T. Rauscher, C. I. Müller, A. Gabler et al., "Femtosecond-laser structuring of Ni electrodes for highly active hydrogen evolution," *Electrochimica Acta*, vol. 247, pp. 1130–1139, 2017.

[65] J. S. Buchanan and L. M. Peter, "Photocurrent spectroscopy of the lead electrode in sulphuric acid," *Electrochimica Acta*, vol. 33, no. 1, pp. 127–136, 1988.

[66] H. Bode, K. Dehmelt, and J. Witte, "Zur Kenntnis der Nickelhydroxidelektrode-I. Über das Nickel (II)-hydroxidhydrat*," *Electrochimica Acta*, vol. 11, no. 8, pp. 1079–1087, 1966.

[67] G. Ou, P. Fan, H. Zhang et al., "Large-Scale Hierarchical Oxide Nanostructures for High-Performance Electrocatalytic Water Splitting," *Nano Energy*, vol. 35, pp. 207–214, 2017.

[68] A. R. Zeradjanin, E. Ventosa, A. S. Bondarenko, and W. Schuhmann, "Evaluation of the catalytic performance of gas-evolving electrodes using local electrochemical noise measurements," *ChemSusChem*, vol. 5, no. 10, pp. 1905–1911, 2012.

[69] J. Bobacka, "Potential stability of all-solid-state ion-selective electrodes using conducting polymers as ion-to-electron transducers," *Analytical Chemistry*, vol. 71, no. 21, pp. 4932–4937, 1999.

[70] B. E. Conway and P. L. Bourgault, "Significance of e.m.f. decay measurements. Applications to the nickel oxide electrode," *Transactions of the Faraday Society*, vol. 58, pp. 593–607, 1962.

[71] B. E. Conway and M. Salomon, "Electrochemical reaction orders: Applications to the hydrogen- and oxygen-evolution reactions," *Electrochimica Acta*, vol. 9, no. 12, pp. 1599–1615, 1964.

[72] M. L. Perry, "Mass Transport in Gas-Diffusion Electrodes: A Diagnostic Tool for Fuel-Cell Cathodes," *Journal of The Electrochemical Society*, vol. 145, no. 1, p. 5, 1998.

[73] J. Eigeldinger and H. Vogt, "The bubble coverage of gas-evolving electrodes in a flowing electrolyte," *Electrochimica Acta*, vol. 45, no. 27, pp. 4449–4456, 2000.

SUPPLEMENTARY INFORMATION

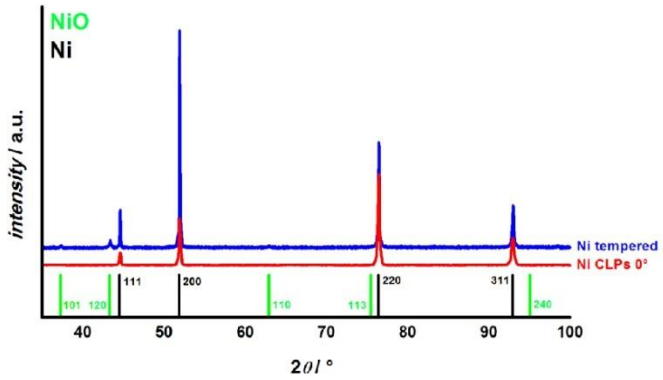

Fig. 1. X-ray diffraction patterns of laser structured Ni electrodes and tempered comparative sample of the region 30° < 2θ < 100°. Theoretical reflex position of Ni and NiO is shown with corresponding MILLER indices.

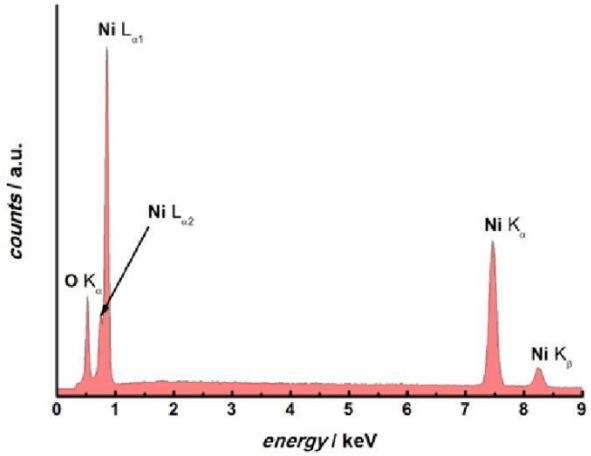

Fig. 2. Energy-dispersive X-ray spectrum of a laser structured Ni electrode.

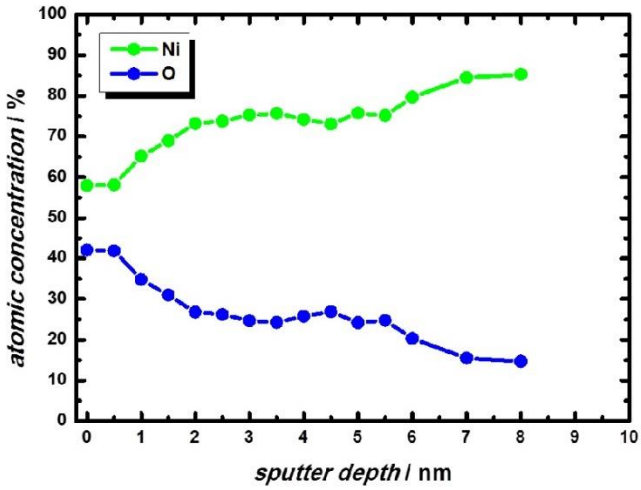

Fig. 3: Depth profile of Ni CLPs 0° with nickel oxide layer thickness of ≈ 4 - 7 nm.

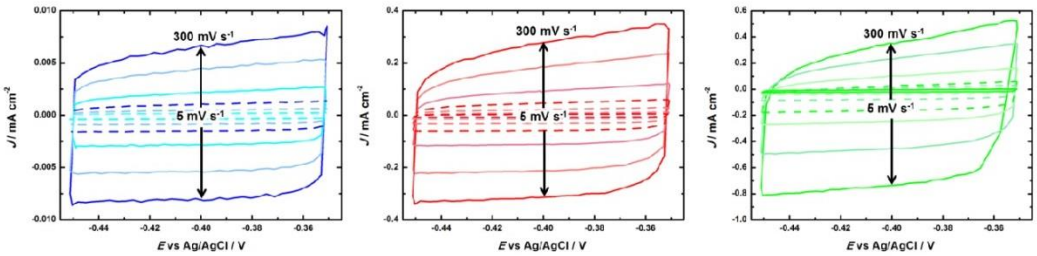

Fig. 4. Cyclic voltammogram cascades for Ni tempered (a), Ni CLPs 0° (b) and Ni CLPs 45° (c), measured with scan speeds between 5 mV s^{-1} and 300 mV s^{-1}.

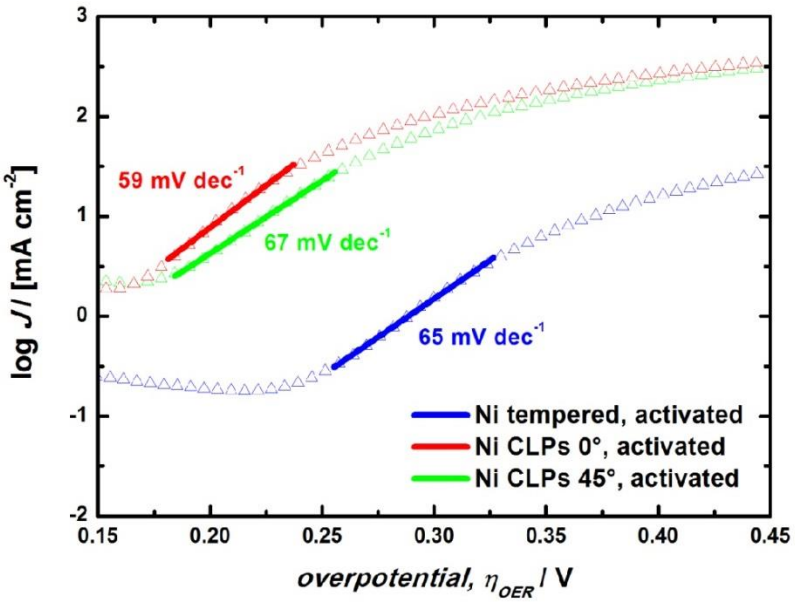

Fig. 5. Tafel plots obtained of laser structured and tempered Ni plates.

4.4 Laser directed dynamic Hydrogen Template Deposition of porous Pt@Ag Networks

Mario Wolf, Jürgen Caro, Armin Feldhoff, Frank Steinbach, Malte Schulz-Ruhtenberg, and **Karsten Lange***,

Electrochimica Acta, 2017, 252, 430-437.

DOI: 10.1016/j.electacta.2017.08.174

Electrochimica Acta 252 (2017) 430–437

Contents lists available at ScienceDirect

Electrochimica Acta

journal homepage: www.elsevier.com/locate/electacta

Research Paper

Laser directed dynamic hydrogen template deposition of porous Pt@Ag networks

Mario Wolf[a], Jürgen Caro[a], Armin Feldhoff[a], Frank Steinbach[a], Malte Schulz-Ruhtenberg[b], Karsten Lange[a,*]

[a] Institute of Physical Chemistry and Electrochemistry, Leibniz University Hannover, Callinstr. 3A, D-30167 Hannover, Germany
[b] LPKF Laser & Electronics AG, Osteriede 7, 30827 Garbsen, Germany

ARTICLE INFO

Article history:
Received 1 June 2017
Received in revised form 7 August 2017
Accepted 29 August 2017
Available online 1 September 2017

Keywords:
Dynamic hydrogen template deposition
Gradient pore structure
Galvanic replacement
Supercapacitor
Laser structuring

ABSTRACT

A porous Ag network has been deposited on laser structured Ni supports by using the dynamic hydrogen template deposition (DHTD) technique. For a better hydrogen evolution, a 10 nm Pt layer has been sputtered on the Ni supports before Ag deposition. In a subsequent step, the Ag network has been modified by electrochemical Pt deposition in a replacement reaction forming a porous Pt@Ag network. Different Pt species are formed at different positions of the Ag network: Pure Pt on top and Ag_1Pt_1 alloy at the interface between the Ag network and the deposited Pt film. Laser structuring the substrate in advance can facilitate mass transport, especially for the galvanic Pt replacement reaction, and improves the performance of the electrode. As a result, the performance of the Pt@Ag network on laser structured electrodes is significantly higher compared to a non-structured electrode.

1. Introduction

Porous electrodes with controlled morphology are of particular interest due to their possible applications in various fields such as catalysis [1], batteries [2], sensors [3] or fuel cells [4]. In these processes, especially the electrode geometry is relevant for improving the properties of the electrodes. In general, an increase of the electrochemically active surface area of the electrodes results in an improvement of performance. [5–7] In order to grow mesoporous metallic structures, sacrificial templates have been extensively studied by developing new kinds of hard and soft templates that can guide the deposition of metals and be removed afterwards to reveal the metal structure. [8,9] Alternatively, free-standing metal nanoparticles can be assembled into large-scale superstructures, but the process tends to be too slow to qualify as a competitive method. [10]

However, for porous electrodes in liquid phase, mass transport through the solution as well as through the pore system is also an important factor. Furthermore, due to the rarity of the noble metals required in most catalytic processes, electrodes with the smallest share of noble metal possible for a sufficient catalytic activity are pursued. Particularly for catalytic applications, in the last decades, great efforts have been made to prepare structured substrates based on a noble metal e.g. Pt [4]. Pt based catalysts, which have found practical application, are porous carbon supported nanoparticles or functionalized highly dendritic support structures with thin Pt films. In addition, nanoparticles of different aspect ratios [11,12], the use of Pt alloys [13,14] and core/shell-nanoparticles [15–17] as well as porous Pt films [18–20] are of particular interest. The latter distinguish themselves through mostly good catalytic activity combined with high surface area and can be relevant for mass transport controlled processes thanks to their defined pore systems. For the preparation of porous metal membranes, electrochemical deposition represents a promising method because of the potential to control both nucleation and growth of Pt layers.

In this paper, the dynamic hydrogen template deposition (DHTD) was used as a soft templating tool to prepare porous electrodes without the utilization of additional organic or inorganic templates, followed by subsequent functionalization with Pt. DHTD causes the formation of honeycomb-like metal films on a substrate by means of electrochemical deposition under in situ hydrogen evolution. [21] The hydrogen acts as a template and ensures a graded porosity of the metal system. [22] The deposition of Cu [22], as well as Ni [23], Sn [24], Zn [25], Pb [26], Ag [27] or Au [28] with this method has already been examined in detail.

* Corresponding author.
E-mail address: karsten.lange@pci.uni-hannover.de (K. Lange).

http://dx.doi.org/10.1016/j.electacta.2017.08.174
0013-4686/

Thereby, the influence of the substrate, the applied potential, the concentration of the metal precursor as well as the role of ammonium chloride and the deposition time have previously been investigated as well. Furthermore, it has been demonstrated that the morphology of the electrochemical Cu deposition can be controlled by addition of surfactants [29,30]. The deposition of binary systems such as CuAu [31], CuPd [32] and CuAg [33] as well as the subsequent galvanic replacement of the Cu with noble metals like Pt [34] or Pd [35] has also been presented. The DHTD method employed for this study is based on the studies of Cherevko et al., who investigated the influence of NH_4^+-ions on the formation of porous Ag films. [27,36] The electrodes thusly prepared have been characterized for possible catalytic or supercapacitor application by means of their electrochemically active surface area. The DHTD method for the preparation of porous Ag films with subsequent functionalization with Pt is schematically illustrated in Fig. 1.

Furthermore, we establish the possibility to direct the formation process and thus the pore system of the Ag network by laser structuring the substrate in advance. Micro structuring of the substrate surface using laser pulses is a novel approach to influence various properties of a network prepared by DHTD. Lasers are widely used in material science to process 3D structures using techniques such as simple thermal sintering in a so-called selective laser melting process (SLM) [37] or to further more complex approaches by combining laser interference lithography and metal-assisted etching to design micro structured surfaces. [38]

Ablation based laser structuring has been reported to influence several properties of a surface such as the hydrophobicity [39] or the surface area [40]. In addition, laser application allows precise surface structuring due to the highly focused laser beam, by virtue of well controllable processing parameters. Laser structuring of different materials such as metals [41], polymers [42] or dielectrics [43] has already been demonstrated at length. Therefore, this technique of surface modification has been used in various fields such as mechanics (cylinder heads) [44], biomedicine (titanium implants) [45] and catalysis (photocatalysis) [46]. For electrodes in aqueous systems, the laser induced structure creates suitable diffusion paths and can facilitate the mass transport through the porous network. Therefore, we prepared Ag and Pt@Ag networks, formed by DHTD method on laser structured Pt/Ni substrates. We characterized these networks in terms of their double layer capacitance and their electrochemically active surface area, later comparing the results with depositions carried out on non-structured Pt/Ni substrates.

2. Experimental Section

2.1. Reagents

KSCN (≥99 %) was obtained from Honeywell, $AgNO_3$ (≥99.9 %) and NH_4Cl (≥99 %) from Roth. H_2PtCl_6 (≥99.9 %) and Ni plates (99.5 %; rolled; 100 mm × 100 mm × 1 mm) were purchased from Alfa Aesar. All aqueous solutions were prepared with ultra-pure water (Purelab classic UV, $\rho = 18.2\ M\Omega\,cm$).

2.2. Electrode preparation

Before sputtering a 10 nm Pt film on the support, the Ni plates (10 mm × 10 mm) were polished on a Phoenix 4000 with a 15 μm, 6 μm, 3 μm and 1 μm polycrystalline diamond suspension (Buehler) and cleaned with isopropyl alcohol and ultra-pure water.

The laser structuring was performed with a TruMicro 5025 system (Yb:YAG, λ = 1030 nm) with 11 W average power, 6 ps pulse duration, a repetition rate of $f = 100$ kHz, scan speed of 200 mm/s and 20 repetitions. The dynamic hydrogen template deposition was conducted with an unstirred aqueous solution containing 1.5 M KSCN as complexing agent, 0.5 M NH_4Cl as proton delivering agent and 0.05 M $AgNO_3$ as metal precursor. The Ag network was deposited at room temperature using a three-electrode configuration placing the working electrode bottom down. As a counter electrode, stainless steel mesh was utilized. The deposition of Ag was achieved by use of chronopotentiometry with a constant current of $350\ mA\,cm^{-2}$. The deposition time was varied from $t = 30$ s to $t = 120$ s in 15 s steps. The Ag networks were washed with water and 1.5 M KSCN solution. Enabling galvanic replacement, the porous Ag networks were stored for 12 h, 24 h and 48 h in an unstirred 0.5 mM H_2PtCl_6 solution.

2.3. Physical characterization

The morphology of the network surfaces after deposition and following galvanic replacement was studied with a field-emission scanning electron microscope (SEM, JEOL JSM-6700F operating at 2 kV and 10 μA). The chemical composition was examined via energy-dispersive X-ray spectrometry (EDXS). The XRD measurements were performed on a Bruker D8 Advance diffractometer operating at 40 kV and 40 mA with Cu-K_α-radiation (λ = 0.154 nm). The height profile images were shot with a 3D laser scanning confocal microscope (Keyence VK-X200). The transmission

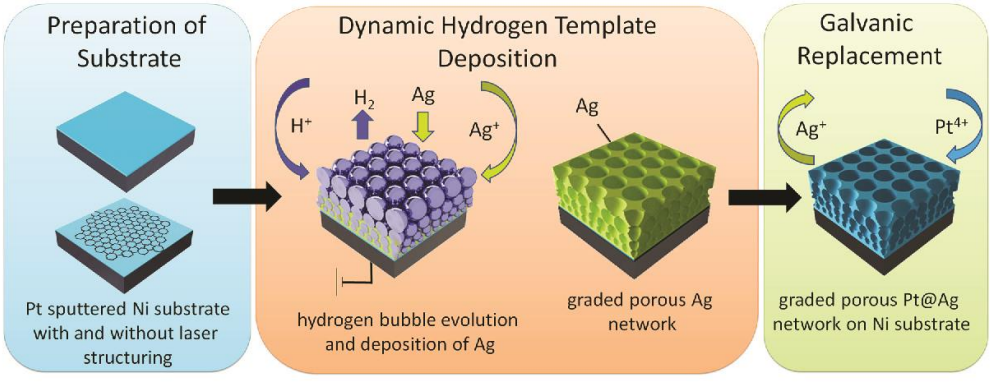

Fig. 1. Illustration of experimental procedure to generate porous Ag networks on non-structured and laser structured Pt/Ni substrates with dynamic hydrogen template deposition and subsequent galvanic replacement with Pt to form porous Pt@Ag networks.

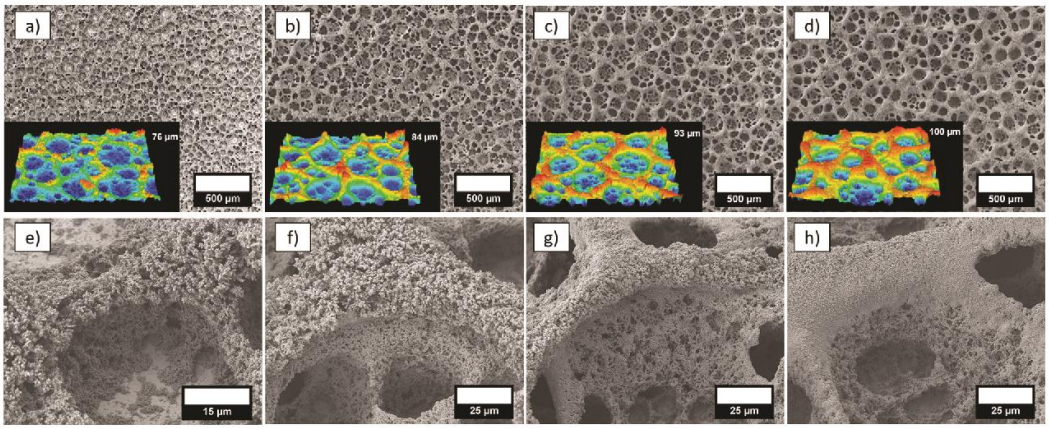

Fig. 2. SEM images of Ag networks at Pt/Ni prepared by dynamic hydrogen template deposition as a function of the deposition time after a,e) 30 s, b,f) 60 s, c,g) 90 s and d,h) 120 s at −350 mA cm^{-2}. Insets in a–d) show the scanning laser microscope images (500 µm × 700 µm sections) of the Ag networks with corresponding structure height. The trend of the double layer capacitance is shown in Fig. 4.

electron microscope (TEM) images were taken with a JEOL JEM-2100F field-emission transmission electron microscope.

2.4. Electrochemical characterization

For the electrochemical characterization, a three-electrode configuration with a graphite rod as counter electrode and Ag/AgCl (3 M KCl) as a reference electrode was used. All potentials refer to this reference electrode. A self-designed rotating disk electrode tip was used as the working electrode. All measurements were carried out in 0.1 M NaOH. The double layer capacitance of the porous electrodes was determined via cyclic voltammetry at E = -0.3 V for the porous Ag networks or at E = -0.55 V for the Pt functionalized network, based on the following equation:

$$C = \frac{j_{\text{cathodic}} + j_{\text{anodic}}}{2 \cdot \mathrm{d}E/\mathrm{d}t} \quad (1)$$

according to which, dE/dt is the potential sweep rate, j_{anodic} and j_{cathodic} are the anodic and cathodic current density, respectively. The factor R_f describes the increase of double layer capacitance C relative to a smooth polycrystalline metal surface $C_{\text{theo}} = 2 \cdot 10^{-5}$ F cm^{-2} [36] and was calculated by using:

$$R_f = \frac{C}{C_{\text{theo}}} \quad (2)$$

Furthermore, the roughness factor Φ was calculated by obtaining the transferred charge Q, associated with the oxidation of Pt-H between −0.95 V and −0.6 V after double layer correction and assuming that $q_{\text{ref}} = 0.21$ mC cm^{-2} [47], corresponding to a surface density of $1.31 \cdot 10^{15}$ Pt atoms per cm^2, which is generally accepted for polycrystalline Pt electrodes and with a geometric surface area A_{geo} by using

$$\Phi = \frac{Q}{q_{\text{ref}} \cdot A_{\text{geo}}}. \quad (3)$$

3. Results and Discussion

3.1. Preparation of graded porous Ag networks

The Ni substrates were sputtered with a 10 nm Pt layer in virtue of the negligible overpotential and the fast kinetics of the hydrogen evolution reaction at such surfaces. The electrochemical Ag deposition was conducted with chronopotentiometry at a current density of -350 mA cm^{-2} to prevent the formation of sulfur compounds, which can form at high current densities [27]. The duration of the deposition was varied and the influence of the deposition time on the Ag structure was retraced via SEM images. Fig. 2 shows the SEM images of the porous Ag networks, which

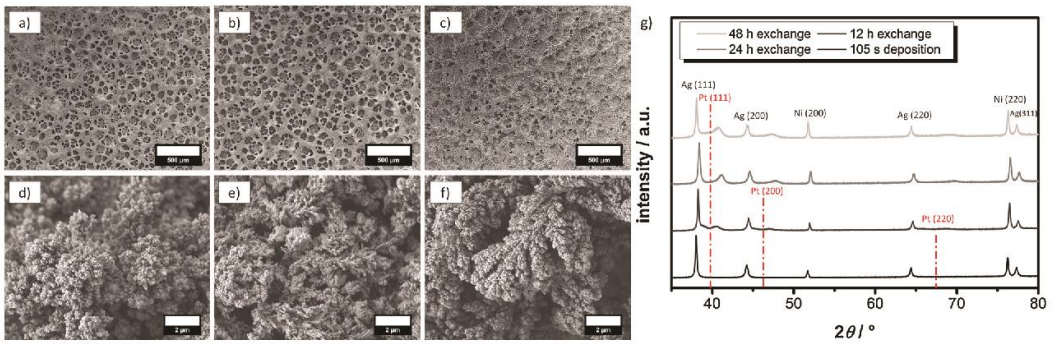

Fig. 3. SEM images of exchanged samples in 0.5 mM H_2PtCl_6 solution for a, d) 12 h, b, e) 24 h and c, f) 48 h and g) XRD patterns of Pt@Ag network on Pt/Ni substrate. The double layer capacitance of these samples is shown in Table 1. For the Pt distribution, see Fig. 5.

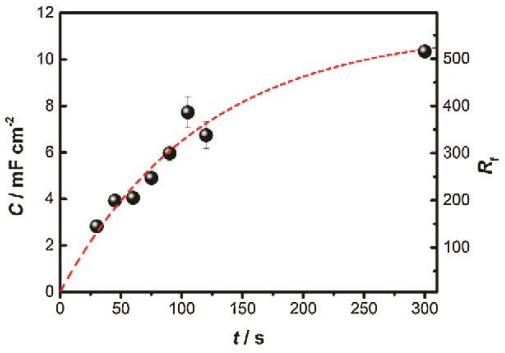

Fig. 4. The trend of double layer capacitance with increasing deposition time. For the SEM images, see Fig. 2.

formed in deposition times ranging from 30 s to 120 s. The inserted scanning laser microscope images depict the enlargement of the Ag structure height with increasing deposition time. The Ag networks exhibit a graded porosity, with small pores close to the substrate surface and larger pores on top. With increasing deposition time, the porous network gains height and the walls of the structure become thicker. The higher magnification images (Fig. 2**e–h**) display dendritic crystals at deposition times of 30 s and 60 s, while the walls of the network become denser. Additionally, the pore diameter increases with deposition time. This observation is consistent with the results of Cherevko et al., who used a higher current density of $-1\,A\,cm^{-2}$ for the Ag deposition. [27]

In addition, Fig. 3outlines a rise of the double layer capacitance C of the Ag networks from $2.7\,mF\,cm^{-2}$ at a 30 s deposition time to $6.4\,mF\,cm^{-2}$ for a 120 s deposition time, please find the corresponding cyclic voltammograms in the supplementary information. Compared to the double layer capacitance of a polished Ag plate ($C_{theo} = 0.02\,mF\,cm^{-2}$), an enlargement of the surface area by a factor up to $R_f = 320$ was achieved, which is in good accordance with the relevant literature. [36] The measured C data can be fitted accordingly by means of an exponential growth function $C(t) = C_{max} \cdot (1\text{-}\exp(-k \cdot t))$ between deposition times of 30 s and 120 s. According to this function, a maximum double layer capacitance of $C_{max} \approx 11.3\,mF\,cm^{-2}$ is to be expected. Consequently, the increase of the double layer capacitance with the deposition time in an unstirred solution is non-linear, because of the diffusion-controlled process of the Ag deposition. For a reference sample, prepared with a deposition time of 300 s, a double layer capacitance of $C = 10.4\,mF\,cm^{-2}$ was determined. This measurement confirms the predicted trend of the double layer capacitance for larger deposition times and approaches the theoretical maximum.

3.2. Galvanic replacement of porous Ag network with Pt

The deposited porous Ag networks with a deposition time of 105 s were subsequently functionalized with Pt by galvanic replacement reaction. For the Pt replacement, the Ag networks were immersed for 12 h, 24 h or 48 h in an unstirred 0.5 mM H_2PtCl_6 solution. The Pt replacement was observed optically via color change of the Ag network from gray to black. SEM images of the Pt functionalized Ag networks are shown in Fig. 4. On the bars and junctions, the formation of dendritic Pt structures can already be observed after 12 h. As the replacement time increases, thinner bars dissolve and Pt will preferably deposit at the junctions.

XRD patterns of the modified Pt@Ag networks are given in Fig. 3**g**. In addition to the reflections of the Ag network and the Pt/Ni substrate, the XRD patterns exhibit further reflections that increase in intensity at high replacement times and shift to higher angles compared to polycrystalline Pt. [48] Along with a Rietveld analysis (see supplementary information), this contraction of the Pt lattice can be assigned to the formation of Ag-Pt alloys such as Ag_1Pt_1. Therefore, it has to be assumed, that galvanic replacement leads to the formation of Ag-Pt alloys of different compositions.

For a more consolidated investigation of the Pt@Ag networks, SEM cross-section images after 12 h replacement were taken (Fig. 5**a–d**). The cross-section generally confirms high porosity within the network. Images taken with back scattered electron contrast (Fig. 5**b**) reveal a Pt film at the top of the Ag network. Elemental mapping confirms these results and in addition the lack of Pt inside the Ag network. This is most probably due to diffusion-induced inhibition of the galvanic replacement within the porous Ag structure. After the consumption of the infiltrated Pt precursor solution by the galvanic replacement reaction, further Pt precursor, supplied by diffusion, deposit mainly on top of the network. In the

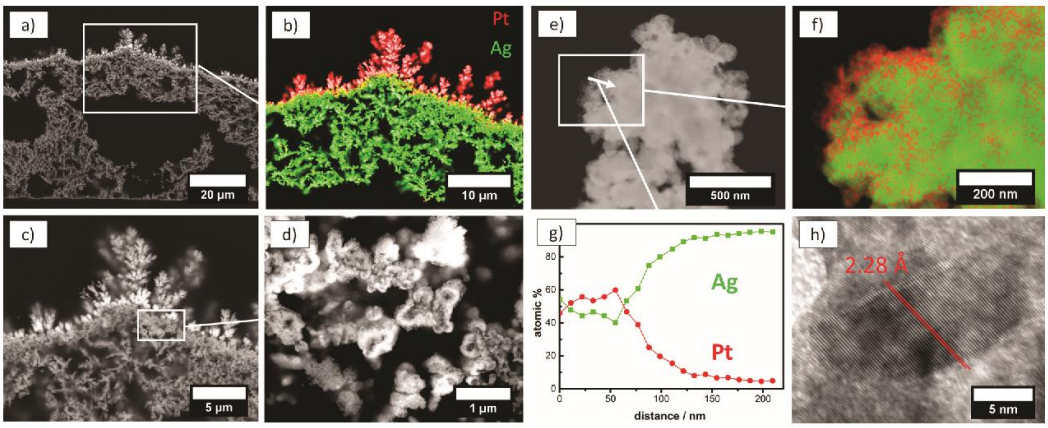

Fig. 5. a) Cross-section SEM image with backscattered electron contrast of exchanged Ag network in 0.5 mM H_2PtCl_6 solution for 12 h b) corresponding elemental mapping (red = Pt, green = Ag), c-d) cross-section SEM images of exchanged Ag network in 0.5 mM H_2PtCl_6 solution for 12 h, e) TEM image of a particle from the Ag-Pt boundary surface, f) elemental mapping (red = Pt, green = Ag), g) EDXS line profile and h) HRTEM image of near-edge particle. The top view SEM image of this sample is given in Fig. 3.

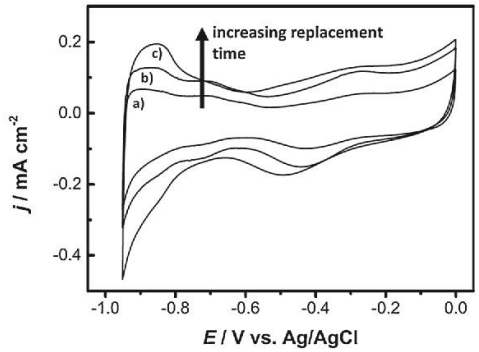

Fig. 6. Cyclic voltammogram of Pt@Ag networks for different Pt replacement times with 0.5 mM H_2PtCl_6 solution for 12 h (a), 24 h (b) and 48 h (c) in N_2-saturated 0.1 M NaOH solution with a sweep rate of 1 mV s^{-1}. The corresponding SEM images are shown in Fig. 3 as a, b and c.

Table 1
Double layer capacitance C and transferred charge Q after 12 h, 24 h and 48 h replacement within the reaction $4Ag + Pt^{4+} \rightarrow 4Ag^{+} + Pt$ and the resulting values for R_f and Φ. For the corresponding SEM images, see Fig. 3.

	C/ mF cm^{-2}	R_f	Q/ mC cm^{-2}	Φ
Ag network after 105 s deposition	7.7	385	–	–
12 h replacement	42.8	2138	11.95	56.9
24 h replacement	71.0	3550	17.98	85.6
48 h replacement	91.0	4550	20.07	95.6

interface between the porous Ag network and the deposited Pt film (Pt@Ag interface, Fig. 5**b** yellow area), non-dendritic Ag aggregates with particular Pt coating can be identified. For further analysis, TEM images of Pt@Ag particles were taken at the Pt@Ag interface (Fig. 5**e**) and inside the Ag network as well as from the dendritic Pt film on top of the Ag network (see supplementary information). The analyzed particles from inside the porous Ag network highlight isolated spots of filigree grown Pt, confirming that only an initial replacement with the infiltrated H_2PtCl_6 solution has taken place. Particles from the above-grown Pt film exhibit dendritic Pt structures.

The particle composition within the Pt@Ag interface was examined via elemental mapping and profiling by EDXS (Fig. 5**f-g**). The elemental mapping shows Ag particles coated with a thin Pt film (Fig. 5f). The line profile confirms a composition of about Pt:Ag 55:45 at the rim, while in the core of the particle almost no Pt is found (Fig. 5**g**). This finding is in complete accordance with our conclusions on the formation of Ag-Pt alloys such as Ag_1Pt_1 from XRD patterns and Rietveld analysis. A HRTEM image (Fig. 5**h**) displays the lattice planes of a particle near the Pt@Ag interface. The lattice plane distance was determined and averaged over several sites and amounts to $d = 2.28$ Å. This value is very close to the theoretical lattice plane distance of Pt $d_{Pt(111)} = 2.27$ Å [48], but it is slightly shifted to the higher lattice plane distance of Ag_1Pt_1 $d_{Ag1Pt1(111)} = 2.30$ Å. [49] The lattice plane distance of pure Ag with $d_{Ag(111)} = 2.36$ Å [48] is markedly wider than that of pure Pt. As a result of the Pt replacement, both, pure Pt phases on top of the network and mainly Ag_1Pt_1 with traces of other Ag-Pt alloys were detected in the Pt@Ag interface, while within the network only a few isolated Pt sites are present.

The Pt@Ag porous networks were then further characterized by cyclic voltammetry. The cyclic voltammograms (Fig. 6) show typical Pt signals. In the range from -0.75 V to -0.95 V, the hydrogen reduction and oxidation on Pt can be observed. The formation/reduction of Pt oxide and Pt hydroxide occurs at the potential range of -0.5 V to 0 V. Due to the formation of dendritic Pt film on top of the Ag network, the Ag surface sites are blocked and the adsorption signals of the OH^- ions on the Ag surface will be reduced. The double layer capacitance C compared to a Ag network increases by a factor of about 12 for a 48 h replacement and the transferred charge increases up to $\Phi = 95.6$, see Table 1. According to the findings in elemental mapping, the relatively low roughness factor is related to the Pt growing mainly on top of the porous Ag network. Our roughness factor is consistent with that of Hu et al., measuring high-surface-area porous platinum electrodes prepared by atomic layer deposition ($\Phi \approx 130$ for layers with 5 μm thickness). [50] While galvanic replacement only takes place on

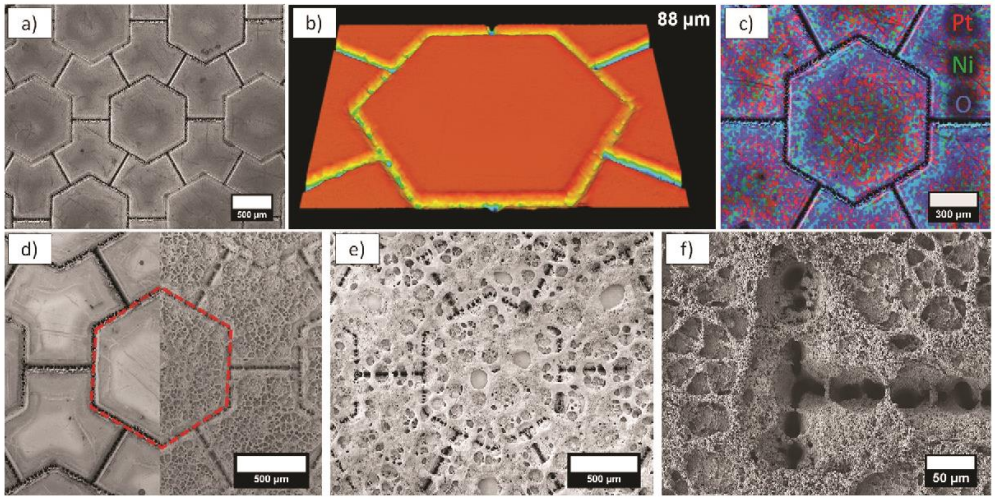

Fig. 7. a) SEM, b) scanning laser microscope and c) elemental mapping (red = Pt, green = Ni, blue = O) images of a laser structured Pt/Ni substrate, the hexagonal structure consist of 88 μm deep cuts. d) SEM images of a laser structured Pt/Ni substrate before and after Ag deposition for 30 s and e) for 120 s. f) SEM image of the porous walls formed alongside the engraved structure.

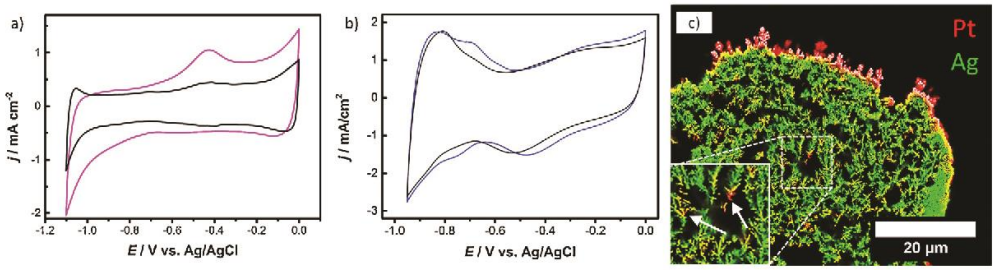

Fig. 8. a) Cyclic voltammogram of 105 s Ag deposition on non-structured Pt/Ni substrate (black), deposition on a laser structured Pt/Ni substrate (magenta) in N_2-saturated 0.1 M NaOH solution at room temperature with a sweep rate of 50 mV s^{-1}, b) cyclic voltammogram of 48 h Pt replacement in 0.5 mM H_2PtCl_6 solution of 105 s network on non-structured Pt/Ni substrate (black) and on a laser structrured Pt/Ni (blue) in N_2-saturated 0.1 M NaOH solution at room temperature with a sweep rate of 10 mV s^{-1}, c) elemental mapping of the Ag network after 48 h of Pt replacement prepared on laser structured Pt/Ni substrate. Pt deposition within the porous Ag network can be observed. For comparison, elemental mapping of a Pt@Ag network at a non-structured Pt/Ni substrate is shown in Fig. 5**b**.

top of the porous network, the resulting Pt film corresponds to a thickness of a few µm (see Fig. 5**b**). An extension of the galvanic replacement into the whole porous Ag network could further increase the amount of active Pt sites and we would expect Φ approaches R_f.

We analyzed the porous Ag networks and Pt@Ag networks with Kr-BET to determine the microscopic surface area of the networks. Therefore, we prudently scratched the deposited networks form the substrates and measured the obtained powders, which have specific surface areas of about 2–3 $m^2 g^{-1}$. Typically surface areas of porous platinum electrodes are 7–30 $m^2 g^{-1}$ [51–54] in size. We contribute the low surface area of our networks to the large primary crystal size of about 300 nm. Nevertheless, the mass dependence of the BET surface area presents a problem for the comparison of different metal networks.

3.3. Preparation of graded porous Ag networks on laser structured substrates

In order to improve the galvanic Pt replacement and the general mass transport within the Ag network, laser structuring of the electrode could represent a potent tool. Therefore, Ag networks were deposited on Pt/Ni substrates previously modified by laser structuring. For this purpose, the Ni plates were engraved with a hexagonal structure by an ultra-short pulse laser. The hexagons consist of 600 µm long and 100 µm wide cuts as displayed in Fig. 7**a**. The depth of the structured regions was determined by scanning laser microscopy and was about 90 µm (Fig. 7**b**). During the laser structuring process, the sputtered Pt layer is removed by evaporation and the Ni is selectively oxidized in the irradiated area (Fig. 7**c**). Due to the selective ablation of Pt and the formation of non-conducting NiO in the cuts, a strong inhibition of hydrogen evolution and Ag deposition occurs. The surface modification leads to a growth of the Ag network around the cuts (Fig. 7**d,e**). For a deposition time of 120 s, the Ag network forms bridges across the cuts. But the engraved hexagonal structure is not filled with Ag so it can be seen through the deposited Ag network.

The Ag networks deposited on the laser structured Pt/Ni substrates were electrochemically characterized. The obtained cyclic voltammograms (Fig. 8**a)** are close to the ones of the Ag networks on non-structured substrates. In general, the double layer capacitance C can be enhanced by laser structuring, although non-conducting NiO has formed. Even for a deposition time of 30 s, the double layer capacitance C increases from about 2.6 mF cm^{-2} (blank) to about 5.8 mF cm^{-2} (laser structured), see supplementary information. For 105 s deposition time, the double layer capacitance C increases from about 7.5 mF cm^{-2} to about 13 mF cm^{-2}. This increase in C can be explained by the porous walls which formed alongside the cuts on the substrate as exhibited in Fig. 7**f**.

3.4. Galvanic Pt replacement of porous Ag networks on laser structured substrates

Afterwards, the Ag network on laser structured Pt/Ni substrates with a deposition time of 105 s was functionalized with Pt via galvanic replacement and electrochemically characterized.

The obtained cyclic voltammogram of the Pt@Ag network on a laser structured Pt/Ni substrate is similar to the Pt@Ag network on a non-structured plate after the same replacement time (Fig. 8**b**). The double layer capacitance slightly increases from C = 91.0 mF cm^{-2} to C = 94.5 mF cm^{-2}. In the transferred charge, a rise to Q = 25.2 mC cm^{-2} occurs, which corresponds to a roughness factor of Φ = 120. The determined roughness factor is about 25 % higher compared to the Pt@Ag network on a non-structured Pt/Ni substrate. This increase is related to the improvement of the galvanic replacement reaction within the porous network by means of the laser structuring. The SEM cross-section image and elemental mapping of the Pt@Ag network on a laser structured substrate are displayed in Fig. 8**c**. In contrast to the Pt@Ag network at non-structured Pt/Ni substrate (Fig. 5**b**), the elemental mapping exhibits several Pt sites (red and yellow spots) within the porous Ag network in addition to the dendritic Pt particles on top of the Ag network. It might be reasonably assumed that, there exists a promoting effect between the substrate's structuring and the improvement of the galvanic replacement reaction resulting in an increase of exposed Pt sites.

As a result of the laser structuring of the substrate, the deposition of the porous network and consequently the functionalization of the network with Pt by galvanic replacement can be tuned.

4. Conclusions

We present a new way of preparing Pt-modified Ag electrodes with high double layer capacitance by directed deposition on laser structured substrates. First, a macro porous Ag network on Pt/Ni substrates is formed by dynamic hydrogen template deposition (DHTD), which was subsequently functionalized with Pt by galvanic replacement. Despite the high porosity of the formed Ag networks, Pt is predominantly deposited on top of the network. Within the network, only deposition of the initially infiltrated Pt solution occurs. The particles at the Pt@Ag interface consist of a Ag core surrounded by Pt. At the Pt@Ag interface, formations of Ag-Pt alloys such as Ag_1Pt_1 can be encountered as well. The Pt@Ag

networks exhibit an increase in the double layer capacitance C up to $R_f = 4550$. The amount of active Pt sites within the Pt@Ag networks is about 96 times higher compared to a smooth polycrystalline Pt surface.

Secondly, it is demonstrated that prior structuring of the substrate with a pulsed laser beam can influence the formation of the pore structure of the Ag network prepared by dynamic hydrogen template deposition. This manner of laser structuring can facilitate the mass transport in the porous system and thus the galvanic replacement reaction of the Ag network, coherently increasing the roughness factor of the Pt@Ag network up to 25 %.

Acknowledgements

This work was done within the framework of the NTH Research Group ElektroBak organized by Uwe Schröder (TU Braunschweig) and financed by the German state of Lower Saxony. Furthermore, we thank LPKF AG for the laser structuring, the technical expertise and general support.

Appendix A. Supplementary data

Supplementary data associated with this article can be found, in the online version, at http://dx.doi.org/10.1016/j.electacta.2017.08.174.

References

[1] C.M. Parlett, K. Wilson, A.F. Lee, Hierarchical porous materials: Catalytic applications, Chemical Society Reviews 42 (2013) 3876–3893, doi:http://dx.doi.org/10.1039/c2cs35378d.
[2] B. Dunn, F. Bonet, L. Noailles, P. Tang, Using Mesoporous Nanoarchitectures to Improve Battery Performance Electrochemical Properties of Vanadium Oxide Aerogels, Los Angeles (2005) ch046, doi:http://dx.doi.org/10.1021/bk-2005-0890.
[3] A. Walcarius, Template-directed porous electrodes in electroanalysis, Analytical and Bioanalytical Chemistry 396 (2010) 261–272, doi:http://dx.doi.org/10.1007/s00216-009-3069-1.
[4] M.K. Debe, Electrocatalyst approaches and challenges for automotive fuel cells, Nature 486 (2012) 43–51, doi:http://dx.doi.org/10.1038/nature11115.
[5] Y. Li, B.P. Bastakoti, V. Malgras, C. Li, J. Tang, J.H. Kim, Y. Yamauchi, Polymeric Micelle Assembly for the Smart Synthesis of Mesoporous Platinum Nanospheres with Tunable Pore Sizes, Angewandte Chemie (Int. Ed.) 54 (2015) 11073–11077, doi:http://dx.doi.org/10.1002/anie.201505232.
[6] L. Wang, Y. Yamauchi, Metallic Nanocages: Synthesis of Bimetallic Pt-Pd Hollow Nanoparticles with Dendritic Shells by Selective Chemical Etching, Journal of the American Chemical Society 135 (2013) 16762–16765, doi:http://dx.doi.org/10.1021/ja407773x.
[7] V. Malgras, H. Ataee-Esfahani, H. Wang, B. Jiang, C. Li, K.C. Wu, J.H. Kim, Y. Yamauchi, Nanoarchitectures for Mesoporous Metals, Advanced Materials 28 (2016) 993–1010, doi:http://dx.doi.org/10.1002/adma.201502593.
[8] C. Li, B. Jiang, Z. Wang, Y. Li, S.A. Hossain, J.H. Kim, T. Takei, J. Henzie, Ö. Dag, Y. Bando, Y. Yamauchi, First Synthesis of Continuous Mesoporous Copper Films with Uniformly Sized Pores by Electrochemical Soft Templating, Angewandte Chemie (Int. Ed.) 55 (2016) 12746–12750, doi:http://dx.doi.org/10.1002/anie.201606031.
[9] S.C. Warren, L.C. Messina, L.S. Slaughter, M. Kamperman, Q. Zhou, S.M. Gruner, F.J. DiSalvo, U. Wiesner, Ordered Mesoporous Materials from Metal Nanoparticle −Block Copolymer Self-Assembly, Science 320 (2008) 1748–1753, doi:http://dx.doi.org/10.1126/science.1159950.
[10] Y.H. Lee, W. Shi, H.K. Lee, R. Jiang, I.Y. Phang, Y. Cui, L. Isa, Y. Yang, Nanoscale surface chemistry directs the tunable assembly of silver octahedra into three two-dimensional plasmonic superlattices, Nature Communications 6 (2015) 1–7, doi:http://dx.doi.org/10.1038/ncomms7990.
[11] J. Wu, J. Zhang, Z. Peng, S. Yang, F.T. Wagner, Truncated Octahedral Pt3Ni Oxygen Reduction Reaction Electrocatalysts, Journal of the American Chemical Society (2010) 4984–4985, doi:http://dx.doi.org/10.1021/ja100571h.
[12] B. Lim, M. Jiang, P.H.C. Camargo, E.C. Cho, J. Tao, X. Lu, Y. Zhu, Y. Xia, Pd-Pt Bimetallic Nanodendrites with High Activity for Oxygen Reduction, Science 324 (2009) 1302–1305, doi:http://dx.doi.org/10.1126/science.1170377.
[13] A. Freund, J. Lang, T. Lehmann, K.A. Starz, Improved Pt Alloy Catalysts for Fuel Cells, Catalysis Today 27 (1996) 279–283, doi:http://dx.doi.org/10.1016/0920-5861(95)00210-3.
[14] J. Zhang, M.B. Vukmirovic, K. Sasaki, A.U. Nilekar, M. Mavrikakis, R.R. Adzic, Mixed-metal Pt monolayer electrocatalysts for enhanced oxygen reduction kinetics, Journal of the American Chemical Society 127 (2005) 12480–12481, doi:http://dx.doi.org/10.1021/ja053695i.
[15] J. Zhang, Y. Mo, M.B. Vukmirovic, R. Klie, K. Sasaki, R.R. Adzic, Platinum monolayer electrocatalysts for O2 reduction: Pt monolayer on Pd(111) and on carbon-supported Pd nanoparticles, Journal of Physical Chemistry B 108 (2004) 10955–10964, doi:http://dx.doi.org/10.1021/jp0379953.
[16] C. Wang, G. Wang, D. van der Vliet, K.-C. Chang, N.M. Markovic, V.R. Stamenkovic, Monodisperse Pt(3)Co nanoparticles as electrocatalyst: the effects of particle size and pretreatment on electrocatalytic reduction of oxygen, Physical Chemistry Chemical Physics: PCCP 12 (2010) 6933–6939, doi:http://dx.doi.org/10.1039/c000822b.
[17] P. Mani, R. Srivastava, P. Strasser, Dealloyed Pt-Cu core-shell nanoparticle electrocatalysts for use in PEM fuel cell cathodes, Journal of Physical Chemistry C 112 (2008) 2770–2778, doi:http://dx.doi.org/10.1021/jp0776412.
[18] S.T. Bliznakov, M.B. Vukmirovic, L. Yang, E.A. Sutter, R.R. Adzic, Pt Monolayer on Electrodeposited Pd Nanostructures: Advanced Cathode Catalysts for PEM Fuel Cells, Journal of the Electrochemical Society 159 (2012) F501–F506, doi:http://dx.doi.org/10.1149/2.006209jes.
[19] D. Van Der Vliet, C. Wang, M. Debe, R. Atanasoski, N.M. Markovic, V.R. Stamenkovic, Platinum-alloy nanostructured thin film catalysts for the oxygen reduction reaction, Electrochimica Acta 56 (2011) 8695–8699, doi:http://dx.doi.org/10.1016/j.electacta.2011.07.063.
[20] R. Imbeault, A. Pereira, S. Garbarino, D. Guay, Oxygen Reduction Kinetics on Pt x Ni100-x Thin Films Prepared by Pulsed Laser Deposition, Journal of The Electrochemical Society 157 (2010) B1051–B1058, doi:http://dx.doi.org/10.1149/1.3428363.
[21] B.J. Plowman, L.A. Jones, S.K. Bhargava, Building with bubbles: the formation of high surface area honeycomb-like films via hydrogen bubble templated electrodeposition, Chemical Communications 51 (2015) 4331–4346, doi:http://dx.doi.org/10.1039/C4CC06638C.
[22] H.C. Shin, J. Dong, M. Liu, Nanoporous Structures Prepared by an Electrochemical Deposition Process, Advanced Materials 15 (2003) 1610–1614, doi:http://dx.doi.org/10.1002/adma.200305160.
[23] C.A. Marozzi, A.C. Chialvo, Development of electrode morphologies of interest in electrocatalysis. Part 1: Electrodeposited porous nickel electrodes, Electrochimica Acta 45 (2000) 2111–2120, doi:http://dx.doi.org/10.1016/S0013-4686(99)00422-3.
[24] J.-H. Jeun, D.-H. Kim, S.-H. Hong, Synthesis of porous SnO2 foams on SiO2/Si substrate by electrochemical deposition and their gas sensing properties, Sensors and Actuators B: Chemical 161 (2012) 784–790, doi:http://dx.doi.org/10.1016/j.snb.2011.11.033.
[25] P.-C. Hsu, S.-K. Seol, T.-N. Lo, C.-J. Liu, C.-L. Wang, C.-S. Lin, Y. Hwu, C.H. Chen, L.-W. Chang, J.H. Je, G. Margaritondo, Hydrogen Bubbles and the Growth Morphology of Ramified Zinc by Electrodeposition, Journal of The Electrochemical Society 155 (2008) D400–D407, doi:http://dx.doi.org/10.1149/1.2894189.
[26] W. Huang, L. Fu, Y. Yang, S. Hu, C. Li, Z. Li, Simultaneous Fabrications of Nanoparticles and 3D Porous Films of Sn or Pb from Pure Electrodes, Electrochemical and Solid-State Letters 13 (2010) K46–K48, doi:http://dx.doi.org/10.1149/1.3339058.
[27] S. Cherevko, X. Xing, C.H. Chung, Electrodeposition of three-dimensional porous silver foams, Electrochemistry Communications 12 (2010) 467–470, doi:http://dx.doi.org/10.1016/j.elecom.2010.01.021.
[28] C. Huang, Y.J. Li, C. Muangphat, Y. Hao, Electroless deposition of Au around electrochemically evolved hydrogen bubbles, Electrochimica Acta 56 (2011) 8319–8324, doi:http://dx.doi.org/10.1016/j.electacta.2011.07.002.
[29] J.H. Kim, R.H. Kim, H.S. Kwon, Preparation of copper foam with 3-dimensionally interconnected spherical pore network by electrodeposition, Electrochemistry Communications 10 (2008) 1148–1151, doi:http://dx.doi.org/10.1016/j.elecom.2008.05.035.
[30] Y. Li, W. Jia, Y. Song, X. Xia, Superhydrophobicity of 3D Porous Copper Films Prepared Using the Hydrogen Bubble Dynamic Template, Chemisty of Materials 19 (2007) 5758–5764, doi:http://dx.doi.org/10.1021/cm071738j.
[31] I. Najdovski, P. Selvakannan, S.K. Bhargava, A.P. O'Mullane, Formation of nanostructured porous Cu–Au surfaces: the influence of cationic sites on (electro)-catalysis, Nanoscale 4 (2012) 6298–6306, doi:http://dx.doi.org/10.1039/c2nr31409f.
[32] I. Najdovski, P. Selvakannan, A.P. O'Mullane, S.K. Bhargava, Rapid synthesis of porous honeycomb Cu/Pd through a hydrogen-bubble templating method, Chemistry – A European Journal 17 (2011) 10058–10063, doi:http://dx.doi.org/10.1002/chem.201101224.
[33] I. Najdovski, P. Selvakannan, A.P. O'Mullane, Electrochemical formation of Cu/Ag surfaces and their applicability as heterogeneous catalysts, RSC Advances 4 (2014) 7207–7215, doi:http://dx.doi.org/10.1039/c3ra47557c.
[34] J.B. Raoof, R. Ojani, A. Kiani, S. Rashid-Nadimi, Fabrication of highly porous Pt coated nanostructured Cu-foam modified copper electrode and its enhanced catalytic ability for hydrogen evolution reaction, International Journal of Hydrogen Energy 35 (2010) 452–458, doi:http://dx.doi.org/10.1016/j.ijhydene.2009.10.069.
[35] P. Shahbazi, A. Kiani, Nanoporous Ag and Pd foam: Redox induced fabrication using electrochemically deposited nanoporous Cu foam with no need to any additive, Electrochimica Acta 56 (2011) 9520–9529, doi:http://dx.doi.org/10.1016/j.electacta.2011.08.062.
[36] S. Cherevko, C.H. Chung, Impact of key deposition parameters on the morphology of silver foams prepared by dynamic hydrogen template deposition, Electrochimica Acta 55 (2010) 6383–6390, doi:http://dx.doi.org/10.1016/j.electacta.2010.06.054.

[37] E.C. Santos, M. Shiomi, K. Osakada, T. Laoui, Rapid manufacturing of metal components by laser forming, International Journal of Machine Tools & Manufacture 46 (2006) 1459–1468, doi:http://dx.doi.org/10.1016/j.ijmachtools.2005.09.005.
[38] J. de Boor, N. Geyer, J.V. Wittmann, U. Gösele, V. Schmidt, Sub-100 nm silicon nanowires by laser interference lithography and metal-assisted etching, Nanotechnology 21 (2010) 1–5, doi:http://dx.doi.org/10.1088/0957-4484/21/9/095302.
[39] M. Barberoglou, V. Zorba, E. Stratakis, E. Spanakis, P. Tzanetakis, S.H. Anastasiadis, C. Fotakis, Bio-inspired water repellent surfaces produced by ultrafast laser structuring of silicon, Applied Surface Science 255 (2009) 5425–5429, doi:http://dx.doi.org/10.1016/j.apsusc.2008.07.130.
[40] K. Lange, M. Schulz-Ruhtenberg, J. Caro, Platinum Electrodes for Oxygen Reduction Catalysis Designed by Ultrashort Pulse Laser Structuring, ChemElectroChem 4 (2016) 570–576, doi:http://dx.doi.org/10.1002/celc.201600630.
[41] J. Byskov-Nielsen, P. Balling, Laser structuring of metal surfaces: Micro-mechanical interlocking, Applied Surface Science 255 (2009) 5591–5594, doi:http://dx.doi.org/10.1016/j.apsusc.2008.07.118.
[42] P. Gečys, G. Račiukaitis, M. Gedvilas, a. Selskis, Laser structuring of thin-film solar cells on polymers, The European Physical Journal Applied Physics 46 (2009) 12508, doi:http://dx.doi.org/10.1051/epjap/2009029.
[43] R. Kohler, H. Besser, M. Hagen, J. Ye, C. Ziebert, S. Ulrich, J. Proell, W. Pfleging, Laser micro-structuring of magnetron-sputtered SnOx thin films as anode material for lithium ion batteries, Microsystem Technologies 17 (2011) 225–232, doi:http://dx.doi.org/10.1007/s00542-011-1259-1.
[44] M. Weikert, C. Fohl, F. Dausinger, Surface structuring of metals with ultrashort laser pulses, Thrid International Symposium on Laser Precision Microfabrication (2003) 501–505, doi:http://dx.doi.org/10.1117/12.486539.
[45] A.Y. Vorobyev, C. Guo, Femtosecond laser structuring of titanium implants, Applied Surface Science 253 (2007) 7272–7280, doi:http://dx.doi.org/10.1016/j.apsusc.2007.03.006.
[46] A. Schoonderbeek, V. Schütz, O. Haupt, U. Stute, Laser Processing of Thin Films for Photovoltaic Applications, Journal of Laser Micro/Nanoengineering 5 (2010) 1–8, doi:http://dx.doi.org/10.2961/jlmn.2010.03.0013.
[47] A. Pozio, M. De Francesco, A. Cemmi, F. Cardellini, L. Giorgi, Comparison of high surface Pt/C catalysts by cyclic voltammetry, J. Power Sources 105 (2002) 13–19, doi:http://dx.doi.org/10.1016/S0378-7753(01)00921-1.
[48] E. Jette, F. Foote, Prescision Determination of Lattice Constants, Journal of Chemical Physics 3 (1935) 605–616, doi:http://dx.doi.org/10.1063/1.1749562.
[49] X.-S. Yan, P. Lin, X. Qi, L. Yang, Finnis –Sinclair potentials for fcc Au –Pd and Ag –Pt alloys, International Journal of Material Research 102 (2011) 381–388, doi:http://dx.doi.org/10.3139/146.110488.
[50] Y. Hu, A. Yella, S. Guldin, M. Schreier, F. Stellacci, M. Grätzel, M. Stefik, High-surface-area porous platinum electrodes for enhanced charge transfer, Advanced Energy Materials 4 (2014) 1–8, doi:http://dx.doi.org/10.1002/aenm.201400510.
[51] J. Bett, J. Lundquist, E. Washington, P. Stonehart, Platinum Crystallite Size Considerations for Electrocatalytic Oxygen Reduction-I, Electrochimica Acta 18 (1973) 343–348, doi:http://dx.doi.org/10.1016/0013-4686(73)85002-9.
[52] M. Mohl, A. Kumar, A. Leela, M. Reddy, A. Kukovecz, Z. Konya, I. Kiricsi, R. Vajtai, P.M. Ajayan, Synthesis of Catalytic Porous Metallic Nanorods by Galvanic Exchange Reaction, Journal of Physical Chemistry C 114 (2010) 389–393, doi:http://dx.doi.org/10.1021/jp9083508.
[53] G.S. Attard, Mesoporous Platinum Films from Lyotropic Liquid Crystalline Phases, Science 278 (1997) 838–840, doi:http://dx.doi.org/10.1126/science.278.5339.838.
[54] J. Xie, Q. Zhang, W. Zhou, J.Y. Lee, D.I.C. Wang, Template-Free Synthesis of Porous Platinum Networks of Different Morphologies, Langmuir 25 (2009) 6454–6459, doi:http://dx.doi.org/10.1021/la900037g.

Supplementary information

The XRD patterns (**S1a**) of the deposited Ag networks confirm the polycrystalline Ag (fcc) phase on top of the Pt/Ni substrate. As the deposition progresses, a decrease in the Ni and an increase in the Ag reflection intensity can be detected, which is due to the higher and denser Ag networks on the substrate. The 10 nm Pt layer sputtered on the Ni substrate could not be identified in the XRD patterns due to the low sensitivity of the XRD method.

In the course of the electrochemical characterization, cyclic voltammograms were measured in N_2-saturated 0.1 M NaOH solution (**S1b**). The recorded voltammograms exhibit three pairs of characteristic asymmetric peaks in the anodic and cathodic section. The peaks between -0.5 V and 0.4 V are related to the adsorption of OH^- ions on the Ag surface, which is based on a two-step process: first the adsorption of OH^- at the Ag surface, followed by the formation of an Ag-OH monolayer. In the potential region of -0.2 V to 0 V, the initial formation of Ag oxide takes place.

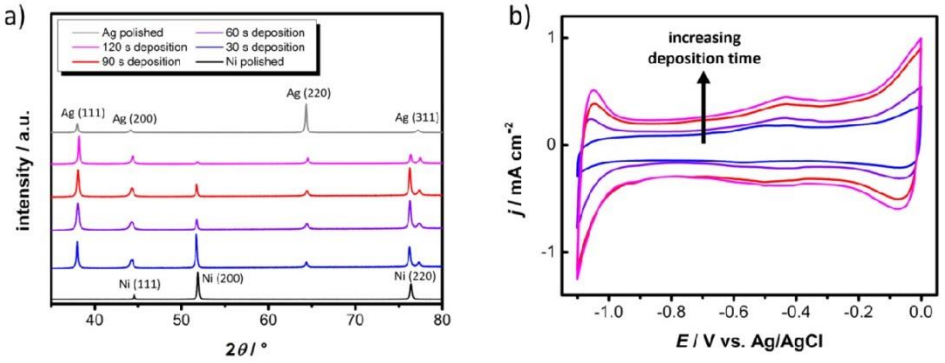

S1: a) XRD patterns of polished Ni plate, Ag networks after 30 s, 60 s, 90 s and 120 s deposition and polished Ag plate, b) cyclic voltammograms of Ag networks after 30 s (blue), 60 s (violet), 90 s (red) and 120 s (magenta) deposition time in N_2-saturated 0.1 M NaOH solution at room temperature with a sweep rate of 50 mV s^{-1}.

S2 shows the performed Rietveld analysis of the XRD patterns of Pt@Ag network, determined with pure Pt and with pure Pt and Ag_1Pt_1 alloy, respectively. It can be seen, that only including alloys such as Ag_1Pt_1 lead to a good accordance of the reflexes obtained at $2\theta = 40.3°$. The Goodness of Fit (GOF) including Ag_1Pt_1 and pure Pt is about GOF = 2.64 compared to pure Pt GOF = 3.18.

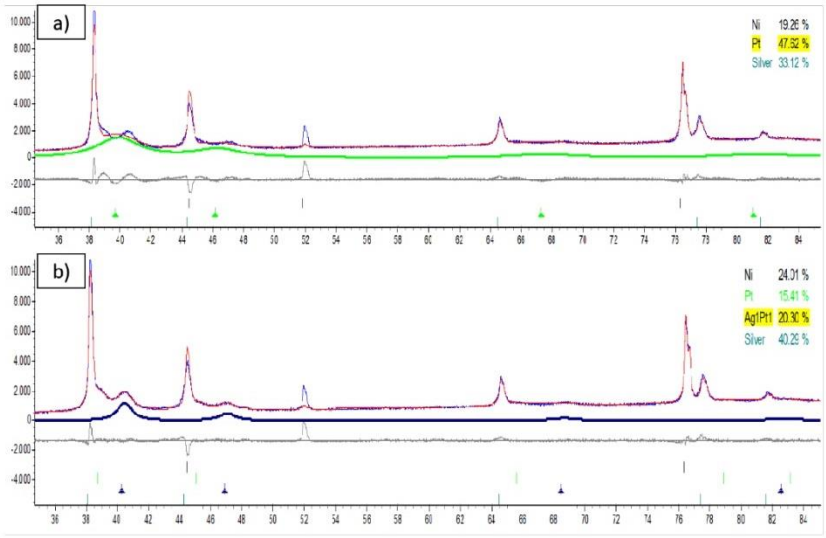

S2: Performed Rietveld analysis of XRD patterns of Pt@Ag network a) with pure Pt phase and b) with pure Pt phase and Ag_1Pt_1 alloy.

S3 shows the TEM image and EDXS mapping of a particle within the porous Pt@Ag network. Here, the dendritic Ag structure can be seen. The EDXS mapping confirms, that only Ag can be found since the galvanic replacement was strongly inhibited. An initial replacement of the infiltrated solution is illustrated by an isolated spot of filigree grown Pt on the particle. The obtained Cu signals are related to the TEM grid containing the measured sample.

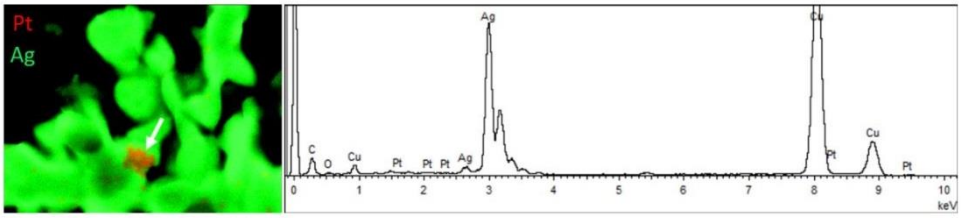

S3: EDXS mapping (red = Pt, green = Ag) of Particles from inside the porous Ag network after galvanic replacement.

S4 shows the TEM image and EDXS of a particle from the deposited Pt film on top of the porous Ag network. The EDXS confirms, that only pure Pt phase deposited on top of the network. The Cu signals are accordingly related to the TEM grid.

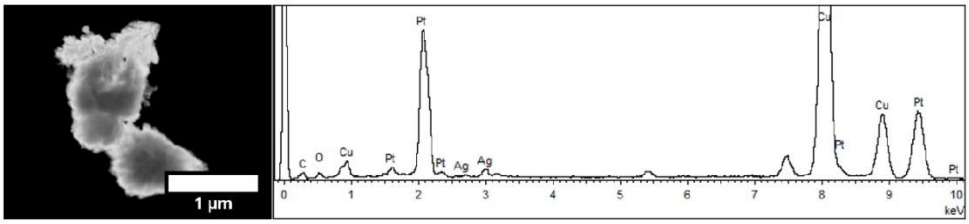

S4: TEM image and EDXS of particle from the Pt film deposited on top of the porous Ag network.

S5 shows the cyclic voltammograms of Ag networks deposited at laser structured substrates compared to a non-structured substrate. The double layer capacitance C increases from about 2.6 mF cm^{-2} without laser structuring to about 5.8 mF cm^{-2} for structure 2.

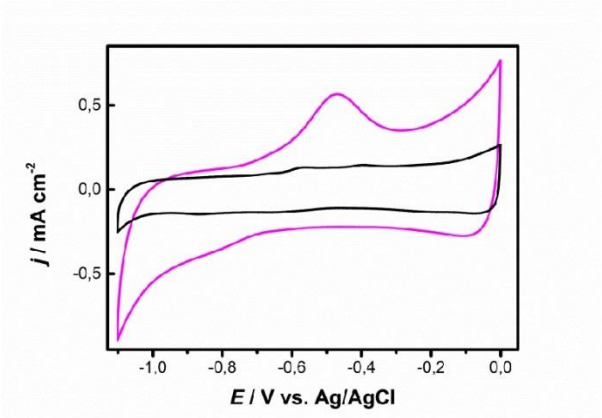

S5: Cyclic voltammograms of 30 s Ag deposition on non-structured Pt/Ni substrate (black) and on a laser structured Pt/Ni substrate (magenta) in N_2-saturated 0.1 M NaOH solution at room temperature with a sweep rate of 50 mV s^{-1}

5 Conclusions & Outlook

Structuring electrodes with ultrashort laser pulses can provide surface structures with large surface area and high catalytic activity towards electrochemical reactions.

The present work showcased that an ultrashort pulse laser is a promising tool to modify metal electrodes with laser-induced surface structures, e.g. LIPSS, CLPs and black metal, in order to increase the accessible surface area of the electrode for electrochemical reactions. This work provides the first systematic study of the surface area enlargement using laser-induced surface structures examined on platinum electrodes. For the black metal structure type, cyclic voltammetry displays surface area enlargement factors of up to 1500 in comparison with a polished platinum surface.

Transferring of the laser structuring method causing the black metal structure to non-noble metals, especially to nickel, required inert gas atmosphere during the structuring process in order to prevent oxidation.

Further development of the structuring method on nickel electrodes led to the discovery of the laser-induced nano-foam (LINF), a new laser-induced structure type. Contrary to other laser ablation processes the generation of the LINF structure uses the base material very efficiently by re-positioning of ablated nanoparticles to a porous network. By changing one particular laser parameter, the surface area of the LINF structure can be adjusted up to a roughness factor of 1600. The large accessible surface area and the excellent pseudocapacitive properties of LINF-modified Ni/NiO electrodes demonstrate the great potential of such LINF structures for charge storage in supercapacitor devices. The modification of nickel electrodes with LINF boosts the electrode's capacity to 2 C cm^{-2} or 5.56 Ah m^{-2}.

Ultrashort pulse laser structuring offers more than a simple enlargement of the accessible surface area of electrodes. The rapid heating and cooling rates in the structuring process cause a wide range of structural defects in the resulting surface structures. This work demonstrates on spiky Ni/NiO microstructures (CLPs) the combination of surface area enlargement and increasing defect density, which boosts the catalytic activity towards the OER. The laser-induced structural defects facilitate the formation of β-NiOOH, the highly active precursor stage of the OER. Furthermore, the wettability of the electrodes improves dramatically during electrochemical treatment due to the favored formation of NiOOH species on the

surface of the CLPs. This results in faster oxygen bubble detachment at industrial applied current densities.

By irradiating only a region of the electrode, non-noble electrode materials can be locally oxidized by the laser beam. The formation of an oxide layer in the irradiated region results in lower electrical conductivity and in some cases in lower catalytic activity. Ultrashort pulse lasers are therefore the only tool that enables full customization of the electrode design due to their ability to activate or deactivate specific regions of an electrode.

However, a lot of research needs to be done to reveal the full potential of ultrashort pulse laser structuring for electrochemical purposes. One critical aspect is the long processing time of the laser structuring process. To speed up the process the average power of the ultrashort pulse lasers needs to be increased. Currently the FRAUNHOFER ILT is developing a 10 kW ultrashort pulse laser system, which will be the most powerful system in the industry. For instance, a 10 W laser processes 1 cm^2 of the porous LINF structure in 21 min. With a 10 kW laser system 1 cm^2 could be structured theoretically in only 1.26 s. This makes the average power of the ultrashort pulse laser systems the key factor to exploit new industrial applications such as electrode structuring.

Experiments, not discussed in this work, confirm that the LINF structure could also be generated on the nonmetal electrode material glassy carbon. Glassy carbon is a carbon form with a highly disordered graphite structure, which exhibits high hardness, low density, low electrical resistance and high chemical resistance. Those properties make glassy carbon an excellent electrode material. LINF structures on glassy carbon enlarged the surface area by extraordinary high roughness factors of over 10000. However, LINF structures on glassy carbon showed stability issues. Therefore, only areas of about 0.25 cm^2 were modified with LINF.

LINF structure on nickel could be a promising porous substrate candidate to be coated with a very thin layer of noble metal, resulting in a cost efficient and highly active electrode. Coating experiments of the Ni LINF structure with platinum were performed by galvanic replacement of Ni with Pt as well as by chemical vapor deposition (CVD) of a gaseous Pt precursor. As a result, platinum was mainly deposited on top of the LINF structure. In order to obtain a complete Pt coating even within the LINF structure, further optimizations of the coating processes are required.

In this work, the special role of gas bubble detachment in gas evolving electrochemical reactions, e. g. OER, was discussed. In order to enhance the bubble release from porous electrodes hydrophobic islands can act as preferential nucleation sites for gas bubbles. [188] The size of the nucleation sites determines the bubble size at detachment and thus the bubble detachment rate. CLPs can be generated with hydrophobic properties. Therefore, they are promising candidates to generate preferential gas bubble nucleation sites on porous electrodes, effectively removing the produced gas while leaving the pores bubble-free.

Hopefully, this work will inspire others to use ultrashort pulse lasers to develop new solutions in the field of electrocatalysis and energy storage. Fortunately, in 2017, the European Union has funded the project LASER4SURF (project number: 768636) within the Horizon 2020 research and innovation program in order to implement ultrashort pulse lasers for mass production of functionalized metallic surfaces.

6 List of References

[1] K. Zhu, X. Zhu, W. Yang, Application of in situ techniques for the characterization of NiFe based oxygen evolution reaction (OER) electrocatalysts, Angew. Chemie - Int. Ed. (2018). doi:10.1002/anie.201802923.

[2] I. Katsounaros, S. Cherevko, A.R. Zeradjanin, K.J.J. Mayrhofer, Oxygen electrochemistry as a cornerstone for sustainable energy conversion, Angew. Chemie - Int. Ed. 53 (2014) 102–121. doi:10.1002/anie.201306588.

[3] Bundesministerium für Wirtschaft und Energie (BMWi), Sechster Monitoring-Bericht zur Energiewende, Berlin, 2018. https://www.bmwi.de/Redaktion/DE/Publikationen/Energie/sechster-monitoring-bericht-zur-energiewende.pdf?__blob=publicationFile&v=29.

[4] M. Rinck, J. Richter, Die Energiewende handelbar machen, Sonderdruck 7303 Aus Ew 9. (2015) 34–35. https://www.eex.com/blob/7488/d0e3321f620ecd36f3b26fd5490d91b6/die-energiewende-handelbar-machen-data.pdf.

[5] D. Teichmann, W. Arlt, P. Wasserscheid, R. Freymann, A future energy supply based on Liquid Organic Hydrogen Carriers (LOHC), Energy Environ. Sci. 4 (2011) 2767–2773. doi:10.1039/c1ee01454d.

[6] S. Curtin, J. Gangi, Fuel Cell Technologies Market Report 2016, Washington, D.C, 2016. https://www.energy.gov/sites/prod/files/2017/10/f37/fcto_2016_market_report.pdf.

[7] Y. Aarakida, M. Watanabe, K. Higashimura, Tokyo 2020, 2018. https://tokyo2020.org/en/games/sustainability/data/20180425-sus-plan-2-EN.pdf.

[8] www.agora-energiewende.de (accessed 14 October 2018).

[9] E. Fabbri, A. Habereder, K. Waltar, R. Kötz, T.J. Schmidt, R. Kotz, T.J. Schmidt, Developments and perspectives of oxide-based catalysts for the oxygen evolution reaction, Catal. Sci. Technol. 4 (2014) 3800–3821. doi:10.1039/C4CY00669K.

[10] S. Marini, P. Salvi, P. Nelli, R. Pesenti, M. Villa, M. Berrettoni, G. Zangari, Y. Kiros, Advanced alkaline water electrolysis, Electrochim. Acta. 82 (2012) 384–391. doi:10.1016/j.electacta.2012.05.011.

[11] H. Gasteiger, N.M. Markovic, Just a Dream - or Future Reality?, Science 324 (2009) 48–49. doi:10.1126/science.1172083.

[12] B. V Tilak, B.E. Conway, High performance electrode materials for the hydrogen evolution reaction from alkaline media, Proc. Indian Acad. Sci. - Chem. Sci. 97 (1986) 359–393. doi:10.1007/BF02849200.

[13] T. Rauscher, C.I. Müller, A. Schmidt, B. Kieback, L. Röntzsch, Ni-Mo-B alloys as cathode material for alkaline water electrolysis, Int. J. Hydrogen Energy. 41 (2016) 2165–2176. doi:10.1016/j.ijhydene.2015.12.132.

[14] C.A. Marozzi, A.C. Chialvo, Development of electrode morphologies of interest in electrocatalysis. Part 1: Electrodeposited porous nickel electrodes, Electrochim. Acta. 45 (2000) 2111–2120. doi:10.1016/S0013-4686(99)00422-3.

[15] A.J. Smith, D.L. Trimm, The Preparation of Skeletal Catalysts, Annu. Rev. Mater. Res. 35 (2005) 127–142. doi:10.1146/annurev.matsci.35.102303.140758.

[16] G. Ou, P. Fan, H. Zhang, K. Huang, C. Yang, W. Yu, H. Wei, M. Zhong, H. Wu, Y. Li, Large-scale hierarchical oxide nanostructures for high-performance electrocatalytic water splitting, Nano Energy. 35 (2017) 207–214. doi:10.1016/j.nanoen.2017.03.049.

[17] H. Wang, H.-W. Lee, Y. Deng, Z. Lu, P.-C. Hsu, Y. Liu, D. Lin, Y. Cui, Bifunctional non-noble metal oxide nanoparticle electrocatalysts through lithium-induced conversion for overall water splitting, Nat. Commun. 6 (2015) 7261. doi:10.1038/ncomms8261.

[18] J. Bonse, S. V. Kirner, M. Griepentrog, D. Spaltmann, J. Krüger, Femtosecond Laser Texturing of Surfaces for Tribological Applications, Materials (Basel). 11 (2018) 1–19. doi:10.3390/ma11050801.

[19] J. Nitsch, M. Fischedick, Eine vollständig regenerative Energieversorgung mit Wasserstoff – Illusion oder realistische Perspektive?, in: Wasserstofftag-Essen, 2002: pp. 1–17.

[20] Wasserstoff–Energieträger der Zukunft, (2018). https://www.siemens.com/global/de/home/produkte/energie/erneuerbare-energien/hydrogen-solutions.html (accessed 6 September 2018).

[21] T. Pregger, D. Graf, W. Krewitt, C. Sattler, M. Roeb, S. Möller, Prospects of solar thermal hydrogen production processes, Int. J. Hydrogen Energy. 34 (2009) 4256–4267. doi:10.1016/j.ijhydene.2009.03.025.

[22] J.R. Rostrup-Nielsen, T. Rostrup-Nielsen, Large-scale Hydrogen Production, T. CATTECH. 6 (2002) 150–159. doi:10.1023/A:1020163012266.

[23] A.G. Stern, A new sustainable hydrogen clean energy paradigm, Int. J. Hydrogen Energy. 43 (2018) 4244–4255. doi:10.1016/j.ijhydene.2017.12.180.

[24] www.nrel.gov (accessed 10 November 2018).

[25] S.P. Cardoso, I.S. Azenha, Z. Lin, A.E. Rodrigues, C.M. Silva, S.P. Cardoso, I.S. Azenha, Z. Lin, Inorganic Membranes for Hydrogen Separation Inorganic Membranes for Hydrogen Separation, Sep. Purif. Rev. 47 (2018) 229–266. doi:10.1080/15422119.2017.1383917.

[26] P. Li, Z. Wang, Z. Qiao, Y. Liu, X. Cao, W. Li, J. Wang, S. Wang, Recent developments in membranes for efficient Hydrogen purification, J. Memb. Sci. 495 (2015) 130–168. doi:10.1016/j.memsci.2015.08.010.

[27] S. Sircar, T.C. Golden, Hydrogen and Syngas Production and Purification Technologies, John Wiley & Sons, New Jersey, USA, 2009. doi:10.1002/9780470561256.

[28] C.L. Reed, C.J. Kuhre, Hydrogen Production from Partial Oxidation of Residual Fuel Oil, in: Hydrog. Prod. Mark., 1980: pp. 95–121. doi:10.1021/bk-1980-0116.ch006.

[29] J.A. Bakked, R. Jensenb, B. Monsenb, O. Raanessb, A.N. Wrernesb, Thermal plasma process development in Norway, Pure Appl. Chem. 70 (1998) 1223–1228. doi:10.1351/pac199870061223.

[30] S.Z. Baykara, Hydrogen production by direct solar thermal decomposition of water, possibilities for improvement of process effciency, Int. J. Hydrogen Energy. 29 (2004) 1451–1458. doi:10.1016/j.ijhydene.2004.02.014.

[31] A. Becker, Chemiewirtschaft in Zahlen 2018, 2018.

[32] I. Moussallem, J. Jörissen, U. Kunz, S. Pinnow, T. Turek, Chlor-alkali electrolysis with oxygen depolarized cathodes: history, present status and future prospects, J. Appl. Electrochem. 38 (2008) 1177–1194. doi:10.1007/s10800-008-9556-9.

[33] D. Pletcher, X. Li, Prospects for alkaline zero gap water electrolysers for hydrogen production, Int. J. Hydrogen Energy. 36 (2011) 1–16. doi:10.1016/j.ijhydene.2011.08.080.

[34] M. Bodner, A. Hofer, V. Hacker, H2 generation from alkaline electrolyzer, WIREs Energy Env. 4 (2015) 365–381. doi:10.1002/wene.150.

[35] H. Yu, J. Tian, F. Chen, P. Wang, X. Wang, Synergistic Effect of Dual Electron-Cocatalysts for Enhanced Photocatalytic Activity: rGO as Electron-Transfer Mediator and Fe(III) as Oxygen-Reduction Active Site, Sci. Rep. 5 (2015) 13083. doi:10.1038/srep13083.

[36] S.J.A. Moniz, S.A. Shevlin, D.J. Martin, Z.-X. Guob, J. Tang, Visible-Light Driven Heterojunction Photocatalysts for Water Splitting – A Critical Review, Energy Environ. Sci. 8 (2015) 731–759. doi:10.1039/c4ee03271c.

[37] Y. Goto, T. Hisatomi, Q. Wang, T. Higashi, K. Ishikiriyama, T. Maeda, Y. Sakata, S. Okunaka, H. Tokudome, M. Katayama, S. Akiyama, H. Nishiyama, Y. Inoue, T. Takewaki, T. Setoyama, T. Minegishi, T. Takata, T. Yamada, K. Domen, A Particulate Photocatalyst Water-Splitting Panel for Large-Scale Solar Hydrogen Generation, Joule. 2 (2018) 509–520. doi:10.1016/j.joule.2017.12.009.

[38] R.L. Doyle, M.E.G. Lyons, The Oxygen Evolution Reaction: Mechanistic Concepts and Catalyst Design, Springer International Publishing, 2016. doi:10.1007/978-3-319-29641-8.

[39] J. Greeley, N.M. Markovic, The road from animal electricity to green energy: combining experiment and theory in electrocatalysis, Energy Environ. Sci. 5 (2012) 9246. doi:10.1039/c2ee21754f.

[40] C. Lamy, From hydrogen production by water electrolysis to its utilization in a PEM fuel cell or in a SO fuel cell: Some considerations on the energy efficiencies *, Int. J. Hydrogen Energy. 41 (2016) 15415–15425. doi:10.1016/j.ijhydene.2016.04.173.

[41] A. Lasia, A. Rami, Kinetics of hydrogen evolution on nickel electrodes, J. Electroanal. Chem. Interfacial Electrochem. 294 (1990) 123–141. doi:10.1016/0022-0728(90)87140-F.

[42] M.E.G. Lyons, R.L. Doyle, D. Fernandez, I.J. Godwin, M.P. Browne, A. Rovetta, The mechanism and kinetics of electrochemical water oxidation at oxidized metal and metal oxide electrodes. Part 1. General considerations: A mini review, Electrochem. Commun. 45 (2014) 60–62. doi:10.1016/j.elecom.2014.04.018.

[43] I.J. Godwin, M.E.G. Lyons, Enhanced oxygen evolution at hydrous nickel oxide electrodes via electrochemical ageing in alkaline solution, Electrochem. Commun. 32 (2013) 39–42. doi:10.1016/j.elecom.2013.03.040.

[44] W. Sheng, H.A. Gasteiger, Y. Shao-Horn, Hydrogen Oxidation and Evolution Reaction Kinetics on Platinum: Acid vs Alkaline Electrolytes, J. Electrochem. Soc. 157 (2010) B1529. doi:10.1149/1.3483106.

[45] R.D. Giles, J.A. Harrison, R.H. Thirsk, Catalytic Hydrogen Evolution on Ruthenium and Platinum Nuclei, Electroanal. Chem. Interfacial Electrochem. 20 (1969) 47–60. doi:10.1016/S0022-0728(69)80006-9.

[46] J.O. Bockris, I.A. Ammar, A.K.M.S. Huq, The Mechanism of the Hydrogen Evolution Reaction on Platinum Silver and Tungsten Surfaces in Acid Solutions, J. Phys. Chem. 61 (1957) 879–886. doi:10.1021/j150553a008.

[47] K. Yamamoto, .M. Kolb, R. Kötz, G. Lehmpfuhl, Hydrogen adsorption and oxide formation on platinum single crystal electrodes, J. Electroanal. Chem. 96 (1979) 233–239. doi:10.1016/S0022-0728(79)80380-0.

[48] S. Marini, P. Salvi, P. Nelli, R. Pesenti, M. Villa, M. Berrettoni, G. Zangari, Y. Kiros, Advanced alkaline water electrolysis, Electrochim. Acta. 82 (2012) 384–391. doi:10.1016/j.electacta.2012.05.011.

[49] W.E. O'Grady, C. Iwakura, J. Huang, E. Yeager, Ruthenium Oxide Catalysts for the Oxygen Electrode, in: Electrocatalysis, The Electrochemical Society, Princeton, N.J., 1974: p. 286.

[50] J.O.M. Bockris, T. Otagawa, The Electrocatalysis of Oxygen Evolution on Perovskites, J. Electrochem. Soc. 131 (1984) 290–302. doi:10.1149/1.2115565.

[51] M.T.M. Koper, Thermodynamic theory of multi-electron transfer reactions: Implications for electrocatalysis, J. Electroanal. Chem. 660 (2011) 254–260. doi:10.1016/j.jelechem.2010.10.004.

[52] M. Schalenbach, A.R. Zeradjanin, O. Kasian, S. Cherevko, K.J.J. Mayrhofer, A Perspective on Low-Temperature Water Electrolysis – Challenges in Alkaline and Acidic Technology, Int. J. Electrochem. Sci. 13 (2018) 1173–1226. doi:10.20964/2018.02.26.

[53] A. Manabe, M. Kashiwase, T. Hashimoto, T. Hayashida, A. Kato, K. Hirao, I. Shimomura, I. Nagashima, Basic study of alkaline water electrolysis, Electrochim. Acta. 100 (2013) 249–256. doi:10.1016/j.electacta.2012.12.105.

[54] S.M. Steen III, F.-Y. Zhang, In-situ and Ex-situ Characterizations of Electrode Interfaces in Energy Storage Electrolyzers, Electrochem. Soc. Trans. 59 (2014) 95–102. doi:10.1149/05901.0095ecst.

[55] K.E. Ayers, E.B. Anderson, C.B. Capuano, B.D. Carter, L.T. Dalton, G. Hanlon, J. Manco, M. Niedzwiecki, Research Advances Towards Low Cost, High Efficiency PEM Electrolysis, ECS Trans. 33 (2010) 3–15. doi:10.1149/1.3484496.

[56] Air Liquide is leading the largest Power to Hydrogen project in Europe, (2016). https://www.airliquide.com/media/air-liquide-leading-largest-power-hydrogen-project-europe (accessed 6 September 2018).

[57] Weltgrösste Wasserstoff-Elektrolyse entsteht in der Rheinland Raffinerie, (2018). https://www.shell.de/medien/shell-presseinformationen/2018/weltweit-groeßte-wasserstoff-elektrolyse-anlage-rheinland.html (accessed 6 September 2018).

[58] SILYZER 300, (2018). https://www.siemens.com/content/dam/webassetpool/mam/tag-siemens-com/smdb/corporate-core/sustainable_energy/hydrogensolutions/broschüren/ct-ree-18-047-db-silyzer-300-db-de-en-rz.pdf (accessed 6 September 2018).

[59] M. Gong, W. Zhou, M.-C. Tsai, J. Zhou, M. Guan, M.-C. Lin, B. Zhang, Y. Hu, D.-Y. Wang, J. Yang, S.J. Pennycook, B.-J. Hwang, H. Dai, Nanoscale nickel oxide/nickel heterostructures for active hydrogen evolution electrocatalysis., Nat. Commun. 5 (2014) 4695. doi:10.1038/ncomms5695.

[60] M. Shalom, D. Ressnig, X. Yang, G. Clavel, T.P. Fellinger, M. Antonietti, Nickel nitride as an efficient electrocatalyst for water splitting, J. Mater. Chem. A. 3 (2015) 8171–8177. doi:10.1039/C5TA00078E.

[61] T. Sun, L. Xu, Y. Yan, A.A. Zakhidov, R.H. Baughman, J. Chen, Ordered Mesoporous Nickel Sphere Arrays for Highly Efficient Electrocatalytic Water Oxidation, ACS Catal. 6 (2016) 1446–1450. doi:10.1021/acscatal.5b02571.

[62] C.A.C. Sequeira, D.M.F. Santos, B. Šljukić, L. Amaral, Physics of Electrolytic Gas Evolution, Brazilian J. Phys. 43 (2013) 1–30. doi:10.1007/s13538-013-0131-4.

[63] C. Gabrielli, F. Huet, M. Keddam, A. Macias, A. Sahar, Potential drops due to an attached bubble on a gas-evolving electrode, J. Appl. Electrochem. 19 (1989) 617–618. doi:10.1007/BF01320636.

[64] H. Cheng, K. Scott, Improvement in methanol oxidation in a centrifugal field, J. Power Sources. 123 (2003) 137–150. doi:10.1016/S0378-7753(03)00526-3.

[65] M. Wang, Z. Wang, Z. Guo, Water electrolysis enhanced by super gravity field for hydrogen production, Int. J. Hydrogen Energy. 35 (2010) 3198–3205. doi:10.1016/j.ijhydene.2010.01.128.

[66] T. Iida, H. Matsushima, Y. Fukunaka, Water Electrolysis under a Magnetic Field, Jounal Electrochem. Soc. 154 (2007) 112–115. doi:10.1149/1.2742807.

[67] W. Kim, K. Park, J. Oh, J. Choi, H.Y. Kim, Visualization and minimization of disruptive bubble behavior in ultrasonic field, Ultrasonics. 50 (2010) 798–802. doi:10.1016/j.ultras.2010.04.002.

[68] S. Rahman, L.M. Al-hadhrami, M.M. Alam, Pumped hydro energy storage system: A technological review, Renew. Sustain. Energy Rev. 44 (2015) 586–598. doi:10.1016/j.rser.2014.12.040.

[69] F. Geth, T. Brijs, J. Kathan, J. Driesen, R. Belmans, An overview of large-scale stationary electricity storage plants in Europe: Current status and new developments, Renew. Sustain. Energy Rev. 52 (2015) 1212–1227. doi:10.1016/j.rser.2015.07.145.

[70] H.-W. Sinn, Buffering volatility: A study on the limits of Germany's energy revolution, Eur. Econ. Rev. 99 (2017) 130–150. doi:10.1016/j.euroecorev.2017.05.007.

[71] ESTORAGE, (2016). https://cordis.europa.eu/news/rcn/125319_en.html (accessed 22 September 2018).

[72] G. Do, P. Preuster, R. Aslam, A. Bösmann, K. Müller, W. Arlt, P. Wasserscheid, Hydrogenation of the Liquid Organic Hydrogen Carrier Compound Dibenzyltoluene – Reaction Pathway Determination by 1H-NMR Spectroscopy, React. Chem. Eng. 1 (2016) 313–320. doi:10.1039/C5RE00080G.

[73] G. Walker, Solid-State Hydrogen Storage: Materials and Chemistry, 1st ed., Woodhead Publishing, Cambrige, 2008.

[74] Hydrogen, (2018). https://encyclopedia.airliquide.com/hydrogen (accessed 11 September 2018).

[75] K.K. Pant, R.B. Gupta, Hydrogen Fuel: Production, Transport, and Storage, CRC Press Taylor & Francis Group, 2009.

[76] A. Ozarslan, Large-scale hydrogen energy storage in salt caverns, Int. J. Hydrogen Energy. 37 (2012) 14265–14277. doi:10.1016/j.ijhydene.2012.07.111.

[77] H.B.J. Stone, I. Veldhuis, R.N. Richardson, H.B.J. Stone, I.V.O. Veldhuis, R.N. Richardson, Underground hydrogen storage in the UK, Geol. Soc. 313 (2009) 217–226. doi:10.1144/SP313.13.

[78] Hydrogen test area at ILK Dresden, (2018). https://www.ilkdresden.de/en/service/research-and-development/project/hydrogen-test-area-at-ilk-dresden/ (accessed 27 September 2018).

[79] Erdgasversorgung in Deutschland, (2018). https://www.bmwi.de/Redaktion/DE/Artikel/Energie/gas-erdgasversorgung-in-deutschland.html (accessed 26 September 2018).

[80] J.L.C. Rowsell, O.M. Yaghi, Minireviews Strategies for Hydrogen Storage in Metal–Organic Frameworks, Angew. Chemie (Int. Ed.). 44 (2005) 4670–4679. doi:10.1002/anie.200462786.

[81] L. Zhou, Progress and problems in hydrogen storage methods, Renew. Sustain. Energy Rev. 9 (2005) 395–408. doi:10.1016/j.rser.2004.05.005.

[82] A. Züttel, Materials for hydrogen storage, Materialstoday. 6 (2003) 24–33. doi:10.1016/S1369-7021(03)00922-2.

[83] A.C. Dillon, K.M. Jones, T.A. Bekkedahl, C.H. Kiang, D.S. Bethune, M.J. Heben, Storage of hydrogen in single-walled carbon nanotubes, Nature. 386 (1997) 377–379. doi:10.1038/386377a0.

[84] W.B. Leung, N.H. March, Primitive phase diagram for hydrogen, Phys. Lett. 56 (1976) 425–426. doi:10.1016/0375-9601(76)90713-1.

[85] O.K. Farha, A.Ö. Yazaydin, I. Eryazici, C.D. Malliakas, B.G. Hauser, M.G. Kanatzidis, S.T. Nguyen, R.Q. Snurr, J.T. Hupp, De novo synthesis of a metal–organic framework material featuring ultrahigh surface area and gas storage capacities, Nat. Chem. 2 (2010) 944–948. doi:10.1038/nchem.834.

[86] U. Eberle, M. Felderhoff, F. Schüth, Chemical and Physical Solutions for Hydrogen Storage, Angew. Chemie - Int. Ed. 48 (2009) 6608–6630. doi:10.1002/anie.200806293.

[87] J. Li, S. Cheng, Q. Zhao, P. Long, J. Dong, Synthesis and hydrogen-storage behavior of metal–organic framework MOF-5, Int. J. Hydrogen Energy. 34 (2009) 1377–1382. doi:10.1016/j.ijhydene.2008.11.048.

[88] N.L. Rosi, J. Eckert, M. Eddaoudi, D.T. Vodak, J. Kim, M.O. Keeffe, O.M. Yaghi, Hydrogen Storage in Microporous Metal-Organic Frameworks, Science 300 (2003) 1127–1130. doi:10.1126/science.1083440.

[89] I. Hadjipaschalis, A. Poullikkas, V. Efthimiou, Overview of current and future energy storage technologies for electric power applications, Renew. Sustain. Energy Rev. 13 (2009) 1513–1522. doi:10.1016/j.rser.2008.09.028.

[90] GfE Speicherlegierungen: Hydralloy C, (2018). https://www.gfe.com/produktbereiche/legierungen/anwendungen/wasserstoffspeicherung/ (accessed 28 September 2018).

[91] K. Müller, K. Stark, V.N. Emel'yanenko, M.A. Varfolomeev, D.H. Zaitsau, E. Shoifet, C. Schick, S.P. Verevkin, W. Arlt, Liquid Organic Hydrogen Carriers: Thermophysical and Thermochemical Studies of Benzyl- and Dibenzyl-toluene Derivatives, Ind. Eng. Chem. Res. 54 (2015) 7967–7976. doi:10.1021/acs.iecr.5b01840.

[92] W.H.J. Graus, M. Voogt, E. Worrell, International comparison of energy efficiency of fossil power generation, Energy Policy. 35 (2007) 3936–3951. doi:10.1016/j.enpol.2007.01.016.

[93] V.C.G. Seydel, Thermodynamische Auslegung und Potentialstudien von Heavy-Duty Gasturbinen für kombinierte Gas- und Dampfkraftwerke, 2014.

[94] P. Chiesa, G. Lozza, L. Mazzocchi, Using Hydrogen as Gas Turbine, J. Eng. Gas Turbines Power. 127 (2005) 73–80. doi:10.1115/1.1787513.

[95] Most efficient combined cycle power plant, (2018). http://www.guinnessworldrecords.com/world-records/431420-most-efficient-combined-cycle-power-plant (accessed 4 October 2018).

[96] C.J. Winter, J. Nitsch, Wasserstoff als Energieträger – Technik, Systeme, Wirtschaft, 2. Auflage, Springer-Verlag, Berlin, Heidelberg, New York, 1989. doi:10.1007/978-3-642-97884-5.

[97] A. Poullikkas, Implementation of distributed generation technologies in isolated power systems, Renew. Sustain. Energy Rev. 11 (2007) 30–56. doi:10.1016/j.rser.2006.01.006.

[98] A. Mehra, X. Zhang, A.A. Ayón, I.A. Waitz, M.A. Schmidt, C.M. Spadaccini, A Six-Wafer Combustion System for a Silicon Micro Gas Turbine Engine, J. Micromechanical Syst. 9 (2000) 517–527. doi:10.1109/84.896774.

[99] H.H. Funke, S. Boerner, J. Keinz, K. Kusterer, D. Kroniger, J. Kitajima, M. Kazari, A. Horikawa, Numerical and Experimental Characterization of low NOx Micromix Combustion Principle for industrial Hydrogen Gas Turbine Applications, in: ASME Turbo Expo 2012 GT2012, 2012: pp. 1–11. doi:10.1115/GT2012-69421.

[100] H.H. Funke, J. Dickhoff, J. Keinz, A.H. Ayed, A. Parente, P. Hendrick, Experimental and Numerical Study of the Micromix Combustion Principle Applied for Hydrogen and Hydrogen- Rich Syngas as Fuel with Increased Energy Density for Industrial Gas Turbine Applications, Energy Procedia. 61 (2014) 1736–1739. doi:10.1016/j.egypro.2014.12.201.

[101] Eine neue Ära der Mobilität beginnt. Der BMW Hydrogen 7., (2006). https://www.press.bmwgroup.com/austria/article/detail/T0026585DE/eine-neue-aera-der-mobilitaet-beginnt-der-bmw-hydrogen-7?language=de (accessed 4 October 2018).

[102] S. Verhelst, T. Wallner, Hydrogen-fueled internal combustion engines, Prog. Energy Combust. Sci. 35 (2009) 490–527. doi:10.1016/j.pecs.2009.08.001.

[103] Y. Haseli, Maximum conversion efficiency of hydrogen fuel cells, Int. J. Hydrogen Energy. 43 (2018) 9015–9021. doi:10.1016/j.ijhydene.2018.03.076.

[104] N.M. Sammes, R. Bove, J. Pusz, F. Barbir, Fuel Cell Technology: Reaching Towards Commercialization, Springer-Verlag, London, 2006.

[105] N.M. Markovic, T.J. Schmidt, V. Stamenkovic, P.N. Ross, Oxygen Reduction Reaction on Pt and Pt Bimetallic Surfaces: A Selective Review, Fuel Cells. 1 (2001) 105–116. doi:10.1002/1615-6854(200107)1:2<105::aid-fuce105>3.3.co;2-0.

[106] M.K. Debe, Electrocatalyst approaches and challenges for automotive fuel cells, Nature. 486 (2012) 43–51. doi:10.1038/nature11115.

[107] P.J. Rheinländer, J. Herranz, J. Durst, H.A. Gasteiger, Kinetics of the Hydrogen Oxidation/Evolution Reaction on Polycrystalline Platinum in Alkaline Electrolyte Reaction Order with Respect to Hydrogen Pressure, J. Electrochem. Soc. 161 (2014) 1448–1457. doi:10.1149/2.0501414jes.

[108] A.L. Dicks, D.A.J. Rand, Fuel Cell Systems Explained, Third Edit, John Wiley & Sons Ltd, 2018.

[109] V. Stamenković, T.J. Schmidt, P.N. Ross, N.M. Marković, Surface segregation effects in electrocatalysis: Kinetics of oxygen reduction reaction on polycrystalline Pt3Ni alloy surfaces, J. Electroanal. Chem. 554–555 (2003) 191–199. doi:10.1016/S0022-0728(03)00177-3.

[110] Y. Jiao, Y. Zheng, M. Jaroniecb, S.Z. Qiao, Design of electrocatalysts for oxygen- and hydrogen-involving energy conversion reactions, Chem. Soc. Rev. 44 (2015) 2023–2576. doi:10.1039/c4cs00470a.

[111] M. Saternus, A. Fornalczyk, J. Cebulski, Analysis of Platinum Content in used Auto Catalytic Converter Carriers and the Possibility of its Revovery, Arch. Metall. Mater. 59 (2014) 557–564. doi:10.2478/amm-2014-0092.

[112] J. Mitzel, A. Friedrich, Keine Zukunft für Brennstoffzellen Fahrzeuge?, HZwei. 14 (2014) 32–34.

[113] K.A. Burke, Fuel Cells for Space Science Applications, in: First Int. Energy Convers. Eng. Conf., 2003: pp. 1–10. doi:10.2514/6.2003-5938.

[114] R. Berger, Fuel Cell Electric Buses - Potential for Sustainable Public Transport in Europe, 2015. https://www.rolandberger.com/de/Publications/Fuel-Cell-Electric-Buses.html.

[115] G. Morrison, J. Stevens, F. Joseck, Relative economic competitiveness of light-duty battery electric and fuel cell electric vehicles, Transp. Res. Part C. 87 (2018) 183–196. doi:10.1016/j.trc.2018.01.005.

[116] Project Portal: Toyota's commitment to reducing transport truck greenhouse gas emissions to zero, (2018). https://www.toyota.ca/toyota/en/connect/2954/project-portal-a-more-environmentally-friendly-transport-truck (accessed 17 October 2018).

[117] Erfolgreiche erste Testfahrt von Alstoms Wasserstoffzug Coradia iLint bei 80 km/h, (2017). https://www.alstom.com/de/press-releases-news/2017/3/erfolgreiche-erste-testfahrt-von-alstoms-wasserstoffzug-coradia-ilint-bei-80-kmh (accessed 18 October 2018).

[118] Erster Brennstoffzellenzug der Welt im Fahrgastbetrieb bei der evb, (2018). https://www.evb-elbe-weser.de/aktuelles/detail/?tx_news_pi1%5Baction%5D=detail&tx_news_pi1%5Bcontroller%5D=News&tx_news_pi1%5Bnews%5D=55&cHash=4a885c6502cc785a5f81aaca66c9bab7&L=0 (accessed 14 November 2018).

[119] Wasserdampf statt Dieselruß, (2018). https://www.rmv.de/c/de/informationen-zum-rmv/der-rmv/rmv-aktuell/ilint-zugfahrt-wasserstoff-antrieb/ (accessed 14 November 2018).

[120] J. Wing, Analyst View: Fuel Cells and Submarines, FuelCellToday. (2013).

[121] HDW Fuel Cell AIP System – proven power, simply silent, (2018). https://www.thyssenkrupp-marinesystems.com/en/hdw-fuel-cell-aip-system.html (accessed 14 November 2018).

[122] An Odyssey for the Future on board the first Hydrogen Vessel around the World, (2018). http://www.energy-observer.org/en/ (accessed 8 October 2018).

[123] H. Gasteiger, S.S. Kocha, B. Sompalli, F.T. Wagner, Activity benchmarks and requirements for Pt, Pt-alloy, and non-Pt oxygen reduction catalysts for PEMFCs, Appl. Catal. B Environ. 56 (2005) 9–35. doi:10.1016/j.apcatb.2004.06.021.

[124] J. Zhang, Z. Xie, J. Zhang, Y. Tang, C. Song, T. Navessin, Z. Shi, D. Song, H. Wang, D.P. Wilkinson, Z. Liu, S. Holdcroft, High temperature PEM fuel cells, J. Power Sources. 160 (2006) 872–891. doi:10.1016/j.jpowsour.2006.05.034.

[125] C. Wang, H. Daimon, T. Onodera, T. Koda, S.H. Sun, A general approach to the size- and shape-controlled synthesis of platinum nanoparticles and their catalytic reduction of oxygen, Angew. Chemie - Int. Ed. 47 (2008) 3588–3591. doi:10.1002/anie.200800073.

[126] J. Greeley, I.E.L. Stephens, a S. Bondarenko, T.P. Johansson, H. a Hansen, T.F. Jaramillo, J. Rossmeisl, I. Chorkendorff, J.K. Nørskov, Alloys of platinum and early transition metals as oxygen reduction electrocatalysts, Nat. Chem. 1 (2009) 552–556. doi:10.1038/nchem.367.

[127] J.K. Nørskov, J. Rossmeisl, A. Logadottir, L. Lindqvist, J.R. Kitchin, T. Bligaard, H. Jónsson, Origin of the Overpotential for Oxygen Reduction at a Fuel-Cell Cathode, J. Phys. Chem. B. 108 (2004) 17886–17892. doi:10.1021/jp047349j.

[128] J.R. Kitchin, J.K. Nørskov, M.A. Barteau, J.G. Chen, Role of Strain and Ligand Effects in the Modification of the Electronic and Chemical Properties of Bimetallic Surfaces, Phys. Rev. Lett. 93 (2004) 156801–1. doi:10.1103/PhysRevLett.93.156801.

[129] L. Gan, C. Cui, M. Heggen, F. Dionigi, S. Rudi, P. Strasser, Element-specific anisotropic growth of shaped platinum alloy nanocrystals., Science 346 (2014) 1502–1506. doi:10.1126/science.1261212.

[130] C. Cui, L. Gan, M. Heggen, S. Rudi, P. Strasser, Compositional segregation in shaped Pt alloy nanoparticles and their structural behaviour during electrocatalysis, Nat. Mater. 12 (2013) 765–771. doi:10.1038/nmat3668.

[131] Y. Lu, S. Du, R. Steinberger-Wilckens, One-dimensional nanostructured electrocatalysts for polymer electrolyte membrane fuel cells-A review, Appl. Catal. B Environ. 199 (2016) 292–314. doi:10.1016/j.apcatb.2016.06.022.

[132] D. Wang, H.L. Xin, R. Hovden, H. Wang, Y. Yu, D. a. Muller, F.J. DiSalvo, H.D. Abruña, Structurally ordered intermetallic platinum–cobalt core–shell nanoparticles with enhanced activity and stability as oxygen reduction electrocatalysts, Nat. Mater. 12 (2012) 81–87. doi:10.1038/nmat3458.

[133] S. Koh, P. Strasser, Electrocatalysis on bimetallic surfaces: Modifying catalytic reactivity for oxygen reduction by voltammetric surface dealloying, J. Am. Chem. Soc. 129 (2007) 12624–12625. doi:10.1021/ja0742784.

[134] C. Baldizzone, L. Gan, N. Hodnik, G.P. Keeley, A. Kostka, M. Heggen, P. Strasser, K.J.J. Mayrhofer, Stability of Dealloyed Porous Pt/Ni Nanoparticles, ACS Catal. 5 (2015) 5000–5007. doi:10.1021/acscatal.5b01151.

[135] V.R. Stamenkovic, B. Fowler, B.S. Mun, G. Wang, P.N. Ross, C. a Lucas, N.M. Marković, Improved oxygen reduction activity on Pt3Ni(111) via increased surface site availability., Science 315 (2007) 493–7. doi:10.1126/science.1135941.

[136] D.A. Cullen, M. Lopez-Haro, P. Bayle-Guillemaud, L. Guetaz, M.K. Debe, A.J. Steinbach, Linking morphology with activity through the lifetime of pretreated PtNi nanostructured thin film catalysts, J. Mater. Chem. A. 3 (2015) 11660–11667. doi:10.1039/C5TA01854D.

[137] M.K. Debe, Tutorial on the Fundamental Characteristics and Practical Properties of Nanostructured Thin Film (NSTF) Catalysts, J. Electrochem. Soc. 160 (2013) 522–534. doi:10.1149/2.049306jes.

[138] M.K. Debe, A.K. Schmoeckel, G.D. Vernstrom, R. Atanasoski, High voltage stability of nanostructured thin film catalysts for PEM fuel cells, J. Power Sources 161 (2006) 1002–1011. doi:10.1016/j.jpowsour.2006.05.033.

[139] C. Hung, P. Lim, J. Chen, H.C. Shih, Corrosion of carbon support for PEM fuel cells by electrochemical quartz crystal microbalance, J. Power Sources 196 (2011) 140–146. doi:10.1016/j.jpowsour.2010.07.015.

[140] R.M. Ormerod, Solid oxide fuel cells, Chem. Soc. Rev. 32 (2003) 17–28. doi:10.1039/b105764m.

[141] BlueGen the world's most efficient micro-CHP, (2016). http://www.solidpower.com/fileadmin/user_upload/pages/Logos_materialien/SOLIDpower_BlueGEN_Brochure_UK_web.pdf (accessed 29 October 2018).

[142] Elcogen Products, (2017). http://www.elcogen.com/products/ (accessed 29 October 2018).

[143] Y. Kobayashi, K. Tomida, M. Nishiura, K. Takenobu, K. Hiwatashi, H. Kishizawa, Development of Next-Generation Large-Scale SOFC toward Realization of a Hydrogen Society, Mitsubishi Heavy Ind. Tech. Rev. 52 (2015) 111–116. doi:10.1299/jsmemecj.2015._S0830303-.

[144] J.R. Wilson, A.T. Duong, M. Gameiro, H.Y. Chen, K. Thornton, D.R. Mumm, S.A. Barnett, Quantitative three-dimensional microstructure of a solid oxide fuel cell cathode, Electrochem. Commun. 11 (2009) 1052–1056. doi:10.1016/j.elecom.2009.03.010.

[145] A. Grimaud, F. Mauvy, J.M. Bassat, S. Fourcade, L. Rocheron, M. Marrony, J.C. Grenier, Hydration Properties and Rate Determining Steps of the Oxygen Reduction Reaction of Perovskite-Related Oxides as H+-SOFC Cathodes, J. Electrochem. Soc. 159 (2012) B683. doi:10.1149/2.101205jes.

[146] H. Rismani-Yazdi, S.M. Carver, A.D. Christy, O.H. Tuovinen, Cathodic limitations in microbial fuel cells: An overview, J. Power Sources 180 (2008) 683–694. doi:10.1016/j.jpowsour.2008.02.074.

[147] F. Zhao, F. Harnisch, U. Schröder, F. Scholz, P. Bogdanoff, I. Herrmann, Application of pyrolysed iron(II) phthalocyanine and CoTMPP based oxygen reduction catalysts as cathode materials in microbial fuel cells, Electrochem. Commun. 7 (2005) 1405–1410. doi:10.1016/j.elecom.2005.09.032.

[148] U. Schröder, Editorial: Microbial Fuel Cells and Microbial Electrochemistry: Into the Next Century!, ChemSusChem. 5 (2012) 959–959. doi:10.1002/cssc.201200319.

[149] P.L. McCarty, J. Bae, J. Kim, Domestic Wastewater Treatment as a Net Energy Producer - Can This be Achieved?, Environ. Sci. Technol. 45 (2011) 7100–7106. doi:10.1021/es2014264 |.

[150] A. Durth, Abwasser und Klärschlamm in Deutschland - statistische Betrachtungen, Korrespondenz Abwasser, Abfall. 61 (2014) 1106–1112. doi:10.3242/kae2014.12.003.

[151] E.S. Heidrich, T.P. Curtis, J. Dolfing, Determination of the Internal Chemical Energy of Wastewater, Environ. Sci. Technol. 45 (2011) 827–832. doi:10.1021/es103058w.

[152] B.E. Logan, K. Rabaey, Conversion of Wastes into Bioelectricity and Chemicals by Using Microbial Electrochemical Technologies, Science 337 (2012) 686. doi:10.1007/s13398-014-0173-7.2.

[153] G.G. Botte, Electrochemical Manufacturing in the Chemical Industry, Electrochem. Soc. Interface. 23 (2014) 49–55. doi:10.1149/2.F04143if.

[154] M.K. Cho, A. Lim, S.Y. Lee, H. Kim, S.J. Yoo, Y. Sung, H.S. Park, J.H. Jang, A Review on Membranes and Catalysts for Anion Exchange Membrane Water Electrolysis Single Cells, Jounral Electrochem. Sci. Technol. 8 (2017) 183–196. doi:10.5229/JECST.2017.8.3.183.

[155] M.S. Brown, C.B. Arnold, Fundamentals of Laser-Material Interaction and Application to Multiscale Surface Modification, in: Laser Precis. Microfabr., Springer, Berlin, Heidelberg, 2010: pp. 91–120. doi:10.1007/978-3-642-10523-4.

[156] K.H. Leitz, B. Redlingshöfer, Y. Reg, A. Otto, M. Schmidt, Metal ablation with short and ultrashort laser pulses, Phys. Procedia. 12 (2011) 230–238. doi:10.1016/j.phpro.2011.03.128.

[157] C. Momma, S. Nolte, B. N. Chichkov, F. v. Alvensleben, A. Tünnermann, Precise laser ablation with ultrashort pulses, Appl. Surf. Sci. 109–110 (1997) 15–19. doi:10.1016/S0169-4332(96)00613-7.

[158] J. Koch, F. Korte, T. Bauer, C. Fallnich, A. Ostendorf, B.N. Chichkov, Nanotexturing of gold films by femtosecond laser-induced melt dynamics, Appl. Phys. A Mater. Sci. Process. 81 (2005) 325–328. doi:10.1007/s00339-005-3212-6.

[159] K. Sugioka, Y. Cheng, Ultrafast lasers—reliable tools for advanced materials processing, Light Sci. Appl. 3 (2014) e149. doi:10.1038/lsa.2014.30.

[160] I.N. Zavestovskaya, A.P. Kanavin, N.A. Men'kova, Crystallization of metals under conditions of superfast cooling when materials are processed with ultrashort laser pulses, J. Opt. Technol. 75 (2008) 353–358. doi:10.1364/JOT.75.000353.

[161] C. Unger, J. Koch, L. Overmeyer, B.N. Chichkov, Time-resolved studies of femtosecond-laser induced melt dynamics, Opt. Express. 20 (2012) 24864–24872. doi:10.1364/OE.20.024864.

[162] E.J.Y. Ling, J. Saïd, N. Brodusch, R. Gauvin, P. Servio, A.-M. Kietzig, Investigating and understanding the effects of multiple femtosecond laser scans on the surface topography of stainless steel 304 and titanium, Appl. Surf. Sci. 353 (2015) 512–521. doi:10.1016/j.apsusc.2015.06.137.

[163] S. Williams, Handbook of Laser Technology and Applications, 1st ed., CRC Press, Bristol and Philadelphia, 2004.

[164] P. Gečys, E. Markauskas, S. Nishiwaki, S. Buecheler, R. De Loor, A. Burn, V. Romano, G. Račiukaitis, CIGS thin-film solar module processing: case of high-speed laser scribing, Sci. Rep. 7 (2017) 40502. doi:10.1038/srep40502.

[165] I. Etsion, E. Sher, Improving fuel efficiency with laser surface textured piston rings, Tribol. Int. J. 42 (2009) 542–547. doi:10.1016/j.triboint.2008.02.015.

[166] S. Bruening, G. Hennig, S. Eifel, A. Gillner, Ultrafast scan techniques for 3D-µm structuring of metal surfaces with high repetitive ps-laser pulses, Phys. Procedia. 12 (2011) 105–115. doi:10.1016/j.phpro.2011.03.112.

[167] Fraunhofer entwickelt neue Lasergeneration, (2018). https://www.ilt.fraunhofer.de/de/presse/pressemitteilungen/pm2018/pressemitteilung-2018-7-4.html (accessed 29 October 2018).

[168] M. Birnbaum, Modulation of the reflectivity of semiconductors, J. Appl. Phys. 36 (1965) 657–658. doi:10.1063/1.1714053.

[169] J. Bonse, S. V. Kirner, S. Höhm, N. Epperlein, D. Spaltmann, A. Rosenfeld, J. Krüger, Applications of laser-induced periodic surface structures (LIPSS), Proc. SPIE. 10092 (2017) 100920N. doi:10.1117/12.2250919.

[170] A.Y. Vorobyev, C. Guo, Direct femtosecond laser surface nano/microstructuring and its applications, Laser Photon. Rev. 407 (2013) 385–407. doi:10.1002/lpor.201200017.

[171] I.N. Zavestovskaya, Laser nanostructuring of materials surfaces, Quantum Electron. 40 (2010) 942–954. doi:10.1070/QE2010v040n11ABEH014447.

[172] A.Y. Vorobyev, C. Guo, Colorizing metals with femtosecond laser pulses, Appl. Phys. Lett. 92 (2008) 41914. doi:10.1063/1.2834902.

[173] T. Knüttel, S. Bergfeld, S. Haas, Laser Texturing of Surfaces in Thin-Film Silicon Photovoltaics - A Comparison of Potential Processes, J. Laser Micro/Nanoengineering. 8 (2013) 222–229. doi:10.2961/jlmn.2013.03.0007.

[174] J. Bonse, R. Koter, M. Hartelt, D. Spaltmann, S. Pentzien, S. Höhm, A. Rosenfeld, J. Krüger, Femtosecond laser-induced periodic surface structures on steel and titanium alloy for tribological applications, Appl. Phys. A. 117 (2014) 103–110. doi:10.1007/s00339-014-8229-2.

[175] A.R. Neale, Y. Jin, J. Ouyang, S. Hughes, D. Hesp, V. Dhanak, G. Dearden, S. Edwardson, L.J. Hardwick, Electrochemical performance of laser micro-structured nickel oxyhydroxide cathodes, J. Power Sources. 271 (2014) 42–47. doi:10.1016/j.jpowsour.2014.07.167.

[176] C.A. Zuhlke, T.P. Anderson, D.R. Alexander, Formation of multiscale surface structures on nickel via above surface growth and below surface growth mechanisms using femtosecond laser pulses, Opt. Express. 21 (2013) 8460–8473. doi:10.1364/OE.21.008460.

[177] A.Y. Vorobyev, C. Guo, Multifunctional surfaces produced by femtosecond laser pulses, J. Appl. Phys. 117 (2015) 33103. doi:10.1063/1.4905616.

[178] S. Schlie, E. Fadeeva, J. Koch, A. Ngezahayo, B.N. Chichkov, Femtosecond laser fabricated spike structures for selective control of cellular behavior., J. Biomater. Appl. 25 (2010) 217–233. doi:10.1177/0885328209345553.

[179] S. Schlie, E. Fadeeva, A. Koroleva, A. Ovsianikov, J. Koch, A. Ngezahayo, B.N. Chichkov, Laser-based nanoengineering of surface topographies for biomedical applications, Photonics Nanostructures - Fundam. Appl. 9 (2011) 159–162. doi:10.1016/j.photonics.2010.09.006.

[180] E.A. Bremus-Koebberling, S. Beckemper, B. Koch, A. Gillner, Nano structures via laser interference patterning for guided cell growth of neuronal cells, J. Laser Appl. 24 (2012) 42013. doi:10.2351/1.4730804.

[181] A.Y. Vorobyev, C. Guo, Femtosecond laser structuring of titanium implants, Appl. Surf. Sci. 253 (2007) 7272–7280. doi:10.1016/j.apsusc.2007.03.006.

[182] T. Rauscher, C. Immanuel, A. Gabler, T. Gimpel, M. Köhring, B. Kieback, W. Schade, L. Röntzsch, Femtosecond-laser structuring of Ni electrodes for highly active hydrogen evolution, Electrochim. Acta. 247 (2017) 1130–1139. doi:10.1016/j.electacta.2017.07.074.

[183] A. Gabler, C.I. Mu, T. Rauscher, T. Gimpel, R. Hahn, K. Michael, Ultrashort-pulse laser structured titanium surfaces with sputter-coated platinum catalyst as hydrogen evolution electrodes for alkaline water electrolysis, Int. J. Hydrogen Energy. 43 (2018) 7216–7226. doi:10.1016/j.ijhydene.2018.02.130.

[184] A.Y. Vorobyev, C. Guo, Femtosecond Laser Blackening of Metals, in: Int. Midwest Symp. Circuits Syst., 2009: pp. 905–908. doi:10.1109/MWSCAS.2009.5235913.

[185] A.Y. Vorobyev, C. Guo, Optical and Wetting Properties of Femtosecond Laser Nanostructured Materials, J. Nano Res. 14 (2011) 57–67. doi:10.4028/www.scientific.net/JNanoR.14.57.

[186] K. Kurselis, R. Kiyan, B.N. Chichkov, Formation of corrugated and porous steel surfaces by femtosecond laser irradiation, Appl. Surf. Sci. 258 (2012) 8845–8852. doi:10.1016/j.apsusc.2012.05.102.

[187] G. Li, J. Li, C. Zhang, Y. Hu, X. Li, J. Chu, W. Huang, D. Wu, Large-Area One-Step Assembly of Three-Dimensional Porous Metal Micro/Nanocages by Ethanol-Assisted Femtosecond Laser Irradiation for Enhanced Antireflection and Hydrophobicity, ACS Appl. Mater. Interfaces. 7 (2015) 383–390. doi:10.1021/am506291f.

[188] T. Kadyk, D. Bruce, M. Eikerling, How to Enhance Gas Removal from Porous Electrodes?, Sci. Rep. 6 (2016) 38780. doi:10.1038/srep38780.

[189] U. Hermens, S. V Kirner, C. Emonts, P. Comanns, E. Skoulas, A. Mimidis, H. Mescheder, K. Winands, J. Krüger, E. Stratakis, J. Bonse, Mimicking lizard-like surface structures upon ultrashort laser pulse irradiation of inorganic materials, Appl. Surf. Sci. 418 (2017) 499–507. doi:10.1016/j.apsusc.2016.12.112.

7 Appendix

LIST OF PUBLICATIONS

Included in this thesis:

1| **Karsten Lange***, Malte Schulz-Ruhtenberg, Jürgen Caro, *ChemElectroChem,* 2017, 4, 570–576
Platinum Electrodes for Oxygen Reduction Catalysis Designed by Ultrashort Pulse Laser Structuring

2| Mario Wolf, Jürgen Caro, Armin Feldhoff, Frank Steinbach, Malte Schulz-Ruhtenberg, **Karsten Lange***, *Electrochimica Acta,* 2017, 252, 430-437
Laser directed dynamic hydrogen template deposition of porous Pt@Ag networks

3| **Karsten Lange*,** Christian Hördemann, Malte Schulz-Ruhtenberg, Jürgen Caro, *ChemElectroChem,* 2018*,* 5, 3688-3694
Porous nickel nano-foam by femtosecond laser structuring for supercapacitor application

4| Felix Rieck genannt Best, Jürgen Koch, Gerhard Lilienkamp, Franz Körkemeyer, Hans Jürgen Maier, Jürgen Caro and **Karsten Lange***, *International Journal of Electrochemistry*, 2018, Volume 2018, 12 pages
Spiky Nickel Electrodes for Electrochemical Oxygen Evolution Catalysis by Femtosecond Laser Structuring

Not included in this thesis:

5| **Karsten Lange**, *Advances in Engineering,* 2017, 9, invited highlight article
Platinum Electrodes for Oxygen Reduction Catalysis Designed by Ultrashort Pulse Laser Structuring

6| Kaiyue Zhu, Xuefeng Zhu*, Weishen Yang*, *Angewandte Chemie*, 2018, 130, accepted
In-situ-Methoden zur Charakterisierung elektrochemischer NiFe-Sauerstoff-entwicklungskatalysatoren
Translation from English to German

CURRICULUM VITAE

Karsten Lange

Born on 13 February 1988 in Jena, Germany.

Klausenberg 6
51429 Bergisch Gladbach
Germany

+49 157 5829 7875
lange.neo@gmail.com
linkedin.com/in/karsten-lange-b69a9716a

Education

2015 – 2018	**Leibniz University Hannover** *PhD in physical chemistry and electrochemistry*	**Hannover**
2012 – 2015	**Leibniz University Hannover** *Master of Science* in material- and nanochemistry	**Hannover**
2008 – 2012	**HTW Aalen** *Bachelor of Science* in chemistry	**Aalen**
2007	**German Armed Forces** Basic military service	**Regensburg**
2004 – 2007	**Higher Technical High School Jena Burgau** *Apprenticeship as Chemical-Technical Assistant* *"Fachhochschulreife"*	**Jena**
1998 – 2004	**Integrated comprehensive school Gerte Unrein** *Secondary school certificate*	**Jena**

Professional Experience

2017 – 2018	**Fraunhofer Institute for Laser Technology (ILT)** *Guest researcher*	**Aachen**
2015 – 2018	**Leibniz University Hannover** *Cumulative PhD thesis* supervised by Prof. Dr. Jürgen Caro ▪ Electrode structuring by ultrashort laser pulses - A new tool for the hydrogen economy	**Hannover**
2014 - 2015	**Evonik Industries AG** *Master's thesis* supervised by Dr. Alexey Merkulov ▪ New Metal Oxide Precursors for Liquid-Phase-Processeable Thin Film Transistors	**Marl**
2012	**Fraunhofer IKTS** *Bachelor's thesis* supervised by Dr. Hannes Richter ▪ Microwave Synthesis of Zeolitic Powders and Membranes for Gas Separation	**Hermsdorf**
2010	**Local Authorities Association for regional water supply** *Internship* ▪ Liquid chromatography–mass spectrometry (LC-MS) of drinking water	**Langenau**